NEW INSIGHTS INTO PECULIAR THERMONUCLEAR SUPERNOVAE AND LINE OF SIGHT EFFECTS IN GRAVITATIONAL LENSING

By

CURTIS MCCULLY

A dissertation submitted to the

Graduate School–New Brunswick

Rutgers, The State University of New Jersey

In partial fulfillment of the requirements

For the degree of

Doctor of Philosophy

Graduate Program in Physics and Astronomy

Written under the direction of

Dr. Saurabh Jha and Dr. Charles Keeton

And approved by

_____

_____

_____

_____

_____

New Brunswick, New Jersey

May, 2014

ABSTRACT OF THE DISSERTATION

New Insights into Peculiar Thermonuclear Supernovae and Line of Sight Effects in Gravitational Lensing

By CURTIS MCCULLY

Dissertation Director:

Dr. Saurabh Jha and Dr. Charles Keeton

Type Ia supernovae (SNe Ia) and gravitational lensing are important cosmological probes, but both are limited by theoretical, systematic uncertainties. One key uncertainty in distances derived using SNe Ia is our lack of understanding of the explosion mechanism for normal SNe Ia. We have studied peculiar type Iax supernovae that appear to be related to normal SNe Ia with the goal of understanding white dwarf explosions as a whole. In Chapter 2, using late-time Hubble Space Telescope (HST) observations of SN 2008A and SN 2005hk, both prototypical SNe Iax, we argue that these objects are pure deflagration explosions that do not unbind the white dwarf. In Chapter 3, we present observations of the type Iax SN 2012Z, one of the nearest ever discovered. Fortunately for us, its host galaxy, NGC 1309, was observed extensively with HST/ACS (to measure a Cepheid distance), giving us incredibly deep pre-explosion images of the site of SN 2012Z. We find that there is a source coincident with the position of the SN. We argue that the source is likely a helium star companion to the white dwarf that exploded.

In galaxy-scale gravitational lenses, one of the largest systematic uncertainties arises due

to other mass in the environment of the lens or along the line of sight (LOS). In Chapter 4, we develop an analytic framework to account for LOS effects. Our framework employs a hybrid approach treating a few perturbing galaxies as strong lenses, making it accurate, while treating the rest in the weak lensing approximation, making it also computationally efficient. In Chapter 5, we test our framework using simulations of realistic mass models. We suggest a method to characterize the strength of the LOS effects allowing us to systematically test when the weak lensing approximation is valid. We show that LOS effects are not equivalent to a single shear, but these non-linear effects are correctly captured by our framework. Our new methodology can be used to constrain cosmological parameters, like the Hubble Constant, in the era of precision gravitational lensing measurements.

Acknowledgments

I am so grateful for everyone who has helped me get to this point. There are so many friends, family, and mentors that there is no way I could list them all here, but I will mention a few. I would like to begin by thanking my advisors Saurabh Jha and Chuck Keeton. You have been wonderful advisors and I am so grateful for your unwavering support throughout my time in graduate school. I have learned so much from both of you as you have shaped me into the scientist and the person I am today.

I would also like to thank my thesis committee; Ted Williams, Mark Croft, and Ann Zabludoff for their guidance and support. I am so grateful to Ann Zabludoff and Adam Riess for their hard work as letter writers and their advice during job application season.

I would like to say thank you to all of the Rutgers astro faculty. Everyone's door is always open and each one of you has taken the time to invest in both my personal and professional growth and development.

I would like to thank Suzanne Brahmia for her support and lessons on pedagogy while I was a TA.

I would like to thank Karen Leighly, one of my undergraduate research advisors, for her direction and support in and before graduate school. I would also like to thank Ed Neuenschwander, my undergraduate advisor, for all of his support, encouragement, and advice. I am so grateful to have you as a mentor and a friend.

I would also like to thank my fellow graduate students for making this such a good work environment. Specifically, I would like to thank Brandon Patel who worked closely with me; also my friends and coffee compatriots, Shruti Panwalker and Chelsea Sharon. I think there are more problems that were solved on the way to get coffee than I can count. I would

also like to thank my dear friends Roger and Rebekah Clayton for all of their support and encouragement.

I would like to thank the students who worked with me as undergraduate researchers: Samia Bouzid, Tom Holoien, Viraj Pandya, and Yssavo Camacho.

I thank my family, Curt, Vicki, Ryan, and Cassaundra McCully, Ernie and Gena Shikles, and Ron Hodges for always supporting me and pushing me to strive to be the best person I can be.

I also thank my daughter Camille for always making me smile, even if it has been a long day. Finally, I am eternally grateful to the love of my life, my wife Christina. You have been by my side every step of this journey and I can't imagine going through this with anyone else. Without your loving support, this would not have been possible.

Much of the work presented here is published or will be published in the near future. Chapter 2 has been accepted by ApJ and is posted at McCully et al. (2013). Chapter 3 has been submitted to Nature. Chapter 4 has been submitted to MNRAS and is posted at McCully et al. (2014). Chapter 5 will be submitted to MNRAS in the near future. Portions of the work presented in Chapter 6 are published in Jones et al. (2013) and Patel et al. (2013). I would like to thank my collaborators on these works: Saurabh W. Jha, Ryan J. Foley, Ryan Chornock, Jon A. Holtzman, David D. Balam, David Branch, Alexei V. Filippenko, Joshua Frieman, Johan Fynbo, Lluis Galbany, Mohan Ganeshalingam, Peter M. Garnavich, Melissa L. Graham, Eric Y. Hsiao, Giorgos Leloudas, Douglas C. Leonard, Weidong Li, Adam G. Riess, Masao Sako, Donald P. Schneider, Jeffrey M. Silverman, Jesper Sollerman, Thea N. Steele, Rollin C. Thomas, J. Craig Wheeler, Chen Zheng, Lars Bildsten, Wen-fai Fong, Robert P. Kirshner, G. H. Marion, Maximilian D. Stritzinger, Charles R. Keeton, Kenneth C. Wong, Ann I. Zabludoff, Steven A. Rodney, David O. Jones, Or Graur, and Brandon Patel.

This work has been supported through NASA/*HST* grants GO-11133.01, GO-11590.01, and GO-12913.01, U.S. Department of Energy (DOE) grant DE-FG02-08ER41562, National

Science Foundation (NSF) CAREER award AST-0847157, NSF CAREER award AST-0747311, a GAANN Fellowship, and an Excellence in Mentoring Fellowship.

Dedication

For my wife and daughter.

Table of Contents

List of Tables

List of Figures

Chapter 1

Introduction

One of biggest outstanding problems in astrophysics today is understanding the dominant components of the Universe: dark matter and dark energy. While these make up $\sim 95\%$ of the energy density of the Universe (Planck Collaboration et al. 2013), they are both still largely a mystery. Dark energy which comprises the largest fraction of the energy density of the Universe, $\sim 75\%$, was discovered by mapping the cosmic expansion history. Using SNe Ia as cosmological distance indicators led to the discovery of the accelerating universe driven by dark energy which was recognized with the Nobel Prize in Physics in 2011 (Riess et al. 1998; Perlmutter et al. 1999).

Dark matter makes up a smaller fraction of the energy density of the universe than dark energy, but is still about four times as abundant as normal baryonic matter. Because gravitational lensing is sensitive to dark matter and normal matter, it is a uniquely capable probe to understand dark matter. Gravitational lensing has provided some of the strongest evidence for the existence of dark matter from measurements of the Bullet Cluster (Clowe et al. 2006).

Despite the tremendous success of both of these probes, we have still not solved the mystery of what these dark components actually are. As we move into an age of "precision cosmology" in which we are no longer limited by statistical uncertainties, mitigating systematics will be key to make progress understanding dark matter and dark energy.

Before we can talk about systematics, we need to step back and discuss both supernovae and gravitational lensing in general.

1.1 Supernovae

1.1.1 SNe Progenitors

A supernova marks the explosive death of a star. Therefore, to understand SNe, it is necessary to begin with some basic stellar evolution. Stars form out of cold gas (mostly hydrogen and helium) that gravitationally collapses until the temperature of the core is high enough to begin fusing hydrogen. As the star depletes the hydrogen in its core, the star begins to collapse again, heating the layer around the core of the star to begin hydrogen shell burning. Eventually, the core reaches a high enough temperature to burn helium in the core. The helium burning leaves carbon and oxygen as "ash" in the core. At this point we differentiate between low mass stars and high mass stars because their final fates are much different.

High mass stars ($\sim 4M_{\odot}$) can collapse again to get a high enough temperature to fuse carbon. If the mass $\sim 8M_{\odot}$, the temperature will increase until neon and eventually oxygen will burn in the core. While this is going on in the core, the temperature in the outer layers of the star increases high enough to have shell burning of hydrogen and helium, creating an onion like structure in the star. The final element to fuse in the core is silicon, which deposits iron. Iron has one of the most stable nuclei of any element. Because it takes more energy to fuse iron than is gained, the core will begin to collapse under its own gravity until it is held up by quantum mechanical degeneracy pressure; the core forms a neutron star. However, the weaker gravity in the outer shells causes the helium, neon, and carbon envelopes to collapse more slowly, giving them a longer infall time. When the outer layers hit the solid core, the outer layers rebound with a supersonic shock front, which unbinds the outer material of the star ($\sim 10^{51}$ ergs). However, the details of this rebound are still uncertain (see Kaufmann 1996; Carroll & Ostlie 2006; Arnett et al. 1989).

The cores of low mass stars, in contrast, cannot obtain high enough temperatures to fuse carbon. Rather than exploding like high mass stars, low mass stars puff off their outer

layers, forming a planetary nebula. The core eventually cools until it is held up by electron degeneracy pressure, leading to its final state: a white dwarf. If the star does not have a companion, the white dwarf will simply fade and cool forever. However, if the white dwarf is part of a close binary, the white dwarf may accrete matter from its companion. As the white dwarf accretes mass from its companion, it eventually approaches the Chandrasekhar mass limit ($1.39M_{\odot}$) at which point the carbon in the core ignites in a thermonuclear runaway destroying the star (Woosley & Weaver 1994). However, the nature of the companion and the details of the explosion are still uncertain.

Both core collapse and thermonuclear SNe affect their environments in a variety of ways. The explosion creates many elements through explosive nucleosynthesis that are not created elsewhere in the universe (Arnett 1996). These elements, other stellar material, and energy from the explosion are all deposited in the interstellar medium. SNe enrich the interstellar medium with metals which can increase star formation by enhancing gas cooling. On the other hand, the SNe explosions also deposit large amounts of energy heating the interstellar gas which quenches star formation, which in turn will affect future star formation and galaxy evolution.

1.1.2 SNe Classification

Historically, SNe were classified by their spectral properties before we understood their underlying explosion mechanism (core collapse or thermonuclear). Supernovae are observationally classified into two broad types, Type I and Type II (Minkowski 1941). Type I SNe are identified by the lack of hydrogen in their optical spectra, while Type II do have significant hydrogen emission features. In the mid 1980's significant variation was observed in Type I SNe so Type I SNe were sub-classified. SNe Ia are distinguished by the deep absorption of Si II around 6150 Å (Wheeler & Harkness 1990). Type Ib and Type Ic do not show this line (Filippenko 1997). Type Ib SNe have moderately strong He lines, especially the He I line at 5876 Å, compared to Type Ic SNe (see Figure 1.1 for examples of spectra

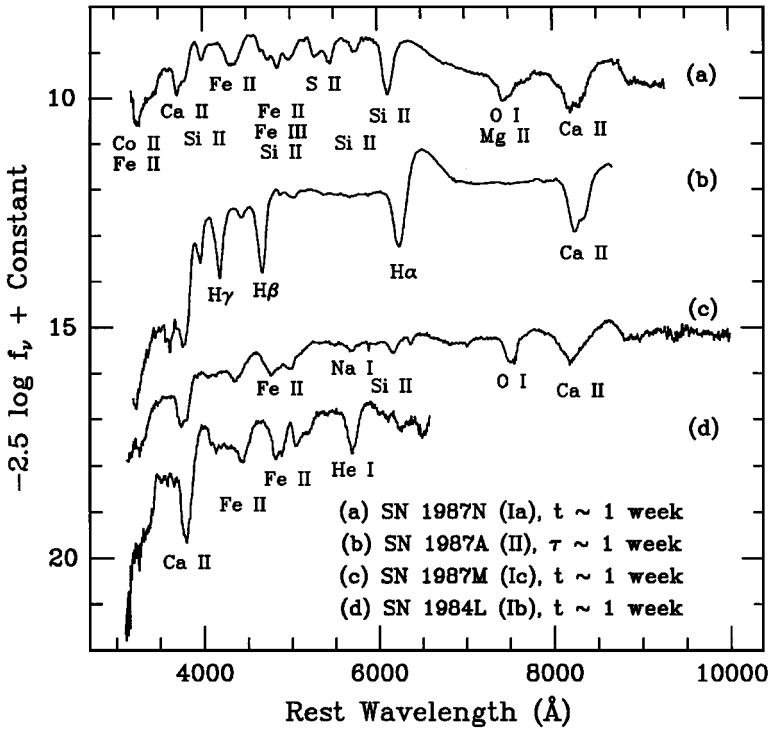

Figure 1.1 Figure from Filippenko (1997) comparing the spectra of different SNe types.

from each type of SNe; Wheeler & Harkness 1990). While the two classes were split up because of the observed heterogeneity, it may be more accurate to say there is a class Type Ibc that has a continuum of objects ranging from helium rich to helium poor (Filippenko 1997).

After some debate, it eventually became clear that the underlying physical mechanism of Type Ib and Type Ic SNe was closer to Type II SNe and was dramatically different than the model for normal SNe Ia. The key to resolving this argument was from studies of the environments of the different types of SNe. SNe II, SNe Ib, and SNe Ic have not been seen in elliptical galaxies and very rarely in S0 galaxies (Filippenko 1997). All three of these types of SNe tend to be in the arms of spiral galaxies near H II regions (van Dyk 1992), connecting these SNe to recent star formation. Specifically, Type Ib and Ic show a strong preference for galaxies that have a Hubble type Sbc or later. This implies that the progenitors of these objects are short-lived (high mass stars:$\sim 8-10M_{\odot}$; Filippenko 1997). SNe Ia on the other

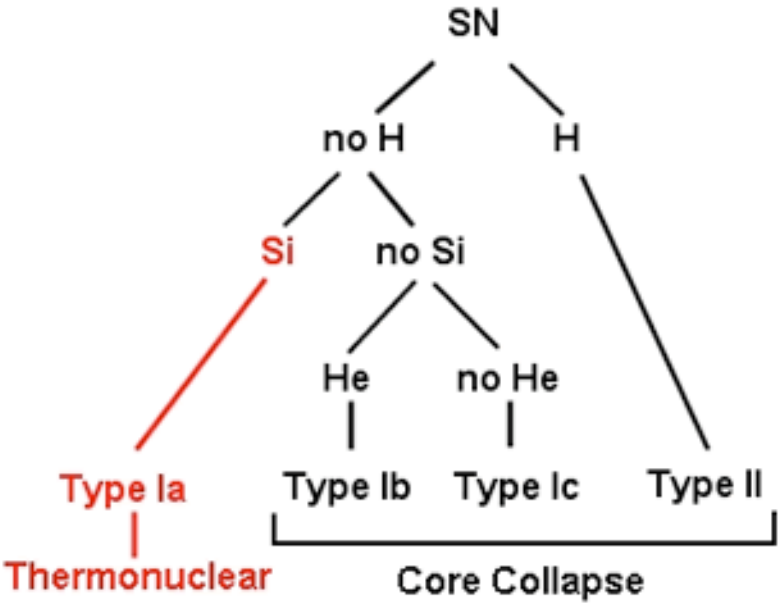

Figure 1.2 A schematic diagram of the spectroscopic classification of SNe including the physical mechanism for each of the major subclass.

hand are seen in elliptical galaxies and do not seem to have a strong preference for the spiral arms of the galaxy (van Dyk 1992). Because of this, SNe Ia are expected to come from long-lived progenitor systems ($\sim 4-7M_{\odot}$; Filippenko 1997). As such, SNe Ia are from low mass systems and are likely thermonuclear explosions of carbon-oxygen white dwarfs. SNe II, SNe Ib, and SNe Ic come from high mass stars and are likely core-collapse supernovae. SNe Ib and Ic do not have hydrogen (or helium for SNe Ic) because they have had their envelopes stripped either by a companion star or by stellar winds (Filippenko 1997). Figure 1.2 shows a diagram summarizing SNe classification and progenitor systems.

1.2 SNe Ia

1.2.1 "Normal SNe Ia"

We now turn our attention from SNe in general to focus on SNe Ia. As mentioned above, one key reason to study SNe Ia in particular is their use as cosmological distance indicators.

Obtaining distances to astronomical objects is very difficult. One of the best tools to determine distances is a standard candle: an object with a known intrinsic brightness. The apparent brightness is given by

$$F_{measured} = \frac{L_{intrinsic}}{4\pi r^2}, \tag{1.1}$$

where r is the luminosity distance from us to the source, $F_{measured}$ is the measured flux, and $L_{intrinsic}$ is the intrinsic luminosity. Therefore, if we know the intrinsic luminosity and we measure the flux, we can infer the distance. SNe Ia are standard candles (more precisely standardizable candles, but this is described in more detail below) that are also bright making them ideal to measure cosmological distances. By combining the distance measurements and the redshifts of the SNe Ia, it has been possible to map out the expansion history of the universe to constrain dark energy and the Hubble Constant.

Empirically, it is well known that SNe Ia are relatively homogeneous. Until the early 1990's, it was thought that SNe Ia were true standard candles, having identical intrinsic luminosities (Filippenko 2005). Since then, it has been shown that there is quantifiable heterogeneity among SNe Ia (Filippenko 1997). The luminosities of SNe Ia at peak form a continuum that spans ~ 2 mag in B or V.

Even though SNe Ia are not perfect standard candles, they can be calibrated standard candles ("standardizeable candles"). It has been established that the shape of the light curve of SNe Ia is strongly correlated with their intrinsic luminosity (e.g. Jha et al. 2007; Guy et al. 2010, and references therein). There have been many different methods of standardizing SNe Ia. One of the simplest methods is using the Phillips Relation, an empirical relationship between the decline in brightness over the first 15 days after peak, Δm_{15} and the intrinsic luminosity. The Phillips Relation is shown in Figure 1.3 including two outliers that will be discussed below and in Chapter 2. Several other methods have been proposed including using more than one band for the Phillips Relation (Phillips et al.

1999), light curve stretch (Perlmutter et al. 1997; Guy et al. 2007, 2010), and the Multi-color light curve shape method (Riess et al. 1996; Jha et al. 2007). For each of these models, the light curve shape is approximately described by a single parameter that can be then used to infer the intrinsic luminosity of the SN. Using the inferred luminosities, SN Ia distances are precise to $\sim 15\%$ and have been used to measure the equation of state of dark energy and the Hubble constant to very high precision (Filippenko 2005). However, large enough samples are being collected such that the systematic uncertainties are beginning to dominate the statistical uncertainties of SN Ia distances (Wood-Vasey et al. 2007; Kessler et al. 2009; Conley et al. 2011). Adding more measurements to the Hubble Diagram no longer improves our constraints on cosmology/dark energy.

Perhaps the most glaring theoretical uncertainty is in our fundamental understanding of the SN event: what explodes, and how? While the basic picture of a "normal" SN Ia as an accreting carbon-oxygen white dwarf that undergoes a thermonuclear runaway seems secure, many questions remain, including the nature of the companion star (normal or degenerate?), the composition of the accreting material (hydrogen or helium?), the mass at which the explosion occurs (Chandra, sub-Chandra, or even super-Chandra?), and the way the explosion proceeds (a deflagration to detonation transition?).

There has been extensive theoretical work on the explosion mechanism of SNe Ia. Originally, a pure detonation was examined, but if the explosion was completely supersonic (a detonation) it would not match observations. A pure detonation would produce too much iron, too much energy, and not enough intermediate mass elements (Arnett et al. 1971). A pure deflagration (purely subsonic burning) model on the other hand does not produce enough luminosity and predicts unburned material deep into the core of the ejecta which is not observed at late times (Khokhlov 1991). One proposed solution is that the explosion begins as a deflagration to account for the observed nucleosynthesis and light curves (Nomoto et al. 1984), but then transitions to a detonation at some point during the explosion (a delayed detonation model; (Khokhlov 1991)).

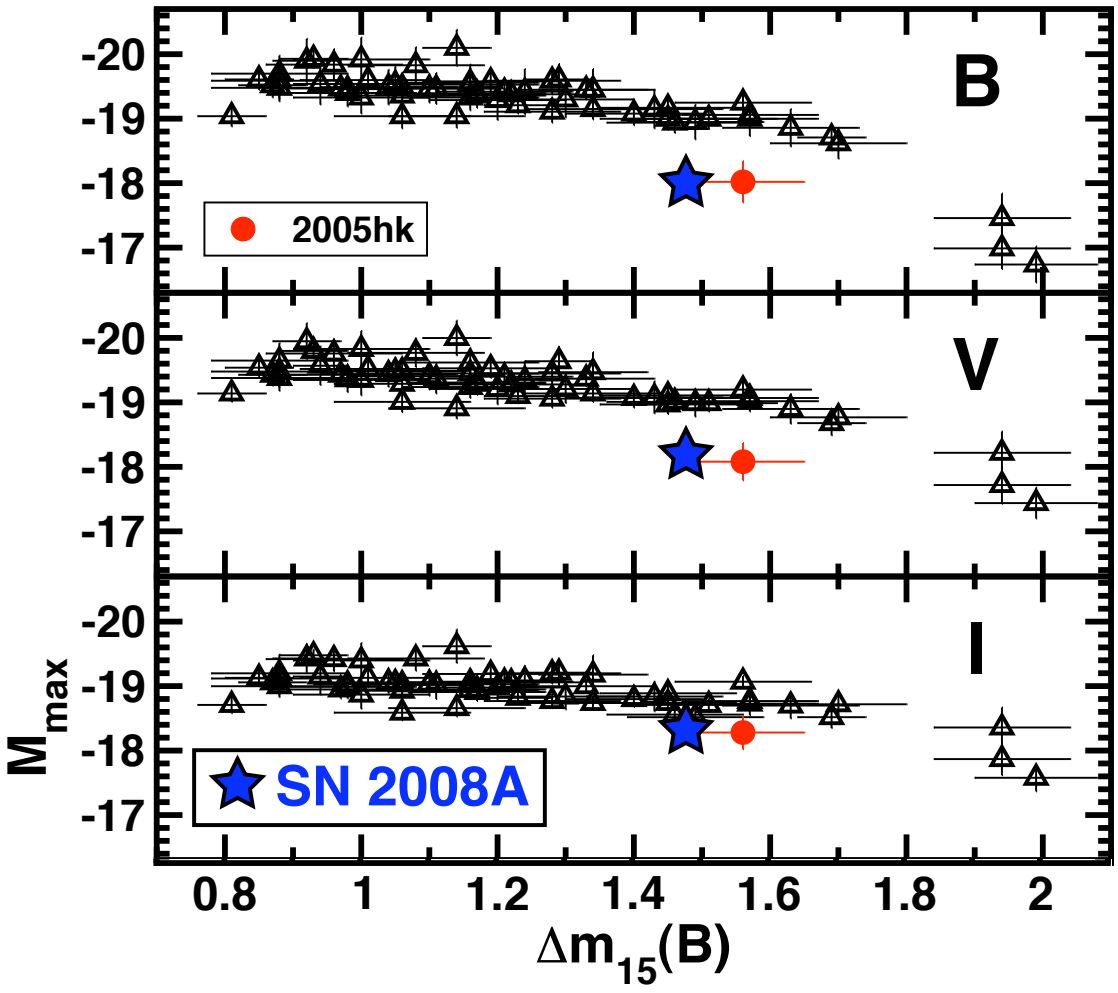

Figure 1.3 Adpated from Phillips et al. (1999) courtesy of Jha, showing the Phillips Relation that is used to standardize the intrinsic luminosities of SNe Ia. We include some of the known outliers that will be the focus of Chapter 2.

Another approach is to study the diversity of SNe Ia, focusing on individual objects at the extremes of the SN Ia luminosity continuum. On the bright, slow declining end of the continuum the SNe look like the prototype SN 1991T, while on the fainter faster declining side objects tend to look more like the prototype SN 1991bg (e.g. Phillips et al. 1999). SN 1991T was originally classified as a peculiar SN and was brighter than most normal SNe Ia by $\sim 0.5 - 0.6$ mag (Filippenko et al. 1992b). Near peak, the spectrum of SN 1991T did not look like any other previously observed SN. The early-time spectra of SN 1991T did not show almost any of the intermediate mass elements found in normal SNe Ia but were

instead dominated by Fe II and Fe III transitions (Filippenko et al. 1992b). The presence of the Fe III lines implied that the temperature of the ejecta for SN 1991T was higher than for normal SNe Ia (Nugent et al. 1995). Within a few weeks after maximum, the spectral shape changed dramatically and looked more like normal SNe Ia.

Late time observations of SN 1991T were used to understand why this object was different than normal SNe Ia. At late times, the photosphere recedes deep into the ejecta. The spectra slowly transition from being dominated by intermediate mass elements to being dominated by forbidden Fe and Co transitions as they enter the "nebular phase" (Axelrod 1980; Filippenko 1997). Using nebular phase spectra, it was shown that SN 1991T produced more ^{56}Fe than typical SNe Ia (Spyromilio et al. 1992). This also explained why SN 1991T was brighter than normal SNe Ia, as the luminosity of SNe Ia is powered by the decay of radioactive ^{56}Ni (Arnett 1996).

The radioactive decay of ^{56}Ni to ^{56}Co to ^{56}Fe, produces gamma rays and positrons that thermalize the ejecta, which powers the light curve of SNe Ia (Axelrod 1980; Kuchner et al. 1994). The energy from the decay is distributed with $\sim 97\%$ in gamma rays and $\sim 3\%$ in positrons (Sollerman et al. 2004). The decline rate is then related to the radioactive decay rate. From radioactive decay we have the number of atoms remaining in the sample from

$$\frac{dN}{dt} = -\lambda N, \tag{1.2}$$

and integrating we get

$$N(t) = N_0 e^{-\lambda t}. \tag{1.3}$$

λ is the decay rate and $\lambda = \frac{\ln 2}{\tau_{1/2}}$ where $\tau_{1/2}$ is the half life. The luminosity is proportional to the number of decays at any time so we can write

$$L \propto \frac{dN}{dt} \propto N \propto e^{-\lambda t} \tag{1.4}$$

$$L = L_0 e^{-\lambda t} \tag{1.5}$$

Converting this to magnitudes we see that

$$M = -2.5 \log_{10} L = -2.5(\log_{10} L_0 - \lambda t \log_{10} e), \tag{1.6}$$

giving a decline rate

$$\frac{dM}{dt} = \frac{0.753}{\tau_{1/2}} \tag{1.7}$$

The half life of ^{56}Co is $\tau_{1/2} = 77.7$ days. Plugging this into (1.7) we see that the decline rate due we expect from the radioactive decay of ^{56}Co is 0.98 mag per 100 days (see Carroll & Ostlie 2006). However, the assumes that all of the gamma rays are trapped; normal SNe Ia decline faster than this rate likely because some of the gamma rays escape (Sollerman et al. 2004).

At the other end of the continuum of SNe Ia is SN 1991bg (Nugent et al. 1995). SN 1991bg was an underluminous SNe Ia being ~ 1.7 mag fainter in the V band and ~ 2.6 mag fainter in B band than a normal SNe Ia. SN 1991bg also declined faster than normal SNe Ia by ~ 0.01 mag per day (Filippenko et al. 1992a). SN 1991bg was much redder than normal SNe Ia near peak. This was originally attributed to dust extinction. However as SN 1991bg evolved, it became comparable if not bluer than normal SNe Ia making significant reddening due to dust unlikely. Unlike SN 1991T, SN 1991bg showed pronounced spectral features from intermediate mass elements, but with lower expansion velocities than normal SNe Ia. The spectrum of SN 1991bg evolved very quickly entering its nebular phase earlier than normal SN Ia (Filippenko et al. 1992a). SN 1991T and SN 1991bg are sometimes labeled as peculiar, but for our purposes these form the extremes of "normal" SNe Ia.

While there are many observational and theoretical clues, we have not yet been able to answer these questions about the progenitor system and explosion mechanism definitively, even with extensive study of normal SNe Ia. An alternative avenue is to look at peculiar

SNe that seem to be related to normal SNe Ia.

1.2.2 Some of These Are Not Like the Others

While many white dwarf explosions produce normal SNe Ia (by which we mean all objects that fall on the Phillips Relation described above), other SNe are also consistent with being produced by an explosion of a white dwarf. Our goal is to understand the differences between normal SNe Ia and their "peculiar cousins" to give us a better picture of exploding white dwarfs as a whole.

The diversity of thermonuclear supernovae is striking. This will be discussed further in Chapter 2, but Figure 2.15 illustrates the range of ejecta masses and radioactive ^{56}Ni masses for a variety of white dwarf SNe. It includes the overluminous "super-Chandrasekhar" candidates like SN 2007if which have derived ejecta masses well in excess of 1.4 $M_{\odot}$ (Scalzo et al. 2010). On the other end of the luminosity scale we have SN 2005E, the prototype of a subclass of fast-declining, calcium-rich SN; SN 2005E looked like a SN Ib, but was in the halo of an early-type galaxy, favoring a white dwarf model (Perets et al. 2010). SN 2002bj resembled a SN Ia, but had very strong helium and carbon features (Poznanski et al. 2010), while SN 2002ic looked similar to normal SNe Ia, except with hydrogen (Hamuy et al. 2003)!

One example of a peculiar subclass of probable thermonuclear SNe are SN 2002cx-like objects, which we have dubbed "SNe Iax" (Li et al. 2003; Jha et al. 2006a; Foley et al. 2013). This class currently has 25 identified members (Foley et al. 2013). These are weak explosions, $\sim$ 1mag fainter than normal SNe Ia with similar light-curve shapes and ejecta velocities $\sim$5,000 km s^{-1}, half those of normal SNe Ia (10,000 km s^{-1}), but otherwise similar maximum light spectra (in fact, most closely resembling the slightly *over*luminous normal SNe Ia like SN 1991T). Surprisingly, though these objects are strange, *they are not rare*, occurring at a rate $\sim$5% (and possibly as high as $\sim$20%) of all SNe Ia in a volume limited sample (Li et al. 2011; Foley et al. 2013). There is diversity even within the subclass; for example, SN 2008ge was spectroscopically similar to SN 2002cx but had a luminosity that

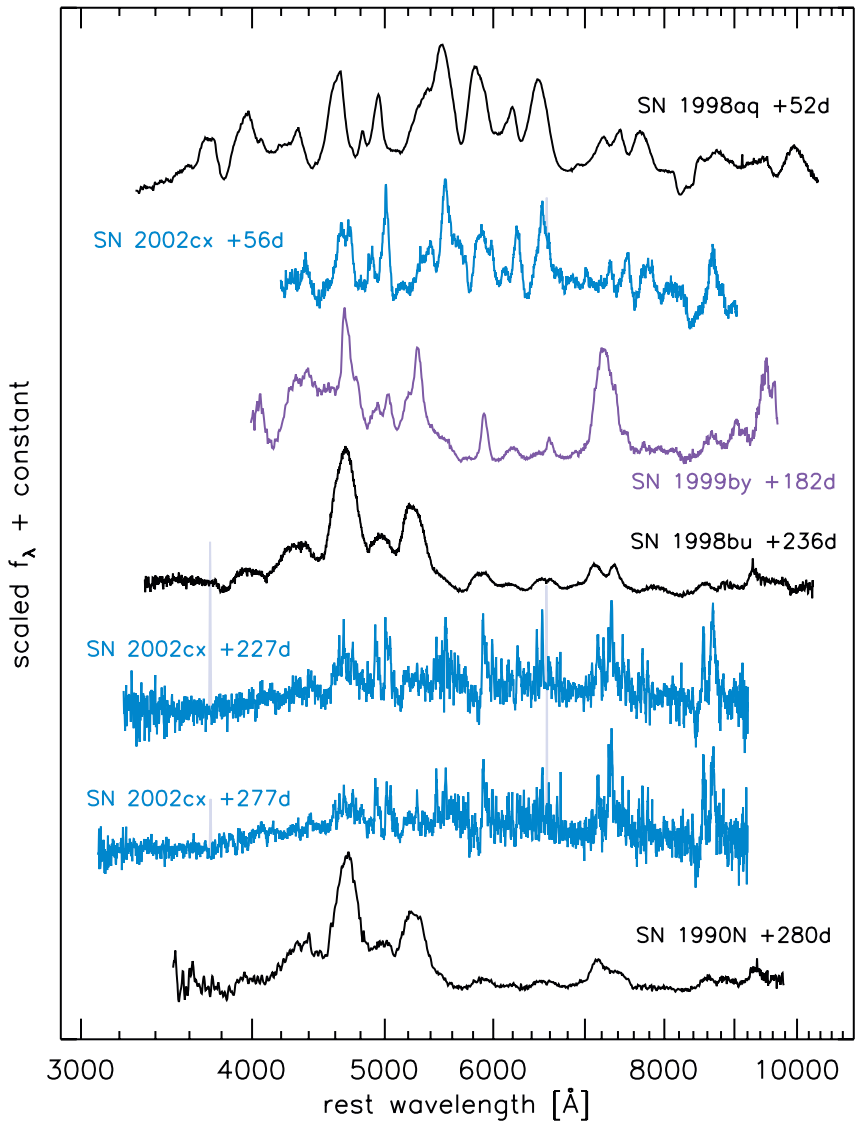

Figure 1.4 Figure from Jha et al. (2006a) showing the spectra of SN 2002cx compared to normal SNe Ia at similar epochs.

was comparable to normal SN Ia (Foley et al. 2010b). SN 2008ha, on the other hand, was an extreme member of this subclass, with even lower maximum light ejecta velocity (∼2,000 km s^{-1}) and was ∼ 4 mag fainter than SN 2008ge (Foley et al. 2009; Valenti et al. 2009; Foley et al. 2010a)!

Chapters 2 and 3 focus on studying a handful of prototypical SNe Iax, with the goal of understanding them in the larger context of exploding white dwarfs. In Chapter 2, we

study the late-time properties of SN 2008A and SN 2005hk, where SNe Iax deviate most dramatically from all other types of SNe (McCully et al. 2013). In Chapter 3, we examine pre-explosion images of NGC 1309, the host of SN 2012Z, the nearest (typical) SN Iax, in hopes of detecting the progenitor system (McCully et al. submitted to Nature).

1.3 Gravitational Lensing

We now turn our attention to gravitational lensing. Einstein's General Theory of Relativity interprets gravity as the curvature of spacetime; even light must follow this curvature (e.g. Carroll 2004). If there is mass between the Earth and a distant astronomical source, the curvature of spacetime can dramatically change what we observe: the source can be magnified or sheared depending on the mass configuration of the lens and the physical configuration of the source. If the mass in the lens is configured such that some of the light that would normally just radiate away from us is bent back into our line of sight, we say that the source is gravitationally "lensed". The position and flux of the extra light can be used to constrain the mass distribution of the lens whether this mass is normal luminous matter or dark matter that we cannot actually see.

To illustrate gravitational lensing phenomena it is useful to consider an analogy. The base of a wine glass has similar optical properties to a gravitational lens (Treu 2010, courtesy of Phil Marshall). Different alignments between the source and the lens produce characteristic patterns. If the source is directly behind the lens, it is possible to get a full ring, referred to as an Einstein Ring (see Figure 1.6). If the source is slightly offset from the mass, you could observe either two or four images that are skewed in a perpendicular direction to the mass (Massey et al. 2010). The analogy of the wine glass best illustrates strong lensing phenomena, but this is not the only flavor of gravitational lensing.

There are three main regimes of lensing: strong lensing, weak lensing, and flexion. Generally, multiply imaged systems and Einstein Rings are classified as strong lensing. This requires very good alignment between the source and the lensing matter, and is therefore

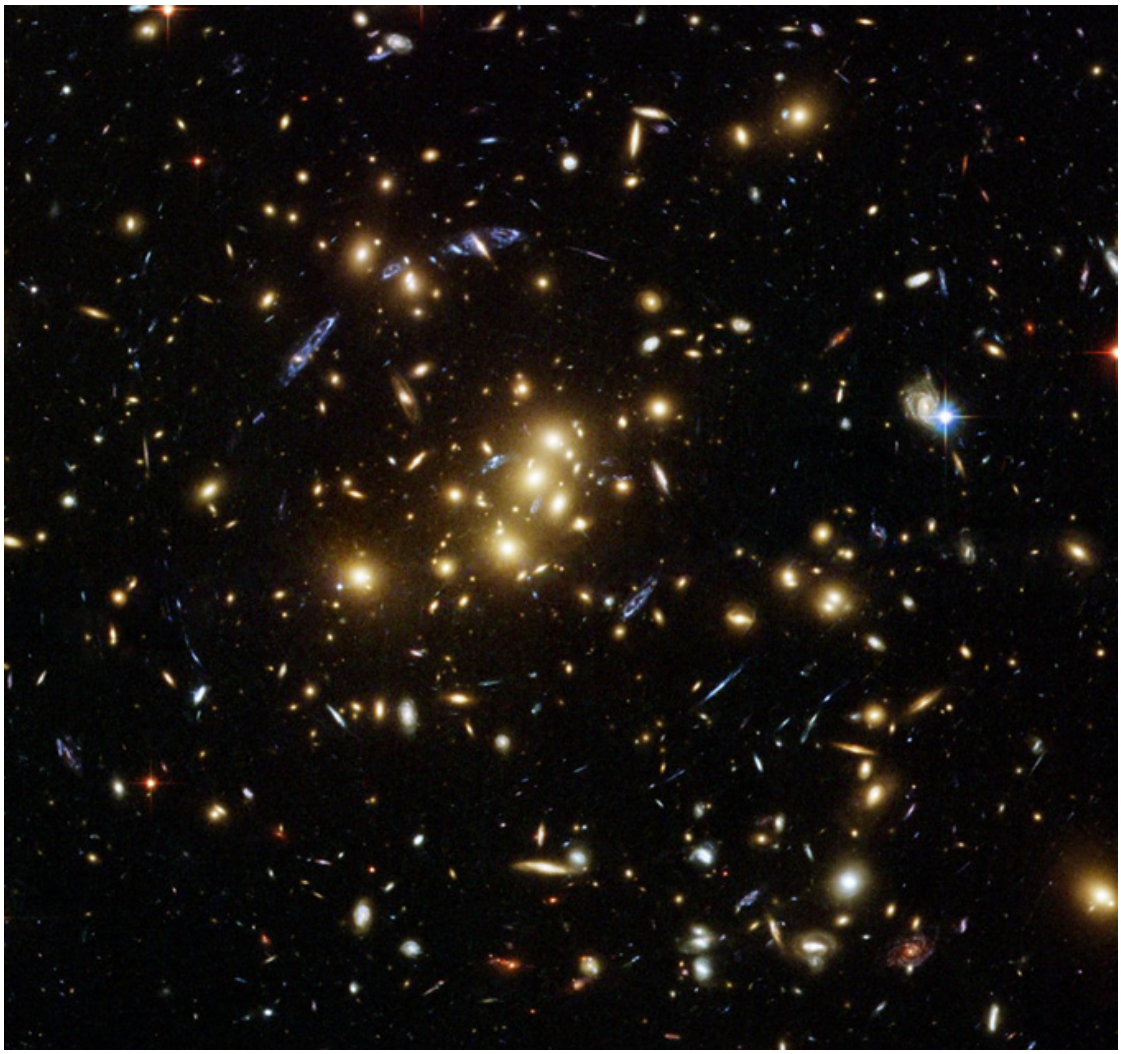

Figure 1.5 Strong gravitational lensing around galaxy cluster CL0024+17. The large yellow elliptical galaxies are members of the cluster, all at a similar redshift, and gravitationally bound inside a large dark matter halo. The faint elongated blue objects are much more distant galaxies, physically unassociated with, and lying behind, the cluster. Gravitational lensing has distorted their apparent images into a series of tangential arcs centered on the foreground cluster. Figure from Massey et al. (2010).

rare. Strong lensing is found near high concentrations of mass, generally near the cores of galaxies or galaxy clusters (Massey et al. 2010).

Weak lensing is on the opposite end of the gravitational lensing spectrum. Weak lensing measurements use the shapes of galaxies: weakly lensed galaxies are stretched perpendicularly to the mass in the lens. Typically, the distortion of any individual weakly lensed galaxy

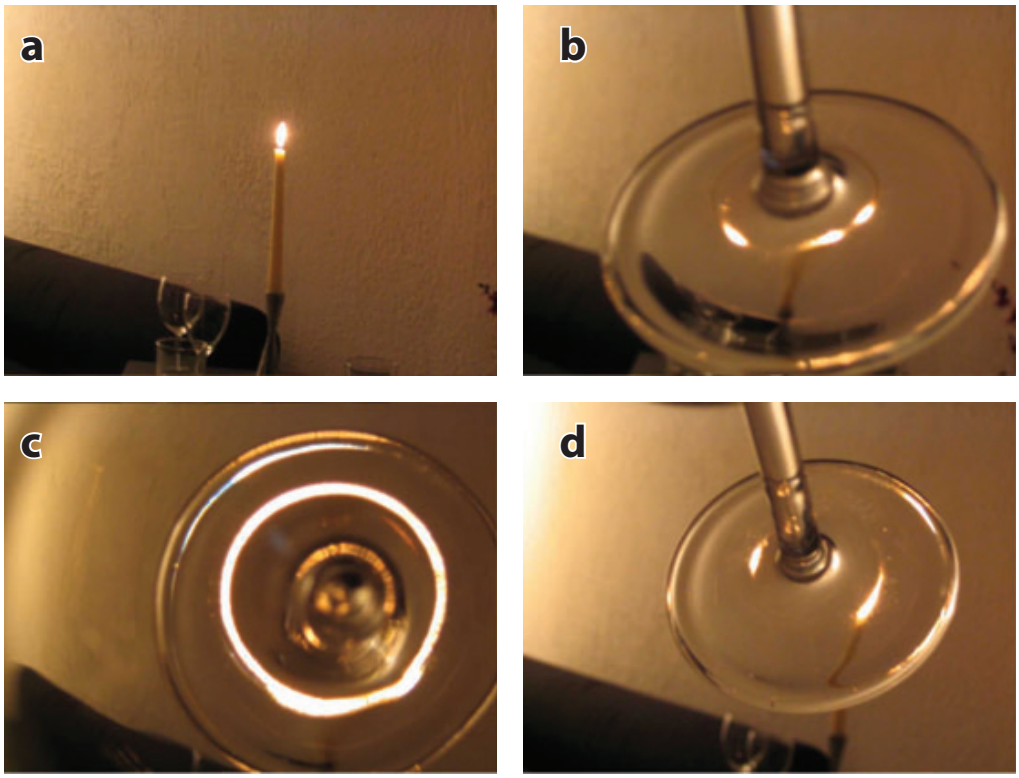

Figure 1.6 Images of a candle flame seen through a wine glass illustrating the common gravitational lensing configurations. The top left shows the unlensed source. The top right shows a four image configuration. The bottom right shows a two image configuration, and the bottom left shows a full ring (called and Einstein Ring in gravitational lensing) looking directly down the stem of the wine glass. Figure from Treu (2010) courtesy of Phil Marshall.

is much smaller than the intrinsic shape variation between galaxies and therefore can only be measured for statistically from a large sample of background galaxies. It is necessary in practice to measure the shear for $\sim$ 100 galaxies to get a signal to noise ratio of order unity for the mass reconstruction; in practice weak lensing analyses use tens or hundreds of thousands of galaxies to build mass models. The sheer number of galaxies needed limits the feasibility of weak lensing measurements: extended lenses with large Einstein Radii are generally used so that there are enough background galaxies to make meaningful claims about the mass reconstruction for individual objects. This typically limits the use of weak lensing measurements to galaxy clusters (Massey et al. 2010). Weak lensing studies of the

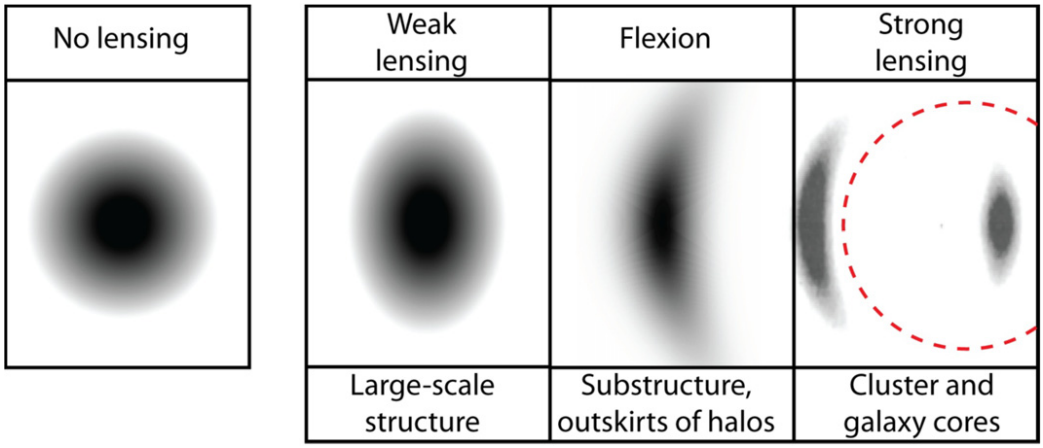

Figure 1.7 This figure illustrates the signatures of the different lensing regimes. The bottom panels list where each of these lensing regimes are most commonly studied. Figure from Massey et al. (2010).

Bullet Cluster led to some of the most compelling evidence for the existence of dark matter (Clowe et al. 2006). Cosmic shear studies, on the other hand, build up their statistics by surveying a large area on the sky, but these measurements probe large scale structure rather than individual objects (e.g., Munshi et al. 2008).

Flexion is in between the strong lensing and weak lensing regimes. Flexion measurements still rely on shape variations like weak lensing, but the distortion for a given galaxy is much greater requiring fewer galaxies for statistics. Flexion is dominant in the outskirts of galaxy halos. In principle, the flexion also captures different information than weak lensing inasmuch that weak lensing probes the second derivative of the lens potential, while the flexion is sensitive to the first derivative. Flexion is the youngest field of these three lensing regimes (Massey et al. 2010).

All three of these three regimes are described formally by the same mathematics. Gravitational lensing in general can be described by a generalized Fermat's principle. The excess light travel time is given by

$$t = \frac{D_d D_s (1+z_i)}{c D_{ds}} \left[\frac{1}{2} |\boldsymbol{\theta} - \boldsymbol{\beta}|^2 - \phi(\theta) \right]. \tag{1.8}$$

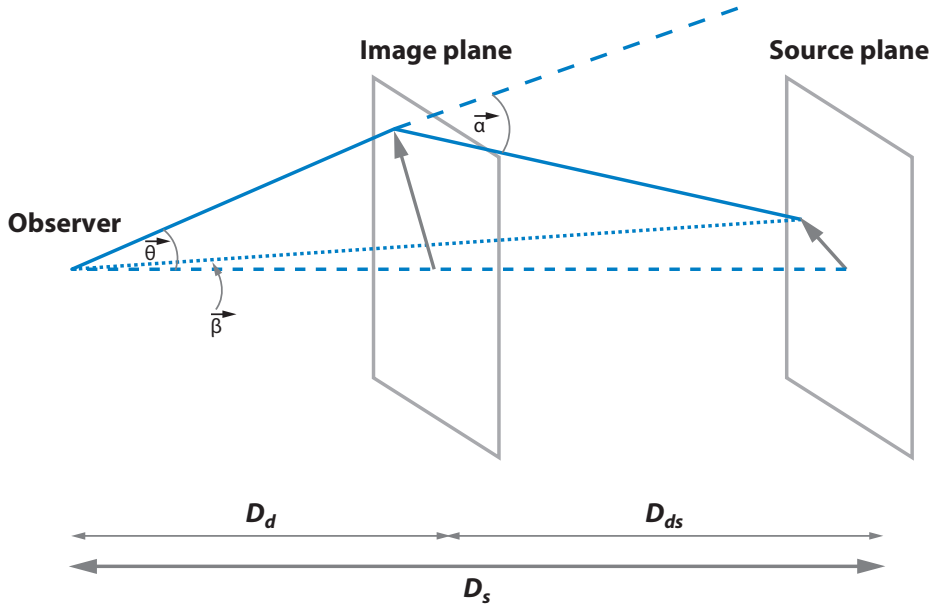

Figure 1.8 Schematic of typical lensing geometry and definitions of variables that will be used throughout this work. Figure from Treu (2010).

D_d, D_s, and D_{ds} are the angular diameter distances between the observer and the lens (or deflector), the observer and the source, and the lens (deflector) and the source respectively (Treu 2010). ϕ is the lensing potential which satisfies the two dimensional Poisson equation

$$\nabla^2\phi = 2\kappa, \tag{1.9}$$

where κ is the convergence, the projected surface mass density of the lens in terms of critical surface mass density $\Sigma_c = c^2 D_s/(4\pi D_d D_{ds})$ (Treu 2010). The two terms in the brackets of Eq. (1.8) are due to different effects on the light arrival time (e.g. Refsdal 1964). The first is light travel time: light bent by different amounts must travel a different distance giving different arrival times for each of the images. The second effect is the relativistic Shapiro Delay: time dilation from the gravitational potential changes the arrival time of a photon to an observer on Earth. The combination of effects leads to an offset in the arrival times of each of the images (Massey et al. 2010; Treu 2010).

From Fermat's principle, images form at extrema of the time-delay surface, defined by

Eq. (1.8), giving the lens equation

$$\boldsymbol{\beta} = \boldsymbol{\theta} - \nabla\phi = \boldsymbol{\theta} - \boldsymbol{\alpha}. \tag{1.10}$$

If there are multiple solutions to lensing equation, we observe multiple images of the background source with time delays derived from Eq. (1.8) (Treu 2010).

We can write the Jacobian of the transformation between the source and the observed image as

$$\frac{\partial\boldsymbol{\beta}}{\partial\boldsymbol{\theta}} = \delta_{ij} - \frac{\partial^2\phi}{\partial\theta_i\partial\theta_j} = \begin{pmatrix} 1-\kappa-\gamma_1 & -\gamma_2 \\ -\gamma_2 & 1-\kappa+\gamma_1 \end{pmatrix} \tag{1.11}$$

where κ is the convergence as was defined above, while γ_1 and γ_2 are the cartesian coordinates of the shear (Treu 2010). The magnification of the image is given by the inverse of the determinant of the Jacobian matrix

$$\mu = \frac{1}{(1-\kappa)^2 - \gamma_1^2 - \gamma_2^2}. \tag{1.12}$$

Typically, the shear and convergence as described above are functions of position in the image plane.

Given the mass distribution of the lens, we can calculate the positions, fluxes, and time delays of the images (Massey et al. 2010). However, we want to go the other direction: we observe the positions, fluxes, and time delays of a multiply imaged background source and want to calculate the mass distribution of the lens. The most straightforward way to convert the lensing observables to the physical parameters of the lens is to use the Einstein radius. The Einstein radius is defined as the region inside which the average surface mass density of a circular lens mass distribution is equal to the critical surface mass density defined above (Treu 2010). Given the lens and source redshifts, the size of the Einstein radius directly

yields the enclosed mass. For illustration, the Einstein radius of a point mass is given by

$$\Theta_E = \sqrt{\frac{4GM}{c^2}\frac{D_{ds}}{D_d D_s}}. \tag{1.13}$$

Another commonly assumed mass profile is a "isothermal sphere" with a three dimensional mass density given by

$$\rho = \frac{\sigma^2}{2\pi G r^2} \tag{1.14}$$

and the Einstein radius in angular distance, given by

$$\Theta_E = 4\pi \left(\frac{\sigma}{c}\right)^2 \frac{D_{ds}}{D_s}. \tag{1.15}$$

The Einstein radius also sets the characteristic length scale for the lensing system and separates the strong lensing regime into smaller subcategories. For large Einstein radii, such as for galaxies and galaxy clusters, the lensing events are classified in the macrolensing category. Dwarf galaxies tend to have Einstein radii of about one milliarcsecond giving its name to the millilensing regime. Stars have even smaller Einstein radii of about one microarcsecond referred to as microlensing. Even when there are not multiple images of a source, we can still learn valuable information about the mass distribution of the lens.

In strong lensing systems, the principal lensing constraints on the mass density profile (e.g. the scale radius of an NFW halo) come from the relative positions and fluxes of multiply-imaged arclets. One challenge is that *relative* positions and magnification *ratios* and are subject to the "mass sheet degeneracy" (Falco et al. 1985): these constraints are not sensitive to the absolute density and therefore total mass of the lens. The radial profile of the mass distribution is also sensitive to the mass sheet degeneracy, (the radial profile degeneracy; Schneider & Sluse 2013). The mass sheet degeneracy is one of the key uncertainties of lensing mass reconstructions (e.g. Treu 2010; Schneider & Sluse 2013).

Gravitational lens time delays (Refsdal 1964) can be used to constrain the expansion

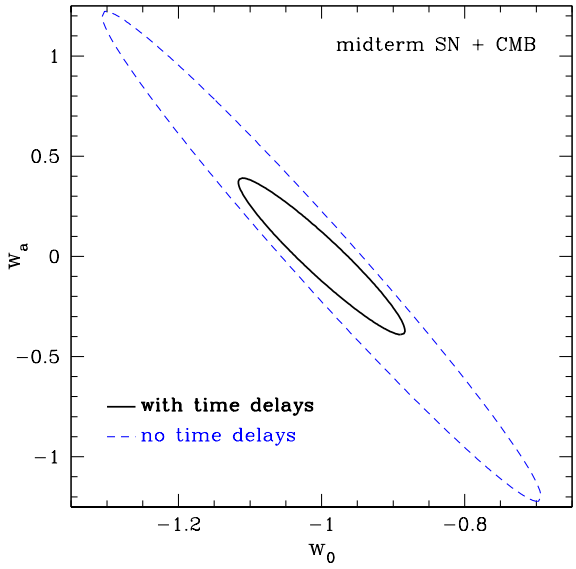

Figure 1.9 Figure from Linder (2011). 68% confidence level constraints on the dark energy equation of state parameters w_0 and w_a using LSST supernova distances and CMB information, and with (solid curve) or without (dashed curve) time delay measurements. The time delay probe demonstrates strong complementarity, increasing the figure of merit by a factor 4.8. This analysis was done using quasars, but we should be able to have similar constraints from fewer SNe with higher quality time delays.

history of the universe, and therefore the Hubble Constant and dark energy (Treu et al. 2013). In strong lenses that have multiple images, the light travel time for each image can be slightly different due to differing path lengths and gravitational potentials as discussed above. The time delay can be used to convert angles measured on the sky into a physical angular diameter distance, the "time-delay distance"(Suyu 2012). By taking ratios of time-delay distances from a range of redshifts, it is possible to constrain cosmological parameters that depend on the expansion history of the universe like the flatness of the universe as characterized by Ω_k and the equation of state parameter of dark energy, w (Treu et al. 2013). The constraints on the Hubble Constant and extending to dark energy are complementary to the luminosity distance that is measured by SNe Ia, as shown in Figure 1.9.

Like SNe Ia distances, we are no longer limited by observations, but are instead limited by theoretical uncertainties. Keeton et al. (1997) found that no quad-image system was fit without adding an external shear and that the required shear values were an order of

magnitude larger than what had been expected (10%-15% instead of 1%-1.5%). These results suggest that treating the lens galaxy as an isolated system is not necessarily a good approximation. It was soon observed that a number of lens galaxies are in groups (e.g. MG 0751+2716, PG 1115+080, B1422+231, and B1608+656; Tonry & Kochanek 1999; Kundic et al. 1997a,b; Tonry 1998; Fassnacht et al. 2006), and several others are in clusters (e.g. RX J0911+0551, Q0957+561, HST 14113+5221, and MG 2016+112; Kneib et al. 2000; Young et al. 1981; Fischer et al. 1998; Soucail et al. 2001). At least some of the external shear for these systems is due to their environment (e.g. Keeton et al. 2000). Keeton & Zabludoff (2004) showed that not only will the overall group/cluster have a significant effects, but that individual group galaxies cannot be ignored when modeling the lens. Momcheva et al. (2006) extended this argument to show that we need to account for not only galaxies that are physically associated with the lens, but also interloping mass at different redshifts along the line of sight (LOS; Bayliss et al. 2014 showed this is also true from cluster-scale lenses).

These environment/LOS effects are now one of the largest components of the uncertainty budget for measuring the Hubble Constant using gravitational time delays (Suyu 2012). There are a variety of methods to try to account for LOS/environment effects. One possibility is to calibrate these effects by ray tracing through simulations (e.g. Suyu et al. 2013). However, fully exploring the parameter space can take months of CPU time and significant amounts of human interaction (Treu et al. 2013).

In our work with Ann Zabludoff and Ken Wong, we have taken a different approach to modeling LOS effects on gravitational lensing: we use photometric and spectroscopic observations of the field to build mass models that are calibrated with empirical relationships like Faber-Jackson (Wong et al. 2011). We have designed a new framework to model the LOS effects of gravitational lensing (McCully et al. 2014), presented in Chapter 4. We adopt a hybrid approach; balancing accuracy treating a few perturbing galaxies exactly, with efficiency by treating the rest of the galaxies using the weak lensing approximation.

In Chapter 5, using realistic mock data, we test the robustness of our framework, checking when the weak lensing approximation is valid. We show that LOS effects are not equivalent to a single shear, but these non-linear effects are correctly captured by our framework. Our new methodology can reproduce the fitted lens quantities, including H_0, with precision that is limited only by the measurement errors of the lensed images without any significant bias. We are currently the only group doing full 3-d lensing calculations for real beams, which include hundreds of galaxies.

Chapter 2

Hubble Space Telescope and Ground-Based Observations of the Type Iax Supernovae SN 2005hk and SN 2008A

Abstract

We present *Hubble Space Telescope* (*HST*) and ground-based optical and near-infrared observations of SN 2005hk and SN 2008A, typical members of the Type Iax class of supernovae (SNe). Here we focus on late-time observations, where these objects deviate most dramatically from all other SN types. Instead of the dominant nebular emission lines that are observed in other SNe at late phases, spectra of SNe 2005hk and 2008A show lines of Fe II, Ca II, and Fe I more than a year past maximum light, along with narrow [Fe II] and [Ca II] emission. We use spectral features to constrain the temperature and density of the ejecta, and find high densities at late times, with $n_e \gtrsim 10^9$ cm^{-3}. Such high densities should yield enhanced cooling of the ejecta, making these objects good candidates to observe the expected "infrared catastrophe," a generic feature of SN Ia models. However, our *HST* photometry of SN 2008A does not match the predictions of an infrared catastrophe. Moreover, our *HST* observations rule out a "complete deflagration" that fully disrupts the white dwarf for these peculiar SNe, showing no evidence for unburned material at late times. Deflagration explosion models that leave behind a bound remnant can match some of the observed properties of SNe Iax, but no published model is consistent with all of our observations of SNe 2005hk and 2008A.

2.1 Introduction

The use of Type Ia supernovae (SNe Ia) as distance indicators has revolutionized cosmology with the discovery that the expansion of the Universe is currently accelerating, probably driven by dark energy (Riess et al. 1998; Perlmutter et al. 1999). Sufficiently large samples have now been collected such that systematic uncertainties are beginning to dominate the statistical uncertainties in SN Ia distances (e.g., Wood-Vasey et al. 2007; Kessler et al. 2009; Conley et al. 2011). Perhaps one of the most fundamental systematic uncertainties stems from the lack of detailed understanding of SN Ia progenitor systems and explosion mechanism. Though exploding white dwarfs typically produce normal SNe Ia (by which we include all objects that fall on the one-parameter family correlating luminosity with light-curve width; Phillips 1993), we are amassing growing evidence that other SNe are also consistent with a white dwarf origin. Understanding what makes these thermonuclear explosions different can shed light on both normal SNe Ia and more general outcomes of stellar evolution.

SN 2002cx was labeled "the most peculiar known SN Ia" by Li et al. (2003); see also Filippenko (2003). While SN 2002cx was peculiar, it is not unique. SN 2002cx is the prototype for the largest class of peculiar SNe, which we have dubbed "Type Iax" supernovae (for a full description of this class, see Foley et al. 2013). These are weak explosions with luminosities that can fall more than a magnitude below the Phillips relation for normal SNe Ia with similar decline rate, and they have ejecta velocities roughly half those of normal SNe Ia (Jha et al. 2006a). Still, near peak brightness, SNe Iax are similar to SNe Ia in the general characteristics of their light curves and spectral features. However, the late-time properties of SNe Iax are unmatched by any other previously discovered SN class. Instead of entering a nebular phase dominated by broad forbidden lines of iron-peak elements, the spectrum of SN 2002cx at $\sim$250 days past maximum brightness[1] was dominated by *permitted* Fe II, with very low expansion velocities $\sim$700 km s^{-1}, much lower

[1]Throughout this paper, SN phases are given in rest-frame days past B-band maximum light.

than ever observed in normal SNe Ia (Jha et al. 2006a). In addition, the late-time spectrum of SN 2002cx showed hints of low-velocity O I, also unprecedented in SNe Ia, and perhaps an indication of unburned material in the inner regions of the white dwarf.

A variety of models have been proposed to explain the origins of SNe Iax. Branch et al. (2004) and Jha et al. (2006a) suggested that these objects might be explained by pure deflagration models. These models do not explain normal SNe Ia well: a pure deflagration model typically produces much less nickel than is required for the luminosity of a normal SN Ia (Gamezo et al. 2004). Moreover, the highly turbulent and convoluted thermonuclear burning front in these models yields clumpy, well-mixed ejecta, with unburned material, partially burned material, and fully burned (to the iron peak) material at all layers (Röpke 2008), and this mixing is not observed in normal SNe Ia (Gamezo et al. 2004). One of the strongest constraints for a pure-deflagration model is the prediction of unburned material (carbon and oxygen) in the innermost layers, which should be easily detectable in late-time spectra and yet has never been observed in normal SNe Ia (Gamezo et al. 2004).

The problems with the pure deflagration model for normal SNe Ia may become strengths for SNe Iax (Jha et al. 2006a). The low production of nickel and the low luminosity are key traits of SNe Iax. Large amounts of mixing of partially burned, fully burned, and possibly unburned material are observed in all layers of the ejecta. The clumpiness predicted by the pure deflagration model could explain the high densities seen at late times (Jha et al. 2006a; Phillips et al. 2007). In SN 2002cx, there was a tentative detection of O I λ7774 (Jha et al. 2006a) and a hint of the line in SN 2005hk, a prototypical SN Iax (Phillips et al. 2007; Stanishev et al. 2007b; Sahu et al. 2008). However, "complete deflagration" models that fully unbind the white dwarf do not predict the high densities at late times seen in SNe Iax, and therefore suggest that oxygen in the inner layers should be revealed by [O I] $\lambda\lambda$6300, 6363 emission (Kozma et al. 2005).

More recently, Jordan et al. (2012) find that if a detonation is not triggered, the explosion is often not powerful enough to unbind the star, leading to the low luminosities and ejecta

velocities like those found in SNe Iax. Kromer et al. (2013) also study the three-dimensional deflagration of a Chandrasekhar-mass white dwarf. Using radiative transfer models, they find that they can reproduce the luminosity, the early-time light curve, and the early-time spectra of SN 2005hk. Similarly, one of the key features of their explosion simulation is a bound remnant.

The discovery of SN 2008ha sparked controversy about the nature of these peculiar SNe. SN 2008ha was spectroscopically a SN Iax, but it was the most extreme member to date (Foley et al. 2009; Valenti et al. 2009), with maximum-light expansion velocities of just $\sim$2000 km s^{-1}, less than half that of even typical SNe Iax. In addition, SN 2008ha was 3 mag fainter than SN 2002cx, with a much more rapid light-curve decline rate. Based on the energetics, and the spectral similarity of SN 2008ha to SN 1997D at late times, Valenti et al. (2009) argued that SN 2008ha was actually a core-collapse SN, rather than a thermonuclear one. Indeed, Moriya et al. (2010) were able to recreate the kinetic energy of SN 2008ha in a core-collapse simulation with large amounts of fallback onto a newly formed black hole (Foley et al. 2009; Valenti et al. 2009). If this model holds for SN 2008ha, Valenti et al. (2009) argued by extension that all SNe Iax might actually be core-collapse SNe. Further support for this idea comes from the fact that, like SN 2008ha, SNe Iax are found almost exclusively in late-type galaxies, similar to core-collapse SNe (Jha et al. 2006a; Foley et al. 2009, 2013). Using Hα maps of a sample of host galaxies of SNe Iax, Lyman et al. (2013) find a statistical association with star forming regions similar to that of SNe IIP. The two objects we focus on in this work, SN 2005hk and SN 2008A, are both in star-forming galaxies, but there is no evidence for star formation at the location of either object (Lyman et al. 2013).

Foley et al. (2010a) published a new set of spectra from earlier epochs of SN 2008ha showing strong evidence for both Si II and S II at maximum light. While some core-collapse SNe do show weak Si II lines, the sulfur lines are usually considered hallmarks of thermonuclear burning in a C/O white dwarf (Sulfur may also be present in the ejecta of

Table 2.1. Ground-based optical photometry of SN 2005hk from the SDSS-II SN Survey

Date (UT)	MJD (days)	Phase (days)	u (mag)	g (mag)	r (mag)	i (mag)	z (mag)
2005 10 28	53671.34	−12	18.586(0.036)	18.733(0.012)	18.954(0.019)	19.284(0.027)	19.604(0.104)
2005 10 31	53674.24	−9	17.018(0.031)	16.977(0.012)	17.097(0.006)	17.348(0.009)	17.570(0.018)
2005 11 02	53676.33	−7	16.649(0.031)	16.511(0.004)	16.592(0.004)	16.807(0.005)	17.010(0.011)
2005 11 05	53679.30	−4	16.409(0.031)	16.046(0.009)	16.148(0.009)	16.393(0.015)	16.570(0.014)
2005 11 07	53681.29	−2	16.400(0.031)	15.903(0.004)	15.977(0.003)	16.214(0.005)	16.343(0.009)
2005 11 11	53685.25	+1	16.524(0.031)	15.777(0.018)	15.743(0.015)	16.003(0.015)	16.120(0.010)
2005 11 23	53697.25	+12	18.423(0.031)	16.778(0.015)	15.810(0.006)	15.820(0.006)	15.917(0.016)
2005 11 26	53700.25	+15	18.991(0.038)	17.125(0.022)	15.988(0.013)	15.888(0.014)	15.967(0.018)
2005 12 01	53705.23	+20	19.637(0.050)	17.625(0.013)	16.307(0.003)	16.170(0.008)	16.190(0.009)
2006 08 28	53975.32	+287	···	21.812(0.069)	20.840(0.042)	20.375(0.039)	20.327(0.149)
2006 09 12	53990.34	+302	···	22.051(0.218)	21.194(0.097)	20.506(0.064)	20.826(0.270)
2006 09 16	53994.35	+306	···	22.242(0.103)	21.121(0.062)	20.528(0.044)	20.666(0.192)
2006 09 18	53996.33	+308	···	22.260(0.127)	21.205(0.064)	20.650(0.062)	20.900(0.301)
2006 09 20	53998.30	+310	···	22.370(0.113)	21.206(0.051)	20.660(0.049)	20.873(0.211)
2006 09 27	54005.33	+317	···	22.299(0.093)	21.251(0.049)	20.674(0.042)	20.695(0.162)
2006 09 30	54008.29	+320	···	22.439(0.120)	21.198(0.066)	20.806(0.057)	20.856(0.220)
2006 10 02	54010.28	+322	···	22.441(0.184)	21.225(0.065)	20.723(0.055)	20.615(0.151)
2006 10 04	54012.28	+324	···	22.270(0.315)	21.321(0.157)	20.677(0.070)	20.680(0.207)
2006 10 12	54020.28	+332	···	22.646(0.288)	21.371(0.100)	20.800(0.077)	20.974(0.318)
2006 10 16	54024.36	+336	···	···	21.360(0.098)	21.000(0.092)	···
2006 10 22	54030.28	+342	···	22.533(0.112)	21.466(0.063)	21.017(0.057)	21.230(0.269)

Note. — 1σ photometric uncertainties are given in parentheses.

other type of SNe, but has never been clearly detected in other type of SNe Foley et al. 2010a); these lines were also seen in SN 2007qd, another SN Iax very similar to SN 2008ha (McClelland et al. 2010). Foley et al. (2010a) proposed that SN 2008ha is better explained by a failed deflagration than a core-collapse model. The host-galaxy distribution is also similar to that of some SNe Ia, specifically SN 1991T-like objects (Foley et al. 2009), and the SN Iax 2008ge exploded in an S0 galaxy with no sign of local star formation to deep limits, inconsistent with a massive star origin (Foley et al. 2010b).

Because these SNe deviate most dramatically from normal SNe (both core-collapse and thermonuclear) at late times, here we present late-time observations of SNe 2005hk and 2008A (Foley et al. 2013), both typical SNe Iax very similar to SN 2002cx, to constrain the nature of this class of SNe. We look for evidence of the [O I] λ6300 line that is predicted for a complete pure deflagration (and is usually seen in core-collapse SNe). We also use

late-time spectra to infer the composition, velocity structure, density, and temperature of the ejecta.

Besides providing insight to the progenitor systems and explosion mechanisms of white dwarf SNe, SNe 2005hk and 2008A may be ideal candidates to observe the "infrared (IR) catastrophe" predicted by Axelrod (1980), a thermal instability that changes the dominant cooling mechanism from optical lines to far-IR fine-structure lines such as [Fe I] 24 μm and [Fe II] 26 μm (Sollerman et al. 2004). This phenomenon has never been observed in normal SNe Ia even out to 700 days past maximum (Leloudas et al. 2009). Because SNe Iax remain at high densities at late times, the objects in this class should cool faster than normal SNe Ia and should undergo this instability sooner. Using two epochs of late-time *HST* observations, we compare the color evolution of SN 2008A to the predictions of IR-catastrophe models.

Throughout this paper we adopt $H_0 = 73$ km s^{-1} Mpc^{-1} and correct redshifts (z) using the Virgo+GA infall model of Mould et al. (2000) via NED[2] to estimate distances to the SN host galaxies.

2.2 Observations and Data Reduction

2.2.1 Ground-Based Optical Photometry and Spectroscopy

For SN 2005hk, we supplement the ground-based optical photometry of Phillips et al. (2007), Stanishev et al. (2007b), and Sahu et al. (2008) with observations of the equatorial "Stripe 82" from the SDSS-II SN survey (Frieman et al. 2008; Sako et al. 2008), following the reduction procedure detailed by Holtzman et al. (2008). The data comprise *ugriz* photometry (Fukugita et al. 1996) from the 2005 and 2006 SDSS-II observing seasons, and are presented in Table 2.1.

The ground-based early-time *BVRI* observations of SN 2008A were obtained with the 0.76 m Katzman Automatic Imaging Telescope (KAIT; Filippenko et al. 2001) and 1 m

[2]http://ned.ipac.caltech.edu.

Table 2.2. Late-Time Spectroscopic Observations of SN 2005hk

UT	MJD	Phase (days)	Telescope/Instrument	Exposure (s)	Range (Å)	Resolution (Å)
2006 06 01	53887.62	+201	Keck I/LRISp	800	5765–7492	3
2006 07 01	53917.58	+231	Keck I/LRISp	4200	3260–9276	7
2006 11 23	54062.22	+374	Keck I/LRIS	1800	3150–9250	7
2006 12 23	54092.21	+403	Keck II/DEIMOS	1800	5000–9300	3
2007 02 14	54145.23	+456	Keck I/LRIS	1800	5500–9240	7

Nickel telescope at Lick Observatory (Ganeshalingam et al. 2010). *BVri* observations of SN 2008A were also taken as part of the CfA4 survey (Hicken et al. 2012).

Optical spectra of SN 2005hk were obtained with the Low Resolution Imaging Spectrometer (LRIS; Oke et al. 1995) (sometimes in polarimetry mode, LRISp) on the Keck I 10 m telescope and the Deep Imaging Multi-Object Spectrograph (DEIMOS; Faber et al. 2003) on the Keck II 10 m telescope. Spectra of SN 2008A were obtained with the Kast double spectrograph (Miller & Stone 1993) on the Lick 3 m Shane telescope, Keck I (+ LRIS), and the Dominion Astrophysical Observatory (DAO) Plaskett 1.8 m telescope. Data-reduction procedures for the Lick and Keck spectra are presented by Silverman et al. (2012); the DAO spectroscopy was reduced with standard techniques. Logs of the observations are provided in Tables 2.2 and 2.3, and spectral time series are shown in Figures 2.1 and 2.2. The former figure includes supplementary spectroscopy of SN 2005hk from Chornock et al. (2006), Phillips et al. (2007), Sahu et al. (2008), and Maund et al. (2010). The listed phases are in the SN rest frame, referenced to B maximum light, which occurred on MJD 53684.2 for SN 2005hk and MJD 54478.3 for SN 2008A.

2.2.2 Late-time *HST* Observations

Our *HST* observations of SNe 2005hk and 2008A include optical photometry from WFPC2 and ACS/WFC and near-IR photometry from NICMOS and WFC3/IR, which are presented

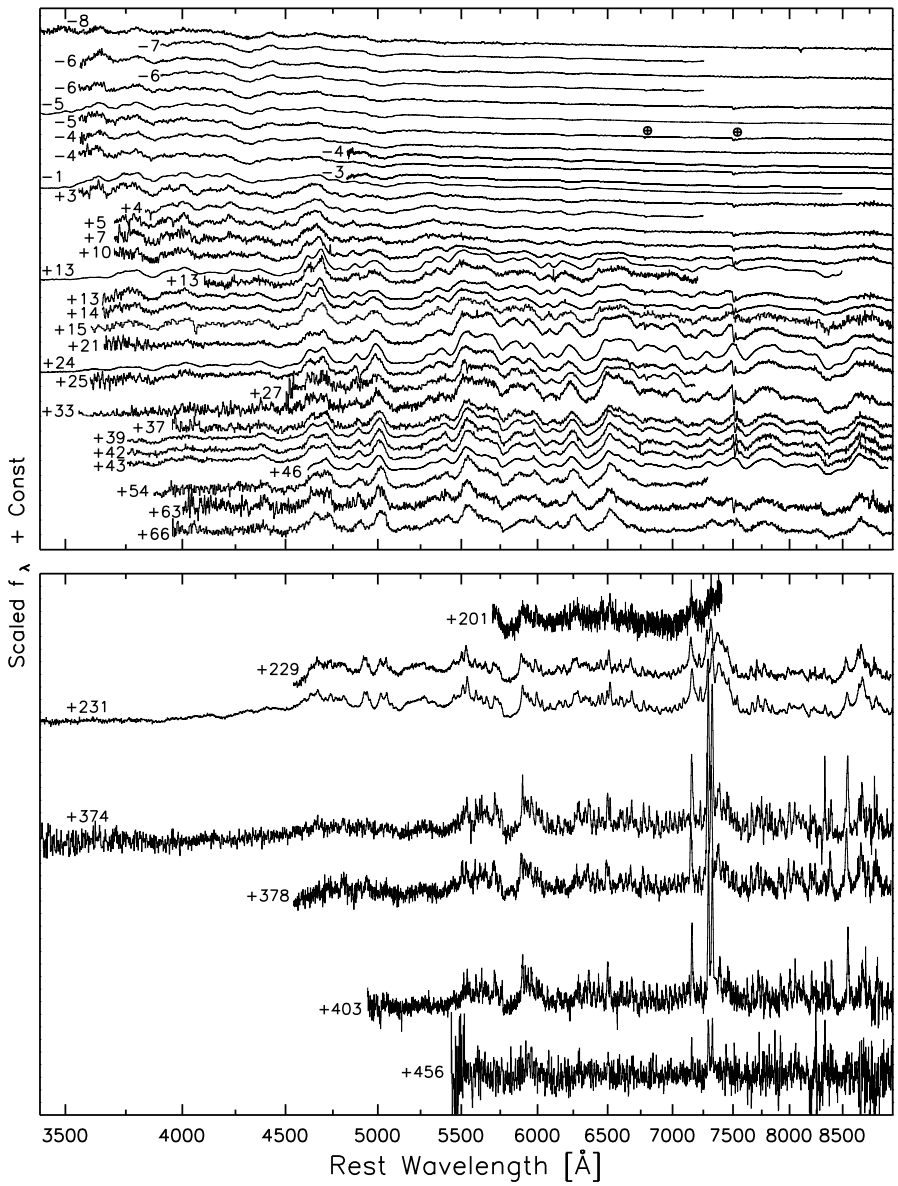

Figure 2.1 Spectral time series of SN 2005hk, labeled by phase (in days). Both the phases and wavelengths are corrected to the SN rest frame using $z = 0.01176$ from the [Ca II] $\lambda\lambda$ 7291, 7323 lines. We include spectra from Chornock et al. (2006), Phillips et al. (2007), Sahu et al. (2008), and Silverman et al. (2012). The top panel shows the early-time spectra and the bottom panel shows the late-time spectra.

in Table 2.4. WFPC2 and NICMOS observations of SN 2005hk were taken as part of *HST* program GO-11133 (PI: Jha). Additional WFPC2 observations of SN 2005hk were available from *HST* snapshot program GO-10877 (PI: Li). SN 2008A was observed in the optical using WFPC2 and ACS and in the near-IR using WFC3/IR as part of *HST* program GO-11590

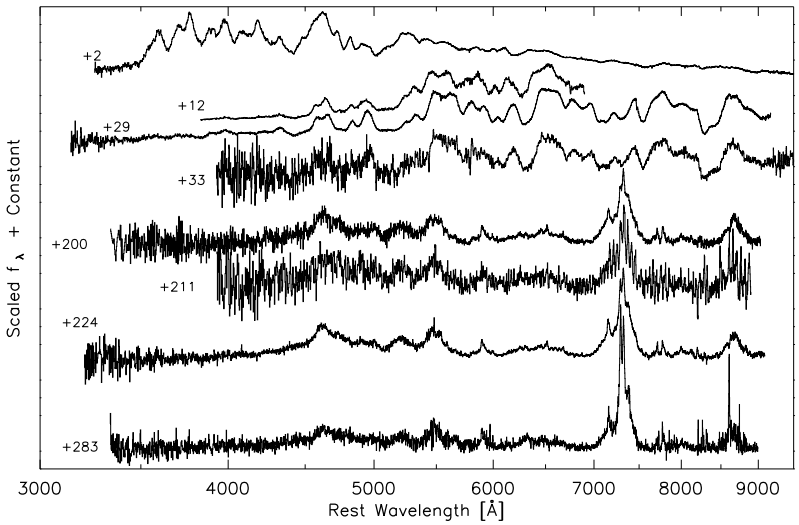

Figure 2.2 Spectral time series of SN 2008A, labeled by phase (in days). Both the phases and wavelengths are corrected to the SN rest frame using $z = 0.01825$ determined from the [Ca II] $\lambda\lambda$ 7291, 7323 lines.

Table 2.3. Spectroscopic Observations of SN 2008A

UT	MJD	Phase (days)	Telescope/Instrument	Exposure (s)	Range (Å)	Resolution (Å)
2008 01 15	54480.28	+2	Lick/Kast	1800+1350	3320–10500	6–12
2008 01 25	54490.11	+12	Plaskett/Cassegrain	9600	3900–7025	6
2008 02 12	54508.27	+29	Keck I/LRIS	200	3075–9340	7
2008 02 16	54512.23	+33	Lick/Kast	1800	3300–10500	6–12
2008 08 03	54681.63	+200	Keck I/LRIS	600+300	3270–9196	7
2008 08 15	54693.18	+211	NOT/ALFOSC	3600	4000-9050	8
2008 08 28	54706.51	+224	Keck I/LRIS	1200	3270–9196	7
2008 10 27	54766.28	+283	Keck I/LRIS	1800	3100–9160	7

(PI: Jha).

The *HST* observations were combined (with cosmic-ray rejection and subsampling) using MultiDrizzle (Fruchter et al. 2009) with standard parameters. The resulting images of SN 2005hk and SN 2008A are shown in Figures 2.3, 2.4, and 2.5. We performed aperture

Table 2.4. Late-Time *HST* observations of SN 2005hk and SN 2008A

Object	UT	MJD	Phase (days)	Instrument/Filter	Exposure (s)	Magnitude (mag)
SN 2005hk	2007 05 31	54251.11	+560	WFPC2/F450W	1600	> 25.50
SN 2005hk	2007 05 31	54251.12	+560	WFPC2/F675W	900	> 24.80
SN 2005hk	2007 05 31	54251.91	+561	WFPC2/F555W	920	> 25.50
SN 2005hk	2007 05 31	54251.92	+561	WFPC2/F814W	1400	24.91(0.22)
SN 2005hk	2007 06 25	54276.09	+585	NIC2/F110W	5120	> 25.86
SN 2005hk	2007 06 27	54278.68	+588	WFPC2/F555W	460	> 25.20
SN 2005hk	2007 06 27	54278.69	+588	WFPC2/F814W	700	> 24.55
SN 2005hk	2007 08 13	54325.45	+634	WFPC2/F606W	4800	26.35(0.15)
SN 2005hk	2007 08 13	54325.91	+634	WFPC2/F814W	1600	> 25.10
SN 2005hk	2007 08 15	54327.24	+636	NIC2/F160W	7680	> 25.08
SN 2008A	2009 02 19	54881.15	+396	WFPC2/F555W	1000	24.20(0.11)
SN 2008A	2009 02 19	54881.17	+396	WFPC2/F791W	900	23.10(0.10)
SN 2008A	2009 02 19	54881.21	+396	WFPC2/F622W	800	24.14(0.13)
SN 2008A	2009 02 19	54881.24	+396	WFPC2/F850LP	1450	23.40(0.26)
SN 2008A	2009 02 20	54882.88	+397	WFPC2/F439W	1500	> 24.35
SN 2008A	2009 08 18	55061.34	+573	ACS/F625W	3530	26.15(0.06)
SN 2008A	2009 08 18	55061.41	+573	ACS/F555W	3750	26.25(0.05)
SN 2008A	2009 08 18	55061.54	+573	ACS/F775W	2484	26.25(0.11)
SN 2008A	2009 08 18	55061.61	+573	WFC3IR/F110W	8335	26.00(0.21)

Note. — 1σ photometric uncertainties are given in parentheses. Upper limits are 3σ.

photometry on all of the images using the APPHOT task in IRAF[3]. We used aperture corrections based on encircled energies given by Holtzman et al. (1995) for WFPC2, Sirianni et al. (2005) for ACS/WFC, and the WFC3 Instrument handbook (Wong et al. 2010) for WFC3/IR. For NICMOS, we generated a point-spread function (PSF) model using the TinyTim software (Krist 1993, but see Hook & Stoehr 2008) and then directly measured encircled energies from the model. For the ACS and WFPC2 data we also corrected for the charge-transfer inefficiency of the detectors, using the models of Dolphin (2009) for WFPC2

[3]IRAF is distributed by the National Optical Astronomy Observatories, which are operated by the Association of Universities for Research in Astronomy, Inc., under cooperative agreement with the National Science Foundation.

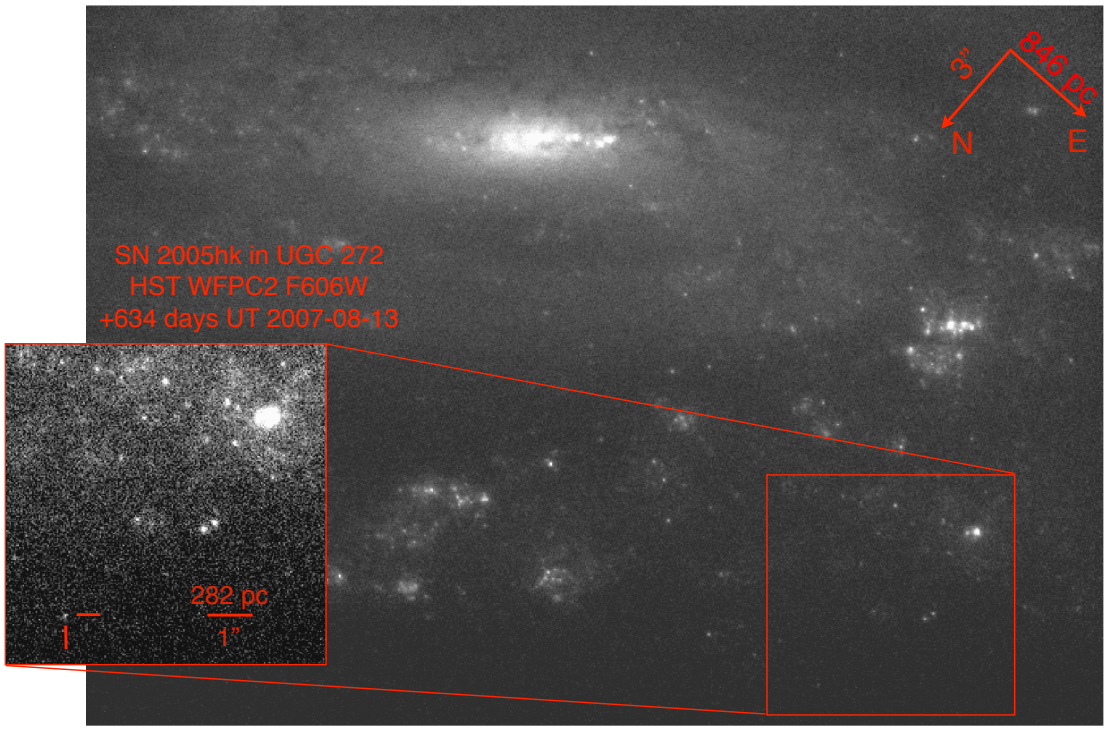

Figure 2.3 F606W observations of SN 2005hk in UGC 272 ($z = 0.013$) using the WFPC2 instrument on *HST* taken 634 days after B maximum. The SN is marked in the inset, which has been rescaled to better show the SN.

and Chiaberge et al. (2009) for ACS/WFC. To derive upper limits in cases without a significant detection of the SN, we injected fake stars with a range of magnitudes into the images. These artificial stars were photometered in the same way as the SNe, with the standard deviation of the recovered magnitudes used to estimate the photometric uncertainty. We list our derived photometry and 3σ upper limits in Table 2.4.

Both SNe 2005hk and 2008A are typical members of the SN Iax class. These two SNe along with SN 2002cx are quite homogeneous in both their light curves and their spectra. Figure 2.6 shows the spectroscopic similarity of SNe 2002cx, 2005hk, and 2008A. In Figure 2.7, we plot photometry for SNe 2002cx (Li et al. 2003; Jha et al. 2006a), 2005hk (Phillips et al. 2007; Sahu et al. 2008, and this work), and 2008A, compared to the normal SN Ia 1992A (Kirshner et al. 1993), all extending to late times.

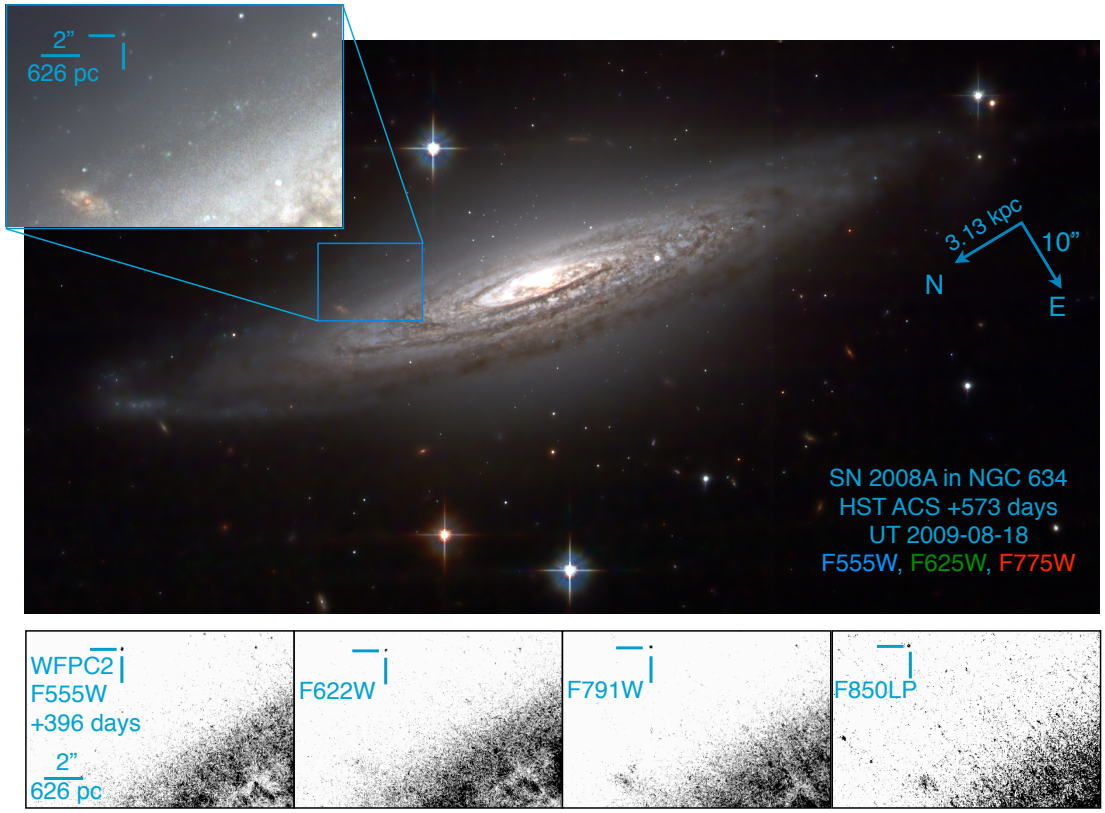

Figure 2.4 *HST* observations of SN 2008A in NGC 634 ($z = 0.016$). The top image is combined from Vri (F555W, F625W, F775W) data taken with ACS, 573 days after maximum light. SN 2008A is marked in the inset image, in the outskirts of its host. Color image was produced using STIFF (Bertin 2012). An unsharp mask filter has been applied to the color figure to emphasize faint sources for display purposes. The bottom panels show WFPC2 observations of SN 2008A taken 396 days after maximum light, in the F555W, F622W, F791W, and F850LP filters. Like SN 2005hk, SN 2008A is located in the outskirts of a spiral galaxy.

2.3 Results

2.3.1 Lack of Near-Infrared Secondary Maxima in SNe Iax

At early times, SN 2008A mimics the photometric behavior shown by SN 2002cx and SN 2005hk, with broader light curves than SN 1992A, particularly in the redder bands, as shown in the insets of Figure 2.7. These SNe Iax do not show a second maximum in the near-infrared (Li et al. 2003; Phillips et al. 2007). This is puzzling if the secondary maximum is ascribed to a transition in the dominant ionization state (Fe III to Fe II; Kasen 2006), because SNe Iax have hot early-time spectra with prominent Fe III, similar to SN

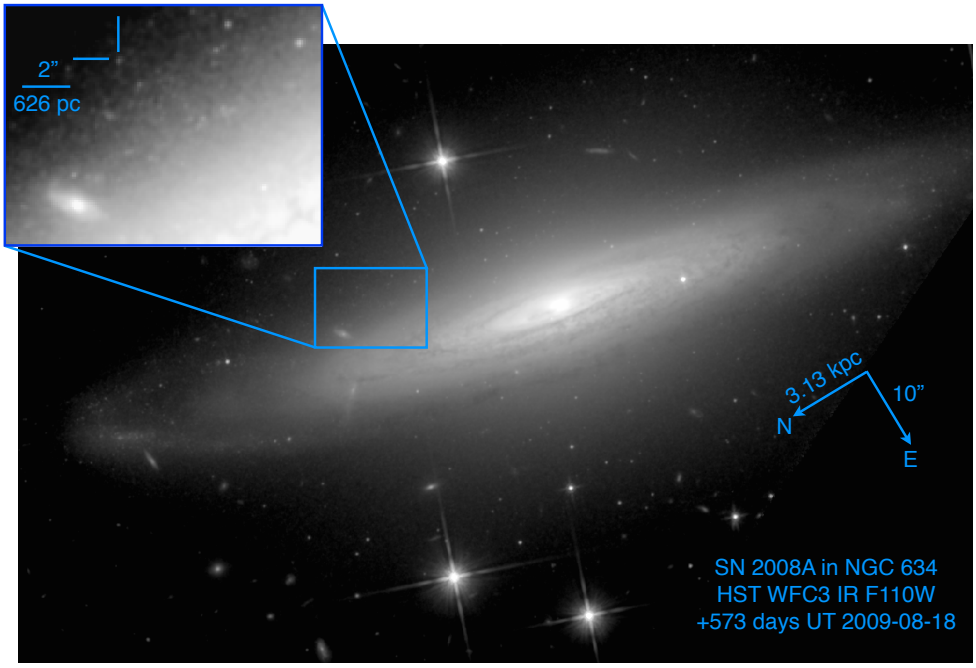

Figure 2.5 *HST* near-infrared observations of SN 2008A in NGC 634, taken in the F110W passband using the WFC3/IR camera, 573 days after maximum light.

1991T-like SNe Ia that do show a strong secondary maximum. Low luminosity SNe Ia like SN 1991bg lack secondary maxima (Filippenko et al. 1992a; Leibundgut et al. 1993); in the ionization model this is explained by an earlier transition onset in the cooler spectra, merging the primary and secondary maxima. SNe Iax could undergo much more rapid cooling near maximum light than normal SNe Ia (to explain the Fe III in the spectrum and yet lack of a secondary maximum). This is plausible as SNe Iax remain at high densities at late times instead of entering a nebular phase, which should enhance the cooling. However, we don't see evidence for rapid cooling in our late time observations, so perhaps an alternate model is needed.

2.3.2 Spectral Features and Velocity Structure

One of the defining characteristics of SNe Iax is the low velocity of their spectral features. At early times, typical SNe Iax have expansion velocities for features such as Si II of $\lesssim$ 5000 km s^{-1}, roughly half those seen in normal SNe Ia (Foley et al. 2013), though the overall

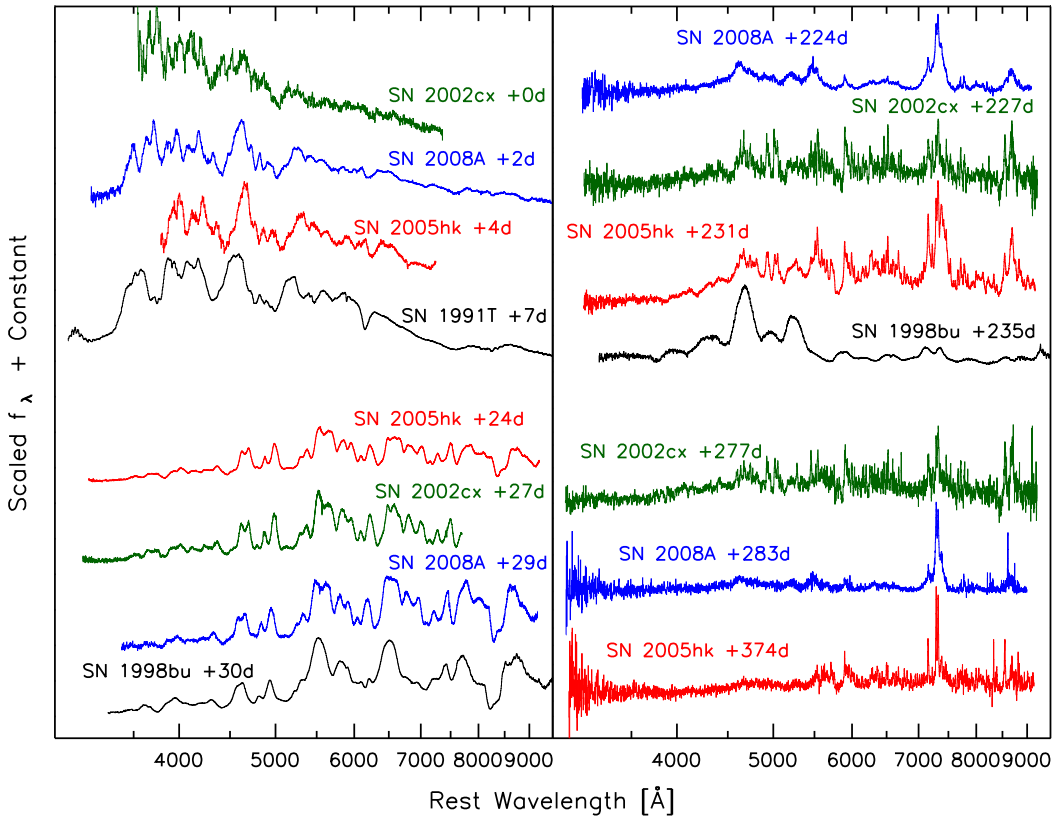

Figure 2.6 Spectra of SN 2008A (this work) and SN 2005hk (Phillips et al. 2007, and this work) compared to those of SN 2002cx (Li et al. 2003; Jha et al. 2006a). These three SNe Iax have remarkably homogeneous spectra throughout their evolution, and diverge dramatically from normal SNe Ia at late times, as shown by comparison spectra of SN 1991T (Filippenko et al. 1992b) and SN 1998bu (Jha et al. 1999; Li et al. 2001; Silverman et al. 2012).

appearance of the spectra is otherwise similar to those of SN 1991T-like and SN 1999aa-like SNe Ia. SNe Iax at late times are dominated by permitted lines from iron-group elements rather than entering a nebular phase like normal SNe Ia (Jha et al. 2006a; Foley et al. 2013). Nonetheless, a few forbidden lines are present, and the strongest features in late-time SN Iax spectra are the [Ca II] $\lambda\lambda 7291, 7323$ doublet and [Fe II] $\lambda 7155$ (Jha et al. 2006a; Sahu et al. 2008; Foley et al. 2013). Using these features, we derive the redshift of the ejecta of SNe 2002cx, 2005hk, and 2008A to be $z = 0.02323$, 0.01176, and 0.01825, respectively. Ideally, we would use the redshift of the progenitor system, but this is not possible, so we adopt these redshifts to compare the shape of spectral features between objects. These emission lines have unprecedentedly low velocities: in the last observed epoch, SN 2005hk

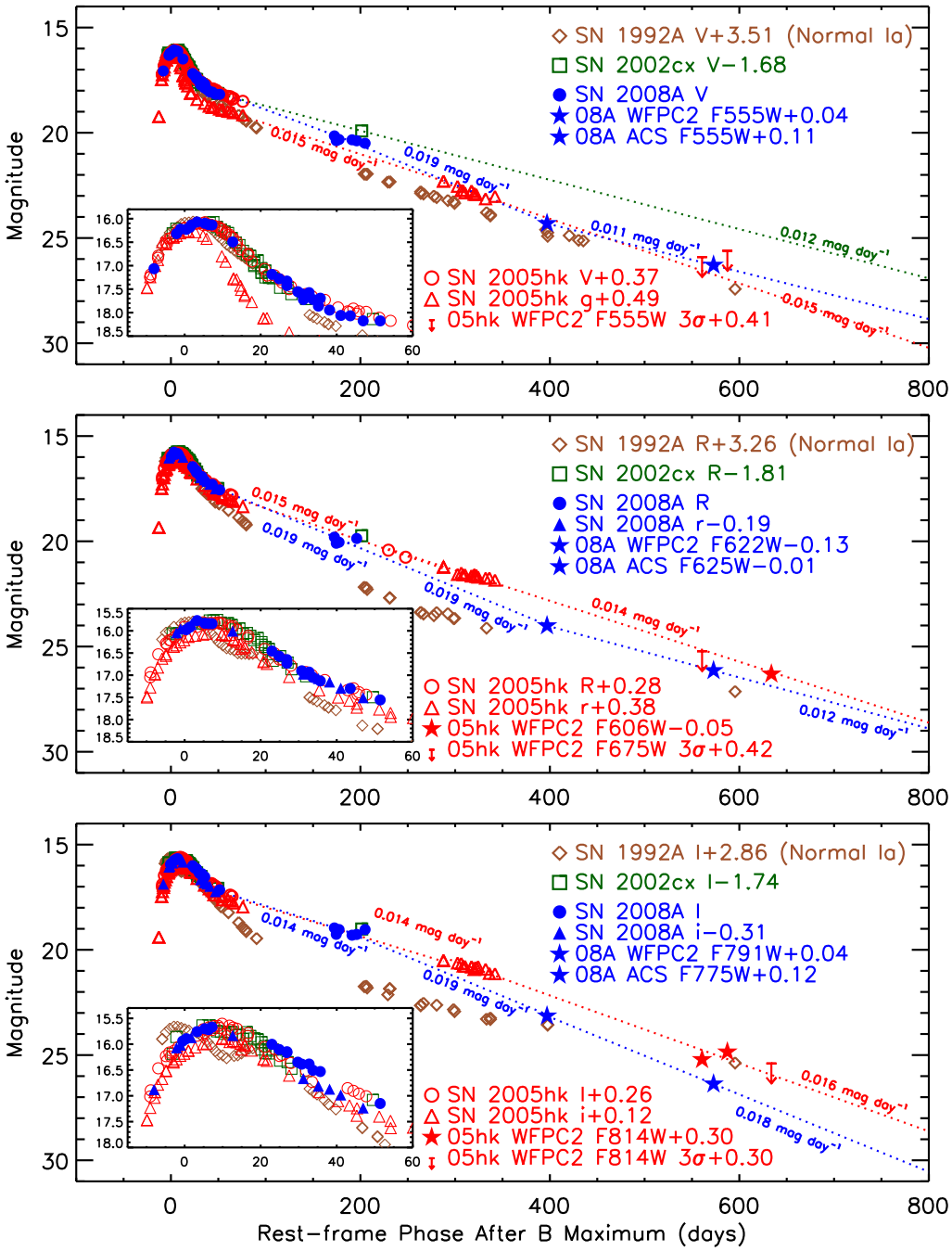

Figure 2.7 Light curves of SN 2002cx (Li et al. 2003; Jha et al. 2006a), SN 2005hk (Phillips et al. 2007; Sahu et al. 2008, and this work), and SN 2008A (Ganeshalingam et al. 2010; Hicken et al. 2012, and this work), compared to those of the normal Type Ia SN 1992A (Kirshner et al. 1993). These include both ground-based and *HST* observations as noted. The light curves have been shifted to match the peak of SN 2008A in V, R, and I. In each of the optical bands the decline rate is faster than the predicted 0.0098 mag day^{-1} for the decay of ^{56}Co.

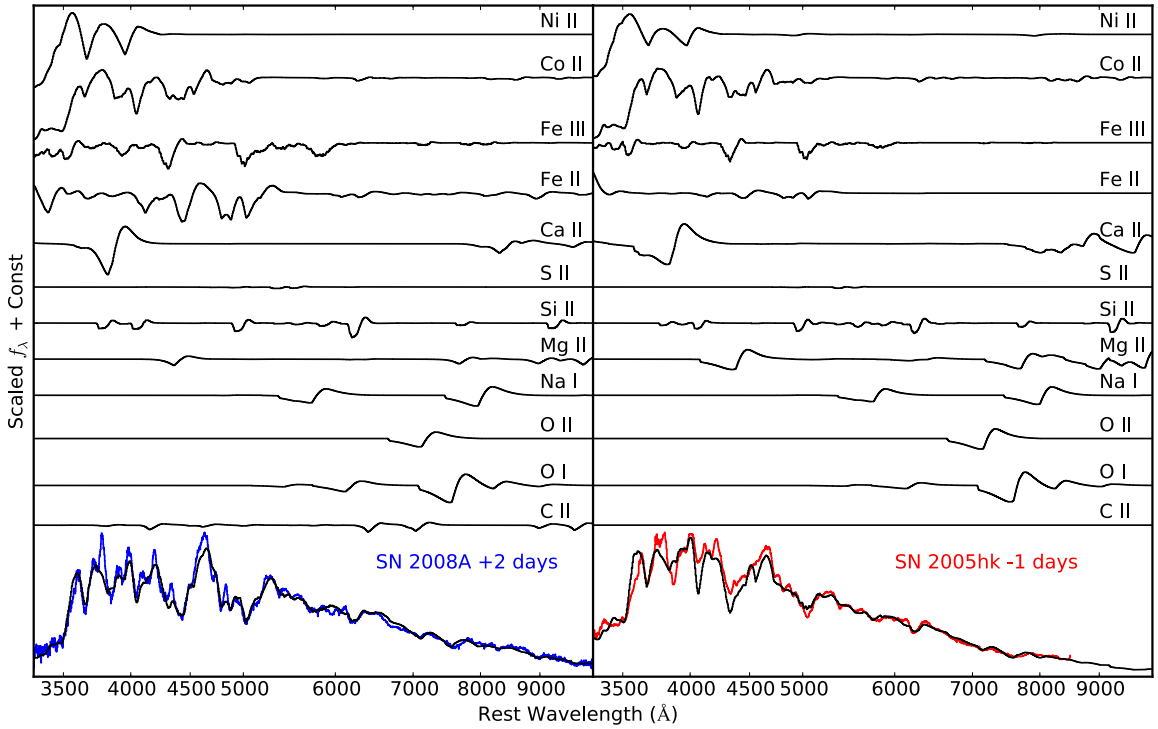

Figure 2.8 Spectral fits for SN 2008A and SN 2005hk near maximum light. The observed spectra for SN 2008A for SN 2005hk are in blue on the left red on the right respectively. The best fit synapps model (Thomas et al. 2011b) is overplotted in black and is decomposed by ion above. We find that the maximum light spectra are dominated by iron group elements, including Fe III, but also includes features due to intermediate mass elements and (presumably) unburned carbon and oxygen. The best fit velocity for SN 2005hk is ∼7000 km s^{-1}, about 1500 km s^{-1} lower than SN 2008A. This velocity difference persists at all epochs.

had velocities with a full-width half maximum (FWHM) as small as $\lesssim$ 500 km s^{-1}, the lowest ever measured for any white-dwarf SN (SN Ia or SN Iax; Phillips et al. 2007). Some faint SNe IIP also have low velocities, within a factor of two of SN 2005hk at similar phase, but these typically do not get to a FWHM of 500 km s^{-1} until $\sim$ 600 days past maximum (Maguire et al. 2012).

Figures 2.1 and 2.2 show the full spectroscopic evolution of SN 2005hk and SN 2008A respectively. The features of SN 2005hk and SN 2008A match well at all epochs as illustrated in Figure 2.6. We used Synapps (an optimizer for Syn++ Thomas et al. 2011b), based on the SYNOW code (Branch et al. 2005), to identify the strongest features in the photospheric

spectra of SN 2005hk and SN 2008A and is shown in Figure 2.8. Both objects are dominated by iron group elements, including Fe III emission similar to 91T-like spectra but with significant contributions from intermediate mass elements. We also detect (presumably) unburned material in both objects: both SN 2005hk and SN 2008A have emission from O I and possibly O II. SN 2008A has strong carbon features (even relative to normal SNe Ia), but SN 2005hk shows no evidence for carbon emission. One of the key differences between these two objects is that the velocities of the spectral features of SN 2008A are higher by 1500 km s^{-1} at maximum than those of SN 2005hk. The spectral features of SN 2005hk remain at lower velocities that those of SN 2008A at all epochs, even out to a year past maximum.

Figure 2.9 compares the late-time spectra of SN 2002cx, SN 2005hk, and SN 2008A. While these spectra are qualitatively similar, there are key differences (also analyzed in detail by Foley et al. 2013). At all epochs the velocities of SN 2008A are higher than those of SN 2005hk, similarly to the photospheric spectra. SN 2002cx shows a stronger Ca near-IR triplet than either SN 2005hk or SN 2008A. In the spectra of SN 2008A, [Fe II] λ7155 has an asymmetric profile. This may be caused by contamination from another line; there is a [Co I] feature at the wavelength in question, but no other [Co I] lines are seen (including lines more easily excited), making this option unlikely.

Sahu et al. (2008) identify [Fe II] λ7389 in their spectra of SN 2005hk. However, there is another strong feature, [Ni II] λ7378, at almost the same wavelength. The feature near these wavelengths is broader than the [Fe II] λ7155 line, so we argue that it is likely a blend of these two lines. There is a strong line that is near [Fe II] λ8617 in SN 2008A that is not seen clearly in SNe 2002cx or 2005hk, but is observed in the normal SN Ia 2003hv and has been used to measure asymmetry in the inner layers of the ejecta (Leloudas et al. 2009).

We used Syn++ (Thomas et al. 2011b) to model the permitted lines in the late-time spectra. Our results are also shown in Figure 2.9. Because the signal-to-noise ratio was the highest in the latest SN 2005hk spectrum, we fit the lines in this spectra and then matched

them to the spectra of SNe 2002cx and 2008A. We find that Fe II is necessary to fit many of the lines between 6000 and 6400 Å, as was found by Jha et al. (2006a) and confirmed by Sahu et al. (2008). While many lines are fit well with Fe II, some had remained unidentified. We find that Fe I significantly improves the fit of the late-time SN 2002cx and SN 2005hk spectra. There are strong lines to the red of the P Cygni profile of Na I λ5891 that can be seen in all three objects (SNe 2002cx, 2005hk, and 2008A) that are well fit by Fe I with an excitation temperature near 5000 K. However, there are also [Fe I] lines that match these features, making the identification of these lines ambiguous.

The velocity structure of the forbidden lines relative to the host galaxy is interesting. Figure 2.10 displays the [Ca II] $\lambda\lambda 7291, 7323$ doublet and [Fe II] $\lambda 7155$ line referenced to the host-galaxy (nucleus) rest frame (as opposed the rest frame of the ejecta used elsewhere in this work). As the figure shows, the line velocities are largely consistent over time, though the line widths decrease as the SNe evolve. Foley et al. (2013) found that the [Ca II] and [Fe II] features were shifted in opposite directions relative to the host rest frame for the majority of SNe Iax, but for these three objects (also part of the Foley et al. 2013 sample), we do not confirm this pattern, and find consistent velocities from both [Ca II] and [Fe II].

In SN 2002cx, these lines were *blueshifted* by 220 ± 52 km s^{-1} relative to the SN host galaxy. In SN 2005hk, the lines were also blueshifted by 370 ± 22 km s^{-1}. Contrarily, in SN 2008A the lines were *redshifted* by 547 ± 10 km s^{-1}. These velocity shifts are significantly in excess of the host-galaxy rotation speeds, which have maximum rotation velocities of 128 ± 14 km s^{-1} (CGCG 044-035, host of SN 2002cx), 108 ± 4 km s^{-1} (UGC 272, host of SN 2005hk), and 225 ± 7 km s^{-1} (NGC 634, host of SN 2008A), respectively (Paturel et al. 2003). This implies that the velocity shifts are intrinsic to the SN explosion. We discuss the interpretation of these results in §2.4.

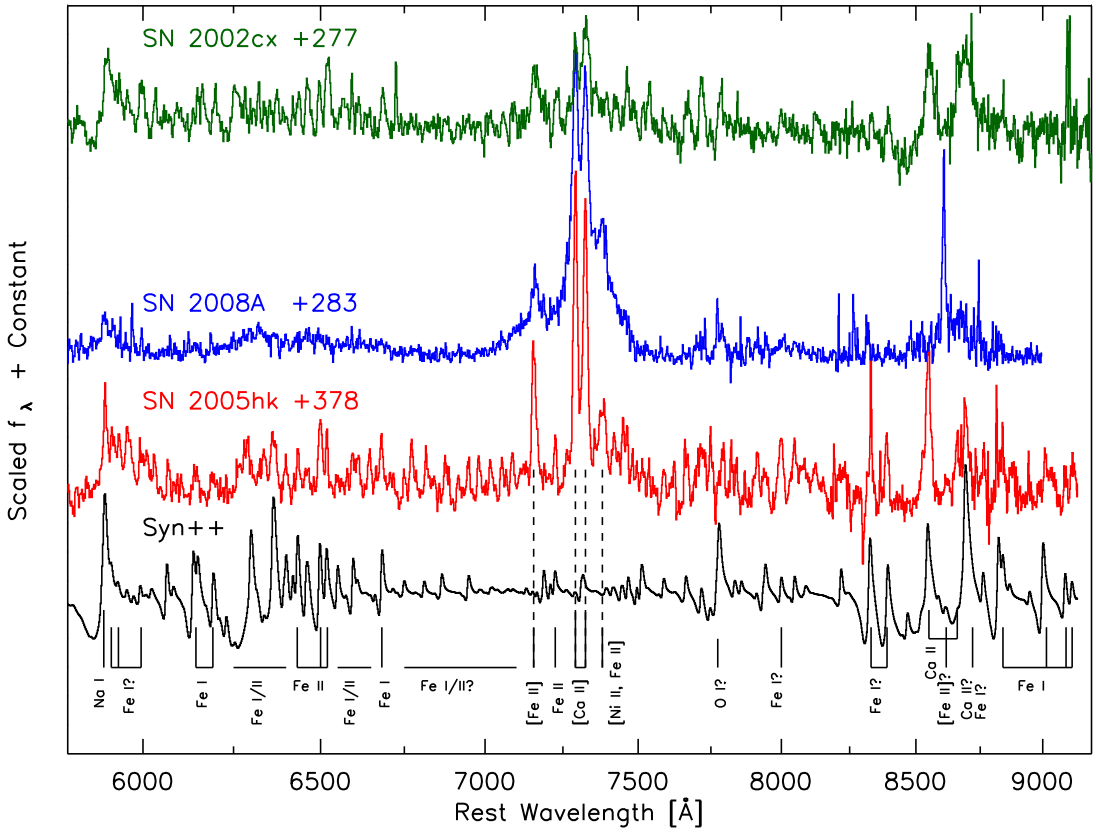

Figure 2.9 Late-time spectra of SN 2002cx (+277 days; top, green), SN 2008A (+283 days; top middle, blue), and SN 2005hk (+378 days; bottom middle, red; Sahu et al. 2008) compared to a synthetic model spectrum (black, bottom). The synthetic spectrum was created with Syn++ (Thomas et al. 2011b, similar to SYNOW (Branch et al. 2005)). The synthetic spectrum assumes Boltzmann excitation and only models the permitted lines. Non-LTE effects and forbidden lines are important for the relative strengths of the lines, but Syn++ is useful for the identification of the lines. We have marked the strongest forbidden emission features, discussed in the text, with dashed lines. The signal-to-noise ratio is substantially better in SN 2005hk, so this was used for the primary fit and then compared to SN 2002cx and SN 2008A. Line identifications are included under the synthetic spectrum.

2.3.3 Temperature and Density

Important constraints for models are provided by the physical properties of the ejecta, specifically the temperature and density at late epochs. As discussed above, the late-time spectra of SNe Iax are dominated by permitted iron transitions which would imply that the electron density has remained higher than in normal SNe Ia. More quantitatively, the ratio of the [Ca II] doublet ($\lambda\lambda$7291, 7323) to the permitted Ca II near-IR triplet can be used

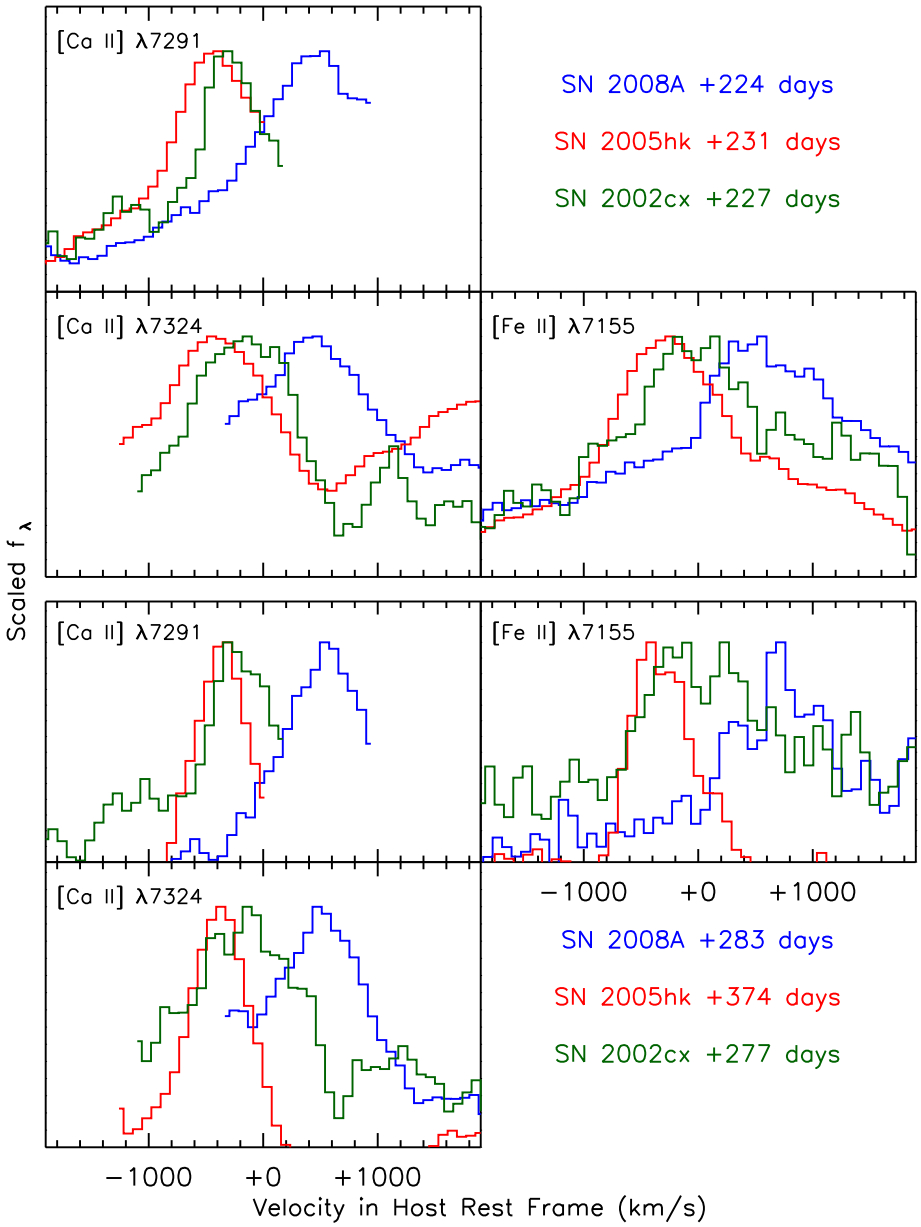

Figure 2.10 Velocity structure of the forbidden lines [Ca II] λ7291, [Ca II] λ7323, and [Fe II] λ7155 in SN 2002cx (green; Jha et al. 2006a), SN 2005hk (red; Sahu et al. 2008, and this work), and SN 2008A (blue; this work). The top three panels show each line at $\sim$230 days past B maximum and the bottom three panels show the same lines at $\sim$300 days past B maximum. The velocities of features are shown relative to the host-galaxy rest frame (in contrast to other figures, which are in the SN rest frame defined by these narrow lines). The host redshifts are $z = 0.023963 \pm 0.000087$ for SN 2002cx in CGCG 044−035 (Meyer et al. 2004; Wong et al. 2006), $z = 0.012993 \pm 0.000041$ for SN 2005hk in UGC 272 (Meyer et al. 2004; Wong et al. 2006), and $z = 0.016428 \pm 0.000027$ for SN 2008A in NGC 634 (Theureau et al. 1998). The line features of SN 2002cx and SN 2005hk are blueshifted compared to their hosts, while the features from SN 2008A are redshifted, with all the objects showing offsets of $\sim$400 km s^{-1}. The features also show a significant decrease in velocity width over time.

to constrain the electron density and temperature (Ferland & Persson 1989). As there is a degeneracy between temperature and density in this method, to infer the electron density we need an independent method for constraining the allowed temperatures.

The presence of both Fe I and Fe II transitions in the spectra of SN 2005hk is only allowed for a narrow range of temperatures, if these lines arise from the same regions in the ejecta, as suggested by the similar line profiles and velocities. The Saha equation predicts a transition between Fe II and Fe I transitions at $\sim$4500 K, and in local thermodynamic equilibrium (LTE) calculations, Hatano et al. (1999) find optical depth exceeding unity in both Fe II and Fe I for $T \lesssim 7000$ K. Although we do not expect equilibrium conditions, and non-LTE effects are likely to be important, we can still use these estimates as a reasonable range for the ejecta temperature, based on the presence and strength of the Fe I features among numerous permitted lines with similar P Cygni line profiles and velocity structure. In Figure 2.11, we show the inferred densities in SN 2002cx, SN 2005hk, and SN 2008A derived from the Ca II flux ratio for our allowed range of temperatures. We are assuming that the iron and calcium are microscopically mixed; this is plausible given their overlapping velocity ranges, but we cannot definitively say they reside in the same physical region.

The spectra of all three of our objects are consistent with little or no density evolution, and all have electron densities $\sim 10^9$ cm^{-3}. Free expansion would predict that the density should go as t^{-3}, but this is in clear contradiction with the observations. Our measurements of the density are marginally consistent with t^{-1}, but only if the temperature decreases slowly. If the temperature decreases more rapidly (as might be expected given the high densities, if radiative cooling dominates), the density is likely evolving even more slowly than t^{-1}, remaining roughly constant, or perhaps even increasing. One possible explanation, given the decreasing line widths we observe (Figure 2.10), is that we are continuing to see the "photosphere" recede to ever lower velocities, and for some reason the emitting region has a roughly constant density as the ejecta dilute.

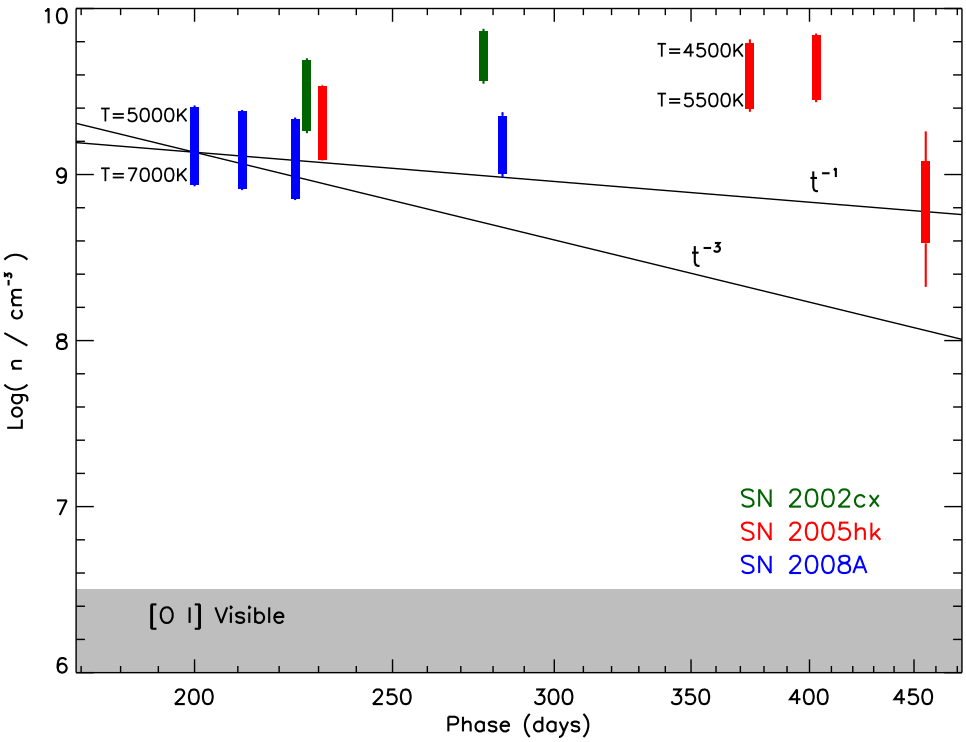

Figure 2.11 Density evolution of SN 2002cx (green), SN 2005hk (red), and SN 2008A (blue) using the measured forbidden to permitted line ratio of Ca II, based on the results of Ferland & Persson (1989). The line ratio does not give a unique temperature and density, so the allowed temperature range was constrained by the presence of both Fe I and Fe II features, yielding the bands of allowed electron densities. Each object has a electron density of $\sim 10^9$ cm^{-3} at $\sim$230 days past maximum light. The electron density is changing very slowly in all three objects; the results are consistent with no change in the electron density producing the observed emission. A density decrease proportional to t^{-3} that would be predicted by simple homologous expansion models is not consistent with the measured density evolution of these three SNe.

2.3.4 Oxygen at Late Times

As described in §2.1, pure deflagration models have been raised as a possibility to explain SN Iax explosions. These models generically predict a turbulent burning front which causes strong mixing in all layers of the ejecta, implying there should be unburned material (presumably C and O) in the innermost layers of the ejecta (Gamezo et al. 2003). At late epochs, one of the strongest spectral features should be [O I] λ6300 (assuming the entire white dwarf is disrupted). (Kozma et al. 2005).

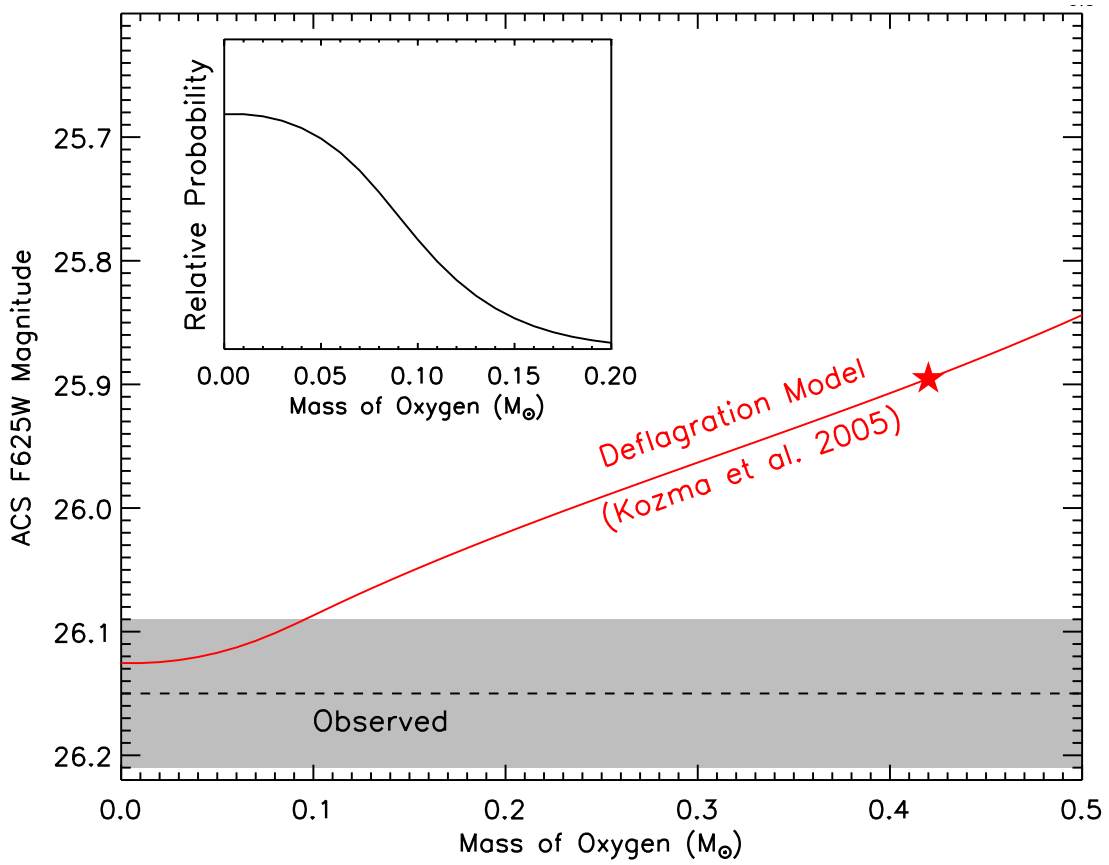

Figure 2.12 Constraints on low-density oxygen from *HST*/ACS photometry of SN 2008A at +573 days past maximum light. The gray region represents the 1σ uncertainty in our measured photometry. The red line shows the predicted r-band magnitude (with flux from the [O I] λ6300 line) assuming different amounts of unburned oxygen based on the models from Kozma et al. (2005). To calculate the probability density function (PDF) shown in the inset, we model the SED with a linear continuum and a Gaussian line profile centered at 6300 Å. We calculate the likelihood of the measured optical photometry (in F555W, F625W, and F775W) and marginalize over the slope and normalization of the continuum to derive our final PDF. The PDF peaks at zero line flux, and puts a 95% confidence upper limit of 0.14 $M_\odot$ of oxygen below the critical density for [O I] λ6300. The pure deflagration model of Kozma et al. (2005) predicts 0.42 $M_\odot$ of low-density unburned oxygen, which is ruled out at $> 5\sigma$.

There is no evidence of this line in the late-time nebular spectra of normal SNe Ia[4]. Instead, the nebular spectra of normal SNe Ia are dominated by forbidden transitions of iron-peak elements. The favored explanation for this is that the burning front transitioned from a subsonic deflagration to a supersonic detonation (Khokhlov 1991; Gamezo et al.

[4]Taubenberger et al. (2013) have recently shown the evidence for nebular [O I] $\lambda\lambda$6300,6363 with a complex line provide in a late-time spectrum of SN 2010lp, a subluminous SN 1991bg-like supernova.

2005), which subsequently burns the central material uniformly to the iron peak.

SNe Iax can have strong carbon features before and at maximum light (like SN 2008A as discussed above), corresponding to unburned material in the outer layers of the ejecta (Foley et al. 2013, and references therein). Some normal SNe Ia also show these lines at early times, but if present, they usually disappear by maximum light (Thomas et al. 2007, 2011a; Parrent et al. 2011; Folatelli et al. 2012; Silverman & Filippenko 2012). This may imply that unburned material is present at higher mass fractions deeper into the ejecta in SNe Iax compared to normal SNe Ia. If SNe Iax are to be explained as pure deflagrations (no transition to supersonic burning), we expect to see evidence of unburned material at all velocities, including the central regions that are revealed at late times.

Jha et al. (2006a) tentatively identified *permitted* O I λ7774 in SN 2002cx at 227 and 277 days after B maximum. As can be seen in Figure 2.9, the same feature is present in SN 2008A, but even stronger. If the identification is correct, this matches the model predictions of a pure deflagration explosion that never transitioned to a detonation. However, this feature is a *permitted* transition, implying that the density of the ejecta is unexpectedly high out to $\sim$280 days past maximum. By this phase, SNe Ia have transitioned to a nebular phase dominated by forbidden transitions of iron-peak elements[5]. If the identification of O I λ7774 is correct and there is unburned oxygen at low velocity, [O I] λ6300 should be a prominent feature in the nebular spectra of these objects. We searched for evidence of [O I] λ6300 in spectra of SN 2005hk taken $\sim$400 days after maximum, but SN 2005hk did not enter a nebular phase even at these late epochs and there was no evidence for [O I] λ6300.

Spectroscopy is no longer feasible after these late epochs because the SN is too faint. Instead, we use photometry to constrain the strength of the [O I] line at +573 days after maximum. [O I] λ6300 is near the center of the r band (F625W) and is reasonably isolated from any other spectral features expected to be present. Therefore, we use the r-band

[5]Branch et al. (2008) argue that permitted lines dominate optical spectra of normal SNe Ia as late as a few months past maximum light, though by about 160 days past maximum typical SNe Ia have nebular spectra (Silverman et al. 2013).

photometric flux as a proxy for the flux in the oxygen line. If the [O I] λ6300 line began to dominate other spectral features and the nearby continuum, as is predicted by the pure deflagration models (Kozma et al. 2005), we would expect a strong $r - i$ and $V - r$ color change as the SN transitions to a nebular phase.

To measure this color change, we examine two epochs of *HST* photometry of SN 2008A: the first epoch is at +396 days, at which we expect no contribution from [O I] λ6300 based on our spectra of SN 2005hk at similar epochs. In our second observation at +573 days, we do see a strong $r - i$ color change, but $V - r$ remains relatively unchanged (see the discussion in §2.3.5); this cannot be easily explained by just the appearance of a strong line in the r band.

Our photometry of SN 2008A at +573 allows us to quantitatively constrain the amount of oxygen in the ejecta below the critical density of $10^{6.5}$ cm^{-3}. The complete deflagration models of Kozma et al. (2005) give us a relationship between the oxygen mass and the [O I] λ6300 line flux. If we unrealistically assume that *all* of the observed flux in F625W is from an oxygen line, we would derive a mass of 0.63 $M_\odot$ of oxygen at low density. In reality, the oxygen line flux is only part of the observed broad-band F625W photometry. If we extrapolate just the r-band photometry from earlier times to day 573, the data allow for only 0.40 $M_\odot$ of oxygen to contribute additional line flux.

However, we can derive much more stringent oxygen mass limits if we constrain the SN spectral energy distribution (SED) in this wavelength region. Based on the observed spectroscopy at earlier times, we see that SNe Iax remain pseudo-continuum dominated in broad-band photometry to ∼400 days past maximum, and the subsequent photometry does not show dramatic changes in late-time behavior among the different passbands. This implies that we can use our measured F555W and F775W flux to bracket and constrain the expected continuum flux in F625W, with any new oxygen line flux showing up as an excess.

To do this we model the SN SED as a linear continuum (in logarithmic wavelength; $f_\lambda \propto \log \lambda$) plus a Gaussian line profile at 6300 Å with a width of 500 km s^{-1}, with a line

flux calibrated to the oxygen mass as above (Kozma et al. 2005). We perform synthetic photometry on the resulting spectra to compare to our *HST*/ACS observations in F555W, F625W, and F775W. Essentially, the F555W and F775W data determine the continuum normalization and slope, and the F625W photometry then constrains the oxygen line flux. Our broad-band measurements are insensitive to the exact shape of the line profile, and using the three bands together, we marginalize over the nuisance parameters of the continuum slope and normalization to derive the oxygen mass limit.

Our constraint is shown in Figure 2.12; we find that the mass of oxygen below the critical density of [O I] λ6300 is < 0.14 $M_\odot$ at 95% confidence. Complete deflagration models that fully disrupt the white dwarf predict $\sim$0.4 $M_\odot$ of unburned oxygen (Kozma et al. 2005). This is ruled out at high confidence ($> 5\sigma$). Either a large amount of unburned material is not present in SNe Iax, or it remains at high density to very late epochs. Even if the ejecta mass were as low as $\sim$0.5 $M_\odot$, we would expect $\sim$0.15 $M_\odot$ of unburned oxygen (assuming the same ratio of oxygen mass to ejecta mass as the models from Kozma et al. 2005) — and this would still be ruled out at $> 95\%$ confidence.

As discussed, our results depend on the assumed shape of the SN SED. However, if we enforce a smooth continuum over the observed wavelength range (so we can incorporate the F555W and F775W data into our analysis), different prescriptions for the exact continuum shape lead to only small changes in the oxygen mass constraint of $\sim$0.02 $M_\odot$.

Based on our temperature and density measurements, the electron density may have been significantly higher than the critical density for [O I] λ6300 of $10^{6.5}$ cm^{-3} during our latest *HST* measurement of SN 2008A, nearly 600 days past maximum brightness. But if the roughly constant observed density is somehow the result of a receding photosphere, this would imply a significant amount of material at higher velocities and lower densities, and any oxygen mixed there should be detectable in [O I] emission as probed by our photometry. Complete deflagration models such as those of Kozma et al. (2005) predict strong mixing, so we disfavor the idea that all the oxygen is at low velocity, shielded by a photospheric

"iron curtain" at higher velocity (Leonard 2007). Sahu et al. (2008) find in their models of SN 2005hk that if a significant fraction of the gamma rays are still exciting photospheric transitions, the resulting [O I] λ6300 is weak enough at +250 days to be consistent with the nondetection in the observations, even in the case of 0.8 $M_{\odot}$ of unburned oxygen. However, it is unclear whether this can be sustained as late as +600 days, where our observations of SN 2008A otherwise significantly constrain any low-density oxygen. It is possible that this points to a diversity between objects like SN 2005hk and SN 2008A, but even for SN 2005hk itself, the suppression of [O I] emission must continue until at least +456 days past maximum, as it is undetected in our latest spectrum. Our conclusion is that either the spectroscopic detection of permitted O I λ7774 at low velocity in SNe 2002cx and 2008A (as seen in Figure 2.9) is a misidentification, or, if not, a more complicated model (perhaps like one that produces a bound remnant) must be developed to explain the apparent contradiction between the permitted and forbidden lines; we discuss further implications of this finding in §2.4.

2.3.5 IR Catastrophe

The "infrared catastrophe" is a long-predicted, generically expected phenomenon that has nonetheless never been observed in normal SNe Ia (Leloudas et al. 2009)[6]. Axelrod (1980) calculated that once the ejecta temperature dropped below a critical value ∼1500 K, there would be a radical redistribution of energy from the optical to the far-IR, dominated by fine-structure lines of iron like [Fe I] 24 μm and [Fe II] 26 μm rather than the forbidden iron-peak lines seen in the optical and near-IR that dominate the SN Ia bolometric luminosity a few hundred days past maximum light (Sollerman et al. 2004). This redistribution of energy has been used to explain the line emission of SN 1987A (Kozma & Fransson 1998), but it has never been observed in a normal SN Ia. One possible explanation is that the ejecta of SNe Ia stay above this critical temperature until after they are too faint to observe.

[6]Taubenberger et al. (2011) suggest that the IR catastrophe could be at play in the rapid late-time decline of the light curve of the "super-Chandrasekhar" SN 2009dc.

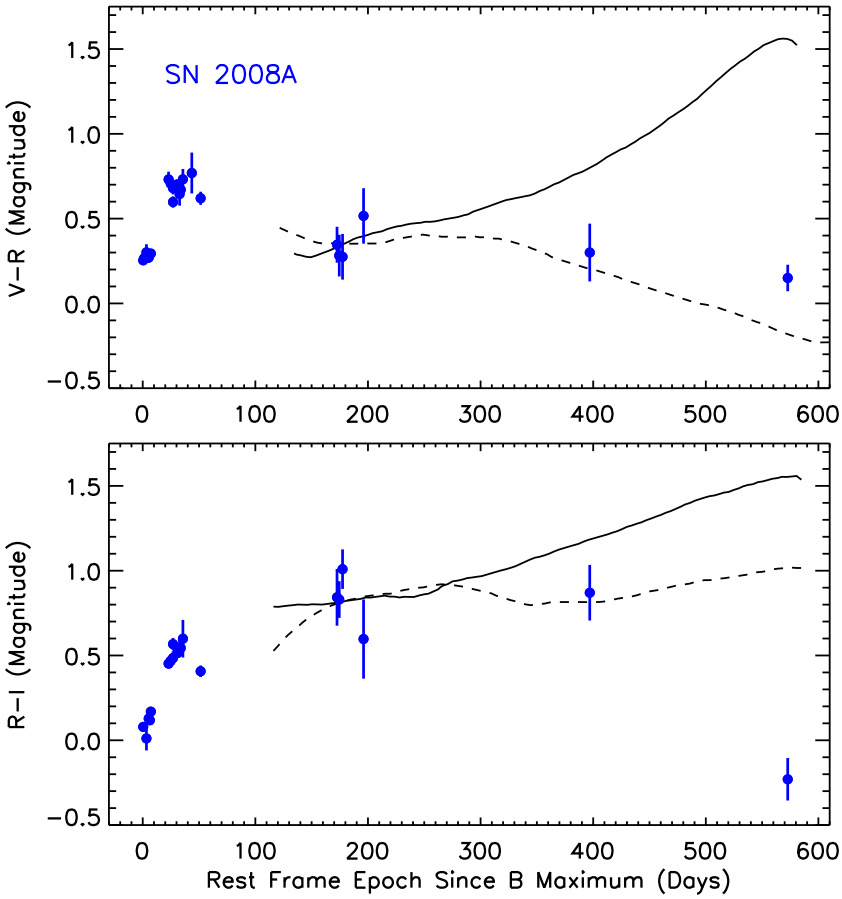

Figure 2.13 $V - R$ (top) and $R - I$ (bottom) color evolution of SN 2008A compared to IR-catastrophe models from Sollerman et al. (2004). The dashed line includes photodisintegration in the model while the solid line does not. The data have been standardized to V, R, and I as in Figure 2.7. The models have been shifted vertically to match the data at $\sim$200 days.

Leloudas et al. (2009) find that even 785 days after B-band maximum brightness, SN 2003hv is not compatible with an IR catastrophe.

SNe Iax are unique testing grounds for this phenomenon. Because these objects remain at high density for so long, we might expect them to have enhanced cooling compared to normal SNe Ia. This could cause the IR catastrophe to happen early enough that it would still be feasible to image the SN. Qualitatively, if we use the excitation temperature of the iron (and assume microscopic mixing), we can estimate what the temperature of the ejecta will be at the time of our final *HST* measurement. Constructing a simple model

that assumes that the excitation temperature of iron is ∼10,000 K at maximum brightness (giving rise to the dominant Fe III lines observed) and ∼4000 K at 300 days after maximum brightness (see §2.3.3), it is plausible (though by no means required) that the temperature at the epoch of our final *HST* measurement could approach the ∼1500 K threshold for the IR catastrophe. Sollerman et al. (2004) model this transition and find that the most easily observable signature (i.e., not in the far-IR) for the IR catastrophe is a dramatic color change in the near-IR, but we only have one near-IR measurement, (J:F110W), so we cannot observe this color change directly.

Sollerman et al. (2004) also show that the optical colors should become significantly redder in all optical bands during and after the IR catastrophe, with significant $V - R$ and $R - I$ color changes of $\sim$1 mag. We compare this model with the observations of SN 2008A in Figure 2.13. Though there is some freedom to shift to model predictions vertically in magnitude and horizontally in time on the plot, we nonetheless see that the colors of SN 2008A change in the *opposite* way of the predicted color changes. Rather than getting redder, $V-I$ and $R-I$ data are bluer at late times (with $V-R$ remaining basically unchanged). Thus, we find no evidence for an IR catastrophe in SN 2008A, out to nearly 600 days past maximum light, despite the high densities.

The late-time spectra of SNe Iax differ significantly from those of normal SNe Ia. Normal SNe Ia cool through forbidden iron lines in the nebular phase. SNe Iax have not been shown to ever become nebular, and the strongest forbidden lines are from [Ca II]. There are iron features in the late-time spectra of SNe Iax, but a significant fraction of the emergent radiation is produced by permitted transitions. It is not even clear that radiative cooling dominates over adiabatic expansion at late times in SNe Iax. Because of these differences, it is possible that the predictions of IR catastrophe models for normal SNe Ia do not apply to SNe Iax. Ironically, it could be that the high densities that should enhance the cooling and lead to an earlier IR catastrophe are instead responsible for quenching the expected changes in forbidden-line emission.

2.3.6 Bolometric Luminosity

We use ground-based and *HST* photometry to estimate the UV/optical/near-IR luminosity $L_{\rm UVOIR}$ of SN 2002cx, SN 2005hk, SN 2008A, and the normal SN Ia 2003hv. Sollerman et al. (2004) and Leloudas et al. (2009) show that the flux in the near-IR becomes a significant fraction of the bolometric luminosity of SNe Ia at late times, and we are able to replicate the near-IR corrections of Leloudas et al. (2009) in our calculations for SN 2003hv.

For SNe 2002cx and 2008A, we do not have much information about the flux in the IR. Phillips et al. (2007) present near-IR light curves of SN 2005hk to a few months past maximum light, showing significantly enhanced near-IR flux compared to normal SNe Ia. However, at these epochs the near-IR contribution to the bolometric luminosity is only a few percent, and it is unclear whether the excess near-IR flux persists to later epochs, or merely becomes more significant earlier in SNe Iax than in normal SNe Ia.

To correct the SNe Iax for the poorly constrained near-IR flux, we integrate our interpolated photometric SED from 3000 Å to 10000 Å and add the IR contribution fraction measured for SN 2003hv (Leloudas et al. 2009). This approach produces results that are consistent with the late-time near-IR data we do have (a WFC3/IR F110W measurement for SN 2008A and NICMOS F110W and F160W upper limits for SN 2005hk; Table 2.4). For the final two *HST* observations of SN 2005hk, we have a detection only in a single optical photometric band; to calculate the bolometric luminosity at these late epochs, we use the SED of SN 2008A at a similar phase and scale the flux to match the SN 2005hk observation.

As shown in Figure 2.14, we find that the bolometric light curves of SNe Iax are markedly different from that of a typical core-collapse SN IIP, SN 2005cs (Pastorello et al. 2009), though of course core-collapse SNe show a wide range of behavior. The SNe Iax are similar to each other, and significantly less luminous than the normal SN Ia 2003hv at maximum light, but broadly similar to SN 2003hv starting $\sim$100 days after maximum light.

The faster decline rate of SN 2003hv compared to SNe Iax for the first 200 days suggests

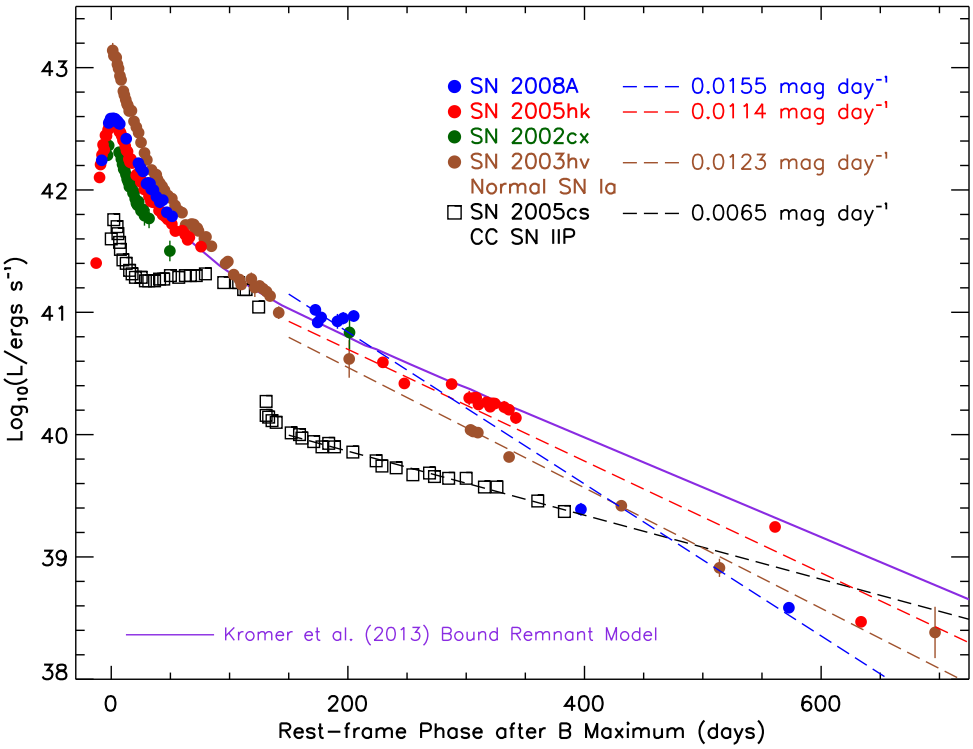

Figure 2.14 Bolometric light curves of SN 2002cx (Li et al. 2003; Jha et al. 2006a), SN 2005hk (Phillips et al. 2007; Sahu et al. 2008, and data from SDSS-II), SN 2008A (Ganeshalingam et al. 2010; Hicken et al. 2012, and this work), the normal Type Ia SN 2003hv (Leloudas et al. 2009), and the Type IIP SN 2005cs (Pastorello et al. 2009). The bolometric luminosities of SNe Iax are similar to those of normal SNe Ia starting a few months after maximum, but differ significantly from those of SNe IIP. SN 2003hv declines much faster than SN 2008A and its counterparts at ∼200 days past maximum. The magenta line shows the model from Kromer et al. (2013) that assumes complete gamma-ray trapping. This model fits most of the data well, but it is not consistent with the latest measurements of SN 2008A and the last measurement of SN 2005hk.

that the escape fraction of gamma-rays in normal SNe Ia increases more quickly than in SNe Iax. This may result from a more rapid decrease in the density of the ejecta in normal SNe Ia (also suggested by our inferred SNe Iax densities; Figure 2.11). The bolometric luminosity of SN 2005hk roughly follows the full gamma-ray trapping model of Kromer et al. (2013) for all but the latest epoch. SN 2008A is also consistent with the full gamma-ray trapping model at early times.

However, in the latest observations, more than ∼400 days past maximum, that trend reverses: SN 2003hv declines more slowly than SN 2005hk or SN 2008A. At these epochs,

the decline rate for SN 2003hv is close to the predicted ^{56}Co to ^{56}Fe decay rate of 0.0098 mag day^{-1}. This may be an indication of *positron trapping* in the ejecta of this normal SN Ia. About 3% of the ^{56}Co decay energy goes to positrons, compared to 97% in gamma-rays (Milne et al. 1999). Even if the gamma-ray escape fraction is near unity, positrons may be trapped by (nonradial) magnetic fields, and can lead to a shallowing of the bolometric luminosity decline rate when the luminosity falls to $\sim$3% of the full gamma-ray trapping prediction.

At the epochs of our last observations of both SNe 2005hk and 2008A, the bolometric luminosity drops below that of the Kromer et al. (2013) model. This could be a sign that the gamma-ray escape fraction is beginning to increase, at a much later epoch than occurs for normal SNe Ia because of the much higher densities in the ejecta. We might then predict that at even later times, again when the bolometric luminosity falls to $\sim$3% of the full gamma-ray trapping prediction, the bolometric light curves of SNe Iax may flatten because of positron trapping. Nonetheless, this remains speculative, as we are not measuring the true bolometric luminosity. If either normal SNe Ia or SNe Iax undergo an IR catastrophe, the UVOIR luminosity will not trace the bolometric luminosity, complicating efforts to constrain the positron trapping. Moreover, many normal SNe Ia show steeper decline rates at late epochs, inconsistent with full positron trapping (e.g., Lair et al. 2006), and in some cases even when the near-IR flux is included in the "bolometric" luminosity (Stanishev et al. 2007a).

2.4 Discussion

As described in §2.3.2, the velocity shifts measured from late-time forbidden lines in SNe 2002cx, 2005hk, and 2008A are larger than can be accounted for by galactic rotation alone. These offsets are measured from [Ca II] and [Fe II] lines; if the ejecta were optically thin in these lines as expected, the velocity offsets could be caused by bulk velocity shifts of the ejecta. This might correspond to the high-velocity remnant predicted by the failed

deflagration model of Jordan et al. (2012), although significant velocity kicks are not found in similar models from Kromer et al. (2013) or Fink et al. (2014).

The velocity shifts could also be the result of an asymmetric explosion. However, Chornock et al. (2006) measured less than 1% polarization for SN 2005hk, implying very little asymmetry at early times (see also Maund et al. 2010). For the normal Type Ia SN 2003hv, Leloudas et al. (2009) measured a velocity shift of $\sim$2600 km s^{-1} in the [Fe II] λ8617 line. Maeda et al. (2010b) show that the large velocity shifts in the inner regions of SN 2003hv could arise in the deflagration phase of a delayed detonation model. Maeda et al. (2010a) use a model with asymmetry of the deflagration phase to explain the variation of SN Ia velocity gradients, and show that different viewing angles can account for much of the diversity of SNe Ia (but see Wang et al. 2013, who find a host-galaxy dependence that cannot be explained by viewing angle alone). In this model, the deflagration stage is characterized by turbulent burning underlying a convective, bipolar structure which creates an asymmetry in the ejecta (Kuhlen et al. 2006; Röpke et al. 2007). The velocity shifts for SNe 2005hk and SN 2008A are much smaller than that for SN 2003hv, which might be caused by a lower kinetic energy during the deflagration phase, and perhaps implying less total burning. The fact that the forbidden-line velocity *offsets* are comparable to line *widths* in both SNe Iax and normal SNe Ia may point to a common physical origin, though this may be generic to all SNe.

The identification of S II and Si II lines in early-time spectra of SNe Iax point to a thermonuclear event (Foley et al. 2010a, 2013). Our identification of late-time [Ni II] λ7378 in SN 2005hk and SN 2008A could thus have important consequences, as Maeda et al. (2010a,b) identify both [Fe II] λ7155 and [Ni II] λ7378 as lines that correspond to *deflagration ashes*. They argue that these lines trace material subject to long exposure to low heat, as opposed to [Fe III] λ4701 that traces the detonation phase. This [Fe III] transition is not obvious in SN Iax spectra at late times, which may imply that there is no transition to a detonation.

What could suppress a transition to a detonation in SNe Iax? From simulations, Röpke et al. (2007) suggest that the number and position of deflagration ignition points could be a significant factor. For example, they claim that a model with two overlapping ignition bubbles at the center of the white dwarf was unlikely to produce a detonation; thus, such a scenario might produce a SN Iax. However, Seitenzahl et al. (2013) find that the conditions are met for a detonation in all of their models ranging from a single ignition point up to 1600 ignition points. Even a pure deflagration does not explain the incredibly low kinetic energy for the most extreme members of the SN Iax class, such as SN 2008ha.

To explore low-energy complete deflagration scenarios for more typical SNe Iax, we examined a homologous expansion model using the density profiles of Röpke (2005). We find that it is possible to produce the high densities observed at late times, but the initial kinetic energy distribution must be several times lower than in the model (also assuming the emitting region moves to lower velocities and roughly constant density, as Figure 2.11 requires). Scaling down the velocity of the density distribution, we find that the speed of material at the radius with 10% of the total enclosed mass ($R_{0.1}$) must be as low as 150 km s^{-1} to approach the observations. At first glance, this result seems like it could qualitatively explain the lack of the [O I] λ6300 flux by keeping a substantial amount of unburned material at high density. However, quantitatively, we find that even for homologous expansion that is scaled to the lower kinetic energies, at 600 days after maximum brightness, $\sim$55% of the oxygen should still be below the critical density. This corresponds to $\sim$0.2 M$_\odot$ of low-density oxygen in the Röpke (2005) models, and is ruled out by our observations at high significance (Figure 2.12). However, our constraint could be weakened if the [O I] excitation is being suppressed by a mechanism where photospheric lines are preferentially excited (Sahu et al. 2008; see §2.3.4), though it is unclear whether this could continue as late as 600 days past maximum light.

Generically, we find that even if there is a photosphere hiding the innermost regions, the models predict oxygen at higher velocities that should be visible, and yet is not seen.

Observationally, the decreasing widths of the forbidden lines of iron and calcium with time (see Figure 2.10) imply that these lines are not being excited everywhere in the ejecta. If these lines are only produced near the "photosphere" responsible for the numerous permitted Fe lines, there must be a large reservoir of lower-density material at higher velocities that is not radiating *either* in these lines, nor is it seen in lower density tracers like [O I] λ6300.

In normal SNe Ia, the widths of nebular lines at late times is of order 10^4 km s^{-1} (Mazzali et al. 1998; Silverman et al. 2013). If, as expected, we are "seeing through" all the excited ejecta in these forbidden transitions, the line profiles directly reveal the velocity structure, and the observed line width is effectively the "final" velocity for the ejecta, v_∞. Moreover, for an exploding white dwarf that is completely disrupted, we expect $v_\infty \gtrsim v_{\rm esc}$, the escape velocity of that material in the white dwarf; otherwise the explosion would need to be finely tuned to barely unbind the white dwarf and leave the ejecta expanding at low velocities.

The widths of forbidden lines of Ca II and Fe II in the late-time spectra of SN 2005hk are unprecedentedly low — 500 km s^{-1}. If this is interpreted as the velocity at infinity for the emitting ejecta, it is an order of magnitude below the escape velocity from the surface of the white dwarf, $v_\infty \ll v_{\rm esc}$. Using a simple model of a Chandrasekhar-mass white dwarf with a polytropic equation of state, we calculated the escape velocity as a function of the enclosed mass throughout the white dwarf. At $v_{\rm esc} = 500$ km s^{-1} the enclosed mass is just $\sim 5 \times 10^{-6}$ of the total mass. It seems implausible that all of the late-time emission arises from just this innermost tiny fraction of the white dwarf.

More likely, we are witnessing a weak explosion, in which the explosion energy is close to or less than the binding energy of the white dwarf. The material emitting in the forbidden lines was barely unbound, and we observe it at low $v_\infty \ll v_{\rm esc}$. In that case, unless again the explosion energy is finely tuned, we would also expect a significant fraction of the original white dwarf to not reach escape velocity, and remain bound, leaving behind a remnant. The high densities observed might also be explained if the white dwarf was not fully disrupted,

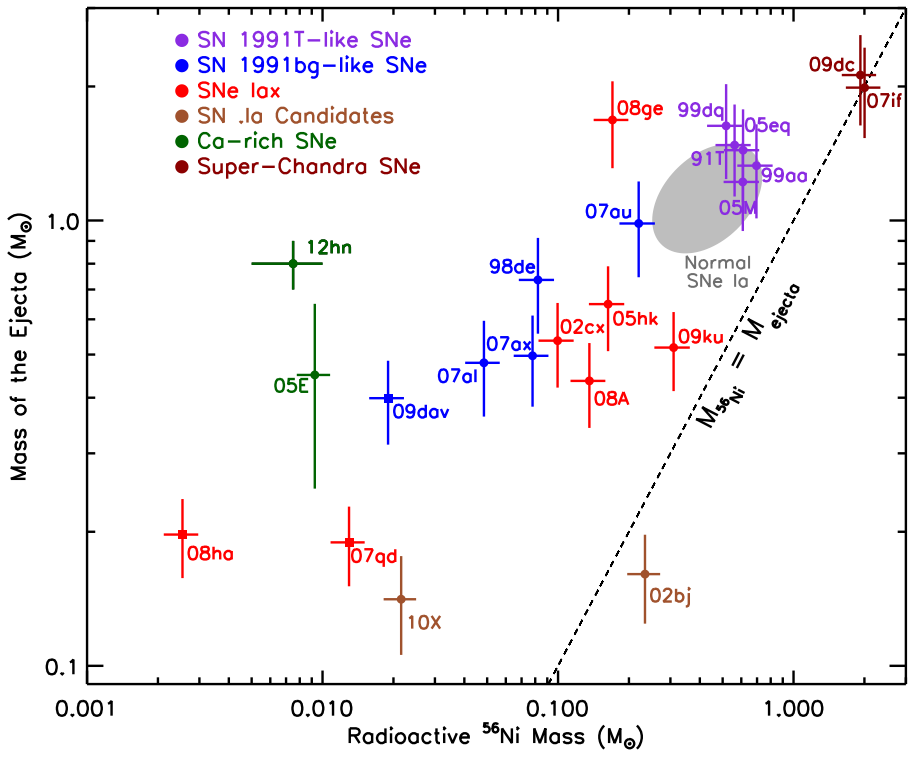

Figure 2.15 Total ejected mass vs. radioactive nickel mass of white-dwarf SNe. Subclasses of objects are grouped by color as indicated in the plot. Circles denote typical members of the subclass, while squares show more extreme members. The dashed line denotes where the ejected mass equals the radioactive nickel mass. Objects to the right of the line (like SN 2002bj) require additional energy sources (beyond ^{56}Ni radioactive power) to explain their luminosity. References: SN 1991T (Filippenko et al. 1992b; Phillips et al. 1992); SN 1998de, SN 2007al, SN 2007au, and PTF 2009dav (Sullivan et al. 2011); SN 1999aa and SN 1999dq (Jha et al. 2006b); SN 2002bj (Poznanski et al. 2010); SN 2002cx (Li et al. 2003; Jha et al. 2006a); SN 2003du (Hicken et al. 2009); SN 2003hv (Leloudas et al. 2009); SN 2005E (Perets et al. 2010; Waldman et al. 2011); SN 2012hn (Valenti et al. 2014); SN 2005M and SN 2005eq (Ganeshalingam et al. 2010); SN 2005hk (Phillips et al. 2007); SN 2007ax (Kasliwal et al. 2008); SN 2007if (Scalzo et al. 2010); SN 2007qd (McClelland et al. 2010); SN 2008A (this work); SN 2008ge (Foley et al. 2010b); SN 2008ha (Foley et al. 2009; Valenti et al. 2009); SN 2009dc (Taubenberger et al. 2011); SN 2009ku (Narayan et al. 2011); and SN 2010X (Kasliwal et al. 2010). Ancillary data were used in the analysis, including ejecta velocities (Foley et al. 2011), rise times (Ganeshalingam et al. 2011), bolometric corrections (Contardo et al. 2000), and distances and luminosities (Ganeshalingam et al. 2013).

with the mixed composition of the unbound ejecta arising from a deflagration. Livne et al. (2005) show that a single ignition that is offset from the center of the white dwarf could form a bubble that would convectively rise and break through the surface, without fusion outside of the bubble. Events like this could explain typical SNe Iax and the extreme SN 2008ha,

yet still show the thermonuclear signature of Si II and S II.

Kromer et al. (2013) and Jordan et al. (2012) find that a failed deflagration of a white dwarf can produce properties similar to those observed for SNe 2005hk and 2008A. A key prediction of these models is that the explosion leaves behind a bound remnant. This is consistent with our argument above about the escape velocity of the white dwarf. Jordan et al. (2012) find that the remnant receives a kick of $\sim$500 km s^{-1}, which is roughly consistent with our measurements of the velocity offsets from the host galaxies. This assumes that the velocities of the forbidden lines are measuring the bulk motion of the ejecta rather than an excitation effect. While Kromer et al. (2013) do not find such significant kick velocities, their model matches the bolometric light curves of SN 2005hk and SN 2008A relatively well, except at the latest observed epochs (Figure 2.14).

While suggestive, the case for a bound remnant is not without problems. If we assume homologous expansion, material at 300 km s^{-1}, about half the width of the forbidden lines, would be at 100 AU about 600 days past explosion. This cannot be the radius of a true photosphere, because the bolometric luminosity at that epoch ($\sim$10^{38} erg s^{-1}) is much too low given the estimated temperature. The bolometric luminosity limits the photospheric radius to $\lesssim$ 3.5 AU, making it difficult to directly connect the high density expanding material with a potential bound remnant. Moreover, these models still require an explanation for the lack of unburned material detected in ejecta that should be well mixed (including intermediate-mass and iron-group elements) and reach low density. Perhaps additional complexity is required, such as back-warming in which inwardly traveling gamma-rays deposit their energy and heat lower-velocity regions, while outwardly traveling gamma-rays escape.

Throughout this paper, we have assumed that radioactive heating from ^{56}Ni dominates the luminosity of these SNe Iax. It is instructive to put SNe Iax in context with other probable thermonuclear explosions of white dwarfs. We compiled a sample of such objects from the literature to infer their radioactive nickel mass and ejecta mass; the results are shown in Figure 2.15. The ^{56}Ni mass was calculated using the Arnett (1982) rule, and

for this comparison we simply adopted a uniform uncertainty of 15% for all bolometric luminosities and a 10% uncertainty for the SN rise times. These correspond to typical published uncertainties for the objects for which error bars were reported. We calculated the ejecta mass following Foley et al. (2009), assuming an opacity of $\kappa = 0.1$ cm^2 g$^-$1 and a uniform 5% uncertainty on the ejecta velocities. The relations are scaled such that normal SNe Ia produce 1.4 $M_\odot$ of ejecta, with $\sim$0.5 $M_\odot$ of ^{56}Ni. Normal SNe Ia form an approximate continuum from the subluminous SN 1991bg-like objects (Filippenko et al. 1992a; Leibundgut et al. 1993) to the superluminous SN 1991T-like (Filippenko et al. 1992b; Phillips et al. 1992), and even to more extreme "super-Chandra" objects such as SN 2009dc (Howell et al. 2006; Scalzo et al. 2010; Taubenberger et al. 2011; Silverman et al. 2011).

The three SNe Iax studied in detail in this work cluster below the SN 1991bg-like objects with $\sim$0.5 $M_\odot$ of ejecta and 0.15 $M_\odot$ of radioactive nickel. However, the SNe Iax class shows significant diversity in both axes: SN 2009ku is very close to having burned a large fraction of its ejecta into ^{56}Ni, while SN 2008ge shows lower amounts of radioactive nickel than normal SNe Ia, but a similar ejecta mass. Two of the most extreme members of the SNe Iax subclass are SN 2008ha and SN 2007qd (McClelland et al. 2010); both events produced low ejecta mass and ^{56}Ni mass, similar to other low-luminosity transients like the "calcium-rich" SN 2005E (Perets et al. 2010) or the "SN .Ia" candidate SN 2010X (Bildsten et al. 2007; Kasliwal et al. 2010). Taken together, the luminosities, rise times, and ejecta velocities of SNe Iax certainly do not contradict the hypothesis that SNe Iax are thermonuclear explosions of white dwarfs in which radioactive nickel provides the UVOIR light, though the observations do pose a significant challenge to models. We note that Sahu et al. (2008) were able to fit the bolometric light curve and some of the spectral features of SN 2005hk with an explosion model that assumed an ejecta mass of 1.4 $M_\odot$ which implies that more complex modeling may be necessary.

2.5 Summary

We present ground-based and *HST* photometry and spectroscopy of SNe 2005hk and 2008A, two typical SNe Iax. These objects remain at high density for ∼2 years after explosion and are not observed to enter the typical nebular phase up to 400 days after B-band maximum brightness. We find no evidence for unburned material at low velocities, either directly through spectroscopy or indirectly with our *HST* photometry. Based on emission-line diagnostics, we find that the density of the emitting region remains roughly constant over the duration of the observations, though the widths of even the forbidden lines decrease. We do not see the signature of the IR catastrophe in optical colors. The bolometric luminosity of SN 2005hk and SN 2008A fades more slowly than that of normal SNe Ia at 100–200 days after maximum brightness, but then declines faster than in normal SNe Ia at phases of 400–600 days. Failed deflagration models that leave a bound remnant (e.g., Jordan et al. 2012; Kromer et al. 2013) show promise for explaining these explosions, but no single proposed model can explain all of our observations.

We dedicate this paper to the lasting memory of our dear friend and cherished colleague, Weidong Li.

We thank Mark Phillips and Roger Romani for help in acquiring the *HST* observations of SN 2005hk. We acknowledge usage of the NASA Extragalactic Database (`http://ned.ipac.caltech.edu`) and the HyperLeda database (`http://leda.univ-lyon1.fr`).

This research at Rutgers University was supported through NASA/*HST* grants GO-11133.01 and GO-11590.01, along with U.S. Department of Energy (DOE) grant DE-FG02-08ER41562, and National Science Foundation (NSF) CAREER award AST-0847157 to S.W.J., and a GAANN Fellowship to C.M. J.M.S. is supported by an NSF Astronomy and Astrophysics Postdoctoral Fellowship under award AST-1302771. The research of J.C.W. is supported in part by NSF Grant AST-1109801. G.L. is supported by the Swedish Research Council through grant No. 623-2011-7117. A.V.F. and his group at UC Berkeley are funded

by Gary and Cynthia Bengier, the Richard and Rhoda Goldman Fund, NSF grant AST-1211916, the TABASGO Foundation, and NASA/*HST* grants GO-10877 and AR-12623.

Support for HST programs GO-10877, GO-11133, GO-11590, and AR-12623 was provided by NASA through a grant from the Space Telescope Science Institute, which is operated by the Association of Universities for Research in Astronomy, Incorporated, under NASA contract NAS5-26555.

Some of the data presented herein were obtained at the W. M. Keck Observatory, which is operated as a scientific partnership among the University of California, the California Institute of Technology, and NASA, made possible by the generous financial support of the W. M. Keck Foundation. The authors recognize and acknowledge the very significant cultural role and reverence that the summit of Mauna Kea has always had within the indigenous Hawaiian community, and we are most privileged to have the opportunity to explore the Universe from this mountain.

Funding for the SDSS and SDSS-II has been provided by the Alfred P. Sloan Foundation, the Participating Institutions, the NSF, the U.S. Department of Energy, NASA, the Japanese Monbukagakusho, the Max Planck Society, and the Higher Education Funding Council for England. The SDSS Web Site is http://www.sdss.org/. The SDSS is managed by the Astrophysical Research Consortium for the Participating Institutions. The Participating Institutions are the American Museum of Natural History, Astrophysical Institute Potsdam, University of Basel, University of Cambridge, Case Western Reserve University, University of Chicago, Drexel University, Fermilab, the Institute for Advanced Study, the Japan Participation Group, Johns Hopkins University, the Joint Institute for Nuclear Astrophysics, the Kavli Institute for Particle Astrophysics and Cosmology, the Korean Scientist Group, the Chinese Academy of Sciences (LAMOST), Los Alamos National Laboratory, the Max-Planck-Institute for Astronomy (MPIA), the Max-Planck-Institute for Astrophysics (MPA), New Mexico State University, Ohio State University, University of Pittsburgh, University of Portsmouth, Princeton University, the United States Naval Observatory, and

the University of Washington.

Chapter 3

A Luminous, Blue Progenitor System for a Type-Iax Supernova

Type-Iax supernovae (SN Iax) are stellar explosions that are spectroscopically similar to some type-Ia supernovae (SN Ia) at maximum light, except with lower luminosities and lower ejecta velocities (Foley et al. 2013; Li et al. 2003). At late times, their spectroscopic properties diverge strikingly from other SN (Jha et al. 2006a; Phillips et al. 2007; Sahu et al. 2008; McCully et al. 2013), but their composition (dominated by iron-group and intermediate-mass elements; Foley et al. 2013; Stritzinger et al. 2014) suggests a physical connection to normal SN Ia. These are not rare supernovae; SN Iax occur at a rate between 5 and 30% of the normal SN Ia rate (Foley et al. 2013). The leading models for SN Iax are thermonuclear explosions of accreting carbon-oxygen white dwarfs (C/O WD) that do not completely unbind the star (Jordan et al. 2012; Kromer et al. 2013; Fink et al. 2014), contrasting with the complete disruption expected in SN Ia. Testing these models would have a major impact not only in our understanding of stellar evolution and thermonuclear runaway in degenerate stars, but could also improve the utility of the premier cosmological distance indicators. Here we report observations of the luminous, blue progenitor system of the type-Iax SN 2012Z in deep pre-explosion *Hubble Space Telescope* (*HST*) imaging. Based on its luminosity, colors, and environment, as well as a similarity to the pre-outburst Galactic helium nova system V445 Puppis (Kato et al. 2008; Woudt et al. 2009; Goranskij et al. 2010), we argue that SN 2012Z was probably the explosion of a WD accreting from a helium-star companion. Future *HST* observations, after SN 2012Z has faded, could test this hypothesis, or else show (if the progenitor disappears) that this supernova was the

explosive death of a massive star.

Located in NGC 1309, SN 2012Z was discovered (Cenko et al. 2012) in the Lick Observatory Supernova Search on UT 2012-Jan-29.15, with an optical spectrum similar to the type-Iax (previously called SN 2002cx-like) SN 2005hk (see Figure 3.3; Jha et al. 2006a; Phillips et al. 2007; Sahu et al. 2008). Members of this class (Foley et al. 2013) have optical spectra that resemble those of luminous, slowly-declining SN Ia near maximum light, except for lower ejecta velocities, with features from iron-group and intermediate-mass elements that are most often associated with thermonuclear fusion of a degenerate C/O white dwarf. SN Iax are also fainter, only reaching $\sim$1–30% of the peak luminosity of a normal SN Ia. These supernovae differ from all others at late times, showing unexpected high-density permitted lines of iron-group elements (Jha et al. 2006a; Phillips et al. 2007; Sahu et al. 2008; McCully et al. 2013) at very low velocities of a few hundred km s^{-1}. Taken together, the observations and theoretical models of these supernovae suggest that they are thermonuclear explosions that only a partially disrupted the white dwarf, "less successful" cousins of normal SN Ia (Jordan et al. 2012; Kromer et al. 2013; McCully et al. 2013; Stritzinger et al. 2014; Fink et al. 2014).

The similarities between SN Iax and normal SN Ia make an understanding of SN Iax progenitors increasingly important. Like core-collapse SN (but also slowly-declining, luminous SN Ia), SN Iax are found preferentially in young, star-forming galaxies (Foley et al. 2009; Lyman et al. 2013). A single SN Iax, SN 2008ge, was in a relatively old (S0) galaxy with no indication of current star formation to deep limits (Foley et al. 2010b). Non-detection of the progenitor of SN 2008ge in *HST* pre-explosion imaging limits its initial mass $\lesssim$12 M$_\odot$, and combined with the lack of hydrogen or helium in the SN 2008ge spectrum, favors a white dwarf progenitor (Foley et al. 2010b).

SN 2012Z provides a unique opportunity to search for a SN Iax progenitor. Its face-on spiral host galaxy was also the site of the nearby, normal type-Ia SN 2002fk, and as such was targeted in 2005-2006 and 2010 by *HST* to observe Cepheid variable stars in order to

anchor the SN Ia distance scale (*HST* programs GO-10497, GO-10802, and GO-11570, PI: A. Riess; GO/DD-10711, PI: K. Noll). These deep, pre-explosion observations are ideal to search for the progenitor of SN 2012Z. To pinpoint the location of SN 2012Z with high precision, we used *HST* images of NGC 1309 (fortuitously including SN 2012Z) taken on UT 2013-Jan-04 (program GO-12880; PI: A. Riess), as well as targeted *HST* images of SN 2012Z taken on UT 2013-Jun-30 (GO-12913; PI: S. Jha). Colour-composite images of the 2005-2006 ACS data (before the explosion of SN 2012Z) and the WFC3/UVIS 2013 images (with SN 2012Z clearly detected) are shown in Figure 3.1. Our photometry of stellar sources in the 2005-2006 ACS and 2010 WFC3/IR data near the position of SN 2012Z is reported in Table 3.1.

The WFC3/UVIS images of SN 2012Z from January and June 2013 provide a precise position for the supernova of R.A. = $3^{\rm h}22^{\rm m}05\overset{\rm s}{.}39641$, Decl. = $-15°23'14\overset{''}{.}9390$ (J2000) with a registration uncertainty of $0\overset{''}{.}0090$ (plus an absolute astrometric uncertainty of $0\overset{''}{.}08$, irrelevant to the relative astrometry). As shown in Figure 3.1 we detect a stellar source (called S1) in the pre-explosion images coincident with the position of the SN with a formal separation, including centroid uncertainties, of $0\overset{''}{.}0082 \pm 0\overset{''}{.}0103$ (equal to 1.3 ± 1.6 pc at 33 Mpc, the distance to NGC 1309; Riess et al. 2009, 2011).

The positions of SN 2012Z and S1 are consistent to within 0.8σ, indicating an excellent match and strong evidence for S1 being the progenitor system of SN 2012Z. Given the observed density of sources detected with S/N > 3 in a 200×200 pixel box centered on SN 2012Z (443 sources), we estimate only a 0.23% (2.1%) chance that a random position near SN 2012Z would be within 1σ (3σ) of any star, making a chance alignment unlikely. Moreover, only 194 of these stars are brighter than S1, so *a posteriori* there was only a 0.16% (1.5%) chance of a 1σ (3σ) alignment with such a bright object. Examining the multiple epochs of ACS F555W imaging of S1 individually, we find some evidence for variability (see Table 3.2), driven primarily by a near doubling in brightness in one of the 14 epochs. This strengthens its identification as the progenitor system of SN 2012Z and disfavors the

possibility that S1 is a compact, unresolved star cluster.

Having established a high likelihood that S1 is connected with SN 2012Z, we investigate its physical properties using the colour-magnitude diagram (CMD) shown in Figure 3.2. Luminous and blue, the B-type S1 is in a well-populated part of the Hertzsprung-Russell diagram, but nonetheless a relatively odd place for a star about to explode. For S1, we adopt a host reddening correction based on high-resolution spectroscopy of SN 2012Z, which yields a host E(B-V) = 0.07 mag from narrow interstellar absorption lines (Stritzinger et al., manuscript in preparation). This low extinction is consistent with the photometry and spectroscopy of SN 2012Z, as well as its location in the outskirts of a face-on spiral host.

If the light of S1 is dominated by a single star, our results show S1 is moderately consistent with a $\sim$18.5 $M_\odot$ main-sequence star, an $\sim$11 $M_\odot$ blue supergiant early in its evolution off the main sequence, or perhaps a $\sim$7.5 $M_\odot$ (initial mass) blue supergiant later in its evolution (with core helium-burning in a blue loop, where models are quite sensitive to metallicity and rotation; Georgy et al. 2013). None of these stars are expected to explode in standard stellar evolution theory, particularly without any signature of hydrogen in the supernova. The blue supergiant progenitor of, e.g., SN 1987A, was significantly more luminous and likely more massive than S1 (Arnett et al. 1989). Indeed, S1 is inconsistent with all confirmed progenitors of core-collapse SN (exclusively SN II), which are mostly red supergiants (Smartt 2009). However, we caution that our theoretical expectations for massive stars could be modified if S1 is in a close binary system where mass transfer has occurred.

The SN 2012Z progenitor S1 is in a similar region in the CMD to some Wolf-Rayet stars (Shara et al. 2013), highly evolved, massive stars, that are expected to undergo core collapse and may produce a supernova. If S1 were a single Wolf-Rayet star, its photometry is most consistent with the WN subtype and an initial mass $\sim$30–40 $M_\odot$, thought perhaps to explode with a helium-dominated outer layer as a SN Ib (Groh et al. 2013). Such a scenario may have been realised with the suspected (but unconfirmed) WR progenitor of

the type-Ib SN iPTF13bvn (Cao et al. 2013). However, Wolf-Rayet stars are unlikely to be the progenitors of SN Iax, given the structure and composition of the SN ejecta, as revealed through spectroscopy (Jha et al. 2006a; Foley et al. 2013; McCully et al. 2013; Stritzinger et al. 2014), as well as the direct progenitor limits from SN 2008ge (Foley et al. 2010b).

The leading models of SN Iax (Jordan et al. 2012; Kromer et al. 2013; Fink et al. 2014) are based on C/O WD explosions, so we argue that S1 is likely to be the companion star to an accreting WD (or emission from the accretion itself). Although there are a variety of potential progenitor systems (including main-sequence and red giant donors, which are inconsistent with S1 if they dominate the system's luminosity), in standard scenarios no companion star can have an initial mass greater than $\sim$7 $M_\odot$; otherwise, there would not be enough time to form the primary C/O WD that explodes. From stellar evolution tracks (Bertelli et al. 2009), the least massive "normal" star consistent with S1 starts at $\sim$7.5 $M_\odot$, perhaps only barely able to accommodate the requirement for a C/O WD primary star. If S1 were a $\gtrsim$8 $M_\odot$ companion to a C/O WD at the time of our observations, recent binary mass transfer must have played a role in its evolution.

An alternative model for a luminous, blue companion star is a relatively massive ($\sim$2 $M_\odot$ when observed) helium star (Iben & Tutukov 1991; Kato et al. 2008; Liu et al. 2010), formed after binary mass transfer and a common envelope phase (e.g., a close binary with initial masses $\sim$7 and 4 $M_\odot$). Although the model parameter space has not been fully explored, the predicted region for helium star donors in a binary system with a 1.2 $M_\odot$ initial-mass accreting C/O WD (Liu et al. 2010) in the CMD is shown in Figure 3.2, and S1 is consistent with being in this region.

We also note that the B and V luminosities of S1 are not far from the predicted thermal emission of a Eddington-luminosity Chandrasekhar mass WD (a super-soft source; SSS), in which case the observed emission may be coming from an accretion disk and the accreting WD. However, its V-I and V-H colours are too red for a SSS model. A composite scenario, with accretion luminosity dominating the blue flux, and another source providing the redder

light (perhaps a fainter, red donor star) may be plausible.

The stars detected in the vicinity of S1 provide clues to the nature of recent star formation in the region. They include red supergiants (like S2 and S3 from Table 3.1) as well as objects bluer and more luminous than S1 (like S5). We show CMDs including these stars in Figure 3.4, and model isochrones (Bertelli et al. 2009) imply that these stars span an age range of ∼10–42 Myr. These tracks favour an initial mass for S1 of ∼7–8 $M_{\odot}$ (neglecting mass transfer) if it is roughly coeval with its neighbours. In other words, if S1 were a 30–40 $M_{\odot}$ initial-mass Wolf-Rayet star with a predicted lifetime of only 5–8 Myr (Groh et al. 2013), it would be the youngest star in the region.

SN 2012Z and the star S1 have an interesting analog in our own Milky Way Galaxy: the helium nova V445 Puppis (Kato et al. 2008; Woudt et al. 2009; Goranskij et al. 2010), thought to be a near-Chandrasekhar mass helium-accreting white dwarf. Though S1 is somewhat brighter than the pre-explosion observations of V445 Pup, their consistent colours and the physical connection between V445 Pup and likely SN Iax progenitors (Jordan et al. 2012; Kromer et al. 2013; Fink et al. 2014) is highly suggestive. Indeed, two SN Iax (though not SN 2012Z itself) have shown evidence for helium in the system (Foley et al. 2009, 2013). If this model is correct, the accretion rate for the helium mass transfer could be low in V445 Pup, leading to helium novae (as observed), whereas for SN 2012Z-S1, a higher mass transfer rate could mean stable helium burning on the C/O WD, and a buildup of mass before the supernova explosion. The accretion likely begins as the helium star begins to evolve and grow in radius; indeed, the observed photometry of S1 is consistent with the evolutionary track of a ∼2 $M_{\odot}$ helium star on its way to becoming a red giant (Kato et al. 2008) (where the mass is interpreted to be when the star became a helium star, i.e., after losing its envelope). Intriguingly, the variability amplitude of S1 is also similar to what was shown by the progenitor of V445 Pup (Goranskij et al. 2010).

Our observations of the progenitor of SN 2012Z, along with the supernova properties (and those of other SN Iax) are best explained by a system containing an exploding C/O

white dwarf with a helium-star companion. Nonetheless, the evidence that SN Iax come from thermonuclear WD explosions, though strong, is indirect. We should remain open to the possibility that S1 was not the binary companion to an exploding WD, but the object that itself exploded. Fortunately, we will soon be in a position to test these two scenarios: future imaging with *HST*, after SN 2012Z has faded, will allow us to determine whether S1 has disappeared. If our favoured model of S1 as the companion star is correct, it should be detected (though perhaps modified by the impact of its exploding neighbour). On the other hand, if S1 has disappeared, it will be a strong challenge to models of SN Iax, and perhaps significantly blur the line between thermonuclear white-dwarf supernovae and massive-star core-collapse supernovae, with important impacts to our understanding of stellar evolution, chemical enrichment, and cosmology. Finally, our study highlights that because local hosts of SN have been shown to be among the most prolific producers of new supernovae, deep imaging of such hosts (in some cases, as here, to observe Cepheids for SN luminosity calibration) provides a valuable legacy whose rewards will outlive *HST* itself.

Supernova 2012Z was discovered just weeks after the passing of our dear friend and colleague, Weidong Li, whose work on the Lick Observatory Supernova Search, SN 2002cx-like supernovae, and Hubble Space Telescope observations of SN progenitors, continues to inspire us. That those three foci of Weidong's research converge here in this paper makes our hearts glad, and we dedicate this paper to his memory.

We thank the SH_0ES team for assistance with data from *HST* program GO-12880, E. Bertin for the development of the STIFF software to produce color images, and A. Dolphin for software and guidance in photometry. This research at Rutgers University was supported through NASA/*HST* grant GO-12913.01, and National Science Foundation (NSF) CAREER award AST-0847157 to S.W.J. NASA/*HST* grant GO-12999.01 to R.J.F. supported this work at the University of Illinois. At UC Santa Barbara, this work was supported by NSF grants PHY 11-25915 and AST 11-09174 to L.B.

Support for *HST* programs GO-12913 and GO-12999 was provided by NASA through

a grant from the Space Telescope Science Institute, which is operated by the Association of Universities for Research in Astronomy, Incorporated, under NASA contract NAS5-26555.

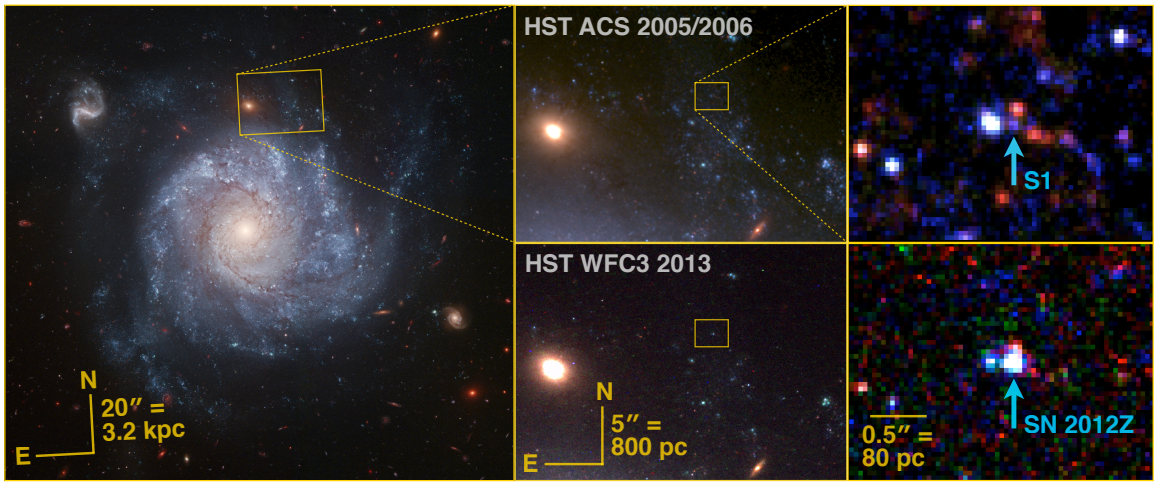

Figure 3.1 *Hubble Space Telescope* colour image of SN 2012Z and its progenitor in the outskirts of the spiral galaxy NGC 1309. The left panel shows the Hubble Heritage image of this field (`http://heritage.stsci.edu/2006/07`) and the top and bottom rows show data from before and after the explosion of the supernova, respectively, with the pre-explosion data being significantly deeper. The middle panels zoom in on the galactic environment of the SN, while the right panels show the supernova and its progenitor (marked by the arrow). The image scales are as shown, with projected physical separations based on a distance (Riess et al. 2009, 2011) to NGC 1309 of 33 Mpc. The left and top panels use data taken in 2005 and 2006 with the Advanced Camera for Surveys (ACS) on *HST*. These include 2 visits totaling 9600s of exposure time in the F435W filter (similar to Johnson B, and shown in the blue channel of the image), 14 visits for a total exposure of 61760 sec F555W (close to Johnson V; green channel), and 5 visits for 24000s in F814W (analogous to Cousins I; red channel). The top right panels show our re-reduction of these data, in which we combined the multiple exposures (including sub-sampling and cosmic ray rejection) using the AstroDrizzle software from the DrizzlePac package (Gonzaga et al. 2012). The bottom right panels show combined *HST* Wide Field Camera 3 (WFC3) F555W (blue; 1836 sec) + F625W (green; 562 sec) +F814W (red; 1836 sec) images from January and June 2013, with SN 2012Z visible. We used the DrizzlePac TweakReg routine to register all of the individual flatfielded ("`flt`") frames to the WFC3/UVIS F555W image taken on UT 2013-Jan-04.The typical root-mean-square (rms) residual of individual stars from the relative astrometric solution was $0\farcs009$, corresponding to 0.18 pixels in ACS and 0.23 pixels in WFC3/UVIS. We drizzle the ACS images to the native scale of UVIS, $0\farcs04$ per pixel (20% smaller than the native $0\farcs05$ ACS pixels) and subsample the ACS point-spread function (psf) correspondingly with a pixel fraction parameter of 0.8.

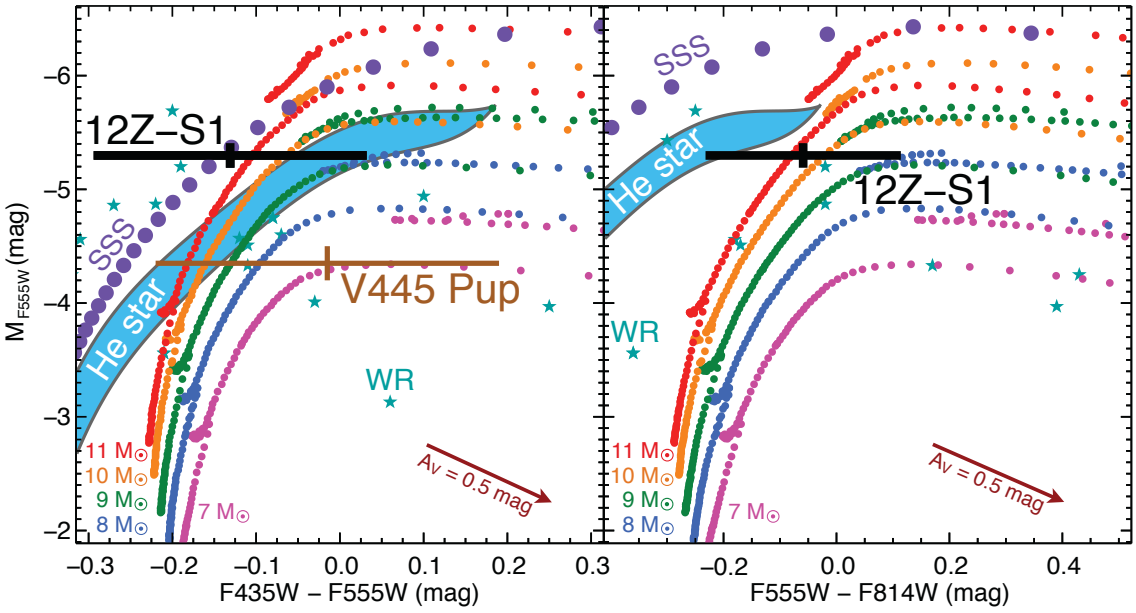

Figure 3.2 F435W−F555W vs. M_{F555W} and F555W−F814W vs. M_{F555W} (roughly B−V vs. M_V and V−I vs. M_V) colour magnitude diagrams. The black and brown crosses represent the progenitor systems for SN 2012Z and V445 Puppis (Woudt et al. 2009), respectively. The SN 2012Z progenitor (S1) has been corrected for Milky Way reddening ($E(B\text{-}V)_{MW}$ = 0.035 mag, corresponding to A_{F435W} = 0.14 mag, A_{F555W} = 0.11 mag, A_{F814W} = 0.06 mag) and host reddening (as estimated from SN 2012Z itself; Stritzinger et al., in preparation; $E(B\text{-}V)_{host}$ = 0.07 mag; A_{F435W} = 0.28 mag, A_{F555W} = 0.22 mag, A_{F814W} = 0.12 mag). For V445 Puppis, we correct for Galactic and circumstellar reddening (Woudt et al. 2009). Stellar evolution tracks (Bertelli et al. 2009) for stars with initial masses of 7, 8, 9, 10, and 11 $M_\odot$ are shown as the coloured dotted curves (with mass increasing from bottom to top), adopting a metallicity of 0.87 solar, based on the H II region metallicity gradient (Riess et al. 2009) for NGC 1309 interpolated to the SN radial location. Eddington-luminosity accreting Chandrasekhar-mass white dwarfs are shown as the large purple dots, with each subsequent dot representing a change in temperature of 1000 K. These "super-soft" sources are fainter in F555W for higher temperatures (and bluer F435W−F555W colours) as the fixed (Eddington-limited) bolometric luminosity emerges in the ultraviolet for hotter systems. Candidate Wolf-Rayet stars (Shara et al. 2013) are shown as blue-gray stars. Finally, the blue region represents the range of helium-star donors for C/O WD SN progenitor models starting with a 1.2 $M_\odot$ white dwarf (Liu et al. 2010). We converted the model temperatures and luminosities to our observed bands assuming a blackbody spectrum. The expected temperature and luminosity for this class of models is expected to vary with white dwarf mass, and therefore, we regard this region as approximate; its shape, size, and location is subject to change.

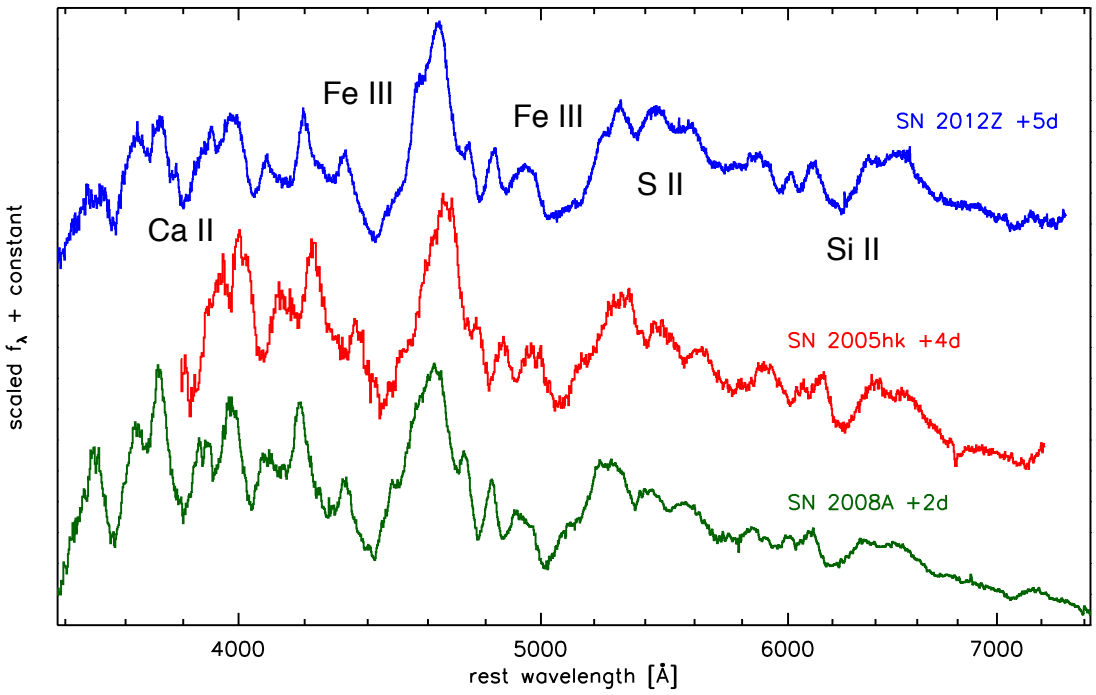

Figure 3.3 Spectra of SN Iax near maximum light, showing the similarity of SN 2012Z (Foley et al. 2013) to SN 2005hk (Phillips et al. 2007) and SN 2008A (McCully et al. 2013), all objects in this class. The SN 2012Z spectrum was taken on UT 2012-02-16 with the Whipple Observatory 1.5m telescope (+FAST spectrograph) with a total exposure time of 1800 sec. Each spectrum is labelled by its rest-frame phase past B maximum light. Prominent features due to intermediate-mass and iron group elements are indicated; these features are also observed in luminous, slowly-declining SN Ia spectra at maximum light, though with higher expansion velocities.

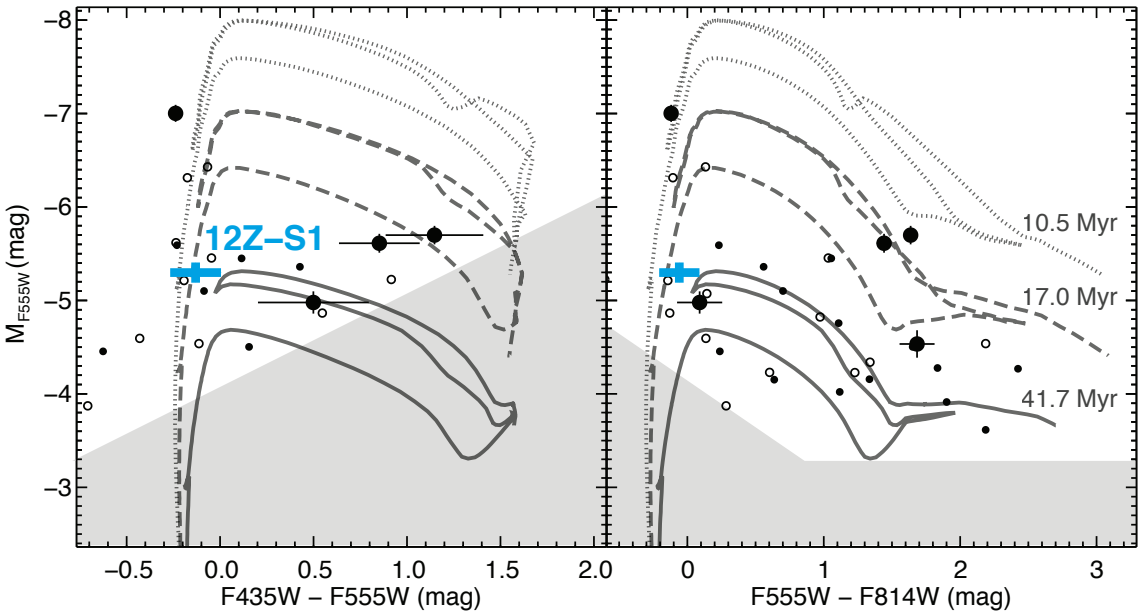

Figure 3.4 The SN 2012Z progenitor system S1 (blue) is shown along with nearby stars, with three isochrones (Bertelli et al. 2009) with ages of 10.5 (dotted), 17.0 (dashed), and 41.7 Myr (solid), adopting a metallicity of 0.87 solar, based on the H II region metallicity gradient (Riess et al. 2009) for NGC 1309 interpolated to the SN location. The large, filled circles correspond to stars within 10 WFC3/UVIS pixels (0.″4) of the SN location, small filled circles are within 20 pixels (0.″8), and the small open circles are within 30 pixels (1.″2). The stars plotted have a signal-to-noise ratio S/N > 3 in the filters shown, and were required to be no closer than 3 pixels to a brighter source to avoid photometric uncertainties from crowding. Objects in the gray shaded regions would not be detected given the depth of the combined images.

Table 3.1. Pre-explosion photometry of SN 2012Z progenitor S1 and nearby stars. The data include *HST* images from ACS in 2005 and 2006 (F435W, F555W, and F814W) described in Figure 3.1, as well as WFC3/IR F160W data (6991 sec of total exposure time) from 2010. The stars are sorted by their proximity to the SN position, and their astrometry is referenced to SDSS images of the field, with an absolute astrometric uncertainty of 0.″080 (but this is irrelevant for the much more precise relative astrometry of SN 2012Z and S1). We photometered the *HST* images using the psf-fitting software DolPhot, an extension of HSTPhot (Dolphin 2000). We combined individual flt frames taken during the same *HST* visit at the same position, and then used DolPhot to measure photometry using recommended parameters for ACS and WFC3. The photometric uncertainty is given in parentheses and non-detections are listed with 3σ upper-limits. No corrections for Galactic or host extinction are made here.

Star	R.A. (J2000)	Decl. (J2000)	F435W (mag)	F555W (mag)	F814W (mag)	F160W (mag)
S1	$3^h22^m05^s.39591$	$-15°23'14''.9350$	27.589 (0.122)	27.622 (0.060)	27.532 (0.135)	26.443 (0.321)
S2	$3^h22^m05^s.39483$	$-15°23'14''.8102$	28.466 (0.258)	27.221 (0.041)	25.435 (0.022)	23.699 (0.027)
S3	$3^h22^m05^s.40280$	$-15°23'14''.9402$	>29.221	28.551 (0.116)	27.463 (0.093)	26.032 (0.238)
S4	$3^h22^m05^s.38460$	$-15°23'15''.0314$	28.258 (0.211)	27.308 (0.046)	25.717 (0.028)	23.887 (0.033)
S5	$3^h22^m05^s.41013$	$-15°23'14''.9362$	25.778 (0.029)	25.918 (0.014)	25.888 (0.030)	25.435 (0.136)
S6	$3^h22^m05^s.37564$	$-15°23'15''.0702$	>28.807	28.386 (0.116)	26.553 (0.055)	24.986 (0.085)
S7	$3^h22^m05^s.41970$	$-15°23'14''.8454$	28.539 (0.286)	27.942 (0.078)	27.703 (0.146)	26.436 (0.322)
S8	$3^h22^m05^s.41735$	$-15°23'15''.0870$	>28.942	>29.672	28.480 (0.303)	25.529 (0.136)
S9	$3^h22^m05^s.37049$	$-15°23'14''.6690$	>28.847	28.763 (0.164)	27.279 (0.101)	25.032 (0.092)
S10	$3^h22^m05^s.37904$	$-15°23'14''.5218$	27.196 (0.083)	27.329 (0.045)	26.949 (0.076)	>26.614
S11	$3^h22^m05^s.36477$	$-15°23'15''.0634$	27.683 (0.127)	27.470 (0.050)	26.266 (0.042)	24.753 (0.069)
S12	$3^h22^m05^s.39605$	$-15°23'15''.4062$	>28.912	29.305 (0.273)	26.969 (0.077)	25.214 (0.102)
S13	$3^h22^m05^s.37556$	$-15°23'14''.4202$	>28.897	28.302 (0.109)	27.095 (0.085)	25.381 (0.131)
S14	$3^h22^m05^s.36527$	$-15°23'14''.5054$	28.085 (0.181)	27.560 (0.055)	26.852 (0.069)	25.740 (0.171)
S15	$3^h22^m05^s.39229$	$-15°23'15''.5730$	>28.820	28.768 (0.163)	27.982 (0.195)	>26.507
S16	$3^h22^m05^s.43040$	$-15°23'14''.4706$	27.937 (0.164)	28.465 (0.122)	28.078 (0.208)	>26.512
S17	$3^h22^m05^s.38194$	$-15°23'14''.2494$	>28.926	29.007 (0.207)	26.957 (0.077)	26.230 (0.260)
S18	$3^h22^m05^s.40432$	$-15°23'15''.5778$	>29.360	28.651 (0.113)	26.078 (0.026)	24.180 (0.042)
S19	$3^h22^m05^s.42376$	$-15°23'14''.3726$	>28.765	28.163 (0.092)	26.905 (0.072)	25.126 (0.094)
S20	$3^h22^m05^s.39387$	$-15°23'14''.2018$	28.670 (0.302)	28.417 (0.118)	26.616 (0.056)	25.072 (0.094)
S21	$3^h22^m05^s.35086$	$-15°23'15''.2402$	27.831 (0.143)	27.819 (0.069)	26.969 (0.077)	25.581 (0.145)
S22	$3^h22^m05^s.38446$	$-15°23'14''.1646$	>28.920	29.190 (0.249)	27.438 (0.124)	25.662 (0.159)
S23	$3^h22^m05^s.41428$	$-15°23'14''.1850$	>28.844	28.899 (0.184)	27.633 (0.135)	26.204 (0.242)
S24	$3^h22^m05^s.37179$	$-15°23'15''.6186$	>28.814	28.643 (0.147)	26.660 (0.059)	24.854 (0.075)
S25	$3^h22^m05^s.35603$	$-15°23'14''.2694$	28.438 (0.244)	29.048 (0.222)	28.615 (0.342)	>26.592
S26	$3^h22^m05^s.39179$	$-15°23'14''.0298$	>28.809	29.135 (0.235)	27.219 (0.100)	25.685 (0.161)
S27	$3^h22^m05^s.34566$	$-15°23'15''.4618$	>28.813	>29.632	27.291 (0.102)	25.572 (0.138)
S28	$3^h22^m05^s.38396$	$-15°23'13''.9958$	28.367 (0.230)	28.382 (0.119)	26.046 (0.035)	24.549 (0.057)
S29	$3^h22^m05^s.33025$	$-15°23'15''.0438$	27.518 (0.109)	27.466 (0.055)	26.284 (0.048)	25.134 (0.094)
S30	$3^h22^m05^s.35072$	$-15°23'15''.6022$	>28.835	28.097 (0.089)	26.975 (0.078)	25.936 (0.202)
S31	$3^h22^m05^s.43718$	$-15°23'15''.6194$	28.340 (0.241)	29.474 (0.331)	>28.665	>26.633

Table 3.2. Photometric variability of the SN 2012Z progenitor star S1. NGC 1309 was imaged over 14 epochs in F555W with ACS before SN 2012Z exploded. Formally, these data rule out the null hypothesis of no variability at 99.95% (3.5σ), with $\chi^2 = 36.658$ in 13 degrees of freedom. However, most of the signal is driven by one data point (MJD 53600.0; a 4.2σ outlier); excluding this data point (though we find no independent reason to do so) reduces the significance of the variability to just 91.1% (1.7σ). Moreover, an empirical test for variability in the photometry of nearby stars of a similar brightness to S1 suggests the photometric uncertainty may be underestimated; using the scatter measured from these data themselves (excluding the outlier point) to determine the typical uncertainty makes the outlier a 3.8σ fluctuation, and yields a significance for the total variability of 99.2% (2.6σ). Overall, we find evidence for variability in S1, but cannot claim a robust detection.

Date (UT)	MJD	Exposure (s)	Counts (e^-)	F555W (mag)
2005-08-06	53588.7	2400	171 (71)	28.36 (0.45)
2005-08-17	53600.0	2400	656 (75)	26.94 (0.13)
2005-08-24	53606.8	2400	282 (67)	27.79 (0.26)
2005-08-27	53610.0	2400	392 (64)	27.49 (0.18)
2005-09-02	53615.6	2400	389 (69)	27.48 (0.19)
2005-09-03	53617.0	2400	308 (66)	27.77 (0.23)
2005-09-05	53618.6	2400	392 (71)	27.49 (0.20)
2005-09-07	53621.0	2400	329 (66)	27.66 (0.22)
2005-09-11	53624.0	2400	429 (68)	27.37 (0.17)
2005-09-16	53629.8	2400	242 (67)	27.98 (0.30)
2005-09-20	53633.4	2400	327 (64)	27.70 (0.21)
2005-09-27	53640.5	2400	193 (66)	28.25 (0.37)
2006-10-24	54032.6	2080	388 (76)	27.26 (0.21)
2006-10-07	54015.3	2080	264 (75)	27.62 (0.31)

Chapter 4

A New Hybrid Framework to Efficiently Model Lines of Sight to Gravitational Lenses

Abstract

In strong gravitational lens systems, the light bending is usually dominated by one main galaxy, but may be affected by other mass along the line of sight (LOS). Shear and convergence can be used to approximate the contributions from objects projected far from the lens, but higher-order effects need to be included for objects that are closer. We develop a framework for multi-plane lensing that can handle an arbitrary combination of planes treated with shear and convergence and planes treated exactly (i.e., including higher-order terms). This framework addresses all of the traditional lensing observables including image positions, fluxes, and time delays to facilitate lens modeling that includes LOS effects. It balances accuracy (accounting for higher-order terms when necessary) with efficiency (compressing all other LOS effects into a set of matrices that can be calculated up front and cached for lens modeling). We identify a generalized multi-plane mass sheet degeneracy, in which the effective shear and convergence are sums over the lensing planes with specific, redshift-dependent weighting factors.

4.1 Introduction

In galaxy-scale strong gravitational lens systems there is often a single galaxy that dominates the lens potential. A few systems are compound lenses having two or three lens galaxies within the Einstein radius (e.g., Koopmans & Fassnacht 1999; Rusin et al. 2001; Winn et al.

2003), and many more have significant contributions from a group or cluster environment (e.g., Young et al. 1981; Kundic et al. 1997a; Fischer et al. 1998; Tonry 1998; Tonry & Kochanek 1999; Keeton et al. 2000; Kneib et al. 2000; Fassnacht et al. 2006; Momcheva et al. 2006). In both cases, the light bending effectively occurs in a single lens plane. If there are any massive objects along the line of sight (like massive galaxies, galaxy groups, or cosmic structure), however, the additional lens planes may affect the light rays in ways that cannot be ignored.

A dramatic example occurs when two massive galaxies are at different redshifts but lie close enough in projection to both act as strong lenses. This "two-screen lensing" can produce new lensing phenomena that have been studied in detail theoretically (Kochanek & Apostolakis 1988; Erdl & Schneider 1993; Petters & Wicklin 1995; Möller & Blain 2001; Werner et al. 2008; Rhie & Bennett 2009). The effect is rare because it requires close alignment; it has been identified in two of the few hundred known galaxy-scale lens systems (Chae et al. 2001; Gavazzi et al. 2008; Sonnenfeld et al. 2012).

It is more common to have many massive objects projected farther from the main lens (e.g., Tonry & Kochanek 2000), producing an accumulation of "small" perturbations, i.e., weak lenses, that need to be included. To study this scenario, one approach is to write down the full multi-plane lens equation (e.g., Blandford & Narayan 1986; Kovner 1987; Schneider et al. 1992; Petters et al. 2001) and then perform ray-tracing simulations through appropriate three-dimensional mass distributions (e.g., Refsdal 1970; Schneider & Weiss 1988a,b; Jaroszynski 1989, 1991, 1992; Rauch 1991; Lee et al. 1997; Premadi et al. 1998; Wambsganss et al. 1998, 2005; Hilbert et al. 2007, 2009; Collett et al. 2013; Petkova et al. 2013). An alternate approach is to derive analytic expressions for the statistics of lensing perturbations in terms of the statistical distribution of galaxies and large-scale structure (e.g., Seljak 1994; Bar-Kana 1996; Keeton et al. 1997). This approach is similar to the one employed by cosmic shear studies (e.g., Munshi et al. 2008). A third approach is to examine multi-plane lensing from the viewpoint of formal mathematics (Levine & Petters

1993; Kayser & Schramm 1993; Petters 1995a,b; Petters et al. 2001).

Each approach has strengths and limitations, which become especially important if we want to account for specific, observed line-of-sight (LOS) structures in models of real lens systems. Formal mathematical studies yield rigorous results, but are typically limited to general issues such as bounds on the number of images, counting rules for different types of lensed images, and classifications of caustic geometry.

The full multi-plane lens equation properly captures the redshift dependencies and the non-linear couplings between redshift planes, but it can be computationally impractical. There may be hundreds of objects projected close enough to a lens to affect the light rays (e.g., Momcheva et al. 2006; Williams et al. 2008; Wong et al. 2011), making it expensive to evaluate the lens equation even once, let alone the enormous number of times required in careful lens modeling.

As an alternative, one could make the approximation that each LOS galaxy acts as a small perturbation (weak lens), contributing only convergence and shear to the lensing potential. Cosmic shear studies employ this weak lensing approximation and integrate over the matter along the LOS, but those calculations are statistical, limiting their applicability to specific observed beams, and they neglect higher-order effects beyond shear. Convergence is usually omitted from lens models because of the mass sheet degeneracy, which can lead to biases in derived physical and cosmological parameters. When convergence is included, that is typically done in post-processing (e.g., Fadely et al. 2010; Nakajima et al. 2009; Suyu et al. 2010, 2013; Collett et al. 2013). Shear is often included in the fit, but usually under the assumption that it originates in the main lens plane. That widely-used approach neglects higher-order effects beyond shear, which may be significant for objects sufficiently close to the optical axis, and it also neglects non-linear effects that arise from having mass in multiple planes (see Jaroszynski & Kostrzewa-Rutkowska 2012). To account for higher-order effects, some lens models feature a hybrid methodology in which galaxies near the lens are modeled explicitly while galaxies farther away are treated with an additional shear

(e.g., Morgan et al. 2004; Kochanek et al. 2006; Vuissoz et al. 2008; Fadely & Keeton 2012). Even in those cases, the galaxies have typically been placed in the lens plane, neglecting any additional redshift effects.

In this paper we present a framework for multi-plane lensing that consolidates the various approaches above. Our approach can handle an arbitrary collection of "main" planes (strong lenses) that are treated exactly and planes that are approximated with shear and convergence (weak lenses), at any location along the line of sight. After reviewing the setup (§4.2), we analyze the lens equation and magnification tensor (§4.3) and time delays (§4.4) in the multi-plane context. We then examine a multi-plane version of the gauge symmetry known as the mass sheet degeneracy (§4.5). Our multi-plane framework provides a general way to quantify LOS effects for observed lens systems (Wong et al. 2011; McCully et al., in prep.).

4.2 Setup

Our discussion of multi-plane gravitational lensing follows Chapter 9 of the book by Schneider et al. (1992) and Section 6.4 of the book by Petters et al. (2001), which in turn draw on papers by Blandford & Narayan (1986) and Kovner (1987). In particular, our analysis of LOS shear in §4.3.1 is equivalent to the discussion of the generalized quadrupole lens in Section 9.3 of Schneider et al. (1992).

4.2.1 Definitions

Consider N galaxies with redshifts z_i, indexed by increasing redshift so $z_1 \leq z_2 \leq \ldots \leq z_N < z_s$. (It is fine to have more than one galaxy at a given redshift.) The source is in plane $N+1$, which is labeled with the index s. Let D_i and D_{is} be the angular diameter distances from the observer to galaxy i and from galaxy i to the source (respectively). For $i < j$ let D_{ij} be the angular diameter distance from galaxy i to galaxy j.

Let galaxy i have lensing potential $\phi_i(\boldsymbol{x}_i)$ and surface mass density $\Sigma_i(\boldsymbol{x}_i)$. We write

$\boldsymbol{x}_i$ to emphasize that the lensing properties are naturally expressed using coordinates $\boldsymbol{x}_i$ in plane i. The lensing potential and surface mass density are related by the Poisson equation

$$\nabla^2\phi_i(\boldsymbol{x}_i) = 2\frac{\Sigma_i(\boldsymbol{x}_i)}{\Sigma_{\mathrm{cr},i}} \ , \tag{4.1}$$

where the critical surface density for lensing for plane i is

$$\Sigma_{\mathrm{cr},i} = \frac{c^2}{4\pi G}\ \frac{D_s}{D_i D_{is}} \ . \tag{4.2}$$

The deflection angle from galaxy i is then

$$\boldsymbol{\alpha}_i(\boldsymbol{x}_i) = \nabla\phi_i(\boldsymbol{x}_i)\,. \tag{4.3}$$

We emphasize that $\boldsymbol{\alpha}_i$ is the deflection angle due to galaxy i and is a function of image position in plane i. The position of the light ray in plane i will depend on how the light has already been bent by other galaxies, but that modification is explicitly built into the multi-plane lens equation (see below). It is useful to introduce the matrix of second derivatives,

$$\boldsymbol{\Gamma}_i = \frac{\partial\boldsymbol{\alpha}_i}{\partial\boldsymbol{x}_i} = \begin{bmatrix} \kappa_i + \gamma_{ci} & \gamma_{si} \\ \gamma_{si} & \kappa_i - \gamma_{ci} \end{bmatrix}, \tag{4.4}$$

where we define the convergence (κ) and shear (γ) components from galaxy i:

$$\kappa_i = \frac{1}{2}\left(\frac{\partial^2\phi_i}{\partial x_i^2} + \frac{\partial^2\phi_i}{\partial y_i^2}\right), \tag{4.5}$$

$$\gamma_{ci} = \frac{1}{2}\left(\frac{\partial^2\phi_i}{\partial x_i^2} - \frac{\partial^2\phi_i}{\partial y_i^2}\right), \tag{4.6}$$

$$\gamma_{si} = \frac{\partial^2\phi_i}{\partial x_i\partial y_i} \ . \tag{4.7}$$

We refer to $\boldsymbol{\Gamma}_i$ as the shear tensor for simplicity, although it contains convergence as well. Note that the convergence can be obtained from the trace of $\boldsymbol{\Gamma}$, while the shear components

are given by the traceless, symmetric part of $\mathbf{\Gamma}$.

If a galaxy lies far from the center of the main lens galaxy (in projection) we can Taylor expand the lens potential about the center of the main galaxy as

$$\phi(\boldsymbol{x}) = \phi(0) + \alpha^i(0)x^a + \frac{1}{2}\Gamma^{ab}x^a x^b + \frac{1}{6}\mathcal{F}^{abc}x^a x^b x^c + \ldots \tag{4.8}$$

where a, b, c are vector component indices and we have adopted the Einstein notation of summing over repeated indices. $\mathcal{F}$ is the flexion tensor of third-derivatives defined by

$$\mathcal{F}^{abc} \equiv \left.\frac{\partial^3\phi}{\partial x^a \partial x^b \partial x^c}\right|_{x=0} . \tag{4.9}$$

The $\phi(0)$ term is the zeropoint of the potential, which is unobservable. The $\boldsymbol{\alpha}(0)$ term corresponds to a uniform deflection that is degenerate with a translation of the source plane coordinates. Thus, the first significant term is the second-order one. If we can neglect higher-order terms and truncate the expansion at second order, we have

$$\phi_i(\boldsymbol{x}_i) \approx \frac{1}{2}\boldsymbol{x}_i \cdot \mathbf{\Gamma}_i(0)\boldsymbol{x}_i \,, \tag{4.10}$$

$$\boldsymbol{\alpha}_i(\boldsymbol{x}_i) \approx \mathbf{\Gamma}_i(0)\boldsymbol{x}_i \,, \tag{4.11}$$

$$\mathbf{\Gamma}_i(\boldsymbol{x}_i) \approx \mathbf{\Gamma}_i(0) \,. \tag{4.12}$$

This defines the shear approximation, which we employ for all planes in which the perturber is projected sufficiently far away from the center of the main lensing galaxy. (We quantify the accuracy of the shear approximation in a forthcoming paper; McCully et al. in prep.) In the remainder of the paper we drop (0) for simplicity. We refer to planes that employ the shear approximation as "shear planes," and planes that are treated exactly as "main planes."

For illustration, the lensing potential of a point mass is given by

$$\phi = R_E^2 \ln |\boldsymbol{x} - \boldsymbol{r}_p| \tag{4.13}$$

where R_E is the Einstein radius of the perturber, $\boldsymbol{x}$ is the image position in the redshift plane of the perturber, and $\boldsymbol{r}_p$ is the position of the perturber. If we let $|\boldsymbol{x}| = x$, $|\boldsymbol{r}_p| = r_p$, and θ be the angle between the perturber and the image position as measured from the origin, then we can rewrite the potential using the law of cosines as

$$\phi = \frac{1}{2} R_E^2 \ln \left(r_p^2 + x^2 - x r_p \cos\theta \right) . \tag{4.14}$$

If we assume the projected offset of the perturber is large compared to the image positions ($r_p \gg x$), then we can expand the logarithm as

$$\phi \approx R_E^2 \left[\ln(r_p) - \cos(\theta)\frac{x}{r_p} - \frac{1}{2}\cos(2\theta)\frac{x^2}{r_p^2} - \frac{1}{3}\cos(3\theta)\frac{x^3}{r_p^3} + \ldots \right] . \tag{4.15}$$

We see that a point mass has $\boldsymbol{\Gamma} \sim R_E^2/r_p^2$ and $\mathcal{F} \sim R_E^2/r_p^3$.

4.2.2 Multi-plane lensing

The lens equation is constructed by working "backwards" from the observer, through the lens planes one by one, until we reach the source. If $\boldsymbol{x}_j$ is the position in plane j, we have (see eq. 9.7a of Schneider et al. 1992, and eq. 6.29 of Petters et al. 2001)

$$\boldsymbol{x}_j = \boldsymbol{x}_1 - \sum_{i=1}^{j-1} \beta_{ij} \boldsymbol{\alpha}_i(\boldsymbol{x}_i) , \tag{4.16}$$

where

$$\beta_{ij} = \frac{D_{ij} D_s}{D_j D_{is}} . \tag{4.17}$$

Notice that the lens equation for plane j depends on all planes in front of j ($i < j$), so this amounts to a recursion relation that we can use to start with angular coordinates on the observer's sky ($\boldsymbol{x}_1$) and work our way up in redshift until we reach the source plane ($\boldsymbol{x}_s = \boldsymbol{x}_{N+1}$). The recursive sums mean there are non-linear couplings among the lens planes. (Hilbert et al. e.g., 2009; Seitz & Schneider e.g., 1994 write the recursion relation in a different form, but we find eq. (4.16) to be useful.)

The Jacobian matrix for the mapping between the coordinates on the sky and the coordinates in plane j is

$$\mathbf{A}_j \;=\; \frac{\partial \boldsymbol{x}_j}{\partial \boldsymbol{x}_1} \;=\; \mathbf{I} - \sum_{i=1}^{j-1} \beta_{ij} \frac{\partial \boldsymbol{\alpha}_i}{\partial \boldsymbol{x}_i} \frac{\partial \boldsymbol{x}_i}{\partial \boldsymbol{x}_1} \;=\; \mathbf{I} - \sum_{i=1}^{j-1} \beta_{ij} \boldsymbol{\Gamma}_i \mathbf{A}_i \,, \tag{4.18}$$

where $\mathbf{I}$ is the 2×2 identity matrix. The lensing magnification tensor is the inverse of the Jacobian matrix for the source plane: $\mu = \mathbf{A}_s^{-1}$. The non-linear couplings among planes enter here: the full expression for $\mathbf{A}_s$ includes terms involving products of different numbers of shear tensors.

The general form for the multi-plane time delay is (see eq. 6.22 of Petters et al. 2001)

$$T = \sum_{i=1}^{s-1} \tau_{i\,i+1} \left[\frac{1}{2} |\boldsymbol{x}_{i+1} - \boldsymbol{x}_i|^2 - \beta_{i\,i+1} \phi_i(\boldsymbol{x}_i) \right], \tag{4.19}$$

where

$$\tau_{ij} = \frac{1 + z_i}{c} \frac{D_i D_j}{D_{ij}} \tag{4.20}$$

is a distance combination with dimensions of time. We can omit the redshift dependence if we measure the D's as comoving rather than angular diameter distances.

Throughout the derivation we use the following identities from the definitions of β_{ij} and

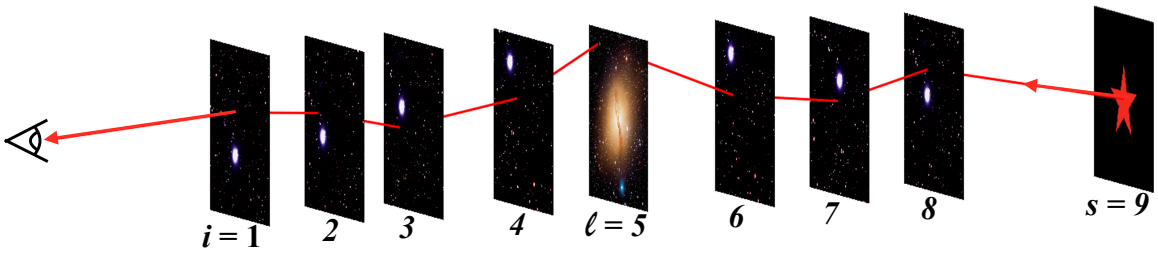

Figure 4.1 Schematic diagram of multi-plane lensing (not to scale). The light bending is dominated by a single main plane ($\ell = 5$) but affected by additional shear planes in the foreground and background of the main plane. Here the source is in plane $s = 9$, but the framework can handle an arbitrary number of planes.

τ_{ij} (see Section 6.4.1 in Petters et al. 2001):

$$\beta_{is} = 1 \qquad (\forall i)\,, \tag{4.21}$$

$$\tau_{is} = \beta_{ij}\tau_{ij} \qquad (\forall ij)\,, \tag{4.22}$$

$$\frac{1}{\tau_{ik}} = \frac{1}{\tau_{ij}} + \frac{1}{\tau_{jk}} \qquad (i < j < k)\,. \tag{4.23}$$

Also, to simplify the notation we define versions of β and τ with a single subscript as

$$\beta_i \equiv \beta_{i\,i+1}\,, \qquad \tau_i \equiv \tau_{i\,i+1}\,. \tag{4.24}$$

4.3 Lens Equation and Magnification Tensor

In this section we work with the multi-plane lens equation and magnification tensor. We start by using the shear approximation for all planes other than the plane containing the main lens galaxy. We then generalize to arbitrary combinations of shear and main planes.

4.3.1 One "main" plane

Suppose there is a single "main" lens plane ($i = \ell$) and all other galaxies can be treated with the shear approximation as illustrated in Figure 4.1. (This case has been studied previously by Kovner 1987 and Schneider et al. 1992.) Using eq. (4.10), we can write the recursion

relations for the position and Jacobian matrix as

$$\boldsymbol{x}_j = \boldsymbol{x}_1 - \sum_{i=1,i\neq\ell}^{j-1} \beta_{ij}\boldsymbol{\Gamma}_i\boldsymbol{x}_i - \beta_{\ell j}\boldsymbol{\alpha}_\ell(\boldsymbol{x}_\ell)\,, \tag{4.25}$$

$$\mathbf{A}_j = \mathbf{I} - \sum_{i=1,i\neq\ell}^{j-1} \beta_{ij}\boldsymbol{\Gamma}_i\mathbf{A}_i - \beta_{\ell j}\boldsymbol{\Gamma}_\ell(\boldsymbol{x}_\ell)\mathbf{A}_\ell\,. \tag{4.26}$$

We separate the terms with $i = \ell$ and write $\boldsymbol{\alpha}_\ell$ and $\boldsymbol{\Gamma}_\ell$ explicitly because we do *not* use the shear approximation for the main plane.

It is interesting to consider the position $\boldsymbol{x}'_j$ and Jacobian matrix $\mathbf{B}_j$ that we would get if we were to omit the main plane. These quantities must be used with care because they do not include contributions from the main plane (which will be added back in later), but they will prove to be valuable. These modified quantities have the form

$$\boldsymbol{x}'_j = \boldsymbol{x}_1 - \sum_{i=1,i\neq\ell}^{j-1} \beta_{ij}\boldsymbol{\Gamma}_i\boldsymbol{x}'_i\,, \tag{4.27}$$

$$\mathbf{B}_j = \mathbf{I} - \sum_{i=1,i\neq\ell}^{j-1} \beta_{ij}\boldsymbol{\Gamma}_i\mathbf{B}_i\,. \tag{4.28}$$

In the foreground of the main lens plane ($j \leq \ell$), we clearly have $\boldsymbol{x}'_j = \boldsymbol{x}_j$ and $\mathbf{B}_j = \mathbf{A}_j$ because the trajectory has not yet been affected by the main plane. (Recall that we trace a light ray backwards from the observer.) The situation is different, however, in the background of the main lens plane ($j > \ell$). Taking the difference between eqs. (4.26) and (4.28), we have

$$\mathbf{A}_j - \mathbf{B}_j = -\beta_{\ell j}\boldsymbol{\Gamma}_\ell\mathbf{A}_\ell - \sum_{i=\ell+1}^{j-1} \beta_{ij}\boldsymbol{\Gamma}_i(\mathbf{A}_i - \mathbf{B}_i)\,. \tag{4.29}$$

Notice that the sum now includes only terms with $i > \ell$, because $\mathbf{A}_i - \mathbf{B}_i = 0$ for $i \leq \ell$. Now if we multiply through by $(-\boldsymbol{\Gamma}_\ell\mathbf{B}_\ell)^{-1}$ from the right and use the fact that $\mathbf{A}_\ell = \mathbf{B}_\ell$,

we obtain

$$\mathbf{C}_{\ell j} \equiv (\mathbf{A}_j - \mathbf{B}_j)(-\mathbf{\Gamma}_\ell \mathbf{B}_\ell)^{-1} \tag{4.30}$$

$$= \beta_{\ell j}\mathbf{I} - \sum_{i=\ell+1}^{j-1} \beta_{ij}\mathbf{\Gamma}_i \mathbf{C}_{\ell i}. \tag{4.31}$$

Equation (4.31) is a recursion relation for $\mathbf{C}_{\ell j}$ that involves only LOS effects, specifically only planes in between the main plane and plane j. In other words, $\mathbf{C}_{\ell j}$ is independent of the main lens. There is, of course, a dependence on the main lens in converting between $\mathbf{C}_{\ell j}$ and $\mathbf{A}_j$:

$$\mathbf{A}_j = \mathbf{B}_j - \mathbf{C}_{\ell j}\mathbf{\Gamma}_\ell \mathbf{B}_\ell \,. \tag{4.32}$$

The matrices $\mathbf{B}_j$ and $\mathbf{C}_{\ell j}$ turn out to have an additional use when we consider the positions. Returning to eqs. (4.26) and (4.27) and writing out terms, we find that in the shear approximation we have the simple relation

$$\boldsymbol{x}'_j = \mathbf{B}_j \boldsymbol{x}_1 \,, \tag{4.33}$$

for all j. In the foreground ($j \leq \ell$) we of course have $\boldsymbol{x}_j = \boldsymbol{x}'_j$. In the background ($j > \ell$), the positions $\boldsymbol{x}_j$ and $\boldsymbol{x}'_j$ are different, and in fact we have

$$\boldsymbol{x}_j = \boldsymbol{x}'_j - \mathbf{C}_{\ell j}\boldsymbol{\alpha}_\ell(\boldsymbol{x}_\ell) \,. \tag{4.34}$$

Note that the deflection depends on the position in the main lens plane $\boldsymbol{x}_\ell$, not the observed sky plane $\boldsymbol{x}_1$. This leads to non-linear effects that cannot be mimicked by an external shear and will be important for the multi-plane mass sheet degeneracy (see §4.5).

To summarize, in the case of a single main plane plus a collection of planes that can be treated with the shear approximation, we can separate the full multi-plane lensing analysis into pieces that depend only on the LOS ($\mathbf{B}_\ell$, $\mathbf{B}_s$, and $\mathbf{C}_{\ell s}$) and pieces that depend on the main lens plane ($\boldsymbol{\alpha}_\ell$ and $\mathbf{\Gamma}_\ell$, both of which are evaluated at the position $\boldsymbol{x}_\ell = \mathbf{B}_\ell \boldsymbol{x}_1$). We

can combine the pieces into the lens equation and Jacobian matrix as follows:

$$\boldsymbol{x}_s = \mathbf{B}_s \boldsymbol{x}_1 - \mathbf{C}_{\ell s} \boldsymbol{\alpha}_\ell (\mathbf{B}_\ell \boldsymbol{x}_1) \,, \tag{4.35}$$

$$\mathbf{A}_s = \mathbf{B}_s - \mathbf{C}_{\ell s} \boldsymbol{\Gamma}_\ell \mathbf{B}_\ell \,, \tag{4.36}$$

This represents a *complete* description of the multi-plane lensing in this scenario; there are no approximations involved in the treatment of multi-plane lensing itself. The only approximation used here is the shear approximation for the perturbing galaxies. Note that $\mathbf{B}_\ell$ is inside the argument of the deflection for the main lens galaxy.

The multi-plane lens equation (4.35) is identical to the quadrupole lens equation in Schneider et al. (1992) and equivalent to the results from Kovner (1987) and Bar-Kana (1996). With a suitable change of variables it can be made equivalent to standard single-plane lens equation (Bar-Kana 1996; Schneider 1997; Keeton 2003). Such a simplification may be useful for theoretical calculations, but strictly speaking it does not apply to lens modeling because the coordinate transformation is not known, and modeling should be done using observed coordinates. This form of the multi-plane lens equation was used by Wong et al. (2011) to quantify shear for a sample of observed lenses. The key advance in our new framework is the extension to an arbitrary combination of main and shear planes (§4.3.3) and then to time delays (§4.4).

4.3.2 Small-shear limit

It is instructive to consider the preceding analysis in the limit where all the LOS shears are small. If we make Taylor series expansions and work to linear order in the LOS shears, we

obtain

$$\mathbf{B}_s \approx \mathbf{I} - \mathbf{\Gamma}_{\rm tot}\,, \tag{4.37}$$

$$\mathbf{B}_\ell \approx \mathbf{I} - \tilde{\mathbf{\Gamma}}_{\rm f}\,, \tag{4.38}$$

$$\mathbf{C}_{\ell s} \approx \mathbf{I} - \tilde{\mathbf{\Gamma}}_{\rm b}, \tag{4.39}$$

where

$$\mathbf{\Gamma}_{\rm tot} = \sum_{i=1, i\neq\ell}^{N} \mathbf{\Gamma}_i \tag{4.40}$$

are simple sums of the foreground and background shear tensors (with uniform weighting), while

$$\tilde{\mathbf{\Gamma}}_{\rm f} = \sum_{i=1}^{\ell-1} \beta_{i\ell}\mathbf{\Gamma}_i \quad \text{and} \quad \tilde{\mathbf{\Gamma}}_{\rm b} = \sum_{i=\ell+1}^{N} \beta_{\ell i}\mathbf{\Gamma}_i \tag{4.41}$$

are sums where the different planes have different weight factors $\beta_{i\ell} \neq 1$ and $\beta_{\ell i} \neq 1$. The different weight factors between $\mathbf{\Gamma}$ and $\tilde{\mathbf{\Gamma}}$ will be important for the discussion of the mass sheet degeneracy (§4.5). Note that Wong et al. (2011) used $\mathbf{\Gamma}_{\rm tot}$ to characterize environmental effects for observed lenses. The sums above are discretized versions of the integrals used in cosmic shear calculations (e.g., Munshi et al. 2008).

4.3.3 Multiple "main" planes

We now extend the framework to allow arbitrary combinations of main planes (which are given full treatment) and shear planes, illustrated in Figure 4.2. We do not make any particular assumptions about how the planes are distributed in redshift; there may be 0, 1, or many shear planes in between any two main planes. As noted above, more than one galaxy may be at a given redshift. Our notation is as follows: Roman letters (i, j) are used to sequentially index all planes (both main and shear). Greek letters (μ, ν) are used to sequentially index main planes only. Also, ℓ_μ denotes the Roman index of the main plane

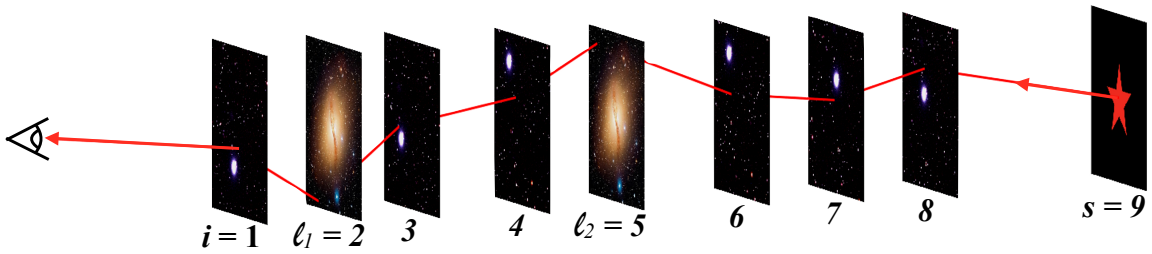

Figure 4.2 Similar to Figure 4.1, but showing a case with two main planes ($\ell_1 = 2$ and $\ell_2 = 5$).

μ; in other words, $\{\ell_1, \ell_2, ..., \ell_\mu, ...\}$ are the indices of the main planes. The source plane counts as a main plane, but with index $s = N + 1$.

To set the stage, let us re-examine the multi-plane lens equations for the case in which all planes are main (eqs. 4.16 and 4.18) and the case with a single main plane (eqs. 4.35 and 4.36). The first term in each case represents what would happen if the main planes were not present: in eq. (4.16) this is characterized by the identity matrix because if we remove all planes we are left with no lensing; while in eq. (4.35) there is distortion from all the shear planes, which is characterized by the matrix $\mathbf{B}_s$. The terms in the sums represent the combined contributions from the main plane(s) in the foreground of the plane being evaluated. In eq. (4.16) the light ray experiences no distortions in between planes, so the connecting factor is just a scalar (β_{ij}) that encodes the relative distances between planes i and j. In eq. (4.35), by contrast, the light ray may be sheared in between main planes, so the connecting factor becomes a matrix ($\mathbf{C}_{\ell s}$) that includes not only the distance factors but also the shears in between the main planes.

We can now understand the form of the lens equations for a general combination of main and shear planes:

$$\boldsymbol{x}_i = \mathbf{B}_i \boldsymbol{x}_1 - \sum_{\ell \in \{\ell_\mu < i\}} \mathbf{C}_{\ell i} \boldsymbol{\alpha}_\ell(\boldsymbol{x}_\ell)\,, \tag{4.42}$$

$$\mathbf{A}_i = \mathbf{B}_i - \sum_{\ell \in \{\ell_\mu < i\}} \mathbf{C}_{\ell i} \boldsymbol{\Gamma}_\ell \mathbf{A}_\ell\,. \tag{4.43}$$

Again notice that the deflections depend on the positions in the main planes $\boldsymbol{x}_\ell$. Also, these sums only include main planes. At each step in the recursion, $\boldsymbol{\alpha}_\ell$ and $\boldsymbol{\Gamma}_\ell$ are to be evaluated at the position $\boldsymbol{x}_\ell$. The matrix $\mathbf{B}_\ell$ represents the net effects of the shear planes in between the observer and the main plane with index ℓ, which can be found recursively as follows:

$$\mathbf{B}_j = \mathbf{I} - \sum_{i=1, i\notin\{\ell_\mu\}}^{j-1} \beta_{ij} \boldsymbol{\Gamma}_i \mathbf{B}_i \tag{4.44}$$

where this sum does not include any of the main planes (even if they happen to lie between the observer and plane j). The matrix $\mathbf{C}_{\ell j}$ represents the net effects of the shear planes in between the main plane ℓ and plane j whose recursion relation is

$$\mathbf{C}_{\ell j} = \beta_{\ell j}\mathbf{I} - \sum_{i=\ell+1, i\notin\{\ell_\mu\}}^{j-1} \beta_{\ell i} \boldsymbol{\Gamma}_i \mathbf{C}_{\ell i}, \tag{4.45}$$

where again this sum only includes shear planes. Note that $\mathbf{B}_j$ and $\mathbf{C}_{\ell j}$ are defined for arbitrary j, but eqs. (4.42) and (4.43) show that only the matrices associated with main planes need to be stored for later use. The benefit of this approach for lens modeling is that the bulk of the computational effort goes into determining $\mathbf{B}_{\ell_\mu}$ and $\mathbf{C}_{\ell_\mu \ell_\nu}$, but that step needs to be done only once. Once those matrices are stored, the mass model in the main plane(s) can be varied without having to recompute the full LOS.

4.4 Time Delay

We now turn to time delays. As before, we start with a single main plane plus a collection of shear planes, and then generalize to an arbitrary combination of shear and main planes. To set the context, it is useful to recall the classic expression for the time delay in single-plane lensing. The single-plane time delay can be written in several different forms, the most familiar of which is

$$T \propto \frac{1}{2}|\boldsymbol{x} - \boldsymbol{x}_s|^2 - \phi(\boldsymbol{x})\,. \tag{4.46}$$

We can expand the quadratic term as

$$T \propto \frac{1}{2}(\boldsymbol{x}^2 - \boldsymbol{x}\cdot\boldsymbol{x}_s - \boldsymbol{x}_s\cdot\boldsymbol{x} + \boldsymbol{x}_s^2) - \phi(\boldsymbol{x})\,. \tag{4.47}$$

In terms of the deflection angle $\boldsymbol{\alpha}$, we can rewrite this as

$$T \propto \frac{1}{2}|\boldsymbol{\alpha}|^2 - \phi(\boldsymbol{x})\,. \tag{4.48}$$

We can even mix these two forms giving

$$T \propto \frac{1}{2}(\boldsymbol{x} - \boldsymbol{x}_s)\cdot\boldsymbol{\alpha} - \phi(\boldsymbol{x})\,. \tag{4.49}$$

While these forms may look rather distinct, they are all equivalent. We will see below how the different forms are useful.

4.4.1 Single "main" plane

Before we plug solutions of the lens equation (4.35) into the time delay, it is useful to rewrite solutions in a slightly different way. We define a scaled source coordinate

$$\boldsymbol{u} \equiv \mathbf{B}_s^{-1}\boldsymbol{x}_s. \tag{4.50}$$

We can use eq. (4.35) evaluated in the source plane to eliminate $\boldsymbol{\alpha}_\ell$ giving

$$\boldsymbol{\alpha}_\ell = \mathbf{C}_{\ell s}^{-1}\mathbf{B}_s(\boldsymbol{x}_1 - \boldsymbol{u}). \tag{4.51}$$

$\boldsymbol{x}_1$ is the coordinates on the observer's sky, so to simplify the notation we drop the subscript. Substituting eq. (4.51) into eq. (4.35) yields

$$\boldsymbol{x}_j = \mathbf{B}_j\boldsymbol{x} - \mathbf{C}_{\ell j}\mathbf{C}_{\ell s}^{-1}\mathbf{B}_s(\boldsymbol{x} - \boldsymbol{u}). \tag{4.52}$$

Defining

$$\mathbf{Q}_j \equiv \mathbf{C}_{\ell j}\mathbf{C}_{\ell s}^{-1}\mathbf{B}_s, \tag{4.53}$$

further simplifies eq. (4.52) to

$$\boldsymbol{x}_j = \mathbf{B}_j\boldsymbol{x} - \mathbf{Q}_j(\boldsymbol{x}-\boldsymbol{u}). \tag{4.54}$$

This is the form we use in the time delay expression.

The general expression for the multi-plane time delay depends explicitly on *all* of the $\boldsymbol{x}_j$ and ϕ_j. Our goal is to write the time delay in terms of $(\boldsymbol{x}, \boldsymbol{x}_s, \phi_\ell)$ or equivalently $(\boldsymbol{x}, \boldsymbol{\alpha}_\ell, \phi_\ell)$. To that end, we substitute for the position coordinates, explicitly separate out the main plane lens potential, and implement the shear approximation for all other planes ($\phi_j \approx \frac{1}{2}\boldsymbol{x}_j\boldsymbol{\Gamma}_j\boldsymbol{x}_j$). This yields

$$\begin{aligned} T = & \sum_{i=1}^{s-1} \tfrac{1}{2}\tau_i \left[\mathbf{B}_{i+1}\boldsymbol{x} - \mathbf{Q}_{i+1}(\boldsymbol{x}-\boldsymbol{u}) - \mathbf{B}_i\boldsymbol{x} + \mathbf{Q}_i(\boldsymbol{x}-\boldsymbol{u})\right]^2 - \tau_{\ell s}\phi_\ell(\boldsymbol{x}_\ell) \\ & - \sum_{i=1, i\neq\ell}^{s-1} \tfrac{1}{2}\tau_i\beta_i \left[(\mathbf{B}_i\boldsymbol{x} - \mathbf{Q}_i\boldsymbol{x} + \mathbf{Q}_i\boldsymbol{u})\boldsymbol{\Gamma}_i(\mathbf{B}_i\boldsymbol{x} - \mathbf{Q}_i\boldsymbol{x} + \mathbf{Q}_i\boldsymbol{u})\right]. \end{aligned} \tag{4.55}$$

We would like to eliminate $\boldsymbol{\Gamma}_i$, so it is now necessary to digress to derive a few useful identities. We start by examining

$$\mathbf{B}_{j+1} - \mathbf{B}_j = -\beta_j\boldsymbol{\Gamma}_j\mathbf{B}_j - \sum_{i\neq\ell}^{j-1}(\beta_{i\,j+1} - \beta_{ij})\boldsymbol{\Gamma}_i\mathbf{B}_i, \tag{4.56}$$

and

$$\mathbf{B}_j - \mathbf{B}_{j-1} = -\beta_{j-1}\boldsymbol{\Gamma}_{j-1}\mathbf{B}_{j-1} - \sum_{i\neq\ell}^{j-2}(\beta_{ij} - \beta_{i\,j-1})\boldsymbol{\Gamma}_i\mathbf{B}_i. \tag{4.57}$$

Combining these and using eq. (4.22), we can cancel the sum to obtain

$$\mathbf{B}_{j+1} = \left[\left(1 + \frac{\tau_{j-1}}{\tau_j}\right)\mathbf{I} - \beta_j\boldsymbol{\Gamma}_j\right]\mathbf{B}_j - \frac{\tau_{j-1}}{\tau_j}\mathbf{B}_{j-1}. \tag{4.58}$$

Rearranging, we can solve for $\mathbf{\Gamma}_j$:

$$\beta_j \mathbf{\Gamma}_j = \left(1 + \frac{\tau_{j-1}}{\tau_j}\right) \mathbf{I} - \mathbf{B}_{j+1}\mathbf{B}_j^{-1} - \frac{\tau_{j-1}}{\tau_j}\mathbf{B}_{j-1}\mathbf{B}_j^{-1}. \tag{4.59}$$

Following the same procedure yields a similar result for $\mathbf{C}_{\ell j}$:

$$\beta_j \mathbf{\Gamma}_j = \left(1 + \frac{\tau_{j-1}}{\tau_j}\right) \mathbf{I} - \mathbf{C}_{\ell\, j+1}\mathbf{C}_{\ell j}^{-1} - \frac{\tau_{j-1}}{\tau_j}\mathbf{C}_{\ell\, j-1}\mathbf{C}_{\ell j}^{-1}. \tag{4.60}$$

These relations have an interesting effect when $\mathbf{B}_j$ or $\mathbf{C}_{\ell j}$ is multiplied from the right:

$$\beta_j \mathbf{\Gamma}_j \mathbf{B}_j = \left(1 + \frac{\tau_{j-1}}{\tau_j}\right) \mathbf{B}_j - \mathbf{B}_{j+1} - \frac{\tau_{j-1}}{\tau_j}\mathbf{B}_{j-1} \tag{4.61}$$

and

$$\beta_j \mathbf{\Gamma}_j \mathbf{C}_{\ell j} = \left(1 + \frac{\tau_{j-1}}{\tau_j}\right) \mathbf{C}_{\ell j} - \mathbf{C}_{\ell\, j+1} - \frac{\tau_{j-1}}{\tau_j}\mathbf{C}_{\ell\, j-1}. \tag{4.62}$$

We plug these identities into eq. (4.55), using eq. (4.59) when $\mathbf{\Gamma}_i$ appears with $\mathbf{B}_i$ and eq. (4.60) when it appears with $\mathbf{Q}_j$ (because that involves $\mathbf{C}_{\ell j}$), and then expand the quadratic term:

$$\begin{aligned} T \;=\; & \sum_{i=1}^{s-1} \frac{1}{2}\tau_i \left[(\mathbf{B}_{i+1}\boldsymbol{x} - \mathbf{Q}_{i+1}(\boldsymbol{x}-\boldsymbol{u}))^2 + (\mathbf{B}_i\boldsymbol{x} - \mathbf{Q}_i(\boldsymbol{x}-\boldsymbol{u}))^2 \right. \\ & - (\mathbf{B}_{i+1}\boldsymbol{x} - \mathbf{Q}_{i+1}(\boldsymbol{x}-\boldsymbol{u})) \cdot (\mathbf{B}_i\boldsymbol{x} - \mathbf{Q}_i(\boldsymbol{x}-\boldsymbol{u})) \\ & \left. - (\mathbf{B}_i\boldsymbol{x} - \mathbf{Q}_i(\boldsymbol{x}-\boldsymbol{u})) \cdot (\mathbf{B}_{i+1}\boldsymbol{x} - \mathbf{Q}_{i+1}(\boldsymbol{x}-\boldsymbol{u})) \right] - \tau_{\ell s}\phi_\ell(\boldsymbol{x}_\ell) \\ & + \sum_{i=1, i\neq\ell}^{s-1} \frac{1}{2}\tau_i (\mathbf{B}_i\boldsymbol{x} - \mathbf{Q}_i\boldsymbol{x} + \mathbf{Q}_i\boldsymbol{u}) \cdot \left[(-\mathbf{I} - \frac{\tau_{i-1}}{\tau_i})(\mathbf{B}_i\boldsymbol{x} - \mathbf{Q}_i\boldsymbol{x} + \mathbf{Q}_i\boldsymbol{u}) \right. \\ & \left. + (\mathbf{B}_{i+1}\boldsymbol{x} - \mathbf{Q}_{i+1}\boldsymbol{x} + \mathbf{Q}_{i+1}\boldsymbol{u}) + \frac{\tau_{i-1}}{\tau_i}(\mathbf{B}_{i-1}\boldsymbol{x} - \mathbf{Q}_{i-1}\boldsymbol{x} + \mathbf{Q}_{i-1}\boldsymbol{u}) \right] \end{aligned} \tag{4.63}$$

The identity term in the second sum is identical to the second quadratic term in the first sum but with opposite sign. Also, the first $i, i+1$ cross term in the first sum matches the $i, i+1$ cross term in the second sum. These terms cancel except for the main plane term

$j = \ell$ that we explicitly removed from the second sum.

The other terms in the first sum are of the same form as the remaining terms in the second sum, but with indices decremented by 1. We therefore reindex the remaining terms in the second sum with $i \to i+1$. These terms become

$$\sum_{i=1,i\neq\ell}^{s-1} \to \sum_{i=0,i\neq\ell-1}^{s-2} \tau_i(\mathbf{B}_{i+1}\boldsymbol{x} - \mathbf{Q}_{i+1}(\boldsymbol{x}-\boldsymbol{u}))^2 \tag{4.64}$$

and

$$\sum_{i=1,i\neq\ell}^{s-1} \to \sum_{i=0,i\neq\ell-1}^{s-2} \tau_i(\mathbf{B}_{i+1}\boldsymbol{x} - \mathbf{Q}_{i+1}(\boldsymbol{x}-\boldsymbol{u}))\cdot(\mathbf{B}_{i}\boldsymbol{x} - \mathbf{Q}_{i}(\boldsymbol{x}-\boldsymbol{u})). \tag{4.65}$$

These match the terms in the first sum but have opposite sign and therefore all of the sums cancel. The only surviving terms are $s-1$ and $\ell-1$ terms from removing the main plane and reindexing. There is also an $i = 0$ term from the second reindexed sum. This term would have $\tau_{0,1}$ as a coefficient. Taking the zero plane to be the observer, we have $D_0 = 0$ and therefore $\tau_{0,1} = 0$. This leaves us with

$$\begin{aligned} T \;=\; & \frac{1}{2}\big[\tau_\ell(\mathbf{B}_\ell\boldsymbol{x} - \mathbf{Q}_\ell(\boldsymbol{x}-\boldsymbol{u}))^2 - \tau_\ell(\mathbf{B}_{\ell+1}\boldsymbol{x} - \mathbf{Q}_{\ell+1}(\boldsymbol{x}-\boldsymbol{u}))\cdot(\mathbf{B}_\ell\boldsymbol{x} - \mathbf{Q}_\ell(\boldsymbol{x}-\boldsymbol{u})) \\ & + \tau_{\ell-1}(\mathbf{B}_\ell\boldsymbol{x} - \mathbf{Q}_\ell(\boldsymbol{x}-\boldsymbol{u}))^2 - \tau_{\ell-1}(\mathbf{B}_\ell\boldsymbol{x} - \mathbf{Q}_\ell(\boldsymbol{x}-\boldsymbol{u}))\cdot(\mathbf{B}_{\ell-1}\boldsymbol{x} - \mathbf{Q}_{\ell-1}(\boldsymbol{x}-\boldsymbol{u})) \\ & + \tau_{s-1}(\mathbf{B}_s\boldsymbol{x} - \mathbf{Q}_s(\boldsymbol{x}-\boldsymbol{u}))^2 - \tau_{s-1}(\mathbf{B}_s\boldsymbol{x} - \mathbf{Q}_s(\boldsymbol{x}-\boldsymbol{u}))\cdot(\mathbf{B}_{s-1}\boldsymbol{x} - \mathbf{Q}_{s-1}(\boldsymbol{x}-\boldsymbol{u}))\big] \\ & -\tau_{\ell s}\phi_\ell(\boldsymbol{x}_\ell). \end{aligned} \tag{4.66}$$

It is now enlightening to reexamine the difference $\mathbf{B}_j - \mathbf{B}_{j-1}$. Multiplying eq. (4.57) through by τ_{j-1} we get

$$\tau_{j-1}\mathbf{B}_j - \tau_{j-1}\mathbf{B}_{j-1} = -\tau_{j-1,s}\mathbf{\Gamma}_{j-1}\mathbf{B}_{j-1} - \sum_{i\neq\ell}^{j-2}\tau_{is}\mathbf{\Gamma}_i\mathbf{B}_i = -\sum_{i\neq\ell}^{j-1}\tau_{is}\mathbf{\Gamma}_i\mathbf{B}_i. \tag{4.67}$$

We then define a new set of matrices

$$\mathbf{F}_j \equiv \tau_{j-1}\mathbf{B}_j - \tau_{j-1}\mathbf{B}_{j-1} = -\sum_{i\neq\ell}^{j-1} \tau_{is}\mathbf{\Gamma}_i\mathbf{B}_i \tag{4.68}$$

and similarly for $\mathbf{C}_{\ell j}$,

$$\mathbf{G}_{\ell j} \equiv \tau_{j-1}\mathbf{C}_{\ell j} - \tau_{j-1}\mathbf{C}_{\ell\, j-1} = \tau_{\ell s}\mathbf{I} - \sum_{i=\ell+1}^{j-1} \tau_{is}\mathbf{\Gamma}_i\mathbf{C}_{\ell i}. \tag{4.69}$$

Both the $\mathbf{F}_j$ and $\mathbf{G}_{\ell j}$ matrices have units of time. Therefore terms in the time delay that include these matrices will not include an explicit τ_{ij} as a coefficient.

Plugging these definitions into eq. (4.63), we have

$$\begin{aligned} T &= \frac{1}{2}(\mathbf{B}_\ell\boldsymbol{x} - \mathbf{Q}_\ell(\boldsymbol{x}-\boldsymbol{u}))\cdot\left[(\mathbf{F}_\ell - \mathbf{F}_{\ell+1})\boldsymbol{x} - (\mathbf{G}_{\ell\,\ell} - \mathbf{G}_{\ell\,\ell+1})\mathbf{C}_{\ell s}^{-1}\mathbf{B}_s(\boldsymbol{x}-\boldsymbol{u})\right] \\ &\quad + \frac{1}{2}(\mathbf{B}_s\boldsymbol{x} - \mathbf{Q}_s(\boldsymbol{x}-\boldsymbol{u}))\cdot(\mathbf{F}_s\boldsymbol{x} - \mathbf{G}_{\ell s}\mathbf{C}_{\ell s}^{-1}\mathbf{B}_s(\boldsymbol{x}-\boldsymbol{u})) - \tau_{\ell s}\phi_\ell(\boldsymbol{x}_\ell). \end{aligned} \tag{4.70}$$

Note that the $\mathbf{F}_j$ do not include the main plane, so $\mathbf{F}_\ell = \mathbf{F}_{\ell+1}$. Also, as the $\mathbf{G}_{\ell j}$ only include the background planes, $\mathbf{G}_{\ell\,\ell} = 0$ and $\mathbf{G}_{\ell\,\ell+1} = \tau_{\ell s}$. We can further simplify this expression for the time delay when we recognize the definition of $\boldsymbol{x}_s$ from eq. (4.54) and replace $\boldsymbol{u}$ with $\mathbf{B}_s\boldsymbol{x}_s$.

With these final simplifications, we have our final expression:

$$T = \frac{1}{2}\tau_{\ell s}\mathbf{B}_\ell\boldsymbol{x}\cdot\mathbf{C}_{\ell s}^{-1}(\mathbf{B}_s\boldsymbol{x} - \boldsymbol{x}_s) + \frac{1}{2}\boldsymbol{x}_s\cdot(\mathbf{F}_s\boldsymbol{x} - \mathbf{G}_{\ell s}\mathbf{C}_{\ell s}^{-1}\mathbf{B}_s\boldsymbol{x} + \mathbf{G}_{\ell s}\mathbf{C}_{\ell s}^{-1}\boldsymbol{x}_s) - \tau_{\ell s}\phi_\ell(\mathbf{B}_\ell\boldsymbol{x}). \tag{4.71}$$

This form is most like eq. (4.47) and will be useful to compare to previous calculations with a single main plane. We can rewrite the result in an equivalent form that more resembles eq. (4.49), reordering terms and substituting for $\boldsymbol{\alpha}$ and $\boldsymbol{x}_\ell$, giving

$$T = \frac{1}{2}\left(\boldsymbol{x}_s\cdot\mathbf{F}_s\boldsymbol{x} + \tau_{\ell s}\boldsymbol{x}_\ell\cdot\boldsymbol{\alpha}_\ell - \boldsymbol{x}_s\cdot\mathbf{G}_{\ell s}\boldsymbol{\alpha}_\ell\right) - \tau_{\ell s}\phi_\ell. \tag{4.72}$$

This is the form that we will compare to our final results for multiple main planes.

Throughout this calculation we have taken a much different approach to finding the time delay than Schneider et al. (1992). We began from the general multi-plane time delay expression given by Petters et al. (2001) and algebraically manipulated the expression looking for cancellations. Schneider et al. (1992) start from the solution of the multi-plane lens equation. By Fermat's principle, the derivative of the time delay should give the lens equation. Therefore, solving for the time delay (up to a constant multiplicative factor) is equivalent to solving the differential equation

$$\frac{\partial T}{\partial \boldsymbol{x}_\ell} = \mathbf{C}_{\ell s}^{-1}\mathbf{B}_s\boldsymbol{x}_1 - \mathbf{C}_{\ell s}^{-1}\boldsymbol{x}_s - \frac{\partial \phi_\ell}{\partial \boldsymbol{x}_\ell} \tag{4.73}$$

as, according to Schneider et al. (1992), the only independent variable can be $\boldsymbol{x}_\ell$. Following this procedure, Schneider et al. (1992) find (in our notation) that

$$T \propto \frac{1}{2}\mathbf{B}_\ell\boldsymbol{x}\cdot\mathbf{C}_{\ell s}^{-1}(\mathbf{B}_s\boldsymbol{x}-\boldsymbol{x}_s) - \frac{1}{2}\boldsymbol{x}_s\cdot\mathbf{C}_{\ell s}^{-1}(\mathbf{B}_\ell\boldsymbol{x}-\mathbf{B}_\ell\mathbf{B}_s^{-1}\boldsymbol{x}_s) - \phi_\ell. \tag{4.74}$$

Comparing eqs. (4.72) and (4.74), we see that the proportionality constant is (not surprisingly) $\tau_{\ell,s}$ (also see Schneider 1997). The terms in the first set of parentheses are identical to our solution, but the terms in the second set of parentheses require more care.

The first term in the second parentheses is not obviously the same as the corresponding term in our expression. However, from quantitative tests using different numbers of planes with random separations and lens potentials, we find that the two are numerically equal. This implies the non-obvious identity

$$\tau_{\ell s}\mathbf{C}_{\ell s}^{-1}\mathbf{B}_\ell = \mathbf{G}_{\ell s}\mathbf{C}_{\ell s}^{-1}\mathbf{B}_s - \mathbf{F}_s. \tag{4.75}$$

While we have not proved this identity analytically, we suspect it is related to the identities in eqs. (4.59) and (4.60).

Unlike the first term, the second term in the second parentheses in eq. (4.74) is not numerically equivalent to our result. We note that this term is quadratic in $\boldsymbol{x}_s$ and does not depend on $\boldsymbol{x}_\ell$ (or equivalently $\boldsymbol{x}_1$). As Schneider et al. (1992) only consider the partial derivative with respect to $\boldsymbol{x}_\ell$, their analysis is insensitive to an additive term that is independent of $\boldsymbol{x}_\ell$. In any case, such a term does not affect *differential* time delays, which are the observables of interest.

4.4.2 Multiple "main" planes

We now extend this analysis to an arbitrary combination of main planes and shear planes. We again do not make any assumptions about the redshift distributions of the planes or how the planes are ordered. As above, we denote the index of main planes as $\ell \in \{\ell_1, \ell_2, ..., \ell_\mu, ...\}$. We begin with the lens equation (4.42) for multiple main planes. We substitute this expression into the full time delay expression, eq. (4.19), and separate the main plane indices giving

$$\begin{aligned} T &= \sum_{i=1}^{s-1} \frac{1}{2}\tau_i \left[\mathbf{B}_{i+1}\boldsymbol{x} - \sum_{\ell\in\{\ell_\mu\}}^{\ell<i+1} \mathbf{C}_{\ell\, i+1}\boldsymbol{\alpha}_\ell - \mathbf{B}_i\boldsymbol{x} + \sum_{\ell\in\{\ell_\mu\}}^{\ell<i} \mathbf{C}_{\ell i}\boldsymbol{\alpha}_\ell \right]^2 \\ &\quad - \sum_{i=1, i\notin\{\ell_\mu\}}^{s-1} \frac{1}{2}\tau_i\beta_i \left(\mathbf{B}_i\boldsymbol{x} - \sum_{\ell\in\{\ell_\mu\}}^{\ell<i} \mathbf{C}_{\ell i}\boldsymbol{\alpha}_\ell \right) \cdot \boldsymbol{\Gamma}_i \left(\mathbf{B}_i\boldsymbol{x} - \sum_{\ell\in\{\ell_\mu\}}^{\ell<i} \mathbf{C}_{\ell i}\boldsymbol{\alpha}_\ell \right) \\ &\quad - \sum_{\ell\in\{\ell_\mu\}} \tau_{\ell s}\phi_\ell(\boldsymbol{x}_\ell). \end{aligned} \tag{4.76}$$

As $\mathbf{B}_j$ and $\mathbf{C}_{\ell j}$ only depend on the shear planes, the relationships between these matrices and $\boldsymbol{\Gamma}_j$, eqs. (4.59) and (4.60), still hold in the multiple main plane case. It is useful to point out that the relationship given in eq. (4.60) now generalizes for each $\ell \in \{\ell_\mu\}$. Using these relations and expanding the quadratic terms, analogous to eq. (4.63), we can rewrite

the time delay as

$$
\begin{aligned}
T &= \sum_{i=1}^{s-1} \frac{1}{2}\tau_i \left[\left(\mathbf{B}_{i+1}\boldsymbol{x} - \sum_{\ell\in\{\ell_\mu\}}^{\ell<i+1} \mathbf{C}_{\ell\, i+1}\boldsymbol{\alpha}_\ell \right)^2 + \left(\mathbf{B}_i\boldsymbol{x} - \sum_{\ell\in\{\ell_\mu\}}^{\ell<i} \mathbf{C}_{\ell i}\boldsymbol{\alpha}_\ell \right)^2 \right. \\
&\quad \left. - 2\left(\mathbf{B}_{i+1}\boldsymbol{x} - \sum_{\ell\in\{\ell_\mu\}}^{\ell<i+1} \mathbf{C}_{\ell\, i+1}\boldsymbol{\alpha}_\ell \right) \cdot \left(\mathbf{B}_i\boldsymbol{x} - \sum_{\ell\in\{\ell_\mu\}}^{\ell<i} \mathbf{C}_{\ell i}\boldsymbol{\alpha}_\ell \right) \right] \\
&\quad + \sum_{i=1, i\notin\{\ell_\mu\}}^{s-1} \frac{1}{2}\tau_i \left(\mathbf{B}_i\boldsymbol{x} - \sum_{\ell\in\{\ell_\mu\}}^{\ell<i} \mathbf{C}_{\ell i}\boldsymbol{\alpha}_\ell \right) \cdot \left[\left(-\mathbf{I} - \frac{\tau_{i-1}}{\tau_i} \right) \left(\mathbf{B}_i\boldsymbol{x} - \sum_{\ell\in\{\ell_\mu\}}^{\ell<i} \mathbf{C}_{\ell i}\boldsymbol{\alpha}_\ell \right) \right. \\
&\quad \left. + \left(\mathbf{B}_{i+1}\boldsymbol{x} - \sum_{\ell\in\{\ell_\mu\}}^{\ell<i+1} \mathbf{C}_{\ell\, i+1}\boldsymbol{\alpha}_\ell \right) + \frac{\tau_{i-1}}{\tau_i} \left(\mathbf{B}_{i-1}\boldsymbol{x} - \sum_{\ell\in\{\ell_\mu\}}^{\ell<i-1} \mathbf{C}_{\ell\, i-1}\boldsymbol{\alpha}_\ell \right) \right] \\
&\quad - \sum_{\ell\in\{\ell_\mu\}} \tau_{\ell s}\phi_\ell(\boldsymbol{x}_\ell). \qquad (4.77)
\end{aligned}
$$

As in the single plane case, the identity term in the second term matches the second quadratic term in the first sum. These cancel, leaving only the main planes from the first sum. Again, the $i, i+1$ cross term in the second sum cancels one of the cross terms in the first sum, leaving only the main plane terms. As in the single plane case, we see that the remaining terms are identical but that the indices in the second sum are decremented by 1. We reindex the sums with $i \to i+1$:

$$
\sum_{i=1, i\notin\{\ell_\mu\}}^{s-1} \to \sum_{i=0, i+1\notin\{\ell_\mu\}}^{s-2} \tau_i \left(\mathbf{B}_{i+1}\boldsymbol{x} - \sum_{\ell\in\{\ell_\mu\}}^{\ell<i+1} \mathbf{C}_{\ell\, i+1}\boldsymbol{\alpha}_\ell \right)^2 \qquad (4.78)
$$

and

$$
\sum_{i=1, i\notin\{\ell_\mu\}}^{s-1} \to \sum_{i=0, i+1\notin\{\ell_\mu\}}^{s-2} \tau_i \left(\mathbf{B}_{i+1}\boldsymbol{x} - \sum_{\ell\in\{\ell_\mu\}}^{\ell<i+1} \mathbf{C}_{\ell\, i+1}\boldsymbol{\alpha}_\ell \right) \cdot \left(\mathbf{B}_i\boldsymbol{x} - \sum_{\ell\in\{\ell_\mu\}}^{\ell<i} \mathbf{C}_{\ell i}\boldsymbol{\alpha}_\ell \right). \qquad (4.79)
$$

These terms now cancel in the sums leaving only the $s-1$ and $\{\ell_\mu - 1\}$ terms.

We are left with

$$
\begin{aligned}
T &= \frac{1}{2}\sum_{\ell\in\{\ell_\mu\}}\Bigg[\tau_\ell\left(\mathbf{B}_\ell\boldsymbol{x}-\sum_{\nu\in\{\ell_\mu\}}^{\nu<\ell}\mathbf{C}_{\nu\ell}\boldsymbol{\alpha}_\nu\right)^2+\tau_{\ell-1}\left(\mathbf{B}_\ell\boldsymbol{x}-\sum_{\nu\in\{\ell_\mu\}}^{\nu<\ell}\mathbf{C}_{\nu\ell}\boldsymbol{\alpha}_\nu\right)^2 \\
&\quad -\tau_\ell\left(\mathbf{B}_{\ell+1}\boldsymbol{x}-\sum_{\nu\in\{\ell_\mu\}}^{\nu<\ell+1}\mathbf{C}_{\nu\,\ell+1}\boldsymbol{\alpha}_\nu\right)\cdot\left(\mathbf{B}_\ell\boldsymbol{x}-\sum_{\nu\in\{\ell_\mu\}}^{\nu<\ell}\mathbf{C}_{\nu\ell}\boldsymbol{\alpha}_\nu\right) \\
&\quad -\tau_{\ell-1}\left(\mathbf{B}_\ell\boldsymbol{x}-\sum_{\mu\in\{\ell_\mu\}}^{\nu<\ell}\mathbf{C}_{\nu\ell}\boldsymbol{\alpha}_\nu\right)\cdot\left(\mathbf{B}_{\ell-1}\boldsymbol{x}-\sum_{\nu\in\{\ell_\mu\}}^{\nu<\ell-1}\mathbf{C}_{\nu\,\ell-1}\boldsymbol{\alpha}_\nu\right)\Bigg] \\
&\quad -\tau_{s-1}\left(\mathbf{B}_s\boldsymbol{x}-\sum_{\nu\in\{\ell_\mu\}}^{\nu<s}\mathbf{C}_{\nu s}\boldsymbol{\alpha}_\nu\right)\cdot\left(\mathbf{B}_{s-1}\boldsymbol{x}-\sum_{\nu\in\{\ell_\mu\}}^{\nu<s-1}\mathbf{C}_{\nu\,s-1}\boldsymbol{\alpha}_\nu\right) \\
&\quad +\tau_{s-1}\left(\mathbf{B}_s\boldsymbol{x}-\sum_{\nu\in\{\ell_\mu\}}^{\nu<s}\mathbf{C}_{\nu s}\boldsymbol{\alpha}_\nu\right)^2-\sum_{\ell\in\{\ell_\mu\}}\tau_{\ell s}\phi_\ell(\boldsymbol{x}_\ell). \qquad (4.80)
\end{aligned}
$$

Our expressions for $\mathbf{F}_j$ and $\mathbf{G}_{\ell j}$ remain basically unchanged except that ℓ is now a free index that runs over the main planes. These are now given by

$$
\mathbf{F}_j \equiv \tau_{j-1}\mathbf{B}_j-\tau_{j-1}\mathbf{B}_{j-1}=-\sum_{i=1,i\notin\{\ell_\mu\}}^{j-1}\tau_{is}\boldsymbol{\Gamma}_i\mathbf{B}_i \qquad (4.81)
$$

and

$$
\mathbf{G}_{\ell j} \equiv \tau_{j-1}\mathbf{C}_{\ell j}-\tau_{j-1}\mathbf{C}_{\ell\,j-1}=\tau_{\ell s}\mathbf{I}-\sum_{i=\ell+1,i\notin\{\ell_\mu\}}^{j-1}\tau_{is}\boldsymbol{\Gamma}_i\mathbf{C}_{\ell i}. \qquad (4.82)
$$

Substituting these matrices into eq. (4.80) yields

$$
\begin{aligned}
T &= \frac{1}{2}\sum_{\ell\in\{\ell_\mu\}}\left(\mathbf{B}_\ell\boldsymbol{x}-\sum_{\nu\in\{\ell_\mu\}}^{\nu<\ell}\mathbf{C}_{\nu\ell}\boldsymbol{\alpha}_\nu\right)\cdot\Bigg[\left(\mathbf{F}_\ell\boldsymbol{x}-\sum_{\nu\in\{\ell_\mu\}}^{\nu<\ell}\mathbf{G}_{\nu\ell}\boldsymbol{\alpha}_\nu\right) \\
&\quad \cdot\left(\mathbf{F}_{\ell+1}\boldsymbol{x}-\sum_{\nu\in\{\ell_\mu\}}^{\nu<\ell+1}\mathbf{G}_{\nu\,\ell+1}\boldsymbol{\alpha}_\nu\right)\Bigg]-\sum_{\ell\in\{\ell_\mu\}}\tau_{\ell s}\phi_\ell(\boldsymbol{x}_\ell) \\
&\quad +\frac{1}{2}\left(\mathbf{B}_s\boldsymbol{x}-\sum_{\nu\in\{\ell_\mu\}}^{\nu<s}\mathbf{C}_{\nu s}\boldsymbol{\alpha}_\nu\right)\cdot\left(\mathbf{F}_s\boldsymbol{x}-\sum_{\nu\in\{\ell_\mu\}}^{\nu<s}\mathbf{G}_{\nu s}\boldsymbol{\alpha}_\nu\right). \qquad (4.83)
\end{aligned}
$$

Recall that $\mathbf{F}_j$ and $\mathbf{G}_{\ell j}$ are both independent of main planes so $\mathbf{F}_\ell=\mathbf{F}_{\ell+1}$ and $\mathbf{G}_{\nu\ell}=$

$\mathbf{G}_{\nu\,\ell+1}$. Therefore, as before, the $\mathbf{F}_j$ and $\mathbf{G}_{\ell j}$ terms cancel. There is an important subtlety here, though. The second sum with the $\mathbf{G}_{\nu\,\ell+1}$ includes one more main plane that the previous corresponding sum, namely $\mathbf{G}_{\ell\,\ell+1}\boldsymbol{\alpha}_\ell = \tau_{\ell s}\boldsymbol{\alpha}_\ell$. We also substitute $\boldsymbol{x}_\ell$ and $\boldsymbol{x}_s$ from the lens equation, eq. (4.42), finally giving us

$$T = \frac{1}{2}\boldsymbol{x}_s \cdot \mathbf{F}_s\boldsymbol{x} + \sum_{\ell\in\{\ell_\mu\}}\left[\frac{1}{2}\tau_{\ell s}\boldsymbol{x}_\ell\cdot\boldsymbol{\alpha}_\ell - \frac{1}{2}\boldsymbol{x}_s\cdot\mathbf{G}_{\ell s}\boldsymbol{\alpha}_\ell - \tau_{\ell s}\phi_\ell\right]. \tag{4.84}$$

This result immediately becomes the single main plane time delay, eq. (4.72), by dropping the sum over main planes.

In practice, we can tabulate all of the line of sight effects by calculating all of the $\mathbf{B}_j$, $\mathbf{C}_{\ell j}$, $\mathbf{F}_j$, and $\mathbf{G}_{\ell j}$ matrices. The benefit of this approach is that all of the line of sight calculations can be done up front and performed only once. We can save these matrices and then vary the main plane potentials without ever having to recalculate the full line of sight.

4.5 Mass Sheet Degeneracy

For traditional, single-plane lensing, Falco et al. (1985) showed that certain transformations of the lens potential leave the image positions and flux ratios unchanged. One notable transformation is the "mass sheet degeneracy." In the single-plane case, the lens equation has the form

$$\boldsymbol{x}_s = \boldsymbol{x} - \nabla\phi(\boldsymbol{x}). \tag{4.85}$$

If we apply the transformation

$$\phi(\boldsymbol{x}) \to (1-\kappa)\phi(\boldsymbol{x}) + \frac{\kappa}{2}\boldsymbol{x}^2 \tag{4.86}$$

the entire right-hand side of eq. (4.85) gets multiplied by $(1-\kappa)$. Because the source position is unobservable, we can define a rescaled source coordinate $(1-\kappa)\boldsymbol{y} = \boldsymbol{x}_s$ and then write

the transformed lens equation as

$$(1-\kappa)\boldsymbol{y} = (1-\kappa)\boldsymbol{x} - (1-\kappa)\nabla\phi(\boldsymbol{x}), \tag{4.87}$$

The $(1-\kappa)$ factors cancel, so the transformed equation is formally equivalent to the original. A similar cancellation occurs for the fluxes if we rescale the source flux, which is permitted if the intrinsic flux of the source is unknown and the constraint come from flux ratios rather than absolute fluxes.[1] Time delays are different, however. The transformation (4.86) causes differential time delays to be rescaled by

$$\Delta T' = (1-\kappa)\Delta T, \tag{4.88}$$

which is important when using time delays to constrain the Hubble constant (e.g., Suyu et al. 2010, 2013; Fadely et al. 2010). Overall, the mass sheet degeneracy can be viewed as a type of gauge invariance analogous to what is seen with potentials in electricity and magnetism.

Before proceeding to the multi-plane case, it is useful to examine a case with external convergence and shear in the lens plane. We can write the potential as

$$\phi(\boldsymbol{x}) = \phi_g(\boldsymbol{x}) + \frac{1}{2}\boldsymbol{x}\cdot\boldsymbol{\Gamma}\cdot\boldsymbol{x} \tag{4.89}$$

where $\phi_g(\boldsymbol{x})$ is the potential due to the main galaxy. The mass sheet degeneracy still applies to this situation, but the transformation is slightly different:

$$\phi_g(\boldsymbol{x}) \to (1-\kappa)\phi(\boldsymbol{x}) + \frac{\kappa}{2}\boldsymbol{x}\cdot(\mathbf{I}-\boldsymbol{\Gamma})\cdot\boldsymbol{x}. \tag{4.90}$$

This form of the mass sheet degeneracy produces the same rescaling of observables as before.

[1] Type Ia supernovae can be used to break the mass-sheet degeneracy because their intrinsic luminosity can be inferred from their light curve shapes (e.g., Kolatt & Bartelmann 1998).

We have found a similar gauge symmetry for the case of a single main plane with an arbitrary collection of shear planes along the line of sight. If we start with the lens equation (4.35) and make the transformation

$$\phi(\boldsymbol{x}_\ell) \to (1-\kappa)\phi + \frac{\kappa}{2}\boldsymbol{x}_\ell^T \mathbf{C}_{\ell s}^{-1}\mathbf{B}_s\mathbf{B}_\ell^{-1}\boldsymbol{x}_\ell \tag{4.91}$$

we find that the observables scale in the same way as the original mass sheet degeneracy. The form of this transformation is reminiscent of eq. (4.90), so we define an "effective" shear by

$$\boldsymbol{\Gamma}_{\rm eff} \equiv \mathbf{I} - \mathbf{C}_{\ell s}^{-1}\mathbf{B}_s\mathbf{B}_\ell^{-1}. \tag{4.92}$$

To build some intuition about this quantity, it is useful to examine the small-shear limit. Substituting expressions from §4.3.2 yields

$$\mathbf{C}_{\ell s}^{-1}\mathbf{B}_s\mathbf{B}_\ell^{-1} \approx (\mathbf{I}-\tilde{\boldsymbol{\Gamma}}_{\rm b})^{-1}(\mathbf{I}-\boldsymbol{\Gamma}_{\rm tot})(\mathbf{I}-\tilde{\boldsymbol{\Gamma}}_{\rm f})^{-1}. \tag{4.93}$$

If we make the additional, stronger assumption that the sums over shear planes are also small, we can further simplify this expression. Using a Taylor series expansion of the inverses and keeping only the first-order terms in $\boldsymbol{\Gamma}$'s, we obtain

$$\mathbf{C}_{\ell s}^{-1}\mathbf{B}_s\mathbf{B}_\ell^{-1} \approx (\mathbf{I}+\tilde{\boldsymbol{\Gamma}}_{\rm b})(\mathbf{I}-\boldsymbol{\Gamma}_{\rm tot})(\mathbf{I}+\tilde{\boldsymbol{\Gamma}}_{\rm f}). \tag{4.94}$$

Multiplying this out and keeping only linear terms in $\boldsymbol{\Gamma}$'s, we find

$$\boldsymbol{\Gamma}_{\rm eff} \approx \sum_{i=1, i\neq\ell}^{N} (1-\beta)\,\boldsymbol{\Gamma}_i, \tag{4.95}$$

where β is $\beta_{i\ell}$ in the foreground and $\beta_{\ell i}$ in the background. Our interpretation is that $\boldsymbol{\Gamma}_{\rm eff}$ is approximately the sum of all of the shear planes weighted by the redshift factor $(1-\beta)$. This has the same form as the effective shear that was found by Momcheva et al. (2006).

We will comment further on the use of $\mathbf{\Gamma}_{\rm eff}$ in §4.6.

The mass sheet degeneracy is more subtle for multiple main planes. There is a transformation that preserves the image positions in eq. (4.16):

$$\phi_1(\boldsymbol{x}_1) \rightarrow (1-\kappa)\phi_1(\boldsymbol{x}_1) + \frac{\kappa}{2}\boldsymbol{x}_1^2, \tag{4.96}$$

$$\phi_i(\boldsymbol{x}_i) \rightarrow (1-\kappa)\phi_i(\boldsymbol{x}_i) \qquad (i>1). \tag{4.97}$$

We interpret this transformation as adding a mass sheet in the observed plane on the sky ($i=1$), i.e., as a "mass-screen" degeneracy. If κ is in any other plane, the image positions are not preserved due to the recursion in the lens equation. In our new hybrid framework, the transformation generalizes to

$$\phi_{\ell_1}(\boldsymbol{x}_{\ell_1}) \rightarrow (1-\kappa)\phi_{\ell_1}(\boldsymbol{x}_{\ell_1}) + \frac{\kappa}{2}\boldsymbol{x}_{\ell_1}^T\mathbf{C}_{\ell_1 s}^{-1}\mathbf{B}_s\mathbf{B}_{\ell_1}^{-1}\boldsymbol{x}_{\ell_1}, \tag{4.98}$$

$$\phi_{\ell}(\boldsymbol{x}_{\ell}) \rightarrow (1-\kappa)\phi_{\ell}(\boldsymbol{x}_{\ell}) \qquad (\ell>\ell_1) \tag{4.99}$$

for all main planes behind the first. While these general transformations preserve the image positions, their effects on time delays are much more complicated than a simple rescaling and is beyond the scope of this work. In practice, the multiple main plane mass sheet degeneracy is not relevant for our lens models (Wong et al. 2011, McCully et al., in prep.) because we explicitly include the measured mass in the LOS planes, rather than adding convergence in post-processing.

4.6 Conclusions

We have presented a framework for multi-plane gravitational lensing that fills the gap between using the full multi-plane lens equation (which can be computationally expensive) and treating everything as shear (which omits higher-order effects that can be significant for objects projected near the lens). The framework can handle any mixture of "main"

planes (strong lenses) that are given full treatment and "shear" planes (weak lenses) that are treated using the shear approximation. Our framework can be used to calculate all of the standard lensing observables. The general expressions for the lens equation, magnification tensor, and time delay are as follows (from eqs. 4.42, 4.43, and 4.84):

$$\begin{aligned}
\boldsymbol{x}_i &= \mathbf{B}_i \boldsymbol{x}_1 - \sum_{\ell \in \{\ell_\mu < i\}} \mathbf{C}_{\ell i} \boldsymbol{\alpha}_\ell(\boldsymbol{x}_\ell), \\
\mathbf{A}_i &= \mathbf{B}_i - \sum_{\ell \in \{\ell_\mu < i\}} \mathbf{C}_{\ell i} \boldsymbol{\Gamma}_\ell \mathbf{A}_\ell, \\
T &= \frac{1}{2} \boldsymbol{x}_s \cdot \mathbf{F}_s \boldsymbol{x} + \sum_{\ell \in \{\ell_\mu\}} \left[\frac{1}{2} \tau_{\ell s} \boldsymbol{x}_\ell \cdot \boldsymbol{\alpha}_\ell - \frac{1}{2} \boldsymbol{x}_s \cdot \mathbf{G}_{\ell s} \boldsymbol{\alpha}_\ell - \tau_{\ell s} \phi_\ell \right],
\end{aligned}$$

These expressions are more accurate than traditional single-plane lensing because they account for LOS effects. In particular, each main plane needs to be evaluated using the positions $\boldsymbol{x}_\ell$, which are not generally the same as the positions $\boldsymbol{x}_1$ on the sky and must be computed with the lens equation; this distinction gives rise to non-linearities that cannot be mimicked by a simple shear and can lead to systematic uncertainties in lens models (McCully et al., in prep.). Our expressions are also more accurate than what we have termed the single main plane case, because they allow higher-order effects in planes other than the main lens plane. Yet they are more efficient than the full multi-plane lens equation because the recursive sums only include main planes. All of the shear planes—which may number in the hundreds for realistic lines of sight—can be compressed into the following

matrices (from eqs. 4.28, 4.31, 4.68, 4.69):

$$\begin{aligned}
\mathbf{B}_j &= \mathbf{I} - \sum_{i=1, i\notin\{\ell_\mu\}}^{j-1} \beta_{ij} \mathbf{\Gamma}_i \mathbf{B}_i, \\
\mathbf{C}_{\ell j} &= \beta_{\ell j}\mathbf{I} - \sum_{i=\ell+1, i\notin\{\ell_\mu\}}^{j-1} \beta_{\ell i} \mathbf{\Gamma}_i \mathbf{C}_{\ell i}, \\
\mathbf{F}_j &\equiv \tau_{j-1}\mathbf{B}_j - \tau_{j-1}\mathbf{B}_{j-1} = -\sum_{i=1, i\notin\{\ell_\mu\}}^{j-1} \tau_{is} \mathbf{\Gamma}_i \mathbf{B}_i, \\
\mathbf{G}_{\ell j} &\equiv \tau_{j-1}\mathbf{C}_{\ell j} - \tau_{j-1}\mathbf{C}_{\ell\, j-1} = \tau_{\ell s}\mathbf{I} - \sum_{i=\ell+1, i\notin\{\ell_\mu\}}^{j-1} \tau_{is} \mathbf{\Gamma}_i \mathbf{C}_{\ell i}.
\end{aligned}$$

These matrices can be computed once at the start of any lens modeling analysis and stored for repeated use.

One way to incorporate LOS effects in lens models is to build full three-dimensional mass models like those used by Wong et al. (2011). Then all of the non-linear effects are automatically included. An alternate approach is to build a standard single-plane lens model and then attempt to correct for LOS effects. The corrections can be calibrated by ray tracing through cosmological simulations (e.g., Hilbert et al. 2009; Collett et al. 2013; Suyu et al. 2010, 2013). To date, the corrections have been applied using the total convergence from a direct sum of all the mass along the LOS. We find, however, that the key quantities are the effective convergence and shear, which are given by (from eqs. 4.92 and 4.95)

$$\mathbf{\Gamma}_{\rm eff} \equiv \mathbf{I} - \mathbf{C}_{\ell s}^{-1}\mathbf{B}_s\mathbf{B}_\ell^{-1} \approx \sum_{i=1, i\neq\ell}^{N} (1-\beta)\mathbf{\Gamma}_i$$

where β is $\beta_{i\ell}$ in the foreground of the main lens plane, and $\beta_{\ell i}$ in the background. The β weight factors depend on the redshift of the main lens galaxy as well as the redshifts of the source and the plane in question, so the effective shear and convergence cannot be tabulated in a general way that is independent of particular lens systems. While the corrective approach is valuable, it typically uses the observed positions on the sky ($\boldsymbol{x}_1$) instead of $\boldsymbol{x}_\ell$, which can lead to systematics as discussed above. In principle, the corrective

approach could account for the non-linear effects by using $\boldsymbol{x}_\ell = \mathbf{B}_\ell \boldsymbol{x}_1$, where the matrix $\mathbf{B}_\ell$ can be calibrated by ray tracing.

In order to employ our hybrid framework effectively, we need to understand when it is acceptable to use the shear approximation and when we need to treat a plane exactly. In a forthcoming paper (McCully et al., in prep.), we use realistic beams like those in Wong et al. (2011) to test the shear approximation. We also quantify bias and scatter in lens models associated with different ways of handling the LOS. The framework presented here serves as the foundation for more detailed treatments of LOS effects in strong lensing.

Acknowledgements

We thank Phil Marshall and Roger Blandford for helpful conversations. CM and CRK acknowledge funding from NSF grant AST-0747311. KCW is supported by an EACOA Fellowship awarded by the East Asia Core Observatories Association, which consists of the Academia Sinica Institute of Astronomy and Astrophysics, the National Astronomical Observatory of Japan, the National Astronomical Observatory of China, and the Korea Astronomy and Space Science Institute. AIZ acknowledges funding from NSF grant AST-0908280, as well as NASA grants ADP-NNX10AD476 and ADP-NNX10AE88G. She also thanks the John Simon Guggenheim Memorial Foundation and the Center for Cosmology and Particle Physics at NYU for their support. Image credits: Centaurus A—Jean-Charles Cuillandre, Giovanni Anselmi, Hawaiian Starlight; Leo I—Oliver Stein.

Chapter 5

Testing our LOS Framework: Numerical Simulations

Abstract

We test our new lensing framework for treating Line of Sight (LOS) galaxies with a set of simulations with a single perturber. This simplification isolates where the shear approximation fails and non-linear effects become important. We show that models with an external shear can accurately account for a perturbing galaxy behind the main lens, but that foreground perturbers can not be mimicked by an external shear in the lens plane. Our LOS framework can reproduce the fitted lens properties of realistic, complex mass models that include hundreds of galaxies without bias and with scatter that is smaller than typical measurement uncertainties. Models with an external shear or that ignore the environment have larger scatter in the recovered parameters of the fit and a bias of $\sim 10\%$ in the inferred Einstein radius of the main lens galaxy. This bias is due to the convergence of perturbing galaxies; the external convergence can be included but must be done explicitly in shear models. In our approach, the convergence and shear arise self-consistently from an underlying mass distribution.

5.1 Introduction

Strong gravitational lensing is an important probe for many facets of cosmology. Analysis of strong lenses has led to constraints on the masses and properties of dark matter halos of galaxies (e.g., Koopmans et al. 2006; Barnabè et al. 2009; Keeton et al. 1998), substructure in galaxy halos (e.g., Mao & Schneider 1998; Metcalf & Madau 2001; Dalal & Kochanek

2002), and the Hubble Constant, independent of the cosmic distance ladder (e.g. Refsdal 1964; Keeton et al. 1997; Kochanek 2003; Saha et al. 2006; Oguri 2007). Strong lensing may also be employed to constrain the properties of dark energy (e.g. Turner 1990; Linder 2004, 2011; Cao et al. 2012; Treu et al. 2013). In recent years, both the quantity and quality of observations of strong lens systems has improved. The relative position and fluxes of lensed images are routinely measured to high precision using the *Hubble Space Telescope* (e.g,. Lehár et al. 2000; Sluse et al. 2012, and references therein; CASTLeS Collaboration). The sample of known quasar strong gravitational lens systems has grown to ~ 100 (e.g., CASTLeS[1]) with a similar number of extended source strong lenses (e.g., Bolton et al. 2008). These samples will increase dramatically in the near future with LSST (e.g., LSST Science Collaboration et al. 2009; Coe & Moustakas 2009; Oguri & Marshall 2010). Our understanding of gravitational lenses and the constraints they place on cosmology are no longer limited by observations, but by systematic uncertainties (Momcheva et al. 2006).

One of the key systematic uncertainties in modeling strong lenses is that the lens galaxy is not an isolated system. In fact, the largest component of the uncertainty budget for measuring the Hubble Constant with lensing is due to external convergence (Suyu 2012). The external convergence (and shear) arise from two components: the lens environment and the line of sight (LOS; e.g., Jaroszynski & Kostrzewa-Rutkowska 2014). Using galaxy demographics, Keeton et al. (2000) estimate that at least 25% of lens galaxies are part of groups or clusters that can cause strong perturbations to the lensing potential. Several lens systems are also spectroscopically observed to lie in groups or clusters (Momcheva et al. 2006, and references therein). There can also be perturbations due to mass that is not physically associated with lens galaxy, but is close in projection along the LOS (e.g., Bar-Kana 1996; Momcheva et al. 2006; Wong et al. 2011).

Keeton & Zabludoff (2004) show that ignoring neighbor galaxies can lead to a bias in the fitted parameters corresponding to a systematic uncertainty in modeling the lens system.

[1] `http://www.cfa.harvard.edu/castles/`

Jaroszynski & Kostrzewa-Rutkowska (2014) show that omitting the effects of LOS and neighbor galaxies can lead to unsuccessful fits for a substantial number of their simulations. When time delay constraints are included, the fits are more likely to fail.

There are a few ways that have been used to treat the local lens environment and line of sight (hereafter, environment/LOS). The first is to ignore the environment/LOS altogether, but this can lead to bias and increased scatter in the fitted lens parameters (Keeton & Zabludoff 2004; Momcheva et al. 2006). The most common way to deal with environment/LOS effects is to fit for an external shear in the lens plane and then add the external convergence in post-processing (e.g., Fadely et al. 2010; Nakajima et al. 2009; Suyu et al. 2010, 2013; Collett et al. 2013). The external convergence can be calibrated by ray tracing through cosmological simulations (e.g., Hilbert et al. 2009; Collett et al. 2013; Suyu et al. 2010, 2013). While this approach is much better than ignoring the LOS/environment, it still has its limitations.

This widely-used approach neglects higher-order effects beyond shear, which may be significant for objects sufficiently close to the optical axis, and it also neglects non-linear effects that arise from having mass in multiple redshift planes (McCully et al. 2014; Jaroszynski & Kostrzewa-Rutkowska 2012). The calibration for the external convergence is also derived from statistical studies that may have limited applicability to individual lens environments (Wong et al. 2011).

We have taken a complementary approach to adding an external convergence in post-processing. If we have observations of the environment/LOS, we can build lens models that incorporate that mass in a more realistic way. We now have an extensive photometric and spectroscopic dataset on ~ 25 strong lensing systems (Momcheva et al. 2006; Williams et al. 2008; Wong et al. 2011). Following the methodology of Wong et al. (2011), we can build beam models that include all of the observed mass along the LOS. While our approach is more complicated and observationally expensive, our models have a direct connection between the convergence in the lens models and the physical mass in the beam. Wong

et al. (2011) also find that the external shear from the fit does not always match the shear calculated from modeling the environment/LOS directly.

In practice, there can be several hundred galaxies projected within ~ 5 arcminutes of the main lens galaxy. We could use the full multiplane lensing formalism (Petters et al. 2001), but the multiplane lens equation is recursive, making this approach computationally infeasible. In our previous paper (McCully et al. 2014, hearafter M14), we derive a new hybrid analytic framework to model the mass in the environment/LOS. Our framework includes the multiplane, non-linear effects, but is also computationally efficient because we employ the tidal approximation for most of the LOS galaxies.

It is becoming clear that environment/LOS effects need to be taken into account, but there are still several open questions. Which lens galaxies are the most sensitive to environment/LOS effects? Is there a sample of "golden" lenses that we can study for which environment/LOS effects are unimportant? Which perturbers need to be included in our mass models? Some models do treat nearby perturbers exactly: for example, HE0435 has a neighbor (Kochanek 2006), MG0414 (Tonry & Kochanek 1999), RXJ1131 (Sluse et al. 2003), and B2114 (King et al. 1999) all have satellites that are presumably close enough to matter. However, typically the decision whether to include a neighbor galaxy is *ad hoc*. If we do decide to include the galaxy in our models, should we treat it exactly as a main (strong) lens plane, or is the tidal (weak lensing) approximation good enough?

In this work, we present a systematic approach to rank order which galaxies have the most important LOS/environment effects. We will also calibrate our new LOS framework using numerical simulations from Lensmodel (Keeton 2001) to quantify the level of detail required in environment/LOS models given precision lensing measurements.

In Section 5.2, we show the lens equation for a single perturbing galaxy, review our environment/LOS framework, and derive analytic expectations for the contribution of higher order terms. In Section 5.3, we outline the setup of the simulations used for this work to test our expectations for the higher order terms, then apply the framework to a set of toy

models that include only a single perturbing galaxy in Section 5.4.1. We then model more realistic, and therefore more complicated, mass models in Section 5.5 to calibrate our framework given typical observational uncertainties. We end by examining properties of main lens galaxies that make the systems more or less sensitive to environment/LOS effects.

Throughout this paper we assume a cosmology with $\Omega_M = 0.274$, $\Omega_\Lambda = 0.726$, and $H_0 = 71$ km s^{-1} Mpc^{-1}.

5.2 Analytic Background

In M14 we presented a hybrid framework for multi-plane gravitational lensing that fills the gap between using the full multi-plane lens equation (which can be computationally expensive) and treating everything as a simple external shear (which omits higher-order effects that can be significant for objects projected near the lens). The framework can handle any mixture of "main" planes (strong lenses) that are given full treatment and "tidal" planes (weak lenses) that are treated using the tidal approximation. Our framework can be used to calculate all of the standard lensing observables including the effects from environment/LOS galaxies. Using the analytic formalism developed in M14, we aim to numerically quantify the effects of non-linearity and higher order terms due to environment/LOS effects for multiply imaged systems.

We first illustrate the difference between the non-linear effects and the higher order terms in the multiplane lens equation. We return to the full multiplane lens equation from Petters et al. (2001):

$$\mathbf{x}_j = \mathbf{x}_1 - \sum_{i=1}^{j-1} \beta_{i,j} \boldsymbol{\alpha}_i(\mathbf{x}_i), \tag{5.1}$$

where $\boldsymbol{\alpha}_j$ is the deflection of the light ray in plane j and

$$\beta_{i,j} = \frac{D_{i,j} D_s}{D_j D_{i,s}}. \tag{5.2}$$

We examine the case with one main lens galaxy and one perturbing LOS galaxy. We

denote the deflection due to the main galaxy as $\boldsymbol{\alpha}_g$ and the deflection due to the perturber as $\boldsymbol{\alpha}_p$. It is useful to define the lensing potential as

$$\boldsymbol{\alpha} \equiv \nabla\phi. \tag{5.3}$$

If the perturbing galaxy is far from the lensed images, we can expand the potential as a Taylor series in offset, r. For a point mass, the lensing potential is given by

$$\phi_p = R_p^2 \ln|\boldsymbol{x} - \mathbf{r}| \tag{5.4}$$

where R_p is the Einstein radius of the perturber, $\boldsymbol{x}$ is the image position *in the redshift plane of the perturber*, and $\mathbf{r}$ is the position of the perturber. If we let $|\mathbf{x}| = x$, $|\mathbf{r}| = r$, and θ is the angle between the perturber and the image position as measured from the origin, then we can rewrite the potential using the law of cosines as

$$\phi = \frac{1}{2} R_p^2 \ln(r^2 + x^2 - rx\cos(\theta)). \tag{5.5}$$

If we assume that $x \ll r$, then we can expand the natural log as

$$\phi = R_p^2 \left[\ln(r) - \cos(\theta)\frac{x}{r} - \frac{1}{2}\cos(2\theta)\frac{x^2}{r^2} - \frac{1}{3}\cos(3\theta)\frac{x^3}{r^3} + \ldots\right]. \tag{5.6}$$

This expansion of the lensing potential for a perturbing galaxy can be extended beyond a point mass model as

$$\phi = \phi(0) + \alpha^i(0)x^i + \frac{1}{2}\Gamma^{ij}x^i x^j + \frac{1}{6}\mathcal{F}^{ijk}x^i x^j x^k + \ldots \tag{5.7}$$

where we have defined

$$\Gamma^{ij} \equiv \left.\frac{\partial^2\phi}{\partial x^i \partial x^j}\right|_{x=0} \tag{5.8}$$

and

$$\mathcal{F}^{ijk} \equiv \left. \frac{\partial^3 \phi}{\partial x^i \partial x^j \partial x^k} \right|_{x=0}. \tag{5.9}$$

Note that we have have adopted the Einstein sum notation, summing over repeated indices. Comparing terms to our expansion above, for a point mass, $\Gamma \propto \frac{R_E^2}{r^2}$ and $\mathcal{F} \propto \frac{R_E^2}{r^3}$.

For a single perturbing galaxy, the lens equation gives

$$\mathbf{x}_2 = \mathbf{x}_1 - \beta_{1\,2}\boldsymbol{\alpha}_1(\mathbf{x}_1) \tag{5.10}$$

and

$$\mathbf{x}_s = \mathbf{x}_1 - \beta_{1\,s}\boldsymbol{\alpha}_1(\mathbf{x}_1) - \beta_{2\,s}\boldsymbol{\alpha}_2(\mathbf{x}_2). \tag{5.11}$$

Combining these equations and recalling that $\beta_{i\,s} \equiv 1$, and setting $\beta \equiv \beta_{1\,2}$, we can write

$$\mathbf{x}_s = \mathbf{x}_1 - \boldsymbol{\alpha}_1(\mathbf{x}_1) - \boldsymbol{\alpha}_2\left(\mathbf{x}_1 - \beta\boldsymbol{\alpha}_1(\mathbf{x}_1)\right). \tag{5.12}$$

We now need to consider two cases: one with the perturber in front of the main lens galaxy and one with the perturber behind the main lens galaxy.

5.2.1 Background Perturber

We begin with the case when the perturbing galaxy is in the background. The first part of this discussion parallels Keeton (2003). We have $\boldsymbol{\alpha}_1 = \boldsymbol{\alpha}_g$ and $\boldsymbol{\alpha}_2 = \boldsymbol{\alpha}_p$. Substituting this into Eq. (5.12), we get

$$\mathbf{x}_s = \mathbf{x}_1 - \boldsymbol{\alpha}_g(\mathbf{x}_1) - \boldsymbol{\alpha}_p(\mathbf{x}_1 - \beta\boldsymbol{\alpha}_g(\mathbf{x}_1)). \tag{5.13}$$

Taylor expanding $\boldsymbol{\alpha}_p$, we get

$$x_s^i = x_1^i - \alpha_g^i(\boldsymbol{x}_1) - \alpha_p^i(0) - \Gamma^{ij}(x_1^j - \beta\alpha_g^j(\boldsymbol{x}_1)) - \frac{1}{2}\mathcal{F}^{ijk}(x_1^j - \beta\alpha_g^j(\boldsymbol{x}_1))(x_1^k - \beta\alpha_g^k(\boldsymbol{x}_1)) + \mathcal{O}(\boldsymbol{x}_1^4). \tag{5.14}$$

If we now remove the higher order terms in $\boldsymbol{\alpha}_p$ by truncating the Taylor series in $\boldsymbol{\alpha}_p$ at the first derivatives of $\boldsymbol{\alpha}_p$ (second derivatives of ϕ_p), which defines the "tidal approximation", and note that $\boldsymbol{\alpha}_p(0)$ corresponds to a constant deflection, which is unobservable, and write Γ^{ij} as a matrix $\boldsymbol{\Gamma}$, we get

$$\mathbf{x}_s = (\mathbf{I} - \boldsymbol{\Gamma})\mathbf{x}_1 - (\mathbf{I} - \beta\boldsymbol{\Gamma})\boldsymbol{\alpha}_g(\mathbf{x}_1) + \mathcal{O}(\mathbf{x}_1^3). \tag{5.15}$$

This equation looks very similar to the single plane lens equation, but with some multiplicative factors. In fact, if we multiply both sides by $(\mathbf{I} - \beta\boldsymbol{\Gamma})^{-1}$ from the left and define a scaled source coordinate $\mathbf{u}_{\rm eff} \equiv (\mathbf{I} - \beta\boldsymbol{\Gamma})^{-1}\mathbf{x}_s$, and define an effective shear as $(\mathbf{I} - \boldsymbol{\Gamma}_{\rm eff}) \equiv (\mathbf{I} - \beta\boldsymbol{\Gamma})^{-1}(\mathbf{I} - \boldsymbol{\Gamma})$, we get

$$\mathbf{u}_{\rm eff} = (\mathbf{I} - \boldsymbol{\Gamma}_{\rm eff})\mathbf{x}_1 - \boldsymbol{\alpha}_g(\mathbf{x}_1), \tag{5.16}$$

which is equivalent to the single plane lens equation with an external shear in the lens plane (see also Schneider 1997). We are allowed to rescale the source position because it is unobservable. Rescaling the source position does require us to also rescale the intrinsic luminosity of the source. However, we typically only measure the ratio of the fluxes of different images, which is insensitive to the absolute intrinsic luminosity of the source.

We now turn our attention to higher order terms, specifically the third order terms, $\mathcal{F}$. While all of the discussion above is general, at this point, we make some assumptions about the lens profiles for both the main lens galaxy and the perturbing galaxy. For the main lens galaxy, we assume a singular isothermal sphere (SIS). The deflection is equal to the

Einstein radius of the main lens:

$$\boldsymbol{\alpha}_g = R_E \hat{\boldsymbol{r}}. \tag{5.17}$$

We model the perturbing galaxy as a point mass, which is likely a good approximation as the perturbing galaxy is far from the image positions. We examine the perturbations to the observed image positions on the sky ($\boldsymbol{x}_1$) due to third order terms.

From above, for the second order terms,

$$\boldsymbol{x}_s = \boldsymbol{x}_1 - \boldsymbol{\alpha}_1(\boldsymbol{x}_1) - \boldsymbol{\alpha}_2(\boldsymbol{x}_2) = \boldsymbol{x}_1 - R_E\hat{\boldsymbol{r}} - \boldsymbol{\Gamma}\boldsymbol{x}_2 = \boldsymbol{x}_1 - R_E\hat{\boldsymbol{r}} - \boldsymbol{\Gamma}(\boldsymbol{x}_1 - \beta R_E\hat{\boldsymbol{r}}). \tag{5.18}$$

If we define $\boldsymbol{x}_1'$ to be the positions including the third order terms, we have

$$\boldsymbol{x}_s = \boldsymbol{x}_1' - R_E\hat{\boldsymbol{r}} - \boldsymbol{\Gamma}\boldsymbol{x}_2' - \frac{1}{2}\boldsymbol{x}_2\mathcal{F}\boldsymbol{x}_2. \tag{5.19}$$

Substituting in for $\boldsymbol{x}_2$, we have

$$\boldsymbol{x}_s = \boldsymbol{x}_1' - R_E\hat{\boldsymbol{r}} - \boldsymbol{\Gamma}\boldsymbol{x}_2' - \frac{1}{2}(\boldsymbol{x}_1' - \beta R_E\hat{\boldsymbol{r}})\mathcal{F}(\boldsymbol{x}_1' - \beta R_E\hat{\boldsymbol{r}}). \tag{5.20}$$

Subtracting Eqs. (5.20) and (5.18), and defining $\Delta_3\boldsymbol{x} \equiv \boldsymbol{x}_1' - \boldsymbol{x}_1$, gives

$$\Delta_3\boldsymbol{x} = \frac{1}{2}(\boldsymbol{x}_1' - \beta R_E\hat{\boldsymbol{r}})\mathcal{F}(\boldsymbol{x}_1' - \beta R_E\hat{\boldsymbol{r}}). \tag{5.21}$$

Now, if we assume spherical symmetry ($\theta = 0$) and that the positions of the multiple images are $\boldsymbol{x}_1' \approx \boldsymbol{x}_1 \approx R_E$, and take the magnitude of $\Delta_3\boldsymbol{x}$, we can substitute in

$$\Delta_3 x = |\Delta_3\boldsymbol{x}| = R_E^2\frac{R_p^2}{r^3}(1-\beta)^2. \tag{5.22}$$

Note that r here is the unlensed distance in the redshift plane of the perturber. To convert to offset as observed on the sky r', we use the lens equation to yield $r' = r - \beta R_E$. As the

perturbing galaxy is many Einstein radii away from the lens [2], $r' \approx r$. We will use $\Delta_3 x$ to characterize the strength of the third order terms in our simulations below.

$\Delta_3 x$ has the units of arcseconds. Physically this quantity corresponds to the perturbation of the image positions at the Einstein radius of the main lens. $\Delta_3 x \propto M$, implying that more massive perturbers have a larger effect as expected. The r^{-3} dependence shows that close perturbers are more important that distant perturbers, and the dependence on radial offset is much stronger than the dependence on the mass of the perturber.

5.2.2 Foreground Perturber

The foreground case is somewhat different. Now $\boldsymbol{\alpha}_1 = \boldsymbol{\alpha}_p$ and $\boldsymbol{\alpha}_2 = \boldsymbol{\alpha}_g$. Again, putting this into Eq. (5.12), we get

$$\mathbf{x}_s = \mathbf{x}_1 - \boldsymbol{\alpha}_p(\mathbf{x}_1) - \boldsymbol{\alpha}_g(\mathbf{x}_1 - \beta\boldsymbol{\alpha}_p(\mathbf{x}_1)). \tag{5.23}$$

Taylor expanding $\boldsymbol{\alpha}_p$, we write

$$x_s^i = x_1^i - \alpha_p^i(0) - \Gamma^{ij}x_1^j - \frac{1}{2}\mathcal{F}^{ijk}x_1^j x_1^k + \ldots - \alpha_g^i\left(x_1^i - \beta\alpha_p^i(0) - \beta\Gamma^{ij}x_1^j - \frac{1}{2}\mathcal{F}^{ijk}x_1^j x_1^k + \ldots\right). \tag{5.24}$$

Notice that in the foreground case, the Taylor expansion of $\boldsymbol{\alpha}_p$ appears *inside* the argument of $\boldsymbol{\alpha}_g$. Now truncating higher order terms, we can simplify this to

$$\mathbf{x}_s = (\mathbf{I} - \boldsymbol{\Gamma})\mathbf{x}_1 - \boldsymbol{\alpha}_g\left((\mathbf{I} - \beta\boldsymbol{\Gamma})\mathbf{x}_1 + \mathcal{O}(\mathbf{x}_1^3)\right) + \mathcal{O}(\mathbf{x}_1^3). \tag{5.25}$$

This looks similar to Eq. (5.15), but there is a key difference: instead of just having a multiplicative effect on the source position like the background perturber, the deflection from the foreground perturber enters the lens equation *inside the argument* of the deflection of the main galaxy. For a foreground perturber, there is no $\boldsymbol{\Gamma}_{\text{eff}}$ that we can define as with

[2] If this is not the case, both galaxies need to be treated exactly as main lens planes, not as perturbers.

the background perturber because $\mathbf{\Gamma}$ is inside the argument of $\boldsymbol{\alpha}_g$; thus the lens equation is not linear in $\mathbf{\Gamma}$ (see also M14). In principle, one can define a scaled coordinate based on the argument of the deflection to transform this equation to look like the standard lens equation (e.g., Schneider 1997; Keeton 2003). However, this requires care, as the new quantities do not correspond to the *observed* image positions that are typically used in lens modeling.

We now consider a similar analysis to that in Section 5.2.1 to define $\Delta_3 x$ and quantify the higher order terms for a foreground perturber. Using the same assumptions of an SIS main lens and a point mass perturber, we have

$$\boldsymbol{x}_s = \boldsymbol{x}_1 - R_E\hat{\boldsymbol{r}} - \mathbf{\Gamma}(\boldsymbol{x}_1 - \beta R_E\hat{\boldsymbol{r}}) \tag{5.26}$$

and

$$\boldsymbol{x}_s = \boldsymbol{x}_1' - R_E\hat{\boldsymbol{r}} - \mathbf{\Gamma}(\boldsymbol{x}_1 - \beta R_E\hat{\boldsymbol{r}}) - \frac{1}{2}\boldsymbol{x}_1\mathcal{F}\boldsymbol{x}_1. \tag{5.27}$$

This yields

$$\Delta_3\boldsymbol{x} = \frac{1}{2}\boldsymbol{x}_1\mathcal{F}\boldsymbol{x}_1. \tag{5.28}$$

In this case, the multiple images form at $\boldsymbol{x}_2 = R_E\hat{\boldsymbol{r}}$, implying that $R_E = \boldsymbol{x}_1 - \beta\mathbf{\Gamma}\boldsymbol{x}_1$. If we assume that $\mathbf{\Gamma} \ll 1$ (which applies if this is truly a perturbing galaxy and not a main lens galaxy), we can write $\boldsymbol{x}_1 \approx R_E\hat{\boldsymbol{r}}$, giving

$$\Delta_3 x = R_E^2\frac{R_p^2}{r^3}. \tag{5.29}$$

Note that in this case, r is the offset of the perturber as measured on the sky. This is the quantity we will use for calculating the contributions of higher order terms for perturbers in the foreground of the main lens. In the main lens plane, $\beta = 0$ and $\Delta_3 x$ is equal to the background case.

5.2.3 General LOS Framework

We now return to the LOS formalism that we developed in M14. The general expressions for the lens equation, magnification tensor, and time delay are as follows:

$$\boldsymbol{x}_i = \mathbf{B}_i \boldsymbol{x}_1 - \sum_{\ell \in \{\ell_\mu < i\}} \mathbf{C}_{\ell i} \boldsymbol{\alpha}_\ell(\boldsymbol{x}_\ell), \tag{5.30}$$

$$\mathbf{A}_i = \mathbf{B}_i - \sum_{\ell \in \{\ell_\mu < i\}} \mathbf{C}_{\ell i} \boldsymbol{\Gamma}_\ell \mathbf{A}_\ell, \tag{5.31}$$

$$T = \frac{1}{2} \boldsymbol{x}_s \cdot \mathbf{F}_s \boldsymbol{x} + \sum_{\ell \in \{\ell_\mu\}} \left[\frac{1}{2} \tau_{\ell s} \boldsymbol{x}_\ell \cdot \boldsymbol{\alpha}_\ell - \frac{1}{2} \boldsymbol{x}_s \cdot \mathbf{G}_{\ell s} \boldsymbol{\alpha}_\ell - \tau_{\ell s} \phi_\ell \right]. \tag{5.32}$$

This framework can be used to calculate the lensing effects for an arbitrary quantity and configuration of main and shear planes. Note that each main plane needs to be evaluated using the positions $\boldsymbol{x}_\ell$, which are not generally the same as the positions $\boldsymbol{x}_1$ on the sky and must be computed with the lens equation. This distinction gives rise to non-linearities that cannot be mimicked by a simple shear, which is an extension of the single foreground case discussed in Section 5.2.2. Our framework is efficient because the recursive sums only include main planes, but is more accurate than fitting a single simple shear. All of the shear planes—which may number in the hundreds for realistic lines of sight—can be compressed into the following matrices:

$$\mathbf{B}_j = \mathbf{I} - \sum_{i=1, i \notin \{\ell_\mu\}}^{j-1} \beta_{ij} \boldsymbol{\Gamma}_i \mathbf{B}_i, \tag{5.33}$$

$$\mathbf{C}_{\ell j} = \beta_{\ell j} \mathbf{I} - \sum_{i=\ell+1, i \notin \{\ell_\mu\}}^{j-1} \beta_{\ell i} \boldsymbol{\Gamma}_i \mathbf{C}_{\ell i}, \tag{5.34}$$

$$\mathbf{F}_j \equiv \tau_{j-1} \mathbf{B}_j - \tau_{j-1} \mathbf{B}_{j-1} = - \sum_{i=1, i \notin \{\ell_\mu\}}^{j-1} \tau_{is} \boldsymbol{\Gamma}_i \mathbf{B}_i, \tag{5.35}$$

$$\mathbf{G}_{\ell j} \equiv \tau_{j-1} \mathbf{C}_{\ell j} - \tau_{j-1} \mathbf{C}_{\ell\, j-1} = \tau_{\ell s} \mathbf{I} - \sum_{i=\ell+1, i \notin \{\ell_\mu\}}^{j-1} \tau_{is} \boldsymbol{\Gamma}_i \mathbf{C}_{\ell i}. \tag{5.36}$$

These matrices can be computed once at the start of any lens modeling analysis and stored for repeated use.

For a single main lens plane, the lens equation becomes

$$\mathbf{x}_s = \mathbf{B}_s\mathbf{x}_1 - \mathbf{C}_{\ell s}\boldsymbol{\alpha}(\mathbf{B}_\ell\mathbf{x}_1). \tag{5.37}$$

Note that $\mathbf{B}_\ell$ is in the argument of the deflection of the main lens galaxy, leading to non-linear effects that we quantify and explore using our numerical results in the following sections.

We will use our definitions of $\Delta_3 x$ above to quantify the strength of higher order terms. If $\Delta_3 x$ is small, the perturber is not important and can be treated using the shear approximation; if $\Delta_3 x$ is large, we must treat the galaxy exactly. In Section 5.5, we will use $\Delta_3 x$ and our realistic environment/LOS models to quantify which galaxies to treat exactly and which to treat using the tidal approximation. In general, these models are too complex to write down analytically, so we need a simple quantity like $\Delta_3 x$ to characterize the strength of a given perturber. Our first set of simulations will test if $\Delta_3 x$ accurately describes the contributions from higher order terms.

5.3 Simulations Setup

In the previous section, we presented analytic arguments about how we expect our new LOS framework to behave. Specifically, we defined the quantity $\Delta_3 x$ to characterize the strength of the higher order terms for a given galaxy. We now shift our focus to numerical simulations using our LOS framework. These results are complementary to the analytic results above, as the numerical simulations can capture significantly more complicated behavior. The parameters in the simulations are allowed to vary to find a "better fit" even if the fit parameters are farther away from the truth. We begin by examining "toy models" that contain a single perturbing galaxy. Our goal is to test if the scatter in the fitted parameters

is related to the perturbations in the image positions given by $\Delta_3 x$. In these simulations, we test the different terms in $\Delta_3 x$ separately, isolating their effects. We then study more realistic environment/LOS models that include ~ 300 galaxies, testing how different cuts on $\Delta_3 x$ affect their recovered lens parameters.

To test our new LOS framework, we use lensmodel (Keeton 2001) to generate Monte Carlo realizations of lensed image configurations. For each simulation, we use a fiducial main lens galaxy modeled as singular isothermal ellipsoid (SIE). We adopt $z_{lens} = 0.3$ and $z_{src} = 2.0$ as lens and source redshifts, respectively. Changing the lens or source redshifts does not change our qualitative results. The only difference comes from the β factors in $\Delta_3 x$. We initially use a fiducial main lens galaxy with an Einstein radius of $R_E = 1''$ and an ellipticity of $e = 0.3$. We then test the effects of selecting different R_E and e in Section 5.5.3.

We choose source positions from a magnification weighted distribution. This is a reasonable approximation of the magnification bias that is present in real observations (see Keeton & Zabludoff 2004). We integrate over the azimuthal position of the perturbing galaxy and the source positions as nuisance parameters. We use a sample of 300 quad and 300 double mock image configurations for each mass model.

In our Monte Carlo simulations, we use the full recursive lens equation given by Eq. (5.1), making no approximations to generate the mock data. We then fit the mock data using three different models for the environment/LOS, described below. We define our fiducial measurement uncertainties as 3 milliarcseconds in the positions of the main galaxy and each of the images, 5% in the flux, and 1 day in the time delay. These values are chosen to represent lenses targeted with some of the best current instruments like *HST* and monitoring campaigns like COSMOGRAIL (Eigenbrod et al. 2005). We use these uncertainties to define a χ^2 of the fit. We do not explicitly add scatter to the mock observed quantities here, although preliminary tests that include such scatter have a "floor" in the χ^2 and in the scatter in the recovered lens parameters. Otherwise these results are qualitatively

similar, so we do not present them here. We will revisit this question in a forthcoming paper (Wong et al. in prep.).

Throughout this analysis, we compare three models that treat the environment/LOS in different ways. The first model ignores the environment/LOS contribution, which we term the "None" model. The second model, the "Shear" model, accounts for the environment/LOS by fitting an external shear in the main lens plane (e.g., Suyu et al. 2013). The Shear model has two more free parameters than the None model. The last model we test uses our full LOS framework and is denoted as the "LOS" model. The LOS model has the same number of free parameters as the None model, two less than the Shear model.

It is important to note the number of constraints, so that we can compute the degrees of freedom for each model. Doubles image lens systems have the following constraints:

- 2 image positions (x & y)
- 1 time delay
- 2 fluxes
- Lens galaxy position (x & y)

giving a total of 9 constraints. Quad image configurations have:

- 4 image positions (x & y)
- 4 fluxes
- 3 time delays
- Lens galaxy position (x & y)

giving a total of 17 constraints.

Each of the models allow the following parameters to vary:

- Source position (x & y)

- Source flux
- h
- Einstein radius of the main lens galaxy
- Lens galaxy position (x & y).
- Lens galaxy ellipticity and orientation
- Lens galaxy power law index

for a total of 10 free parameters. The Shear model has two more free parameters that characterize the external shear: x and y pseudo-Cartesian components of the shear.

Double image configurations are under-constrained with -1 degrees of freedom (dof) for the None and LOS models and -3 dof for the Shear model. Quad image configurations have 7 dof for the None and LOS models and 5 dof for the Shear model.

We assume a weak Gaussian prior on the Hubble Constant: $h = 0.71 \pm 0.3$. Because doubles have fewer constraints than free parameters, the priors on the models play a very strong role in the fits. While the results from the fits from the double and quad image configurations are quantitatively different, they are qualitatively similar. Therefore, throughout our analysis we will focus on the results for quad image configurations. The models with a single perturbing galaxy are summarized in Table 5.1.

Because the Shear model has a different number of dof, care must be taken when comparing the results to the other models. For the single perturber "toy" models, we compare the distribution of the best fit values, scaling the χ^2 by the 95% confidence limit for number of dof for each model. For the realistic LOS simulations, we use the Monte Carlo Markov Chain (MCMC) method to marginalize over the fitted parameters, so the distribution of recovered lens properties is the proper marginalized, one dimensional posterior distribution. For the recovered lens quantities, rather than showing the full distribution, we present the median value of the fitted parameters and estimate the scatter by measuring half of the

Mock Lenses	Fits	dof	
Background: Exact $\mathbf{x}_s = \mathbf{x}_1 - \boldsymbol{\alpha}_g(\mathbf{x}_1) - \boldsymbol{\alpha}_p(\mathbf{x}_1 - \beta\boldsymbol{\alpha}_g(\mathbf{x}_1))$	LOS $\mathbf{x}_s = (\mathbf{I} - \boldsymbol{\Gamma})\mathbf{x}_1 - (\mathbf{I} - \beta\boldsymbol{\Gamma})\tilde{\boldsymbol{\alpha}}_g(\mathbf{x}_1)$	Doubles Quads	-1 7
	Shear $\mathbf{x}_s = (\mathbf{I} - \tilde{\boldsymbol{\Gamma}})\mathbf{x}_1 - \tilde{\boldsymbol{\alpha}}_g(\mathbf{x}_1)$	Doubles Quads	-3 5
	None $\mathbf{x}_s = \mathbf{x}_1 - \tilde{\boldsymbol{\alpha}}_g(\mathbf{x}_1)$	Doubles Quads	-1 7
Foreground: Exact $\mathbf{x}_s = \mathbf{x}_1 - \boldsymbol{\alpha}_p(\mathbf{x}_1) - \boldsymbol{\alpha}_g(\mathbf{x}_1 - \beta\boldsymbol{\alpha}_p(\mathbf{x}_1))$	LOS $\mathbf{x}_s = (\mathbf{I} - \boldsymbol{\Gamma})\mathbf{x}_1 - \tilde{\boldsymbol{\alpha}}_g((\mathbf{I} - \beta\boldsymbol{\Gamma})\mathbf{x}_1)$	Doubles Quads	-1 7
	Shear $\mathbf{x}_s = (\mathbf{I} - \tilde{\boldsymbol{\Gamma}})\mathbf{x}_1 - \tilde{\boldsymbol{\alpha}}_g(\mathbf{x}_1)$	Doubles Quads	-3 5
	None $\mathbf{x}_s = \mathbf{x}_1 - \tilde{\boldsymbol{\alpha}}_g(\mathbf{x}_1)$	Doubles Quads	-1 7
Background: LOS $\mathbf{x}_s = (\mathbf{I} - \boldsymbol{\Gamma})\mathbf{x}_1 - (\mathbf{I} - \beta\boldsymbol{\Gamma})\boldsymbol{\alpha}_g(\mathbf{x}_1)$	Shear $\mathbf{x}_s = (\mathbf{I} - \tilde{\boldsymbol{\Gamma}})\mathbf{x}_1 - \tilde{\boldsymbol{\alpha}}_g(\mathbf{x}_1)$	Doubles Quads	-3 5
	None $\mathbf{x}_s = \mathbf{x}_1 - \tilde{\boldsymbol{\alpha}}_g(\mathbf{x}_1)$	Doubles Quads	-1 7
Foreground: LOS $\mathbf{x}_s = (\mathbf{I} - \boldsymbol{\Gamma})\mathbf{x}_1 - \boldsymbol{\alpha}_g((\mathbf{I} - \beta\boldsymbol{\Gamma})\mathbf{x}_1)$	Shear $\mathbf{x}_s = (\mathbf{I} - \tilde{\boldsymbol{\Gamma}})\mathbf{x}_1 - \tilde{\boldsymbol{\alpha}}_g(\mathbf{x}_1)$	Doubles Quads	-3 5
	None $\mathbf{x}_s = \mathbf{x}_1 - \tilde{\boldsymbol{\alpha}}_g(\mathbf{x}_1)$	Doubles Quads	-1 7

Table 5.1 Summary of Monte Carlo mock lenses and fitted models. Quantities with a tilde are allowed to vary in the fits.

difference between the 16^{th} and 84^{th} percentiles. When plotting our results, we show the fractional changes in the fitted parameters to emphasize the variation.

5.4 Simulation Results

5.4.1 Single Perturber Toy Models

Our goal is to answer two main questions: when does the shear approximation break down (i.e., when are the higher order terms in the potential non-negligible?) and when are the non-linear effects in the lens equation significant? To begin, we examine the recovered lens model parameters to the perturbations in the image positions characterized by $\Delta_3 x$.

Throughout this section, we use a perturbing galaxy with of a mass of $10^{12} M_\odot$.

As discussed above, we expect that the mass of the perturbing galaxy, its projected offset from the main lens, and its redshift to affect its contribution to the higher order terms. If

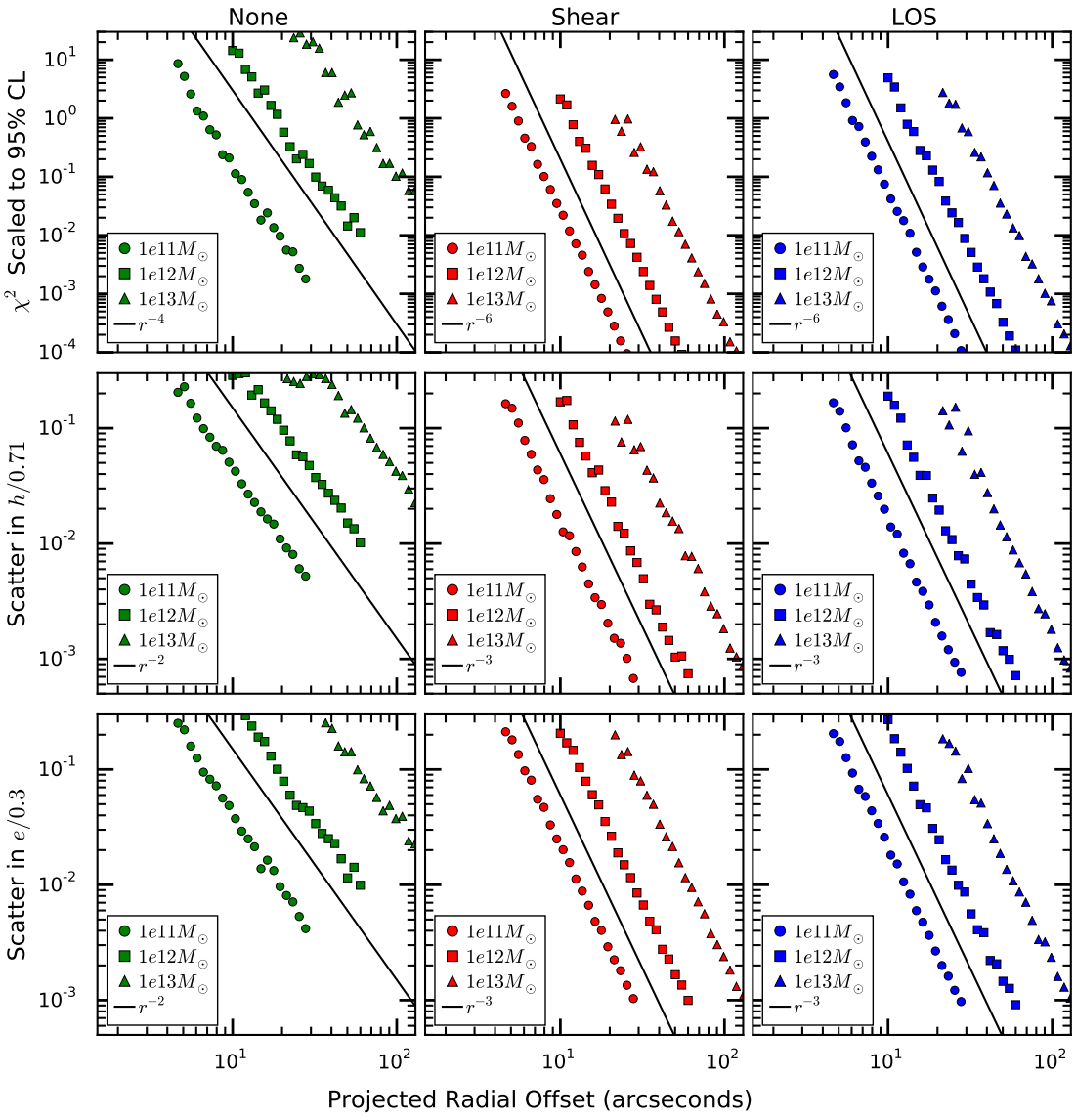

Figure 5.1 Fit parameters for single perturber models as a function of projected radial offset of the perturber. The perturbing galaxy is at the same redshift as the main lens galaxy ($z_{\rm lens} = 0.3$). Each column represents a different model: None, Shear, and LOS models, respectively. Each row shows the results for a different parameter: χ^2, scatter in the Hubble Constant, h, and scatter in ellipticity, e, respectively. Both the scatter and the χ^2 follow power laws in radial offset. Our expectations for the power law indices are shown in black for each of the parameters. The None models ignore even the second order terms so we expect the scatter to go as r^{-2} and the χ^2 as the square of the scatter r^{-4}. The LOS and Shear models omit third order terms and higher, so we expect the scatter to follow r^{-3} and the χ^2 to follow r^{-6}, respectively. Three decades of mass are shown for each of the models. In every case, the contribution due to higher order terms scales linearly with the mass.

the strongest constraints on χ^2 are from the image positions (as they often are), we might expect the χ^2 and scatter in the fitted parameters to follow the perturbations in the image

positions ($\Delta_3 x$). We begin by isolating the dependence on projected offset and mass. Figure 5.1 shows the χ^2 of the fits and the recovered values for the Hubble Constant, h, and the galaxy halo ellipticity, e, for a point mass perturber in the lens plane ($z_{\rm pert} = 0.3$) for the LOS, Shear, and None models described in Section 5.3.

In all of these models, the χ^2 increases as the perturber gets closer to the main galaxy and the higher order terms become more important. Both the χ^2 and the scatter approximately follow a power law. For the None models, the χ^2 and the scatter follow power laws of r^{-4} and r^{-2}, respectively. The None models ignore the perturber entirely, we are not even taking into account the shear that goes as $1/r^2$ consistent with the power law slope we find. The χ^2 goes as the square of the residuals which also agrees with the r^{-4} power law. For the Shear and LOS models, we do take into account the shear terms, but ignore third order (flexion) terms and higher. As such, $\chi^2 \propto r^{-6}$ and the scatter $\propto r^{-3}$ for the LOS and Shear models.

The next parameter of the perturber we consider is the halo mass. Figure 5.1 also shows the χ^2 and scatter in h and the ellipticity for three decades of mass for the None, Shear, and LOS models. For all masses, the power law indices are the same and the normalization of the power law is simply different by a factor of the mass. This follows our expectations as both the shear and flexion terms are $\propto M$. For more general mass models, the third order term in the potential goes as R_p^2/r^3 (recall for a point mass $R_p^2 \propto M$) and is what we use in our definition of $\Delta_3 x$.

The last characteristic of interest of the perturbing galaxy is its redshift. As for the analytic expectation, the redshift dependency is the most complicated of three. Fixing the mass of the perturber at $10^{12} M_\odot$, we grid over projected offset from the main lens galaxy to the perturbing galaxy and the redshift of the perturbing galaxy. We show the scatter in the Hubble Constant from the fits for the LOS models in Figure 5.2. When plotting the results, we use an asinh color scaling to illustrate the dynamic range of the variation. At large values, asinh acts like a logarithm, but at small values, it becomes linear. The asinh

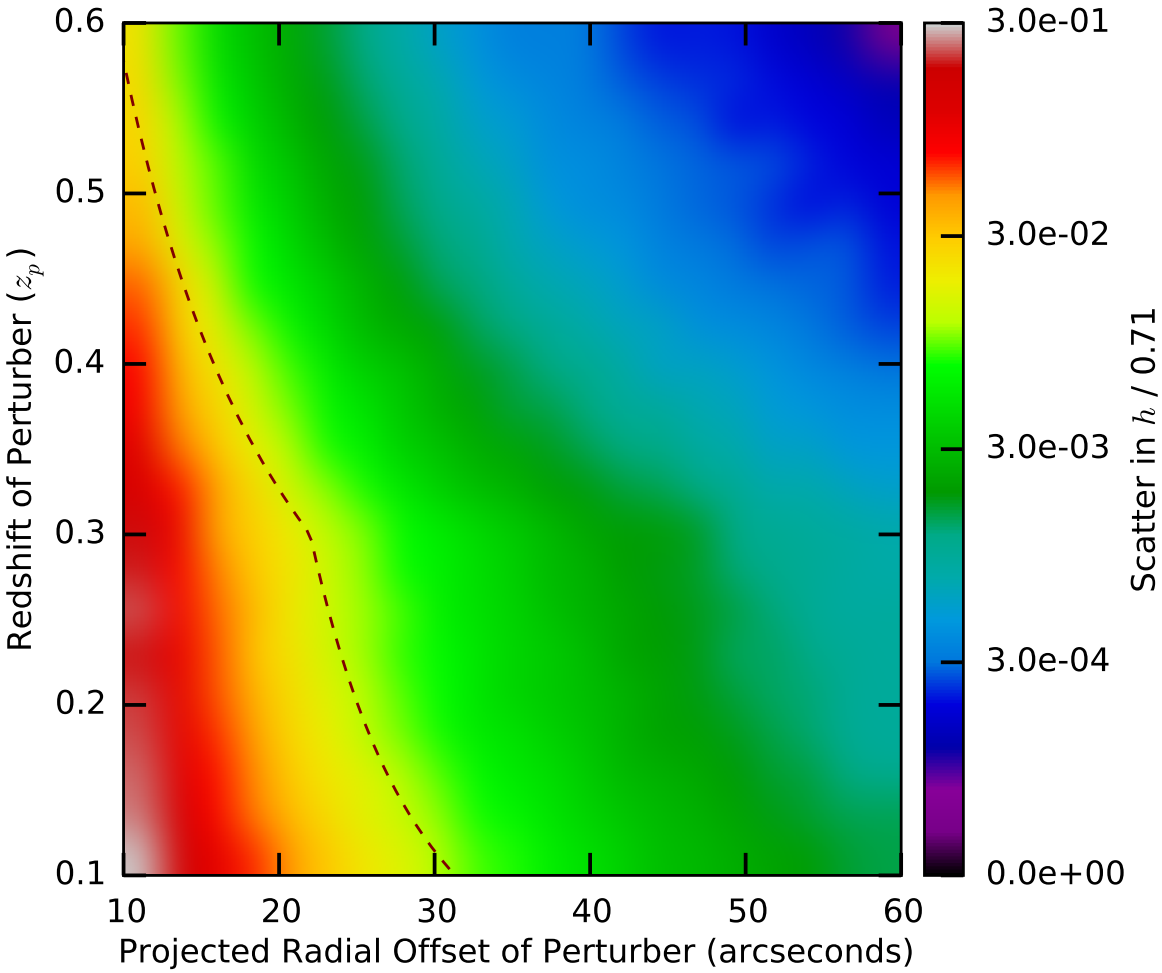

Figure 5.2 Scatter in the recovered Hubble Constant, h, for the LOS models scaled to the input value of $h = 0.71$ for quad images. The main lens has a redshift of $z_\ell = 0.3$ and the perturber has mass of 10^{12} $M_\odot$. We have overplotted a line of constant $\Delta_3 x$ that follows the lines of constant scatter in h.

is well defined for both positive and negative numbers and is conveniently antisymmetric. We find that perturbers behind the lens must be closer in projection than perturbers in the lens plane to have the same effect on the scatter in h. We have plotted a contour of constant $\Delta_3 x$, which nicely traces contours of constant scatter in the Hubble Constant, h. In the background, the effects of the point mass perturber are weaker because of the β factors in $\Delta_3 x$. In the foreground, the strength of the perturber increases as $z \to 0$ due to its increasing Einstein radius as $z \to 0$.

Now that we have justified each piece of $\Delta_3 x$ for a single perturber, we use $\Delta_3 x$ to

characterize the environment/LOS contribution for each of the galaxies in our realistic and more complex mass models in Section 5.5. However, it is first useful to use the single perturber simulations to build intuition about the differences between the different None, Shear, and LOS models.

5.4.2 Non-linearities in the LOS Framework

To isolate the effects of non-linearity, we use a second set of MC simulations to generate mock data under the tidal approximation from our LOS framework. We then fit the data either treating the perturber as an external shear (Shear Model) in the lens plane or ignoring it entirely (None Model). Like our first set of simulations, we consider a fixed perturber mass of $10^{12} M_{\odot}$, varying its position and redshift with respect to the main lens galaxy ($z_{\rm Lens} = 0.3$). We also do a sanity check by refitting the mock data with our environment/LOS framework to make sure that we recover our input parameters. In all cases, we do recover our input parameters with a perfect χ^2 of 10^{-8}.

Figure 5.3 shows the χ^2 values when the higher order terms are removed and only the non-linearity of the multiplane lens equation is taken into account. The models that include an external shear show a striking difference between the foreground and background perturbers. As argued in Section 5.2, the shear matrix of a foreground perturbing galaxy goes into the argument of the deflection angle making it impossible for the Shear model to mimic this effect. Figure 5.3 confirms that all of the non-linearity in the shear terms is from foreground perturbers. However, the fitted shear, even in the case of the background perturber, is fit in the lens plane, and is thus not the true shear in the redshift plane of the perturbing galaxy. The χ^2 of the None models, on the hand, follows a combination of the strength of the shear which gives a "suspension bridge" shape (Momcheva et al. 2006) and the foreground contributions seen in the Shear models.

The middle panels of Figure 5.3 show the scatter in h for models with the higher order terms removed. For the Shear models, the scatter in h is negligible in the background, but

can be tens of percent in the foreground. In the None models that ignore the perturber, the scatter in h can be biased high by as much as $\sim 35\%$ and follows the "suspension bridge" shape, similar to the χ^2.

The bottom panels of Figure 5.3 shows the scatter in the ellipticity, e, for the fits excluding higher order terms. The scatter from the Shear model peaks at $\sim 50\%$ and shows similar front to back difference as describe above. The None model has larger up to $\sim 100\%$ of the input e. Our interpretation of this scatter is that the model fit is trying to use the ellipticity to account for non-linear effects, but as the ellipticity is only a quadrapole, it cannot mimic these effects in general.

While these single perturber MC simulations only toy modles, we can still learn valuable lessons. The non-linear effects due to LOS structures are different between foreground and background perturbers. Background perturbers can in general be described by an external shear, whereas foreground perturbers cannot. The residuals due to higher order terms go as M/r^3 for a point mass perturber in the lens plane, which generalizes into $\Delta_3 x$. We now use this $\Delta_3 x$ parameter to characterize contributions to the LOS effects from realistic mass models that include ~ 300 galaxies. Simulations are the most natural tool to study these complex models, as a analytic solutions are impractical.

5.5 Realistic LOS

5.5.1 Fiducial Results

The toy models described above are useful to isolate and understand the effects of a single perturber. However, in reality lenses rarely have only one perturber. We need to employ more realistic lines of sight to quantify environment/LOS effects. One approach would be to choose beams from cosmological simulations (e.g., Hilbert et al. 2009; Collett et al. 2013; Jaroszynski & Kostrzewa-Rutkowska 2012, 2014). An alternate approach would be to use observations of real lens fields.

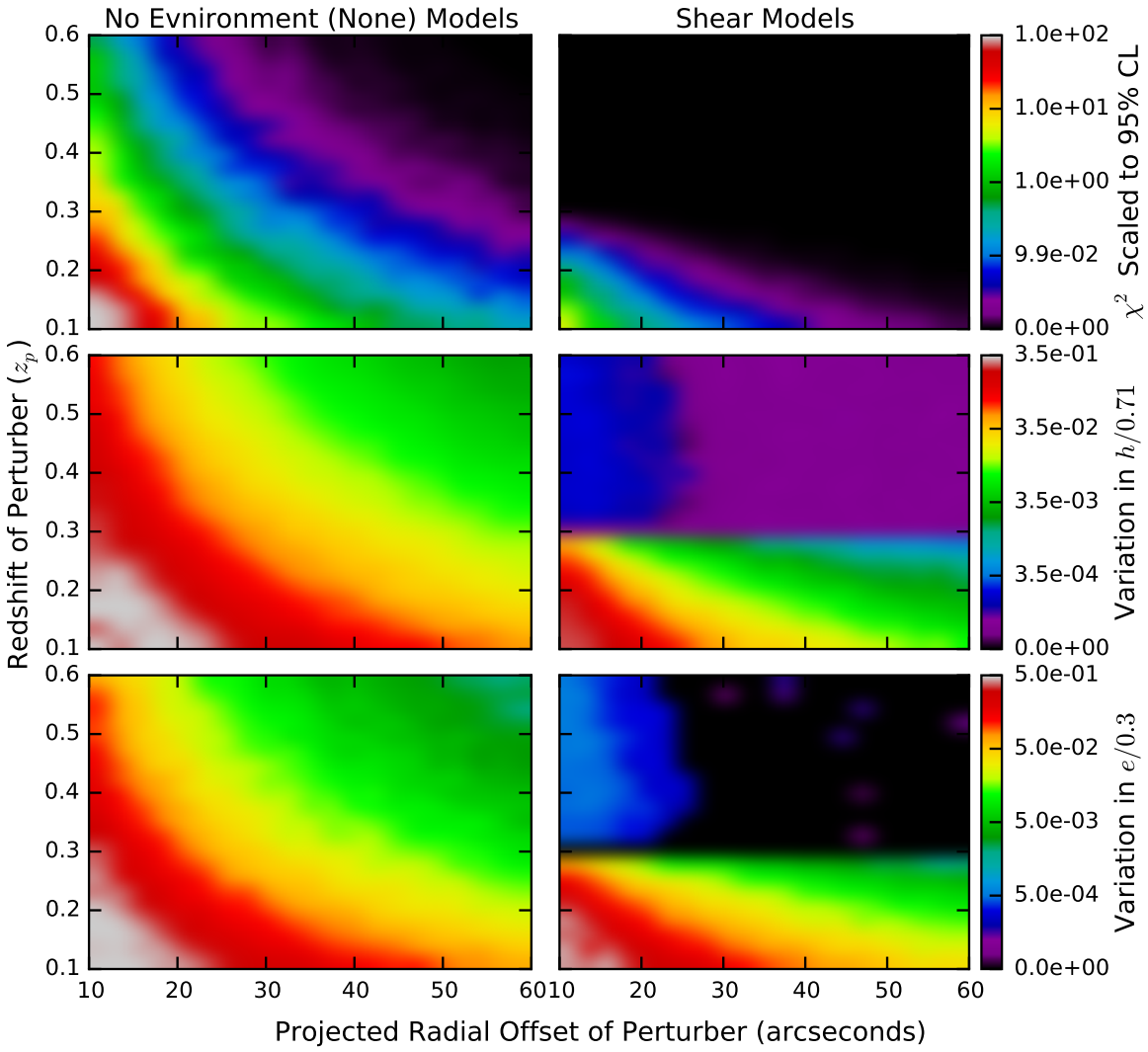

Figure 5.3 Fitted parameters for simulations that do not include higher order terms. The main lens has a redshift of $z_\ell = 0.3$ and the perturber has mass of 10^{12} $M_\odot$. For these models, we have taken out the higher order terms in the lensing potential by generating mock data to emphasize the differences between our environment/LOS framework and the traditional ways of accounting for the LOS. The None model contours look very similar to the previous simulations that included higher order terms. The Shear model results are strikingly different than in previous simulations: in the background, the Shear models have a χ^2 of effectively 0, whereas, in the foreground, the fits are much worse due to non-linear effects.

We take the latter approach. To analyze realistic environment/LOS mass models, we use our extensive spectroscopic and photometric data on several lens systems (Wong et al. 2011). We follow the method of Wong et al. (2011) to convert the observations into lensing mass models that include galaxies in any group surrounding the lens, a common dark matter halo

for that group, and all other individual galaxies along the LOS. The group halo is assumed to be an NFW profile (Navarro et al. 1996), and the mass is derived from the group velocity dispersion. The galaxies are modeled as truncated singular isothermal spheres with mass assigned using the Faber-Jackson relation (Faber & Jackson 1976). For this work, we are less focused on reproducing actual beams in the universe than on using plausible mass models to use to validate our methodology, calibrate the shear approximation, and test the fitted parameters for biases and scatter due to LOS/environment effects.

Real lens galaxies have many perturbers, typically ~ 300 out to $5'$ from the lens, but deciding which are important is not a simple problem. Our key concern is whether to treat each LOS galaxy exactly or using the shear approximation. We begin by using the field B0712+472 (hereafter B0712; Jackson et al. 1998) as a fiducial mass model to draw general conclusions about LOS effects for realistic beams. Note that B0712 does not have a group at the main lens redshift. We then test the robustness of our results by considering a field for which the main lens galaxy lies in a group (Section 5.5.2) and varying the properties of the main lens galaxy (Section 5.5.3).

Figure 5.4 illustrates $\Delta_3 x$ for the lens B0712. $\Delta_3 x$ generally increases near the center have a larger $\Delta_3 x$, but there is no radial cut that can be used to determine the importance of a perturber because perturber mass and redshift must also be taken into account. By following contours of constant $\Delta_3 x$, as illustrated in Figure 5.4, we can determine the effective radial offset for the perturber if it was in the main lens plane. Background perturbers are downweighted by $(1-\beta)^2$, so they must have a smaller projected offset to have the same effect as if it was in the main lens plane.

Figures 5.5 shows the recovered lens parameters for B0712. Our goal is to find the sweet spot in the middle that speeds up the modeling without introducing systematic uncertainties that are larger than the measurement uncertainties.

All models do poorly when none of the LOS galaxies are treated exactly. However, if we treat the closest few perturbers exactly (as shown by the histogram in the bottom of

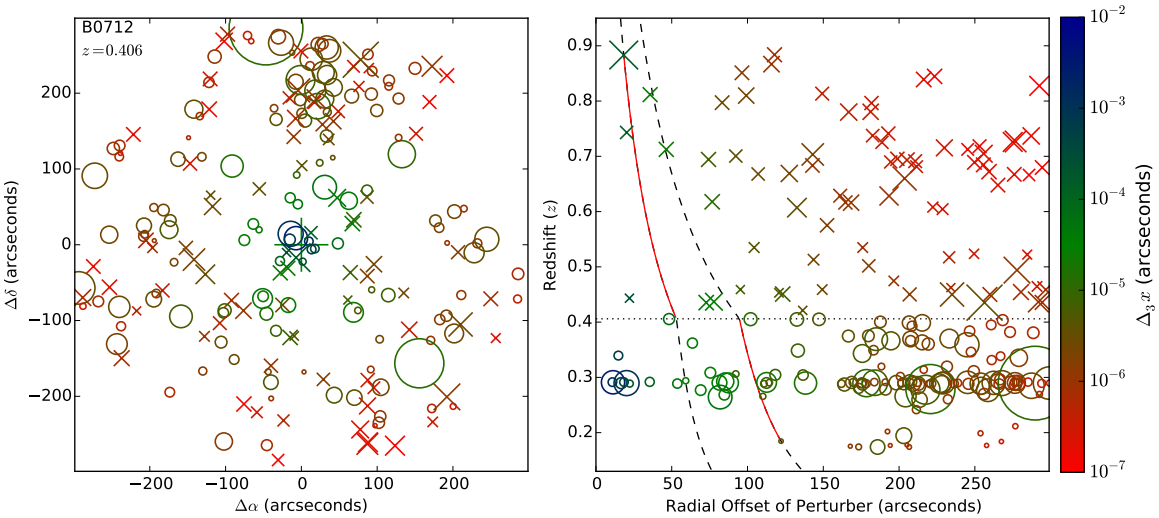

Figure 5.4 $\Delta_3 x$ for each of the components of the lensing mass model for B0712. On the left, each galaxy in the mass model is shown in projection on the sky. The areas of the points are proportional to the mass of the galaxy. The main lens redshift is indicated by the dotted line in the right panel. X's are behind the main lens galaxy, while the O's are in front of the main lens galaxy. The color of the points represents the strength of the higher order terms measured by $\Delta_3 x$. The right panel shows the same galaxies plotted in the r-z projection. Two $\Delta_3 x$ contours have been shown to guide the eye. The red section of the contour shows how to translate the perturbing galaxy to its effective distance if it was in the lens plane.

the panels), the bias and scatter become negligible in our LOS models. A cutoff of 10^{-4} arcseconds has negligible scatter in all of the recovered parameters. This cut leaves ~ 8 perturbers that need to be treated exactly out of the ~ 300 total, a factor of more than 10^3 increase in efficiency.

For all of the fitted parameters, models that ignore LOS galaxies do worse than the other models. Ignoring the LOS can lead to increased scatter and significant bias in the recovered parameters.

The Shear models perform better than the None models, but do not perform as well as our LOS models. In all of the parameters except χ^2, the Shear models have a larger bias and scatter in the recovered parameters than the LOS models. This can be a problem: if the χ^2 is low, it might appear that the fit is good, but the fitted parameters are not actually correct. Like the toy models in Section 5.4.1, the ellipticity has a large scatter likely due the model using it to try account for the perturbing galaxies.

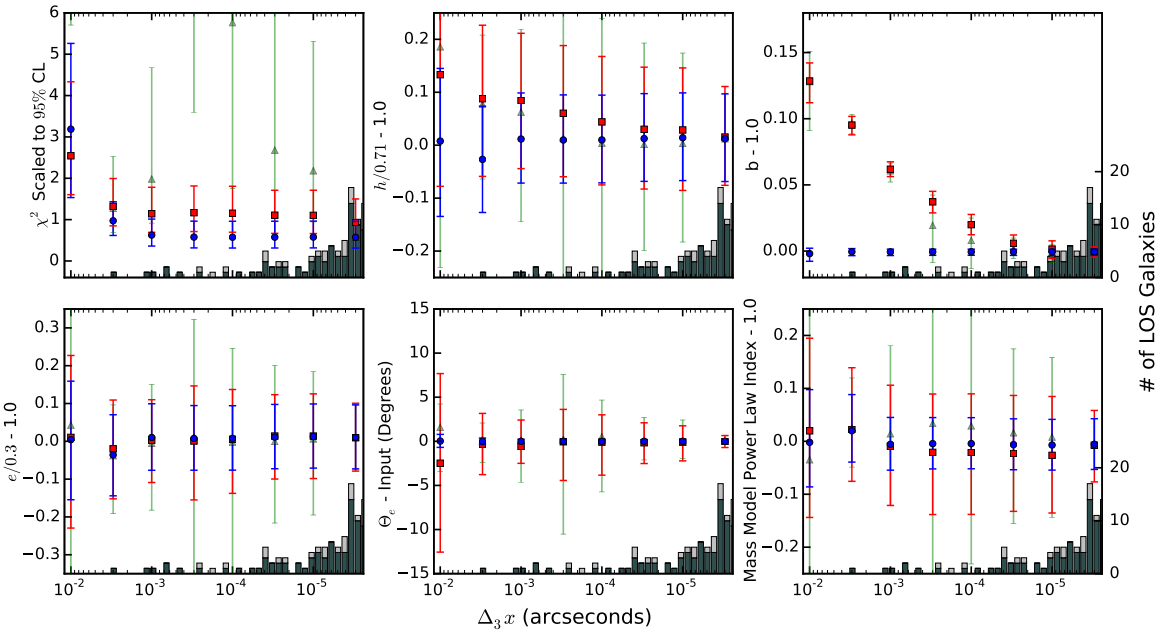

Figure 5.5 Recovered lens model parameters for the B0712 field. The LOS models are shown in blue, the Shear models in red, and the None models in green. We used MCMC to calculate the full posterior probability distribution. The errorbars have contributions from both measurement uncertainties and and scatter from varying source positions and orientations of the main lens. A histogram of LOS/environment galaxies is shown along the bottom with the axis labels on the far right. Dark grey bins correspond to perturbers in the foreground of the main lens, and the light grey bins correspond to background perturbers. The x-axis shows the cutoff in $\Delta_3 x$. Any galaxy to the left of a point is treated exactly as a main plane (strong lens), while everything to the right is treated according to the model: the None models ignore the environment, the Shear models fit only a simple shear, and the LOS models use our framework using the tidal approximation. The leftmost point corresponds to using the shear approximation for all galaxies. If we went all the way to the right (there are many galaxies beyond the edge of what is shown) all of the galaxies would be taken into account exactly. Note that moving to the right corresponds to taking galaxies into account exactly that are farther away from the main lens.

The orientation of the main lens galaxy does not show any bias for any of the models. We chose the position angle of the main lens galaxy uniformly from -$\pi/2$ to $\pi/2$. This implies that both the prior and posterior distributions of the main lens galaxy are unbiased. There is some scatter in the None and Shear models ($\sim 10°$), whereas the LOS framework models only show a scatter of $\sim 1°$.

One key point is that the fitted Einstein radii of the Shear and None models are both $\sim$ 15% higher than the input value. Taking a few close galaxies fully into account removes some

of the bias. This offset in the recovered Einstein radius is due to the cumulative external convergence from all of the perturbing galaxies. Because of the mass sheet degeneracy (Falco et al. 1985), convergence is typically not included in the Shear or None models. If the convergence is added, it is typically done in post-processing (Collett et al. 2013; Suyu et al. 2010). Our models explicitly include mass/convergence in the correct (i.e., measured) redshift plane, so our models are insensitive to this effect. Rather than treating shear and convergence separately, we build a physical model and then extract the shear and convergence from it. We favor this approach because the shear and convergence both arise from the same underlying mass distribution, i.e., they are not independent.

The total mass of the of the real lens system includes contributions from the LOS and the environment, so if we assign all of that mass to the single main lens galaxy, as in the Shear models, we will overestimate the true mass of the galaxy.

5.5.2 Different Fields

So far, we have only presented results for a single realization of a realistic distribution of galaxies. However, we would like for our qualitative results to be general, so we test our assumptions the about the lensing beam and main lens galaxy.

One of the simplest tests is to compare the results between two different fields. Using the same fiducial main lens galaxy ($R_E = 1$" and $e = 0.3$), we compare simulations for the B1422+231 field (hereafter B1422; Kundic et al. 1997b; Tonry 1998) shown in Figure 5.6 to B0712 shown in Figure 5.5. One of the key differences between these fields is that the main lens galaxy in B1422 is a a member of a group. We model the group halo as an NFW profile (Navarro et al. 1997, note that the group halo is also subject to our cuts on $\Delta_3 x$). The results from B0712 and B1422 are qualitatively similar. Quantitatively the deviations from the input parameters are worse for B1422 than B0712, confirming that the environment is more important for B1422. A detailed comparison across many different fields is beyond the scope of this paper, but we will briefly address this issue below and will revisit it later

(Wong et al., in prep.).

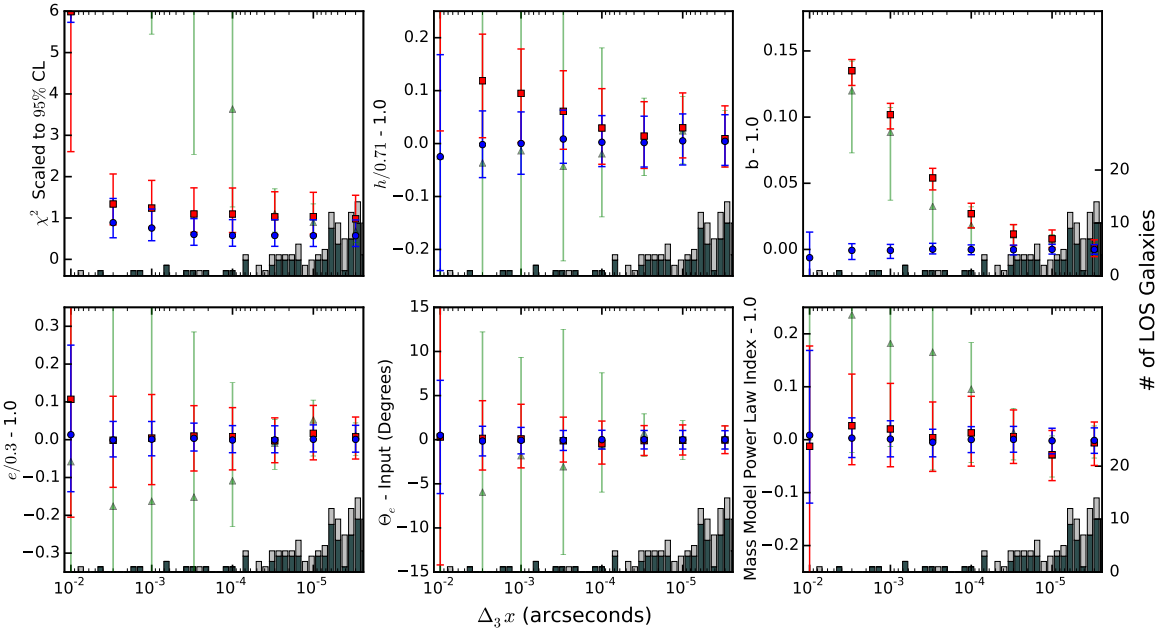

Figure 5.6 Recovered lens model parameters for the B1422 field, which includes a group of galaxies at the main lens redshift. Similar to Figure 5.5. The environment/LOS effects are stronger here than for B0712. Otherwise, the qualitative trends of the recovered parameters are the same between the two fields.

Figure 5.7 shows $\Delta_3 x$ for nine other actual multiply-imaged QSO fields from Wong et al. (2011). Not surprisingly, these fields are also very complex. There is not a simple radial cut that can characterize the contributions from higher order terms. There is striking diversity among the strength of the environments of the fields. The fields that have groups (a star at the position of the NFW halo, with group members shown as diamonds) tend to have more galaxies with a high $\Delta_3 x$. There is no a single universal number of galaxies that are important. Each field must be considered on an individual basis.

5.5.3 Varying the Main Lens Galaxy

We next explore how changing the ellipticity, e, or Einstein radius, R_E of the main lens galaxy affects our results. Figure 5.8 compares the results for $e = 0.1, 0.3, 0.5$. χ^2 decreases as the ellipticity increases, implying that the environment effects are weaker for more elliptical, asymmetric lens galaxies. To lowest order, the environment can be characterized with

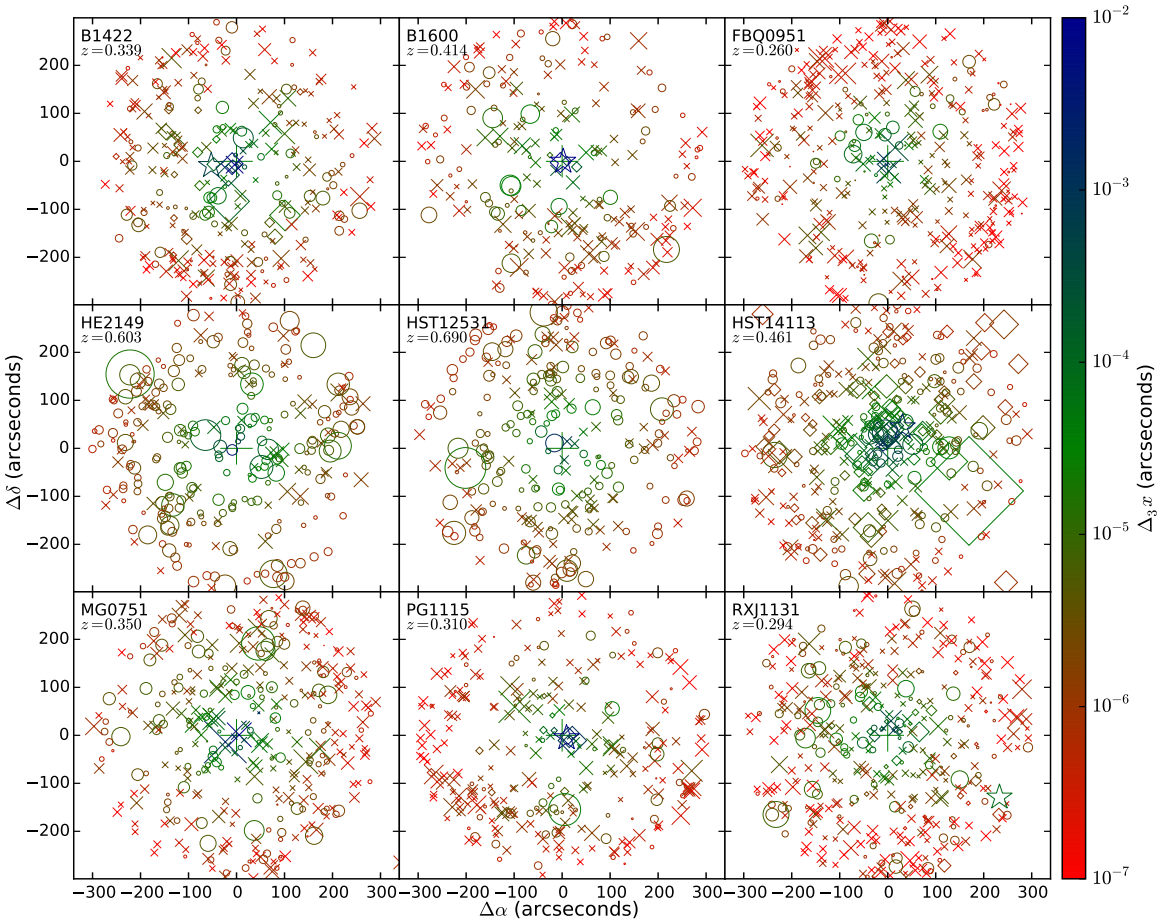

Figure 5.7 $\Delta_3 x$ for nine other fields. Similar to the left panel in Figure 5.4. Each galaxy in the mass model is shown in projection on the sky. The areas of the points are proportional to the mass of the galaxy. X's are behind the main lens galaxy, while O's are in the foreground, and the diamonds represent group members. The color of the points represents the strength of the higher order terms characterized by $\Delta_3 x$. There is dramatic variation in the LOS/environment strengths across the different fields. There is also no single projected radial cut that can be used across all of the fields.

a quadrapole (the shear approximation). Our results suggest that when the quadrapole due to the ellipticity is large, the LOS quadradpole is less important.

Regardless of the ellipticity, the Shear models overpredict the Hubble Constant. This effect is due to the mass sheet degeneracy, as the Shear models do not include convergence. Remarkably, as the e increases, the scatter in the recovered h values decreases. Part of this effect is due to the relative strength of the environment/LOS and internal quadrapoles as discussed above. However, there is also a second effect here. The relative precision that can be achieved in measurements of the Hubble Constant is directly proportional

to the fractional uncertainty in the time delay measurement. Therefore, if the fractional uncertainties in the time delays for two different lenses are the same, their precision in h will also be the same. However, as stated above, we do not assume a constant fractional uncertainty on the time delay, but an absolute uncertainty of one day, because the accuracy of the time delay is more related to the cadence of the observations than the length of the time delay. For highly elliptical, asymmetric lens configurations, the time delays are longer, as illustrated in Figure 5.9 (see also Witt et al. 2000). Assuming an absolute time delay uncertainty, longer time delays will have a smaller fractional uncertainty, leading to stronger constraints on the Hubble Constant.

As with the Hubble Constant, as e increases, the scatter in the recovered e decreases. As the asymmetry of the lens increases, there a few possibilities. Either the absolute value of the scatter remains unchanged while e increases or the image configurations can only be produced for a smaller range of lens models, leading to stronger constraints on e.

A second key parameter of the main lens galaxy is the Einstein radius, R_E (the mass of the lens galaxy). Figure 5.10 shows χ^2, h, and the scatter in e for different values of R_E. As R_E decreases, so do the environment/LOS effects. We can understand this effect by looking at the definition of $\Delta_3 x \propto R_E^2$. If we assume that the positions of the environement/LOS galaxies are fixed, their contribution to the lensing goes down as R_E decreases. The environment/LOS galaxies are more Einstein radii away from the main lens galaxy for smaller lenses.

However, there is a trade-off. The lens with the smaller R_E will have a shorter time delay, leading to a weaker constraint on the h as described above. All of these tests show that our qualitative results are general for a variety of lens parameters.

LSST will find an immense number of new strong lens systems. There are a variety of strategies on how to use this upcoming dataset for cosmology. One possibility is to use all of the lenses to beat down the uncertainties using statistics. However, if we are entering the systematics-dominated regime, this approach will be limited unless one can

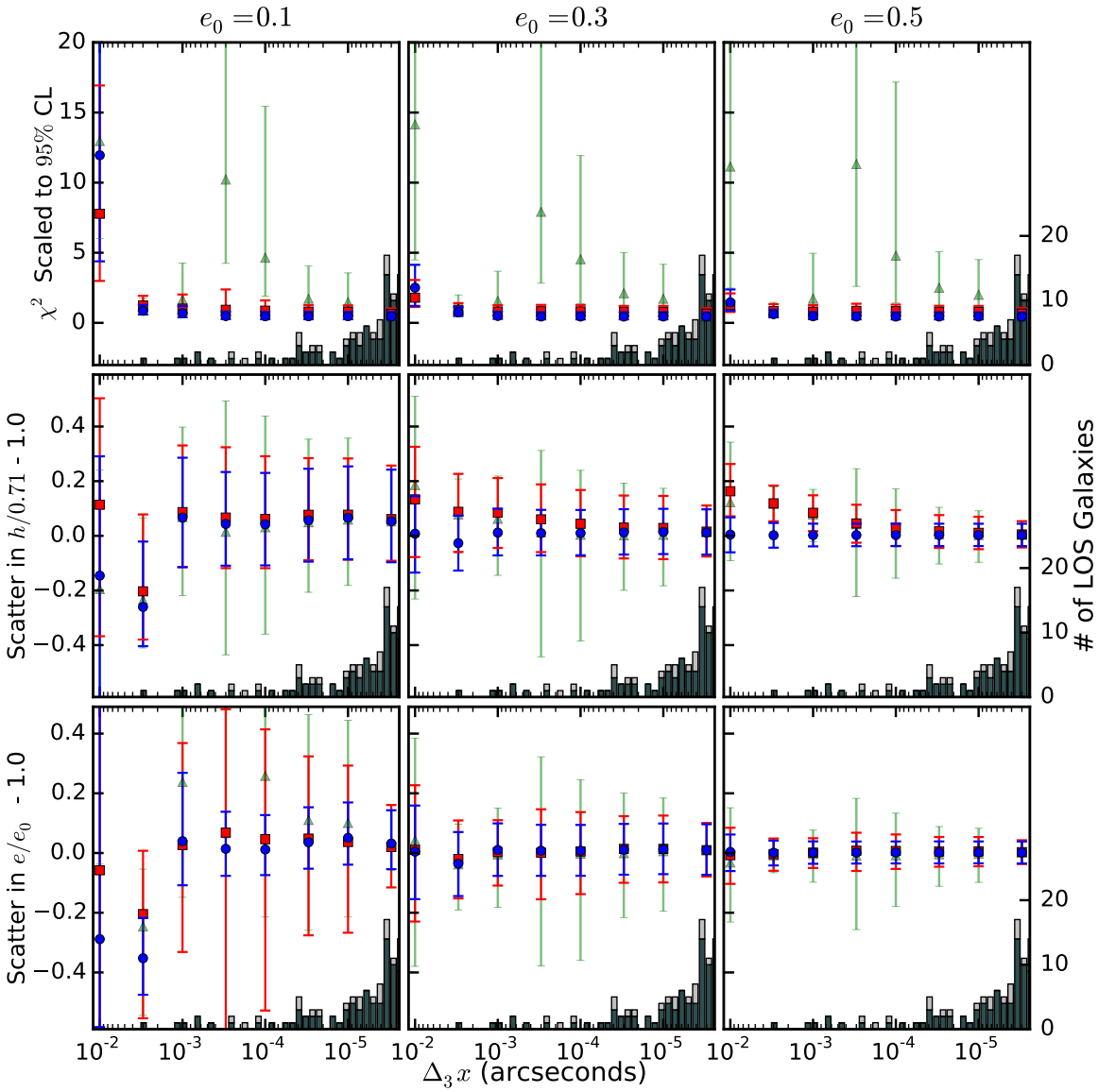

Figure 5.8 Recovered lens parameters for main lens galaxies with different ellipticities for the B0712 field. Each column corresponds to $e = 0.1, 0.3, 0.5$, respectively. Systems with larger e have better χ^2 and less scatter in the Hubble Constant.

account for the systematic uncertainties (e.g., with our LOS framework). Another strategy is to use the large number of lenses discovered by LSST to search for a few rare, "golden" lenses, whose systematic uncertainties are small. One possible criterion for a "golden" lens could be to have a have weaker environment/LOS effects (see Figure 5.7). Based on our analysis above, to minimize environment/LOS effects, we search for lenses with a small R_E, but high e. Smaller R_E will make the lens less sensitive to the environment, but we

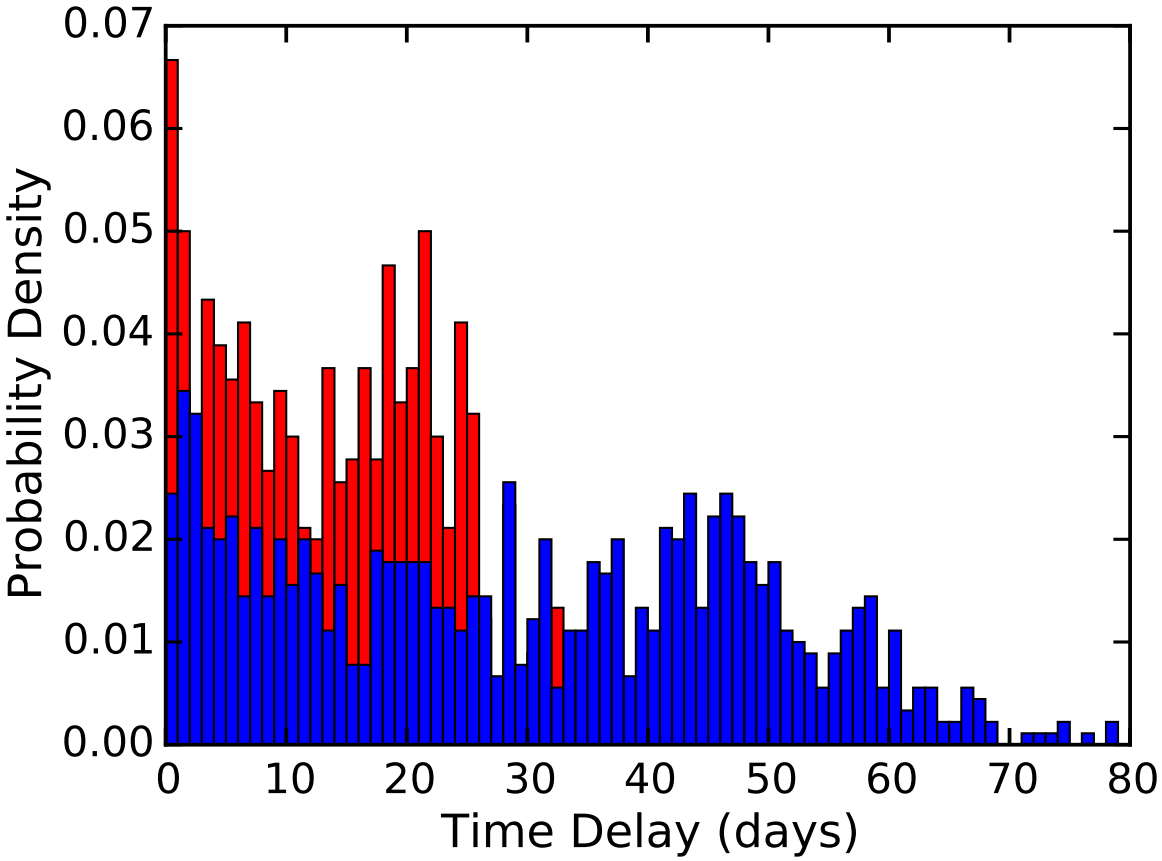

Figure 5.9 Time delay distributions for lens galaxies with different ellipticities. The red histogram shows the time delays for $e = 0.3$ while the blue shows the distribution for $e = 0.5$. Assuming a constant absolute uncertainty on the time delay implies that more elliptical, asymmetric lenses will have a smaller fractional uncertainty on the time delay leading to stronger constraints on h.

also need high-quality time delay measurements. Assuming an absolute uncertainty of a day (which may or may not be a good assumption) suggests that our strongest constraints on the Hubble Constant will come from systems with long time delays, like those from highly elliptical, asymmetric systems. The strong quadrapole due to the ellipticity would also dominate the quadrapole from the environment/LOS, further reducing the contribution of environment/LOS effects to lensing observables. While suggestive, these results merit further investigation to get the most out of future surveys like LSST.

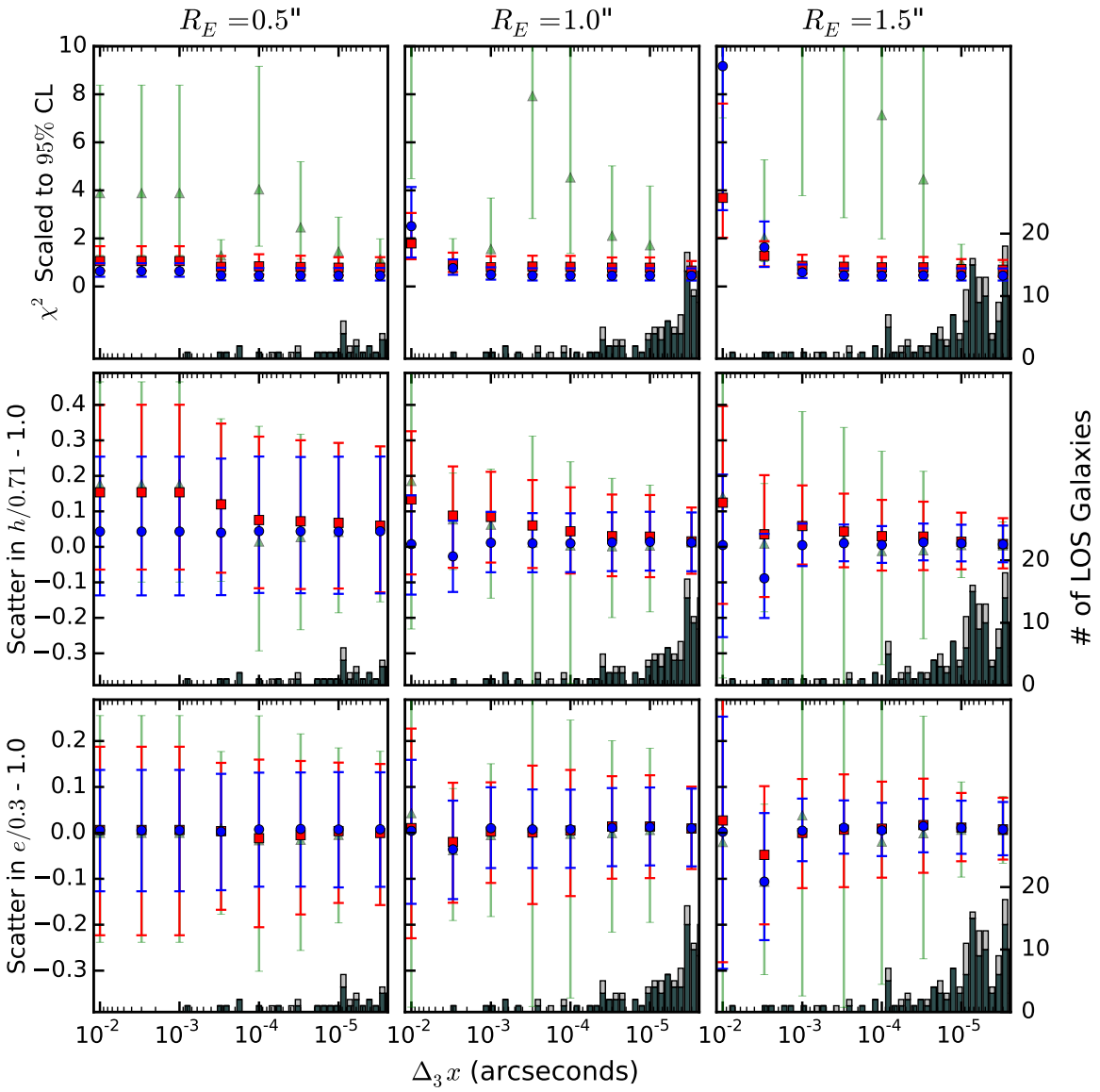

Figure 5.10 Recovered lens parameters for main lens galaxies with different Einstein radii for the B0712 field. Similar to Figure 5.8. Each column corresponds to a different Einstein radius $R_E = 0.5, 1.0, 1.5$, respectively. The systems with a smaller R_E have smaller χ^2 but more scatter in the Hubble Constant. The larger scatter is due to the shorter time delays leading to a larger fractional uncertainty, which directly translates into a weaker constraint on the Hubble Constant.

5.6 Conclusions

As our lensing data improve, it becomes more important to take into account systematic effects like the perturbations due to galaxies in the environment and along the LOS. Our results show that if we want to do "precision lensing", the environment/LOS cannot be

ignored. Environment/LOS effects can lead to systematics in h up to $\sim 10\%$.

We present numerical simulations of galaxy lenses using our new environment/LOS framework. The framework is a computationally efficient way to calculate the lens equation, using the shear approximation for most perturbers instead of doing the full recursive multi-plane lens equation. We test our framework using a single perturber to study where the shear approximation is not valid and where non-linear effects are important. The scatter in the fitted parameters follows the perturbations in the image positions due to higher order terms, characterized by $\Delta_3 x$. The Shear models that fit the environment/LOS as an external shear, can accurately account for a perturbing galaxy behind the main lens, but foreground perturbers can not be mimicked by an external shear in the lens plane. We apply this formalism to realistic fields based on Wong et al. (2011) and find that our environment/LOS framework can reproduce the fitted lens properties without bias and with a scatter that is smaller than typical measurement uncertainties. None models, that ignore the environment/LOS, and Shear models both have larger scatter in the recovered parameters of the fit and a bias of $\sim 10\%$ in the inferred Einstein radius of the main lens galaxy. This bias is likely due to the convergence of perturbing galaxies that is ignored in these models but is accounted for properly in our LOS framework. There is no universal radial cut that can be used to determine the importance of a perturber because perturber mass and redshift are also important. Using a cut of $\Delta_3 x$ of ~ 0.01 times the uncertainty in the lensed image positions is sufficient to recover all of the lens parameters without introducing extra systematic uncertainties for all of the observed fields tested here.

Our framework can account these perturbing galaxies in an efficient and effective way; the scatter and bias from our LOS framework compared to the full recursive multi-plane lens equation are negligible. Our test validate our new framework, which can be the foundation for more detailed modeling of the lens environment and LOS for strong lensing.

Our simulations here are limited to test the scatter and bias introduced by the framework itself. There is also uncertainty in generating the environment mass models. This source of

noise will be explored in a forthcoming paper (Wong et al., in prep.).

Chapter 6

Conclusions

6.1 Ongoing Work

6.1.1 SNe Iax

We have presented observations focusing on three prototypical SNe Iax. Our late time observations of SN 2005hk and SN 2008A suggest that these explosions leave a bound remnant. While some explosion models match some of the properties of SNe Iax, no model has made predictions for what to expect for observations of the bound remnant. This will be key to understanding the origin of these SNe.

Our detection of a coincident source in the pre-explosion image of NGC 1309, the host galaxy of the SN Iax 2012Z, is an important piece in the puzzle of the progenitor systems of SNe Iax. We present a variety of possibilities for the future of the star we detected. If SNe Iax are core collapse SNe and we observed the star that exploded, it should disappear in future observations. If instead, it is the companion star of an exploding white dwarf, it is consistent with the properties of a helium star. This would mark the first detection of a companion star for a white dwarf SN. The last possibility is that the source is physically unassociated with the SN. Further observations will help us to distinguish these different scenarios, although distinguishing between the last two possibilities may be difficult if the interaction of the SN with the companion star doesn't produce an observable signature.

We have recently proposed to expand the wavelength coverage we have on SNe Iax; we have obtained near-UV spectroscopy of SN 2013dh, a SN Iax, using *HST*/STIS, shown in Figure 6.1. Both the models and hints in the data point to the ultraviolet as a key window

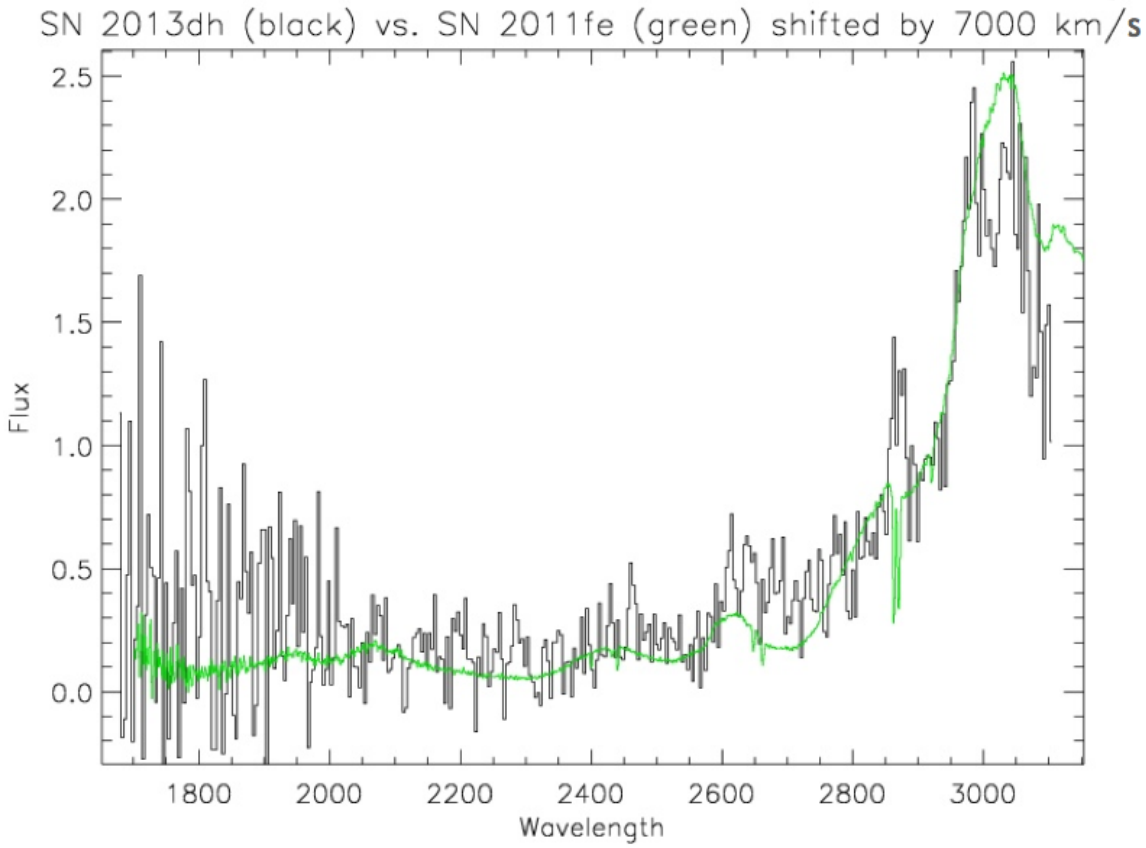

Figure 6.1 Near UV spectrum of the SN Iax 2013dh compared to the normal SN Ia 2011fe taken with *HST*/STIS, GO-12973, PI: C. McCully. Figure courtesy of R. Foley.

into sorting out these questions. Because of the high metal opacity, the UV emission comes from the outermost layers of the ejecta, and is therefore a useful place to look for a signature of the progenitor system. Data also provide a clear signal that the path to understanding these peculiar supernovae goes through the UV. Milne et al. (2010) used the Swift UVOT instrument to measure near-UV photometry for several normal SNe Ia as well as 02cx-like SN 2005hk and SN 2008A (Figure 6.2). Curiously, the Swift photometry shows that near maximum light SN 2008A was nearly as bright in the UV as normal SNe Ia, even though it was more than a magnitude fainter than normal SNe Ia in B and V. Moreover, the UV photometry for SN 2005hk and SN 2008A show them to peak earlier and evolve more rapidly than normal SNe Ia. We have just began the analysis of this data and look forward to the lessons we learn about SNe Iax.

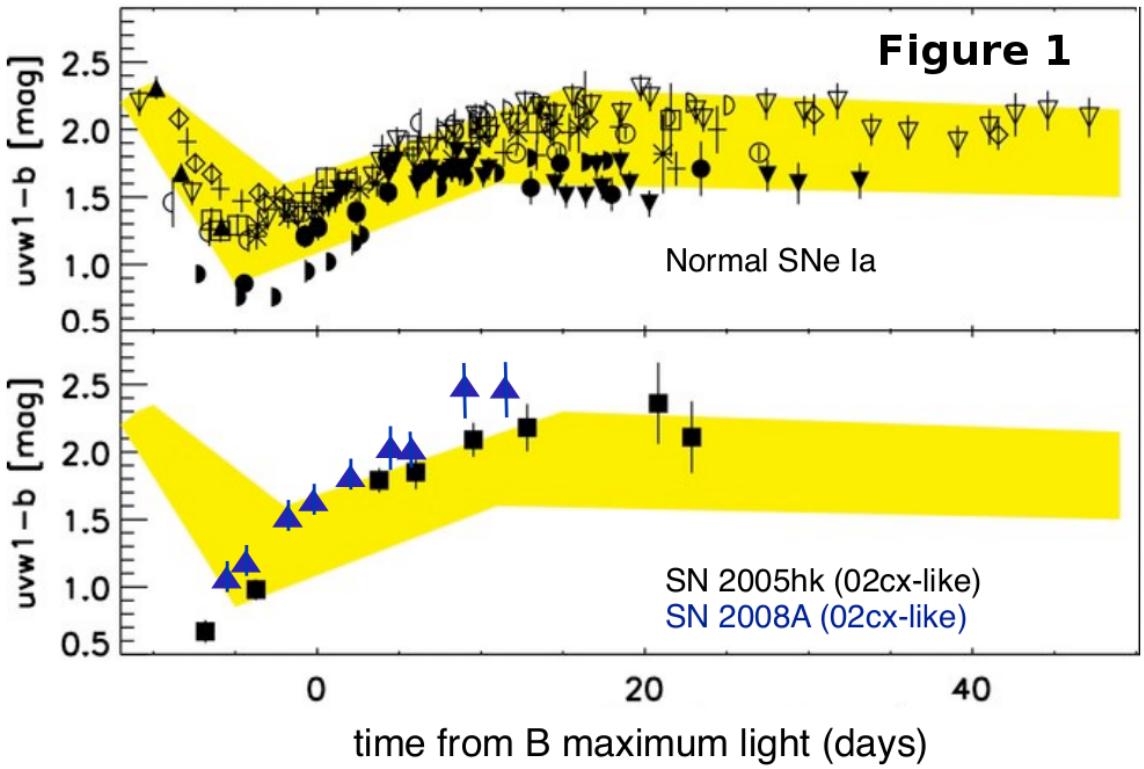

Figure 6.2 Figure adapted from Milne et al. (2010). UV-optical color evolution for SN 2005hk and SN 2008A from data taken with the Swift/UVOT instrument. The yellow band shows region of the color evolution of normal SNe Ia. Normal SNe Ia follow evolutionary tracks along the band: i.e. blue (red) objects tend to remain blue (red) compared to the normal color evolution. Note that SN 2005hk and SN 2008A both cross from the blue end of the band to the red end of the band, evolving much more dramatically than normal SNe Ia.

6.1.2 LOS Effects in Gravitational Lensing

As discussed in Chapter 4, the external convergence due to the mass sheet degeneracy is one of the largest outstanding uncertainties in using time delays to constrain the Hubble Constant or dark energy. One way to account for the external convergence is to apply the convergence correction in post-processing. In Chapter 4 we derive the effective convergence that should be used for these corrections. Another method is to use full 3D mass models like those described in Chapter 5. We have shown that our new methodology is robust and accurately reproduces the true lens parameters in a self consistent and unbiased way. A third alternative is described below.

Now that we have shown that our LOS framework is robust, we can turn our attention to the uncertainties in generating the LOS mass models. One of our goals is to quantify the possible precision in measuring the Hubble Constant from time delays. We also look to explore how well future surveys like LSST will be able to constrain cosmology with strong lensing and if certain gravitational lenses are less sensitive to systematic uncertainties than others. Even if these "golden" lenses are rare, LSST will discover so many strong lenses that we should have enough golden lenses to place strong constraints on cosmology.

6.2 Gravitationally Lensed SNe Ia

While both SNe Ia and gravitational lensing have been extremely successful cosmological probes, with the advent of "time domain astronomy", we have the opportunity to combine these probes and learn about the dark components of the Universe by studying gravitationally lensed SNe Ia. We begin by treating gravitational lensing as systematic uncertainty in the derived distance for SN Wilson, the highest redshift SN Ia discovered to date, presented in Jones et al. (2013). We will then discuss the exciting prospects of using lensed SNe Ia as cosmological probes.

6.2.1 Bias in SNe Ia Distances Due to Magnification from Lensing

Our ability to use SNe Ia as accurate distance indicators to constrain cosmological parameters requires a precise measurement of the intrinsic luminosity of the SN. Even without multiple images, gravitational lensing can significantly magnify the SN confounding our ability to measure the correct intrinsic luminosity of the source. In Jones et al. (2013) we present SN Wilson from the CANDELS survey, the highest redshift SN Ia ever discovered, $z = 1.91$. It is an important object to have on the Hubble Diagram to constrain dark energy, so it is important to estimate any systematic bias on the derived distance like magnification due to lensing.

Gravitational lensing as discussed above occurs when light from a high redshift source

passes close in projection to mass on the line of sight. As lensing requires good alignment between the source and the lensing mass, large magnifications of ~ 2 or more are rare. However, SN Wilson is close in projection to another galaxy separated by only 1.54" warranting more detailed lens modeling to estimate any bias due to magnification.

We use the Spectral Energy Distribution (SED) fitting technique as described in Wiklind et al. (2008) to characterize the physical properties of the candidate lens galaxy. To account for photometric uncertainties, we draw Monte Carlo samples for the measured photometry of the galaxy and measure the best fitting SED model to characterize SED distribution. The SED fit suggests a low mass galaxy with a photometric redshift of $z = 0.283 \pm 0.080$ and a stellar mass $\log(M_\star) = 7.968 \pm 0.222$. We use these parameters to create a plausible mass model of the galaxy to estimate the possible magnification of the SN.

To model the stellar component, we fit the HST I band image using GALFIT (Peng et al. 2010). The galaxy is well fit by an inclined exponential disk model with a mass distribution given by $\kappa(\xi) = \kappa_0 q^{-1} e^{-\xi/R_s}$ where $\xi = \sqrt{x^2 + y^2/q^2}$ is the ellipse coordinate in the major axis frame with minor to major axis ratio q. The total mass of the disk $M_\star$ is related to $\kappa_0 = qM_\star/(2\pi\Sigma_{cr}R_s^2)$ where Σ_{cr} is the critical surface mass density for lensing. Σ_{cr} is defined in terms of the angular diameter distances to the source D_s, the lens D_ℓ, and between the lens and the source $D_{\ell s}$ as $\Sigma_{cr} = (c^2 D_s)/(4\pi G D_{\ell s} D_\ell)$. The best fitting model from galfit ($\chi^2/\nu = 0.961$) has a minor to major axis ratio of $q = 0.41$ and a scale length of $R_s = 0.2895$".

Presumably, the stellar component of the galaxy is embedded in a dark matter halo which we model as using a Navarro, Frenk, and White (NFW) profile (Navarro et al. 1997) with

$$\rho = \frac{\rho_s}{(r/r_s)(1 + r/r_s)^2}. \tag{6.1}$$

Lensing due to an NFW profile is typically parametrized using $\kappa_s = \rho_s r_s/\Sigma_{cr}$ and r_s (Bartelmann 1996). These parameters can be written in terms of the virial mass, M_v, and the

concentration of the halo. The concentration is defined as the ratio of the virial radius to the scale radius: $c_v = r_v/r_s$. We can define the virial mass as

$$M_v = \frac{4\pi}{3}\Delta_c \rho_c r_v^3 \tag{6.2}$$

(Coe 2010) where $\rho_c = 3H^2/8\pi G$ is the critical density of the universe and $\Delta_c \approx 18\pi^2 - 82\Omega_\Lambda - 39\Omega_\Lambda^2$ (Bryan & Norman 1998) is the overdensity of required for collapse of a halo. The critical density of the universe ρ_c is written in terms of the Hubble rate which for a flat universe is given by $(H/H_0)^2 = \Omega_\Lambda + \Omega_m(1+z)^3$.

By requiring that our above definition of the viral mass be consistent with the mass calculated by integrating an NFW density profile we find that

$$\frac{\rho_s}{\rho_c} = \frac{\Delta_c}{3}\frac{c_v^3}{\ln(1+c_v) - c_v/(1+c_v)} \tag{6.3}$$

(Navarro et al. 1996). Using these relations, we can rewrite κ_s and r_s in terms of the mass and concentration as

$$r_s = \frac{1}{c_v}\left(\frac{2GM_v}{\Delta_c H^2}\right)^{1/3} \tag{6.4}$$

and

$$\kappa_s = \frac{\left(2GMH^4\Delta_c^2\right)^{1/3}}{8\pi G\Sigma_{cr}}\frac{c_v^2}{\ln(1+c_v) - c_v/(1+c_v)}. \tag{6.5}$$

Therefore, the lensing potential can be fully characterized by two parameters: the mass of the halo and the concentration.

In principle, these two parameters are independent. However, simulations have found a relationship between the halo mass and concentration. Macciò et al. (2008) found the best fitting mass-concentration relation in their simulations to be

$$c = 8.414\left(\frac{M}{10^{12}h^{-1}M_\odot}\right)^{-0.108}\left(\frac{H}{H_0}\right)^{-2/3}. \tag{6.6}$$

$\log(M_0)$	$\log(M_1)$	α	β	γ_1	γ_2	γ_3	γ_4	γ_5
10.56	11.31	0.22	3.54	-0.9	-0.25	0.42	-0.16	0.03

Table 6.1 Best fit parameters for the stellar to halo mass relation from Yang et al. (2012) used in this work.

This allows us to fully characterize the NFW halo with only a single parameter: the mass, albeit with some scatter.

The relationship between stellar mass and dark matter halo mass is difficult to constrain observationally so we again turn to simulations. Yang et al. (2012) fit a broken power-law to relate the stellar mass $M_\star$ to the halo mass M of the form

$$M_\star = M_0 \frac{(M/M_1)^{\alpha+\beta}}{(1+M/M_1)^\beta}. \tag{6.7}$$

This relationship is for the median halo of a log normal distribution of halo masses to stellar masses with a scatter of $\sigma_{\log M} = 0.173$ dex. They assume the following redshift dependences:

$$\log(M_0(z)) = \log(M_0) + \gamma_1 z \tag{6.8}$$

$$\log(M_1(z)) = \log(M_1) + \gamma_2 z \tag{6.9}$$

$$\alpha(z) = \alpha + \gamma_3 z \tag{6.10}$$

$$\log(\beta(z)) = \min(\log(\beta) + \gamma_4 z + \gamma_5 z^2, 2) \tag{6.11}$$

$$\sigma_{\log M}(z) = \max(0.173, 0.2z) \tag{6.12}$$

.

The best fit parameters from Yang et al. (2012) that we use are listed in Table 6.1. Using these relations we can fully characterize the dark matter halo with only the stellar mass which we can infer from our SED fit of the galaxy.

Both the mass-concentration and stellar to halo mass relations have significant scatter

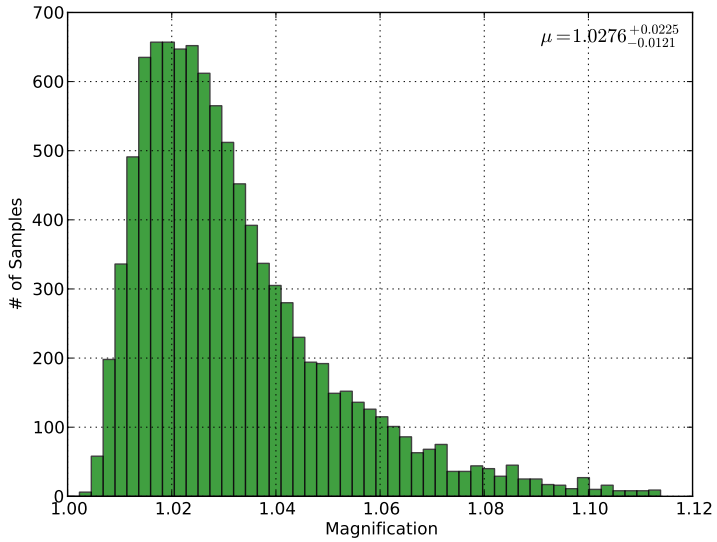

Figure 6.3 Distribution of lensing magnifications predicted for neighboring galaxy of SN Wilson. We assume log normal distibutions in both the mass-concentration relation and stellar to halo mass relation with a scatters of $\sigma_c = 0.15$ dex and $\sigma_{\log M} = 0.173$ respectively.

around the median relations. To account for this scatter, we take 10000 Monte Carlo realizations of lensing potentials to calculate the expected magnification distribution. We draw a photo-z and stellar mass value from our Monte Carlo realizations of our SED fits. Using these drawn values, we calculate the median halo mass from the equations above. Using the median halo mass, we choose a halo mass from the log normal distribution centered around the median with $\sigma_{\log M} = 0.173$ from Yang et al. (2012). We then draw a concentration using the chosen mass as the mean of a log normal distribution with scatter $\sigma_c = 0.15$ dex as found by Comerford & Natarajan (2007).

Figure 6.3 shows the resulting distribution of lensing magnifications. The median magnification is $2.8^{+2.3}_{-1.2}\%$ where the lower and upper uncertainties represent the 16^{th} and 84^{th} percentiles respectively. These models do assume a spherical NFW profile, but adding ellipticity to the halo does not significantly change our results. One might have expected that such a small galaxy would not magnify a SN significantly, but this quantitatively shows how much magnification can really be expected from this neighboring galaxy. This systematic offset due to the lensing is much smaller than the photometric uncertainties, but it can now

be properly accounted for in our total uncertainties when we put this object on a Hubble Diagram.

6.2.2 Lensed SNe Ia as Cosmological Probes

We now turn from treating lensing as a source of systematic uncertainty to discuss how we can use lensed SNe Ia for cosmology. Gravitationally lensed SNe Ia differ from traditional lensed sources, like quasars, in two key ways: we can infer the absolute luminosity of lensed SNe Ia, and their variation is smooth and predictable. The utility of these characteristics applies to different scale lenses. Galaxy cluster scale lenses will benefit more from knowing the intrinsic luminosity of the SN while the smooth variation has the biggest potential for galaxy-scale lenses.

One key challenge in modeling gravitational lenses is that the constraints are from *relative* positions and magnification *ratios*. This leads to the "mass sheet degeneracy" as discussed in Chapter 1 (Falco et al. 1985). Because SNe Ia are standardizable candles, we can use SNe Ia to break the mass sheet degeneracy (and the radial profile degeneracy). The intrinsic luminosity of a SN Ia can be calibrated to better than 10% (Wood-Vasey et al. 2007), yielding a direct measurement of the absolute magnification at a given point in the lens that can be used to measure the *absolute* mass of the cluster. Figure 6.4 illustrates the use of a SN Ia to measure the magnification of a galaxy cluster. The distribution of total masses of a sample of clusters can be used to constrain structure formation of the universe and cosmological parameters like σ_8. In principle, SNe Ia that are lensed by cluster-scale masses can be multiply imaged, but the time delay between images are typically long ranging from thousands of days to hundreds of years (Li et al. 2012).

Galaxy-scale lenses on the other hand, have time delays of tens to hundreds of days. As discussed in Chapter 1, the time delays between images can be used to measure the "time-delay distance" (Suyu 2012). By taking ratios of time-delay distances from a range of redshifts, we can map the cosmic expansion history and build a Hubble Diagram (Treu

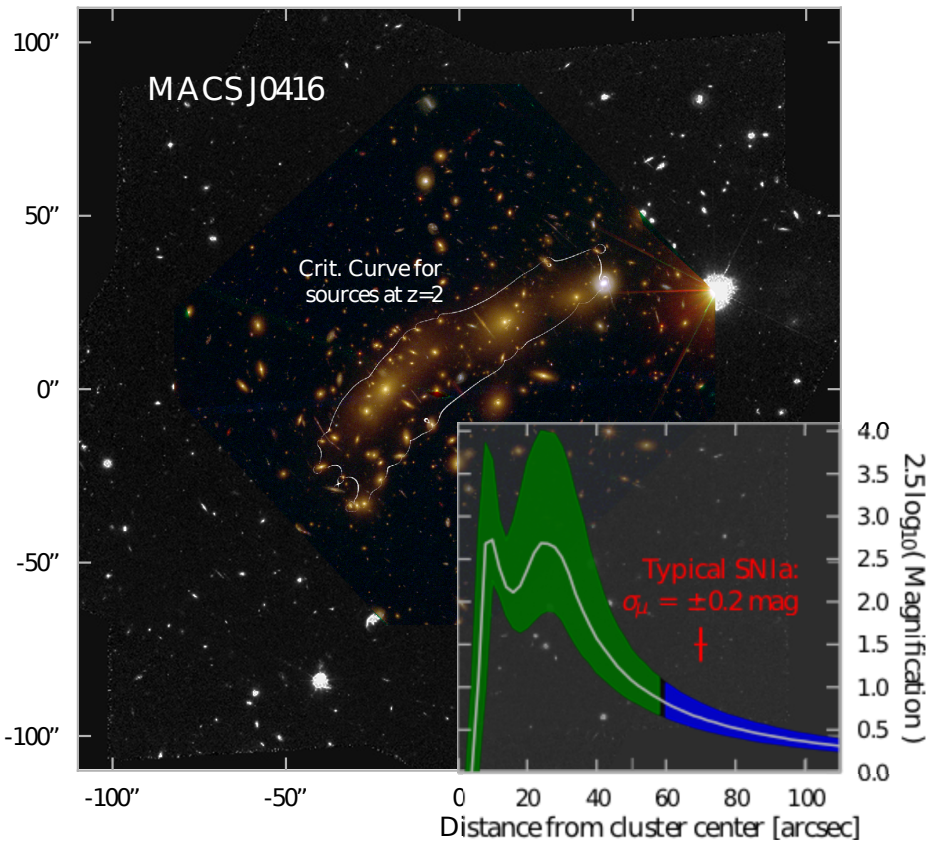

Figure 6.4 Figure adapted from the Frontier Field SN team. The background image shows one of the Frontier Field galaxy clusters, MACSJ0416, overlaid with the critical curve for sources at z=2 from the Zitrin et al. (2013) model. Inset: A simple example of a magnification profile and 1σ errors for a NFW halo (in magnitudes; as a function of radial distance from the center). The error bar in red illustrates the typical precision in measuring the observed magnification that can be achieved by fitting the light curve shape of a SN Ia at $z > 1$. For illustration, the NFW magnification curve is shaded green where the model uncertainty exceeds the observable SN uncertainty and blue where the SN error is larger than the model error.

et al. 2013). To place meaningful constraints on cosmological parameters (e.g. the energy density of dark energy, Ω_Λ), requires having time delay uncertainties $\sim 5\%$ (Treu et al. 2013) which scale directly from the relative precision of the longest time delay. A typical lensed SN has the potential to yield a more precise time delay than traditional lensed sources. High redshift galaxies and quasars are the most typical lensed sources. Galaxies may or may not vary on human time scales making time delays impossible to measure. Quasars vary but the variation is random and unpredictable (e.g. Treu et al. 2013). Finding enough overlap of features in the variation can make time delay measurements difficult and observationally

expensive (e.g. COSMOGRAIL; Eigenbrod et al. 2005). However, SNe vary on the timescale of days and vary smoothly. By following the light curves of each of the images, we will be able to constrain the relative time delay with high precision. Another benefit of lensed SNe Ia is that they fade making it possible to study the lens galaxy and the lensed host galaxy in detail.

Like any cosmological probe, lensed SNe Ia have systematic uncertainties that need to be taken into account. Even if we have high quality light curves of the SN, measuring the time delay may be complicated by microlensing due to stars in the lens galaxy. However, the original predictions for the microlensing of SNe was done by Dobler & Keeton (2006) using a simple expanding photosphere model, which may not be a good approximation for real SNe Ia. Microlensing is sensitive to the size of the source, so a different photospheric model may produce different quantities of microlensing. On the other hand, microlensing also has the potential to resolve the ejecta of SNe at a level that is not possible outside our own galaxy, making it a potential way to study the SNe Ia explosion mechanism. As the SN ejecta expands, it sweeps over microlensing caustics magnifying different regions of the ejecta giving us a "gravitational microscope" to study the explosion physics of SNe.

We have recently submitted results on the SNe discovered behind the CLASH clusters showing proof of concept that we can use SNe Ia to measure the absolute magnification of galaxy clusters (Patel et al. 2013). We compare the absolute magnification predicted by the lens models with the magnification predicted from the two lensed SNe Ia and find good agreement between both techniques.

Although SNe Ia have traditionally been used to study dark energy, SNe Ia can be used to constrain the dark matter distribution in galaxy clusters by directly measuring the absolute magnifications. Using SNe Ia to measure the absolute magnification of a lens, we can break the mass sheet degeneracy eliminating the uncertainty due to the external convergence described above. Gravitationally lensing has been traditionally used to study dark matter, but future surveys like LSST (LSST Science Collaboration et al. 2009) will

also us to use time delays to constrain dark energy. LSST will discover hundreds of lensed SNe Ia giving us the opportunity to combine these unique cosmological probes to constrain both of the two dominant components of the universe: dark matter and dark energy.

Bibliography

Arnett, D. 1996, Supernovae and Nucleosynthesis (Princeton University Press)

Arnett, W. D. 1982, ApJ, 253, 785

Arnett, W. D., Bahcall, J. N., Kirshner, R. P., & Woosley, S. E. 1989, ARA&A, 27, 629

Arnett, W. D., Truran, J. W., & Woosley, S. E. 1971, ApJ, 165, 87

Axelrod, T. S. 1980, PhD thesis, AA(California Univ., Santa Cruz.)

Bar-Kana, R. 1996, ApJ, 468, 17

Barnabè, M., Czoske, O., Koopmans, L. V. E., Treu, T., Bolton, A. S., & Gavazzi, R. 2009, MNRAS, 399, 21

Bartelmann, M. 1996, A&A, 313, 697

Bayliss, M. B., Johnson, T., Gladders, M. D., Sharon, K., & Oguri, M. 2014, ApJ, 783, 41

Bertelli, G., Nasi, E., Girardi, L., & Marigo, P. 2009, A&A, 508, 355

Bertin, E. 2012, in Astronomical Society of the Pacific Conference Series, Vol. 461, Astronomical Data Analysis Software and Systems XXI, ed. P. Ballester, D. Egret, & N. P. F. Lorente, 263

Bildsten, L., Shen, K. J., Weinberg, N. N., & Nelemans, G. 2007, ApJ, 662, L95

Blandford, R., & Narayan, R. 1986, ApJ, 310, 568

Bolton, A. S., Burles, S., Koopmans, L. V. E., Treu, T., Gavazzi, R., Moustakas, L. A., Wayth, R., & Schlegel, D. J. 2008, ApJ, 682, 964

Branch, D., Baron, E., Hall, N., Melakayil, M., & Parrent, J. 2005, PASP, 117, 545

Branch, D., Baron, E., Thomas, R. C., Kasen, D., Li, W., & Filippenko, A. V. 2004, PASP, 116, 903

Branch, D., Jeffery, D. J., Parrent, J., Baron, E., Troxel, M. A., Stanishev, V., Keithley, M., Harrison, J., & Bruner, C. 2008, PASP, 120, 135

Bryan, G. L., & Norman, M. L. 1998, ApJ, 495, 80

Cao, S., Covone, G., & Zhu, Z.-H. 2012, ApJ, 755, 31

Cao, Y., Kasliwal, M. M., Arcavi, I., Horesh, A., Hancock, P., Valenti, S., Cenko, S. B., Kulkarni, S. R., Gal-Yam, A., Gorbikov, E., Ofek, E. O., Sand, D., Yaron, O., Graham, M., Silverman, J. M., Wheeler, J. C., Marion, G. H., Walker, E. S., Mazzali, P., Howell, D. A., Li, K. L., Kong, A. K. H., Bloom, J. S., Nugent, P. E., Surace, J., Masci, F., Carpenter, J., Degenaar, N., & Gelino, C. R. 2013, ApJ, 775, L7

Carroll, B. W., & Ostlie, D. A. 2006, An Introduction to Modern Astrophysics and Cosmology (Pearson Education Inc., publishing as Addison-Wesley)

Carroll, S. M. 2004, Spacetime and geometry. An introduction to general relativity

Cenko, S. B., Li, W., Filippenko, A. V., Brimacombe, J., Meyer, S., Emig, K., Kaleida, C., Mamajek, E. E., Cohen, D. P., Silverman, J. M., & Ganeshalingam, M. 2012, Central Bureau Electronic Telegrams, 3014, 1

Chae, K., Mao, S., & Augusto, P. 2001, MNRAS, 326, 1015

Chiaberge, M., Lim, P. L., Kozhurina-Platais, V., Sirianni, M., & Mack, J. 2009, Updated CTE photometric correction for WFC and HRC, Tech. rep., STSci

Chornock, R., Filippenko, A. V., Branch, D., Foley, R. J., Jha, S., & Li, W. 2006, PASP, 118, 722

Clowe, D., Bradač, M., Gonzalez, A. H., Markevitch, M., Randall, S. W., Jones, C., & Zaritsky, D. 2006, ApJ, 648, L109

Coe, D. 2010, ArXiv, 1005.0411

Coe, D., & Moustakas, L. A. 2009, ApJ, 706, 45

Collett, T. E., Marshall, P. J., Auger, M. W., Hilbert, S., Suyu, S. H., Greene, Z., Treu, T., Fassnacht, C. D., Koopmans, L. V. E., Bradač, M., & Blandford, R. D. 2013, MNRAS, 432, 679

Comerford, J. M., & Natarajan, P. 2007, MNRAS, 379, 190

Conley, A., Guy, J., Sullivan, M., Regnault, N., Astier, P., Balland, C., Basa, S., Carlberg, R. G., Fouchez, D., Hardin, D., Hook, I. M., Howell, D. A., Pain, R., Palanque-Delabrouille, N., Perrett, K. M., Pritchet, C. J., Rich, J., Ruhlmann-Kleider, V., Balam, D., Baumont, S., Ellis, R. S., Fabbro, S., Fakhouri, H. K., Fourmanoit, N., González-Gaitán, S., Graham, M. L., Hudson, M. J., Hsiao, E., Kronborg, T., Lidman, C., Mourao, A. M., Neill, J. D., Perlmutter, S., Ripoche, P., Suzuki, N., & Walker, E. S. 2011, ApJS, 192, 1

Contardo, G., Leibundgut, B., & Vacca, W. D. 2000, A&A, 359, 876

Dalal, N., & Kochanek, C. S. 2002, ApJ, 572, 25

Dobler, G., & Keeton, C. R. 2006, MNRAS, 365, 1243

Dolphin, A. E. 2000, PASP, 112, 1383

—. 2009, PASP, 121, 655

Eigenbrod, A., Courbin, F., Vuissoz, C., Meylan, G., Saha, P., & Dye, S. 2005, A&A, 436, 25

Erdl, H., & Schneider, P. 1993, A&A, 268, 453

Faber, S. M., & Jackson, R. E. 1976, ApJ, 204, 668

Faber, S. M., Phillips, A. C., Kibrick, R. I., Alcott, B., Allen, S. L., Burrous, J., Cantrall, T., Clarke, D., Coil, A. L., Cowley, D. J., Davis, M., Deich, W. T. S., Dietsch, K., Gilmore, D. K., Harper, C. A., Hilyard, D. F., Lewis, J. P., McVeigh, M., Newman, J., Osborne, J., Schiavon, R., Stover, R. J., Tucker, D., Wallace, V., Wei, M., Wirth, G., & Wright, C. A. 2003, in Society of Photo-Optical Instrumentation Engineers (SPIE) Conference Series, Vol. 4841, Society of Photo-Optical Instrumentation Engineers (SPIE) Conference Series, ed. M. Iye & A. F. M. Moorwood, 1657–1669

Fadely, R., & Keeton, C. R. 2012, MNRAS, 419, 936

Fadely, R., Keeton, C. R., Nakajima, R., & Bernstein, G. M. 2010, ApJ, 711, 246

Falco, E. E., Gorenstein, M. V., & Shapiro, I. I. 1985, ApJ, 289, L1

Fassnacht, C. D., Gal, R. R., Lubin, L. M., McKean, J. P., Squires, G. K., & Readhead, A. C. S. 2006, ApJ, 642, 30

Ferland, G. J., & Persson, S. E. 1989, ApJ, 347, 656

Filippenko, A. V. 1997, ARA&A, 35, 309

Filippenko, A. V. 2003, in From Twilight to Highlight: The Physics of Supernovae, ed. W. Hillebrandt & B. Leibundgut, 171

Filippenko, A. V. 2005, in Astrophysics and Space Science Library, Vol. 332, White dwarfs: cosmological and galactic probes, ed. E. M. Sion, S. Vennes, & H. L. Shipman, 97–133

Filippenko, A. V., Li, W. D., Treffers, R. R., & Modjaz, M. 2001, in Astronomical Society of the Pacific Conference Series, Vol. 246, IAU Colloq. 183: Small Telescope Astronomy on Global Scales, ed. B. Paczynski, W.-P. Chen, & C. Lemme, 121

Filippenko, A. V., Richmond, M. W., Branch, D., Gaskell, M., Herbst, W., Ford, C. H., Treffers, R. R., Matheson, T., Ho, L. C., Dey, A., Sargent, W. L. W., Small, T. A., & van Breugel, W. J. M. 1992a, AJ, 104, 1543

Filippenko, A. V., Richmond, M. W., Matheson, T., Shields, J. C., Burbidge, E. M., Cohen, R. D., Dickinson, M., Malkan, M. A., Nelson, B., Pietz, J., Schlegel, D., Schmeer, P., Spinrad, H., Steidel, C. C., Tran, H. D., & Wren, W. 1992b, ApJ, 384, L15

Fink, M., Kromer, M., Seitenzahl, I. R., Ciaraldi-Schoolmann, F., Röpke, F. K., Sim, S. A., Pakmor, R., Ruiter, A. J., & Hillebrandt, W. 2014, MNRAS, 438, 1762

Fischer, P., Schade, D., & Barrientos, L. F. 1998, ApJ, 503, L127

Folatelli, G., Phillips, M. M., Morrell, N., Tanaka, M., Maeda, K., Nomoto, K., Stritzinger, M., Burns, C. R., Hamuy, M., Mazzali, P., Boldt, L., Campillay, A., Contreras, C., González, S., Roth, M., Salgado, F., Freedman, W. L., Madore, B. F., Persson, S. E., & Suntzeff, N. B. 2012, ApJ, 745, 74

Foley, R. J., Brown, P. J., Rest, A., Challis, P. J., Kirshner, R. P., & Wood-Vasey, W. M. 2010a, ApJ, 708, L61

Foley, R. J., Challis, P. J., Chornock, R., Ganeshalingam, M., Li, W., Marion, G. H., Morrell, N. I., Pignata, G., Stritzinger, M. D., Silverman, J. M., Wang, X., Anderson, J. P., Filippenko, A. V., Freedman, W. L., Hamuy, M., Jha, S. W., Kirshner, R. P., McCully, C., Persson, S. E., Phillips, M. M., Reichart, D. E., & Soderberg, A. M. 2013, ApJ, 767, 57

Foley, R. J., Chornock, R., Filippenko, A. V., Ganeshalingam, M., Kirshner, R. P., Li, W., Cenko, S. B., Challis, P. J., Friedman, A. S., Modjaz, M., Silverman, J. M., & Wood-Vasey, W. M. 2009, AJ, 138, 376

Foley, R. J., Rest, A., Stritzinger, M., Pignata, G., Anderson, J. P., Hamuy, M., Morrell, N. I., Phillips, M. M., & Salgado, F. 2010b, AJ, 140, 1321

Foley, R. J., Sanders, N. E., & Kirshner, R. P. 2011, ApJ, 742, 89

Frieman, J. A., Bassett, B., Becker, A., Choi, C., Cinabro, D., DeJongh, F., Depoy, D. L., Dilday, B., Doi, M., Garnavich, P. M., Hogan, C. J., Holtzman, J., Im, M., Jha, S., Kessler, R., Konishi, K., Lampeitl, H., Marriner, J., Marshall, J. L., McGinnis, D., Miknaitis, G., Nichol, R. C., Prieto, J. L., Riess, A. G., Richmond, M. W., Romani, R., Sako, M., Schneider, D. P., Smith, M., Takanashi, N., Tokita, K., van der Heyden, K., Yasuda, N., Zheng, C., Adelman-McCarthy, J., Annis, J., Assef, R. J., Barentine, J., Bender, R., Blandford, R. D., Boroski, W. N., Bremer, M., Brewington, H., Collins, C. A., Crotts, A., Dembicky, J., Eastman, J., Edge, A., Edmondson, E., Elson, E., Eyler, M. E., Filippenko, A. V., Foley, R. J., Frank, S., Goobar, A., Gueth, T., Gunn, J. E., Harvanek, M., Hopp, U., Ihara, Y., Ivezić, Ž., Kahn, S., Kaplan, J., Kent, S., Ketzeback, W., Kleinman, S. J., Kollatschny, W., Kron, R. G., Krzesiński, J., Lamenti, D., Leloudas, G., Lin, H., Long, D. C., Lucey, J., Lupton, R. H., Malanushenko, E., Malanushenko, V., McMillan, R. J., Mendez, J., Morgan, C. W., Morokuma, T., Nitta, A., Ostman, L., Pan, K., Rockosi, C. M., Romer, A. K., Ruiz-Lapuente, P., Saurage, G., Schlesinger, K., Snedden, S. A., Sollerman, J., Stoughton, C., Stritzinger, M., Subba Rao, M., Tucker, D., Vaisanen, P., Watson, L. C., Watters, S., Wheeler, J. C., Yanny, B., & York, D. 2008, AJ, 135, 338

Fruchter, A., Sosey, M., Hack, W., Dressel, L., Koekemoer, A. M., Mack, J., Mutchler, M., & Pirzkal, N. 2009, HST MultiDrizzle Handbook

Fukugita, M., Ichikawa, T., Gunn, J. E., Doi, M., Shimasaku, K., & Schneider, D. P. 1996, AJ, 111, 1748

Gamezo, V. N., Khokhlov, A. M., & Oran, E. S. 2004, Physical Review Letters, 92, 211102

—. 2005, ApJ, 623, 337

Gamezo, V. N., Khokhlov, A. M., Oran, E. S., Chtchelkanova, A. Y., & Rosenberg, R. O. 2003, Science, 299, 77

Ganeshalingam, M., Li, W., & Filippenko, A. V. 2011, MNRAS, 416, 2607

—. 2013, MNRAS, 433, 2240

Ganeshalingam, M., Li, W., Filippenko, A. V., Anderson, C., Foster, G., Gates, E. L., Griffith, C. V., Grigsby, B. J., Joubert, N., Leja, J., Lowe, T. B., Macomber, B., Pritchard, T., Thrasher, P., & Winslow, D. 2010, ApJS, 190, 418

Gavazzi, R., Treu, T., Koopmans, L. V. E., Bolton, A. S., Moustakas, L. A., Burles, S., & Marshall, P. J. 2008, ApJ, 677, 1046

Georgy, C., Ekström, S., Granada, A., Meynet, G., Mowlavi, N., Eggenberger, P., & Maeder, A. 2013, A&A, 553, A24

Gonzaga, S., Hack, W., Fruchter, A., & Mack, J. 2012, The DrizzlePac Handbook (STScI, Baltimore)

Goranskij, V., Shugarov, S., Zharova, A., Kroll, P., & Barsukova, E. A. 2010, Peremennye Zvezdy, 30, 4

Groh, J. H., Meynet, G., Georgy, C., & Ekström, S. 2013, A&A, 558, A131

Guy, J., Astier, P., Baumont, S., Hardin, D., Pain, R., Regnault, N., Basa, S., Carlberg, R. G., Conley, A., Fabbro, S., Fouchez, D., Hook, I. M., Howell, D. A., Perrett, K., Pritchet, C. J., Rich, J., Sullivan, M., Antilogus, P., Aubourg, E., Bazin, G., Bronder, J., Filiol, M., Palanque-Delabrouille, N., Ripoche, P., & Ruhlmann-Kleider, V. 2007, A&A, 466, 11

Guy, J., Sullivan, M., Conley, A., Regnault, N., Astier, P., Balland, C., Basa, S., Carlberg, R. G., Fouchez, D., Hardin, D., Hook, I. M., Howell, D. A., Pain, R., Palanque-Delabrouille, N., Perrett, K. M., Pritchet, C. J., Rich, J., Ruhlmann-Kleider, V., Balam, D., Baumont, S., Ellis, R. S., Fabbro, S., Fakhouri, H. K., Fourmanoit, N., González-Gaitán, S., Graham, M. L., Hsiao, E., Kronborg, T., Lidman, C., Mourao, A. M., Perlmutter, S., Ripoche, P., Suzuki, N., & Walker, E. S. 2010, A&A, 523, A7

Hamuy, M., Phillips, M. M., Suntzeff, N. B., Maza, J., González, L. E., Roth, M., Krisciunas, K., Morrell, N., Green, E. M., Persson, S. E., & McCarthy, P. J. 2003, Nature, 424, 651

Hatano, K., Branch, D., Fisher, A., Millard, J., & Baron, E. 1999, ApJS, 121, 233

Hicken, M., Challis, P., Jha, S., Kirshner, R. P., Matheson, T., Modjaz, M., Rest, A., Wood-Vasey, W. M., Bakos, G., Barton, E. J., Berlind, P., Bragg, A., Briceño, C., Brown, W. R., Caldwell, N., Calkins, M., Cho, R., Ciupik, L., Contreras, M., Dendy, K.-C., Dosaj, A., Durham, N., Eriksen, K., Esquerdo, G., Everett, M., Falco, E., Fernandez, J., Gaba, A., Garnavich, P., Graves, G., Green, P., Groner, T., Hergenrother, C., Holman, M. J., Hradecky, V., Huchra, J., Hutchison, B., Jerius, D., Jordan, A., Kilgard, R., Krauss, M., Luhman, K., Macri, L., Marrone, D., McDowell, J., McIntosh, D., McNamara, B., Megeath, T., Mochejska, B., Munoz, D., Muzerolle, J., Naranjo, O., Narayan, G., Pahre, M., Peters, W., Peterson, D., Rines, K., Ripman, B., Roussanova, A., Schild, R., Sicilia-Aguilar, A., Sokoloski, J., Smalley, K., Smith, A., Spahr, T., Stanek, K. Z., Barmby, P., Blondin, S., Stubbs, C. W., Szentgyorgyi, A., Torres, M. A. P., Vaz, A., Vikhlinin, A., Wang, Z., Westover, M., Woods, D., & Zhao, P. 2009, ApJ, 700, 331

Hicken, M., Challis, P., Kirshner, R. P., Rest, A., Cramer, C. E., Wood-Vasey, W. M., Bakos, G., Berlind, P., Brown, W. R., Caldwell, N., Calkins, M., Currie, T., de Kleer, K., Esquerdo, G., Everett, M., Falco, E., Fernandez, J., Friedman, A. S., Groner, T., Hartman, J., Holman, M. J., Hutchins, R., Keys, S., Kipping, D., Latham, D., Marion, G. H., Narayan, G., Pahre, M., Pal, A., Peters, W., Perumpilly, G., Ripman, B., Sipocz,

B., Szentgyorgyi, A., Tang, S., Torres, M. A. P., Vaz, A., Wolk, S., & Zezas, A. 2012, ApJS, 200, 12

Hilbert, S., Hartlap, J., White, S. D. M., & Schneider, P. 2009, A&A, 499, 31

Hilbert, S., White, S. D. M., Hartlap, J., & Schneider, P. 2007, MNRAS, 382, 121

Holtzman, J. A., Hester, J. J., Casertano, S., Trauger, J. T., Watson, A. M., Ballester, G. E., Burrows, C. J., Clarke, J. T., Crisp, D., Evans, R. W., Gallagher, III, J. S., Griffiths, R. E., Hoessel, J. G., Matthews, L. D., Mould, J. R., Scowen, P. A., Stapelfeldt, K. R., & Westphal, J. A. 1995, PASP, 107, 156

Holtzman, J. A., Marriner, J., Kessler, R., Sako, M., Dilday, B., Frieman, J. A., Schneider, D. P., Bassett, B., Becker, A., Cinabro, D., DeJongh, F., Depoy, D. L., Doi, M., Garnavich, P. M., Hogan, C. J., Jha, S., Konishi, K., Lampeitl, H., Marshall, J. L., McGinnis, D., Miknaitis, G., Nichol, R. C., Prieto, J. L., Riess, A. G., Richmond, M. W., Romani, R., Smith, M., Takanashi, N., Tokita, K., van der Heyden, K., Yasuda, N., & Zheng, C. 2008, AJ, 136, 2306

Hook, R., & Stoehr, F. 2008, WFC3 Support in Tiny Tim, Tech. rep.

Howell, D. A., Sullivan, M., Nugent, P. E., Ellis, R. S., Conley, A. J., Le Borgne, D., Carlberg, R. G., Guy, J., Balam, D., Basa, S., Fouchez, D., Hook, I. M., Hsiao, E. Y., Neill, J. D., Pain, R., Perrett, K. M., & Pritchet, C. J. 2006, Nature, 443, 308

Iben, Jr., I., & Tutukov, A. V. 1991, ApJ, 370, 615

Jackson, N., Nair, S., Browne, I. W. A., Wilkinson, P. N., Muxlow, T. W. B., de Bruyn, A. G., Koopmans, L., Bremer, M., Snellen, I., Miley, G. K., Schilizzi, R. T., Myers, S., Fassnacht, C. D., Womble, D. S., Readhead, A. C. S., Blandford, R. D., & Pearson, T. J. 1998, MNRAS, 296, 483

Jaroszynski, M. 1989, Acta Astron, 39, 301

—. 1991, MNRAS, 249, 430

—. 1992, MNRAS, 255, 655

Jaroszynski, M., & Kostrzewa-Rutkowska, Z. 2012, MNRAS, 424, 325

—. 2014, MNRAS, 439, 2432

Jha, S., Branch, D., Chornock, R., Foley, R. J., Li, W., Swift, B. J., Casebeer, D., & Filippenko, A. V. 2006a, AJ, 132, 189

Jha, S., Garnavich, P. M., Kirshner, R. P., Challis, P., Soderberg, A. M., Macri, L. M., Huchra, J. P., Barmby, P., Barton, E. J., Berlind, P., Brown, W. R., Caldwell, N., Calkins, M. L., Kannappan, S. J., Koranyi, D. M., Pahre, M. A., Rines, K. J., Stanek, K. Z., Stefanik, R. P., Szentgyorgyi, A. H., Väisänen, P., Wang, Z., Zajac, J. M., Riess, A. G., Filippenko, A. V., Li, W., Modjaz, M., Treffers, R. R., Hergenrother, C. W., Grebel, E. K., Seitzer, P., Jacoby, G. H., Benson, P. J., Rizvi, A., Marschall, L. A., Goldader, J. D., Beasley, M., Vacca, W. D., Leibundgut, B., Spyromilio, J., Schmidt, B. P., & Wood, P. R. 1999, ApJS, 125, 73

Jha, S., Kirshner, R. P., Challis, P., Garnavich, P. M., Matheson, T., Soderberg, A. M., Graves, G. J. M., Hicken, M., Alves, J. F., Arce, H. G., Balog, Z., Barmby, P., Barton, E. J., Berlind, P., Bragg, A. E., Briceño, C., Brown, W. R., Buckley, J. H., Caldwell, N., Calkins, M. L., Carter, B. J., Concannon, K. D., Donnelly, R. H., Eriksen, K. A., Fabricant, D. G., Falco, E. E., Fiore, F., Garcia, M. R., Gómez, M., Grogin, N. A., Groner, T., Groot, P. J., Haisch, Jr., K. E., Hartmann, L., Hergenrother, C. W., Holman, M. J., Huchra, J. P., Jayawardhana, R., Jerius, D., Kannappan, S. J., Kim, D.-W., Kleyna, J. T., Kochanek, C. S., Koranyi, D. M., Krockenberger, M., Lada, C. J., Luhman, K. L., Luu, J. X., Macri, L. M., Mader, J. A., Mahdavi, A., Marengo, M., Marsden, B. G., McLeod, B. A., McNamara, B. R., Megeath, S. T., Moraru, D., Mossman, A. E., Muench, A. A., Muñoz, J. A., Muzerolle, J., Naranjo, O., Nelson-Patel, K., Pahre, M. A., Patten, B. M., Peters, J., Peters, W., Raymond, J. C., Rines, K., Schild, R. E., Sobczak, G. J., Spahr, T. B., Stauffer, J. R., Stefanik, R. P., Szentgyorgyi, A. H., Tollestrup, E. V., Väisänen, P., Vikhlinin, A., Wang, Z., Willner, S. P., Wolk, S. J., Zajac, J. M., Zhao, P., & Stanek, K. Z. 2006b, AJ, 131, 527

Jha, S., Riess, A. G., & Kirshner, R. P. 2007, ApJ, 659, 122

Jones, D. O., Rodney, S. A., Riess, A. G., Mobasher, B., Dahlen, T., McCully, C., Frederiksen, T. F., Casertano, S., Hjorth, J., Keeton, C. R., Koekemoer, A., Strolger, L.-G., Wiklind, T. G., Challis, P., Graur, O., Hayden, B., Patel, B., Weiner, B. J., Filippenko, A. V., Garnavich, P., Jha, S. W., Kirshner, R. P., Ferguson, H. C., Grogin, N. A., & Kocevski, D. 2013, ApJ, 768, 166

Jordan, IV, G. C., Perets, H. B., Fisher, R. T., & van Rossum, D. R. 2012, ApJ, 761, L23

Kasen, D. 2006, ApJ, 649, 939

Kasliwal, M. M., Kulkarni, S. R., Gal-Yam, A., Yaron, O., Quimby, R. M., Ofek, E. O., Nugent, P., Poznanski, D., Jacobsen, J., Sternberg, A., Arcavi, I., Howell, D. A., Sullivan, M., Rich, D. J., Burke, P. F., Brimacombe, J., Milisavljevic, D., Fesen, R., Bildsten, L., Shen, K., Cenko, S. B., Bloom, J. S., Hsiao, E., Law, N. M., Gehrels, N., Immler, S., Dekany, R., Rahmer, G., Hale, D., Smith, R., Zolkower, J., Velur, V., Walters, R., Henning, J., Bui, K., & McKenna, D. 2010, ApJ, 723, L98

Kasliwal, M. M., Ofek, E. O., Gal-Yam, A., Rau, A., Brown, P. J., Cenko, S. B., Cameron, P. B., Quimby, R., Kulkarni, S. R., Bildsten, L., Milne, P., & Bryngelson, G. 2008, ApJ, 683, L29

Kato, M., Hachisu, I., Kiyota, S., & Saio, H. 2008, ApJ, 684, 1366

Kaufmann, W. J. 1996, Universe (W. H. Freeman and Company, New York)

Kayser, R., & Schramm, T. 1993, A&A, 278, L13

Keeton, C. R. 2001, ArXiv, 0102340, arXiv:astro-ph/0102340

—. 2003, ApJ, 584, 664

Keeton, C. R., Christlein, D., & Zabludoff, A. I. 2000, ApJ, 545, 129

Keeton, C. R., Kochanek, C. S., & Falco, E. E. 1998, ApJ, 509, 561

Keeton, C. R., Kochanek, C. S., & Seljak, U. 1997, ApJ, 482, 604

Keeton, C. R., & Zabludoff, A. I. 2004, ApJ, 612, 660

Kessler, R., Becker, A. C., Cinabro, D., Vanderplas, J., Frieman, J. A., Marriner, J., Davis, T. M., Dilday, B., Holtzman, J., Jha, S. W., Lampeitl, H., Sako, M., Smith, M., Zheng, C., Nichol, R. C., Bassett, B., Bender, R., Depoy, D. L., Doi, M., Elson, E., Filippenko, A. V., Foley, R. J., Garnavich, P. M., Hopp, U., Ihara, Y., Ketzeback, W., Kollatschny, W., Konishi, K., Marshall, J. L., McMillan, R. J., Miknaitis, G., Morokuma, T., Mörtsell, E., Pan, K., Prieto, J. L., Richmond, M. W., Riess, A. G., Romani, R., Schneider, D. P., Sollerman, J., Takanashi, N., Tokita, K., van der Heyden, K., Wheeler, J. C., Yasuda, N., & York, D. 2009, ApJS, 185, 32

Khokhlov, A. M. 1991, A&A, 245, 114

King, L. J., Browne, I. W. A., Marlow, D. R., Patnaik, A. R., & Wilkinson, P. N. 1999, MNRAS, 307, 225

Kirshner, R. P., Jeffery, D. J., Leibundgut, B., Challis, P. M., Sonneborn, G., Phillips, M. M., Suntzeff, N. B., Smith, R. C., Winkler, P. F., Winge, C., Hamuy, M., Hunter, D. A., Roth, K. C., Blades, J. C., Branch, D., Chevalier, R. A., Fransson, C., Panagia, N., Wagoner, R. V., Wheeler, J. C., & Harkness, R. P. 1993, ApJ, 415, 589

Kneib, J.-P., Cohen, J. G., & Hjorth, J. 2000, ApJ, 544, L35

Kochanek, C. S. 2003, ApJ, 583, 49

Kochanek, C. S. 2006, in Saas-Fee Advanced Course 33: Gravitational Lensing: Strong, Weak and Micro, ed. G. Meylan, P. Jetzer, & P. North, 91–268

Kochanek, C. S., & Apostolakis, J. 1988, MNRAS, 235, 1073

Kochanek, C. S., Morgan, N. D., Falco, E. E., McLeod, B. A., Winn, J. N., Dembicky, J., & Ketzeback, B. 2006, ApJ, 640, 47

Kolatt, T. S., & Bartelmann, M. 1998, MNRAS, 296, 763

Koopmans, L. V. E., & Fassnacht, C. D. 1999, ApJ, 527, 513

Koopmans, L. V. E., Treu, T., Bolton, A. S., Burles, S., & Moustakas, L. A. 2006, ApJ, 649, 599

Kovner, I. 1987, ApJ, 316, 52

Kozma, C., & Fransson, C. 1998, ApJ, 497, 431

Kozma, C., Fransson, C., Hillebrandt, W., Travaglio, C., Sollerman, J., Reinecke, M., Röpke, F. K., & Spyromilio, J. 2005, A&A, 437, 983

Krist, J. 1993, in Astronomical Society of the Pacific Conference Series, Vol. 52, Astronomical Data Analysis Software and Systems II, ed. R. J. Hanisch, R. J. V. Brissenden, & J. Barnes, 536

Kromer, M., Fink, M., Stanishev, V., Taubenberger, S., Ciaraldi-Schoolman, F., Pakmor, R., Röpke, F. K., Ruiter, A. J., Seitenzahl, I. R., Sim, S. A., Blanc, G., Elias-Rosa, N., & Hillebrandt, W. 2013, MNRAS, 429, 2287

Kuchner, M. J., Kirshner, R. P., Pinto, P. A., & Leibundgut, B. 1994, ApJ, 426, L89

Kuhlen, M., Woosley, S. E., & Glatzmaier, G. A. 2006, ApJ, 640, 407

Kundic, T., Cohen, J. G., Blandford, R. D., & Lubin, L. M. 1997a, AJ, 114, 507

Kundic, T., Hogg, D. W., Blandford, R. D., Cohen, J. G., Lubin, L. M., & Larkin, J. E. 1997b, AJ, 114, 2276

Lair, J. C., Leising, M. D., Milne, P. A., & Williams, G. G. 2006, AJ, 132, 2024

Lee, M. H., Babul, A., Kofman, L., & Kaiser, N. 1997, ApJ, 489, 522

Lehár, J., Falco, E. E., Kochanek, C. S., McLeod, B. A., Muñoz, J. A., Impey, C. D., Rix, H.-W., Keeton, C. R., & Peng, C. Y. 2000, ApJ, 536, 584

Leibundgut, B., Kirshner, R. P., Phillips, M. M., Wells, L. A., Suntzeff, N. B., Hamuy, M., Schommer, R. A., Walker, A. R., Gonzalez, L., Ugarte, P., Williams, R. E., Williger, G., Gomez, M., Marzke, R., Schmidt, B. P., Whitney, B., Coldwell, N., Peters, J., Chaffee, F. H., Foltz, C. B., Rehner, D., Siciliano, L., Barnes, T. G., Cheng, K.-P., Hintzen, P. M. N., Kim, Y.-C., Maza, J., Parker, J. W., Porter, A. C., Schmidtke, P. C., & Sonneborn, G. 1993, AJ, 105, 301

Leloudas, G., Stritzinger, M. D., Sollerman, J., Burns, C. R., Kozma, C., Krisciunas, K., Maund, J. R., Milne, P., Filippenko, A. V., Fransson, C., Ganeshalingam, M., Hamuy, M., Li, W., Phillips, M. M., Schmidt, B. P., Skottfelt, J., Taubenberger, S., Boldt, L., Fynbo, J. P. U., Gonzalez, L., Salvo, M., & Thomas-Osip, J. 2009, A&A, 505, 265

Leonard, D. C. 2007, ApJ, 670, 1275

Levine, H. I., & Petters, A. O. 1993, A&A, 272, L17

Li, W., Chornock, R., Leaman, J., Filippenko, A. V., Poznanski, D., Wang, X., Ganeshalingam, M., & Mannucci, F. 2011, MNRAS, 412, 1473

Li, W., Filippenko, A. V., Chornock, R., Berger, E., Berlind, P., Calkins, M. L., Challis, P., Fassnacht, C., Jha, S., Kirshner, R. P., Matheson, T., Sargent, W. L. W., Simcoe, R. A., Smith, G. H., & Squires, G. 2003, PASP, 115, 453

Li, W., Filippenko, A. V., Treffers, R. R., Riess, A. G., Hu, J., & Qiu, Y. 2001, ApJ, 546, 734

Li, X., Hjorth, J., & Richard, J. 2012, JCAP, 11, 15

Linder, E. V. 2004, Phys. Rev. D, 70, 043534

—. 2011, Phys. Rev. D, 84, 123529

Liu, W.-M., Chen, W.-C., Wang, B., & Han, Z. W. 2010, A&A, 523, A3

Livne, E., Asida, S. M., & Höflich, P. 2005, ApJ, 632, 443

LSST Science Collaboration, Abell, P. A., Allison, J., Anderson, S. F., Andrew, J. R., Angel, J. R. P., Armus, L., Arnett, D., Asztalos, S. J., Axelrod, T. S., & et al. 2009, ArXiv, 0912.0201

Lyman, J. D., James, P. A., Perets, H. B., Anderson, J. P., Gal-Yam, A., Mazzali, P., & Percival, S. M. 2013, MNRAS, 434, 527

Macciò, A. V., Dutton, A. A., & van den Bosch, F. C. 2008, MNRAS, 391, 1940

Maeda, K., Benetti, S., Stritzinger, M., Röpke, F. K., Folatelli, G., Sollerman, J., Taubenberger, S., Nomoto, K., Leloudas, G., Hamuy, M., Tanaka, M., Mazzali, P. A., & Elias-Rosa, N. 2010a, Nature, 466, 82

Maeda, K., Taubenberger, S., Sollerman, J., Mazzali, P. A., Leloudas, G., Nomoto, K., & Motohara, K. 2010b, ApJ, 708, 1703

Maguire, K., Jerkstrand, A., Smartt, S. J., Fransson, C., Pastorello, A., Benetti, S., Valenti, S., Bufano, F., & Leloudas, G. 2012, MNRAS, 420, 3451

Mao, S., & Schneider, P. 1998, MNRAS, 295, 587

Massey, R., Kitching, T., & Richard, J. 2010, Reports on Progress in Physics, 73, 086901

Maund, J. R., Wheeler, J. C., Wang, L., Baade, D., Clocchiatti, A., Patat, F., Höflich, P., Quinn, J., & Zelaya, P. 2010, ApJ, 722, 1162

Mazzali, P. A., Cappellaro, E., Danziger, I. J., Turatto, M., & Benetti, S. 1998, ApJ, 499, L49

McClelland, C. M., Garnavich, P. M., Galbany, L., Miquel, R., Foley, R. J., Filippenko, A. V., Bassett, B., Wheeler, J. C., Goobar, A., Jha, S. W., Sako, M., Frieman, J. A., Sollerman, J., Vinko, J., & Schneider, D. P. 2010, ApJ, 720, 704

McCully, C., Jha, S. W., Foley, R. J., Chornock, R., Holtzman, J. A., Balam, D. D., Branch, D., Filippenko, A. V., Frieman, J., Fynbo, J., Galbany, L., Ganeshalingam, M., Garnavich, P. M., Graham, M. L., Hsiao, E. Y., Leloudas, G., Leonard, D. C., Li, W., Riess, A. G., Sako, M., Schneider, D. P., Silverman, J. M., Sollerman, J., Steele, T. N., Thomas, R. C., Wheeler, J. C., & Zheng, C. 2013, ArXiv, 1309.4457, 1309.4457

McCully, C., Keeton, C. R., Wong, K. C., & Zabludoff, A. I. 2014, ArXiv, 1401.0197

Metcalf, R. B., & Madau, P. 2001, ApJ, 563, 9

Meyer, M. J., Zwaan, M. A., Webster, R. L., Staveley-Smith, L., Ryan-Weber, E., Drinkwater, M. J., Barnes, D. G., Howlett, M., Kilborn, V. A., Stevens, J., Waugh, M., Pierce, M. J., Bhathal, R., de Blok, W. J. G., Disney, M. J., Ekers, R. D., Freeman, K. C., Garcia, D. A., Gibson, B. K., Harnett, J., Henning, P. A., Jerjen, H., Kesteven, M. J., Knezek, P. M., Koribalski, B. S., Mader, S., Marquarding, M., Minchin, R. F., O'Brien, J., Oosterloo, T., Price, R. M., Putman, M. E., Ryder, S. D., Sadler, E. M., Stewart, I. M., Stootman, F., & Wright, A. E. 2004, MNRAS, 350, 1195

Miller, J. S., & Stone, R. P. S. 1993, Lick Obs. Tech. Rep. 66 (Santa Cruz: Lick Obs.)

Milne, P. A., Brown, P. J., Roming, P. W. A., Holland, S. T., Immler, S., Filippenko, A. V., Ganeshalingam, M., Li, W., Stritzinger, M., Phillips, M. M., Hicken, M., Kirshner, R. P., Challis, P. J., Mazzali, P., Schmidt, B. P., Bufano, F., Gehrels, N., & Vanden Berk, D. 2010, ApJ, 721, 1627

Milne, P. A., The, L.-S., & Leising, M. D. 1999, ApJS, 124, 503

Minkowski, R. 1941, PASP, 53, 224

Möller, O., & Blain, A. W. 2001, MNRAS, 327, 339

Momcheva, I., Williams, K., Keeton, C., & Zabludoff, A. 2006, ApJ, 641, 169

Morgan, N. D., Caldwell, J. A. R., Schechter, P. L., Dressler, A., Egami, E., & Rix, H. 2004, AJ, 127, 2617

Moriya, T., Tominaga, N., Tanaka, M., Nomoto, K., Sauer, D. N., Mazzali, P. A., Maeda, K., & Suzuki, T. 2010, ApJ, 719, 1445

Mould, J. R., Hughes, S. M. G., Stetson, P. B., Gibson, B. K., Huchra, J. P., Freedman, W. L., Kennicutt, Jr., R. C., Bresolin, F., Ferrarese, L., Ford, H. C., Graham, J. A., Han, M., Hoessel, J. G., Illingworth, G. D., Kelson, D. D., Macri, L. M., Madore, B. F., Phelps, R. L., Prosser, C. F., Rawson, D., Saha, A., Sakai, S., Sebo, K. M., Silbermann, N. A., & Turner, A. M. 2000, ApJ, 528, 655

Munshi, D., Valageas, P., van Waerbeke, L., & Heavens, A. 2008, Phys. Rep., 462, 67

Nakajima, R., Bernstein, G. M., Fadely, R., Keeton, C. R., & Schrabback, T. 2009, ApJ, 697, 1793

Narayan, G., Foley, R. J., Berger, E., Botticella, M. T., Chornock, R., Huber, M. E., Rest, A., Scolnic, D., Smartt, S., Valenti, S., Soderberg, A. M., Burgett, W. S., Chambers, K. C., Flewelling, H. A., Gates, G., Grav, T., Kaiser, N., Kirshner, R. P., Magnier, E. A., Morgan, J. S., Price, P. A., Riess, A. G., Stubbs, C. W., Sweeney, W. E., Tonry, J. L., Wainscoat, R. J., Waters, C., & Wood-Vasey, W. M. 2011, ApJ, 731, L11

Navarro, J. F., Frenk, C. S., & White, S. D. M. 1996, ApJ, 462, 563

—. 1997, ApJ, 490, 493

Nomoto, K., Thielemann, F.-K., & Yokoi, K. 1984, ApJ, 286, 644

Nugent, P., Phillips, M., Baron, E., Branch, D., & Hauschildt, P. 1995, ApJ, 455, L147

Oguri, M. 2007, ApJ, 660, 1

Oguri, M., & Marshall, P. J. 2010, MNRAS, 405, 2579

Oke, J. B., Cohen, J. G., Carr, M., Cromer, J., Dingizian, A., Harris, F. H., Labrecque, S., Lucinio, R., Schaal, W., Epps, H., & Miller, J. 1995, PASP, 107, 375

Parrent, J. T., Thomas, R. C., Fesen, R. A., Marion, G. H., Challis, P., Garnavich, P. M., Milisavljevic, D., Vinkò, J., & Wheeler, J. C. 2011, ApJ, 732, 30

Pastorello, A., Valenti, S., Zampieri, L., Navasardyan, H., Taubenberger, S., Smartt, S. J., Arkharov, A. A., Bärnbantner, O., Barwig, H., Benetti, S., Birtwhistle, P., Botticella, M. T., Cappellaro, E., Del Principe, M., di Mille, F., di Rico, G., Dolci, M., Elias-Rosa, N., Efimova, N. V., Fiedler, M., Harutyunyan, A., Höflich, P. A., Kloehr, W., Larionov, V. M., Lorenzi, V., Maund, J. R., Napoleone, N., Ragni, M., Richmond, M., Ries, C., Spiro, S., Temporin, S., Turatto, M., & Wheeler, J. C. 2009, MNRAS, 394, 2266

Patel, B., McCully, C., Jha, S. W., Rodney, S. A., Jones, D. O., Graur, O., Merten, J., Zitrin, A., Riess, A. G., Matheson, T., Sako, M., Holoien, T. W.-S., Postman, M., Coe, D., Bartelmann, M., Balestra, I., Benitez, N., Bouwens, R., Bradley, L., Broadhurst, T., Cenko, S. B., Donahue, M., Filippenko, A. V., Ford, H., Garnavich, P., Grillo, C., Infante, L., Jouvel, S., Kelson, D., Koekemoer, A., Lahav, O., Lemze, D., Maoz, D., Medezinski, E., Melchior, P., Meneghetti, M., Molino, A., Moustakas, J., Moustakas, L. A., Nonino, M., Rosati, P., Seitz, S., Strolger, L. G., Umetsu, K., & Zheng, W. 2013, ArXiv, 1312.0943

Paturel, G., Petit, C., Prugniel, P., Theureau, G., Rousseau, J., Brouty, M., Dubois, P., & Cambrésy, L. 2003, A&A, 412, 45

Peng, C. Y., Ho, L. C., Impey, C. D., & Rix, H.-W. 2010, AJ, 139, 2097

Perets, H. B., Gal-Yam, A., Mazzali, P. A., Arnett, D., Kagan, D., Filippenko, A. V., Li, W., Arcavi, I., Cenko, S. B., Fox, D. B., Leonard, D. C., Moon, D.-S., Sand, D. J., Soderberg, A. M., Anderson, J. P., James, P. A., Foley, R. J., Ganeshalingam, M., Ofek, E. O., Bildsten, L., Nelemans, G., Shen, K. J., Weinberg, N. N., Metzger, B. D., Piro, A. L., Quataert, E., Kiewe, M., & Poznanski, D. 2010, Nature, 465, 322

Perlmutter, S., Aldering, G., Goldhaber, G., Knop, R. A., Nugent, P., Castro, P. G., Deustua, S., Fabbro, S., Goobar, A., Groom, D. E., Hook, I. M., Kim, A. G., Kim, M. Y., Lee, J. C., Nunes, N. J., Pain, R., Pennypacker, C. R., Quimby, R., Lidman, C., Ellis, R. S., Irwin, M., McMahon, R. G., Ruiz-Lapuente, P., Walton, N., Schaefer, B., Boyle, B. J., Filippenko, A. V., Matheson, T., Fruchter, A. S., Panagia, N., Newberg, H. J. M., Couch, W. J., & The Supernova Cosmology Project. 1999, ApJ, 517, 565

Perlmutter, S., Gabi, S., Goldhaber, G., Goobar, A., Groom, D. E., Hook, I. M., Kim, A. G., Kim, M. Y., Lee, J. C., Pain, R., Pennypacker, C. R., Small, I. A., Ellis, R. S., McMahon, R. G., Boyle, B. J., Bunclark, P. S., Carter, D., Irwin, M. J., Glazebrook, K., Newberg, H. J. M., Filippenko, A. V., Matheson, T., Dopita, M., Couch, W. J., & The Supernova Cosmology Project. 1997, ApJ, 483, 565

Petkova, M., Metcalf, R. B., & Giocoli, C. 2013, ArXiv, 1312.1536

Petters, A. O. 1995a, Journal of Mathematics and Physics, 36, 4263

—. 1995b, Journal of Mathematics and Physics, 36, 4276

Petters, A. O., Levine, H., & Wambsganss, J. 2001, Singularity theory and gravitational lensing, ed. Petters, A. O., Levine, H., & Wambsganss, J.

Petters, A. O., & Wicklin, F. J. 1995, MNRAS, 277, 1399

Phillips, M. M. 1993, ApJ, 413, L105

Phillips, M. M., Li, W., Frieman, J. A., Blinnikov, S. I., DePoy, D., Prieto, J. L., Milne, P., Contreras, C., Folatelli, G., Morrell, N., Hamuy, M., Suntzeff, N. B., Roth, M., González, S., Krzeminski, W., Filippenko, A. V., Freedman, W. L., Chornock, R., Jha, S., Madore, B. F., Persson, S. E., Burns, C. R., Wyatt, P., Murphy, D., Foley, R. J., Ganeshalingam, M., Serduke, F. J. D., Krisciunas, K., Bassett, B., Becker, A., Dilday, B., Eastman, J., Garnavich, P. M., Holtzman, J., Kessler, R., Lampeitl, H., Marriner, J., Frank, S., Marshall, J. L., Miknaitis, G., Sako, M., Schneider, D. P., van der Heyden, K., & Yasuda, N. 2007, PASP, 119, 360

Phillips, M. M., Lira, P., Suntzeff, N. B., Schommer, R. A., Hamuy, M., & Maza, J. 1999, AJ, 118, 1766

Phillips, M. M., Wells, L. A., Suntzeff, N. B., Hamuy, M., Leibundgut, B., Kirshner, R. P., & Foltz, C. B. 1992, AJ, 103, 1632

Planck Collaboration, Ade, P. A. R., Aghanim, N., Armitage-Caplan, C., Arnaud, M., Ashdown, M., Atrio-Barandela, F., Aumont, J., Baccigalupi, C., Banday, A. J., & et al. 2013, ArXiv, 1303.5062

Poznanski, D., Chornock, R., Nugent, P. E., Bloom, J. S., Filippenko, A. V., Ganeshalingam, M., Leonard, D. C., Li, W., & Thomas, R. C. 2010, Science, 327, 58

Premadi, P., Martel, H., & Matzner, R. 1998, ApJ, 493, 10

Rauch, K. P. 1991, ApJ, 374, 83

Refsdal, S. 1964, MNRAS, 128, 307

—. 1970, ApJ, 159, 357

Rhie, S. H., & Bennett, C. S. 2009, ArXiv, 0911.3050

Riess, A. G., Filippenko, A. V., Challis, P., Clocchiatti, A., Diercks, A., Garnavich, P. M., Gilliland, R. L., Hogan, C. J., Jha, S., Kirshner, R. P., Leibundgut, B., Phillips, M. M., Reiss, D., Schmidt, B. P., Schommer, R. A., Smith, R. C., Spyromilio, J., Stubbs, C., Suntzeff, N. B., & Tonry, J. 1998, AJ, 116, 1009

Riess, A. G., Macri, L., Casertano, S., Lampeitl, H., Ferguson, H. C., Filippenko, A. V., Jha, S. W., Li, W., Chornock, R., & Silverman, J. M. 2011, ApJ, 730, 119

Riess, A. G., Macri, L., Li, W., Lampeitl, H., Casertano, S., Ferguson, H. C., Filippenko, A. V., Jha, S. W., Chornock, R., Greenhill, L., Mutchler, M., Ganeshalingham, M., & Hicken, M. 2009, ApJS, 183, 109

Riess, A. G., Press, W. H., & Kirshner, R. P. 1996, ApJ, 473, 88

Röpke, F. K. 2005, A&A, 432, 969

Röpke, F. K. 2008, ArXiv, 0804.2147

Röpke, F. K., Woosley, S. E., & Hillebrandt, W. 2007, ApJ, 660, 1344

Rusin, D., Kochanek, C. S., Norbury, M., Falco, E. E., Impey, C. D., Lehár, J., McLeod, B. A., Rix, H., Keeton, C. R., Muñoz, J. A., & Peng, C. Y. 2001, ApJ, 557, 594

Saha, P., Coles, J., Macciò, A. V., & Williams, L. L. R. 2006, ApJ, 650, L17

Sahu, D. K., Tanaka, M., Anupama, G. C., Kawabata, K. S., Maeda, K., Tominaga, N., Nomoto, K., Mazzali, P. A., & Prabhu, T. P. 2008, ApJ, 680, 580

Sako, M., Bassett, B., Becker, A., Cinabro, D., DeJongh, F., Depoy, D. L., Dilday, B., Doi, M., Frieman, J. A., Garnavich, P. M., Hogan, C. J., Holtzman, J., Jha, S., Kessler, R., Konishi, K., Lampeitl, H., Marriner, J., Miknaitis, G., Nichol, R. C., Prieto, J. L., Riess, A. G., Richmond, M. W., Romani, R., Schneider, D. P., Smith, M., Subba Rao, M., Takanashi, N., Tokita, K., van der Heyden, K., Yasuda, N., Zheng, C., Barentine, J., Brewington, H., Choi, C., Dembicky, J., Harnavek, M., Ihara, Y., Im, M., Ketzeback, W., Kleinman, S. J., Krzesiński, J., Long, D. C., Malanushenko, E., Malanushenko, V., McMillan, R. J., Morokuma, T., Nitta, A., Pan, K., Saurage, G., & Snedden, S. A. 2008, AJ, 135, 348

Scalzo, R. A., Aldering, G., Antilogus, P., Aragon, C., Bailey, S., Baltay, C., Bongard, S., Buton, C., Childress, M., Chotard, N., Copin, Y., Fakhouri, H. K., Gal-Yam, A., Gangler, E., Hoyer, S., Kasliwal, M., Loken, S., Nugent, P., Pain, R., Pécontal, E., Pereira, R., Perlmutter, S., Rabinowitz, D., Rau, A., Rigaudier, G., Runge, K., Smadja, G., Tao, C., Thomas, R. C., Weaver, B., & Wu, C. 2010, ApJ, 713, 1073

Schneider, P. 1997, MNRAS, 292, 673

Schneider, P., Ehlers, J., & Falco, E. E. 1992, Gravitational Lenses, ed. Schneider, P., Ehlers, J., & Falco, E. E.

Schneider, P., & Sluse, D. 2013, A&A, 559, A37

Schneider, P., & Weiss, A. 1988a, ApJ, 327, 526

—. 1988b, ApJ, 330, 1

Seitenzahl, I. R., Ciaraldi-Schoolmann, F., Röpke, F. K., Fink, M., Hillebrandt, W., Kromer, M., Pakmor, R., Ruiter, A. J., Sim, S. A., & Taubenberger, S. 2013, MNRAS, 429, 1156

Seitz, S., & Schneider, P. 1994, A&A, 287, 349

Seljak, U. 1994, ApJ, 436, 509

Shara, M. M., Bibby, J. L., Zurek, D., Crowther, P. A., Moffat, A. F. J., & Drissen, L. 2013, AJ, 146, 162

Silverman, J. M., & Filippenko, A. V. 2012, MNRAS, 425, 1917

Silverman, J. M., Foley, R. J., Filippenko, A. V., Ganeshalingam, M., Barth, A. J., Chornock, R., Griffith, C. V., Kong, J. J., Lee, N., Leonard, D. C., Matheson, T., Miller, E. G., Steele, T. N., Barris, B. J., Bloom, J. S., Cobb, B. E., Coil, A. L., Desroches, L.-B., Gates, E. L., Ho, L. C., Jha, S. W., Kandrashoff, M. T., Li, W., Mandel, K. S., Modjaz, M., Moore, M. R., Mostardi, R. E., Papenkova, M. S., Park, S., Perley, D. A., Poznanski, D., Reuter, C. A., Scala, J., Serduke, F. J. D., Shields, J. C., Swift, B. J., Tonry, J. L., Van Dyk, S. D., Wang, X., & Wong, D. S. 2012, MNRAS, 425, 1789

Silverman, J. M., Ganeshalingam, M., & Filippenko, A. V. 2013, MNRAS, 430, 1030

Silverman, J. M., Ganeshalingam, M., Li, W., Filippenko, A. V., Miller, A. A., & Poznanski, D. 2011, MNRAS, 410, 585

Sirianni, M., Jee, M. J., Benítez, N., Blakeslee, J. P., Martel, A. R., Meurer, G., Clampin, M., De Marchi, G., Ford, H. C., Gilliland, R., Hartig, G. F., Illingworth, G. D., Mack, J., & McCann, W. J. 2005, PASP, 117, 1049

Sluse, D., Chantry, V., Magain, P., Courbin, F., & Meylan, G. 2012, A&A, 538, A99

Sluse, D., Surdej, J., Claeskens, J.-F., Hutsemékers, D., Jean, C., Courbin, F., Nakos, T., Billeres, M., & Khmil, S. V. 2003, A&A, 406, L43

Smartt, S. J. 2009, ARA&A, 47, 63

Sollerman, J., Lindahl, J., Kozma, C., Challis, P., Filippenko, A. V., Fransson, C., Garnavich, P. M., Leibundgut, B., Li, W., Lundqvist, P., Milne, P., Spyromilio, J., & Kirshner, R. P. 2004, A&A, 428, 555

Sonnenfeld, A., Treu, T., Gavazzi, R., Marshall, P. J., Auger, M. W., Suyu, S. H., Koopmans, L. V. E., & Bolton, A. S. 2012, ApJ, 752, 163

Soucail, G., Kneib, J.-P., Jaunsen, A. O., Hjorth, J., Hattori, M., & Yamada, T. 2001, A&A, 367, 741

Spyromilio, J., Meikle, W. P. S., Allen, D. A., & Graham, J. R. 1992, MNRAS, 258, 53P

Stanishev, V., Goobar, A., Benetti, S., Kotak, R., Pignata, G., Navasardyan, H., Mazzali, P., Amanullah, R., Garavini, G., Nobili, S., Qiu, Y., Elias-Rosa, N., Ruiz-Lapuente, P., Mendez, J., Meikle, P., Patat, F., Pastorello, A., Altavilla, G., Gustafsson, M., Harutyunyan, A., Iijima, T., Jakobsson, P., Kichizhieva, M. V., Lundqvist, P., Mattila, S., Melinder, J., Pavlenko, E. P., Pavlyuk, N. N., Sollerman, J., Tsvetkov, D. Y., Turatto, M., & Hillebrandt, W. 2007a, A&A, 469, 645

Stanishev, V., Taubenberger, S., Blanc, G., Anupama, G. C., Benetti, S., Cappellaro, E., Elias-Rosa, N., Féron, C., Goobar, A., Krisciunas, K., Pastorello, A., Sahu, D. K., Salvo, M. E., Schmidt, B. P., Sollerman, J., Thöne, C. C., Turatto, M., & Hillebrandt, W. 2007b, in American Institute of Physics Conference Series, Vol. 924, The Multicolored Landscape of Compact Objects and Their Explosive Origins, ed. T. di Salvo, G. L. Israel, L. Piersant, L. Burderi, G. Matt, A. Tornambe, & M. T. Menna, 336–341

Stritzinger, M. D., Hsiao, E., Valenti, S., Taddia, F., Rivera-Thorsen, T. J., Leloudas, G., Maeda, K., Pastorello, A., Phillips, M. M., Pignata, G., Baron, E., Burns, C. R., Contreras, C., Folatelli, G., Hamuy, M., Höflich, P., Morrell, N., Prieto, J. L., Benetti, S., Campillay, A., Haislip, J. B., LaClutze, A. P., Moore, J. P., & Reichart, D. E. 2014, A&A, 561, A146

Sullivan, M., Guy, J., Conley, A., Regnault, N., Astier, P., Balland, C., Basa, S., Carlberg, R. G., Fouchez, D., Hardin, D., Hook, I. M., Howell, D. A., Pain, R., Palanque-Delabrouille, N., Perrett, K. M., Pritchet, C. J., Rich, J., Ruhlmann-Kleider, V., Balam, D., Baumont, S., Ellis, R. S., Fabbro, S., Fakhouri, H. K., Fourmanoit, N., González-Gaitán, S., Graham, M. L., Hudson, M. J., Hsiao, E., Kronborg, T., Lidman, C., Mourao,

A. M., Neill, J. D., Perlmutter, S., Ripoche, P., Suzuki, N., & Walker, E. S. 2011, ApJ, 737, 102

Suyu, S. H. 2012, MNRAS, 426, 868

Suyu, S. H., Auger, M. W., Hilbert, S., Marshall, P. J., Tewes, M., Treu, T., Fassnacht, C. D., Koopmans, L. V. E., Sluse, D., Blandford, R. D., Courbin, F., & Meylan, G. 2013, ApJ, 766, 70

Suyu, S. H., Marshall, P. J., Auger, M. W., Hilbert, S., Blandford, R. D., Koopmans, L. V. E., Fassnacht, C. D., & Treu, T. 2010, ApJ, 711, 201

Taubenberger, S., Benetti, S., Childress, M., Pakmor, R., Hachinger, S., Mazzali, P. A., Stanishev, V., Elias-Rosa, N., Agnoletto, I., Bufano, F., Ergon, M., Harutyunyan, A., Inserra, C., Kankare, E., Kromer, M., Navasardyan, H., Nicolas, J., Pastorello, A., Prosperi, E., Salgado, F., Sollerman, J., Stritzinger, M., Turatto, M., Valenti, S., & Hillebrandt, W. 2011, MNRAS, 412, 2735

Taubenberger, S., Kromer, M., Pakmor, R., Pignata, G., Maeda, K., Hachinger, S., Leibundgut, B., & Hillebrandt, W. 2013, ApJ, 775, L43

Theureau, G., Bottinelli, L., Coudreau-Durand, N., Gouguenheim, L., Hallet, N., Loulergue, M., Paturel, G., & Teerikorpi, P. 1998, A&AS, 130, 333

Thomas, R. C., Aldering, G., Antilogus, P., Aragon, C., Bailey, S., Baltay, C., Baron, E., Bauer, A., Buton, C., Bongard, S., Copin, Y., Gangler, E., Gilles, S., Kessler, R., Loken, S., Nugent, P., Pain, R., Parrent, J., Pécontal, E., Pereira, R., Perlmutter, S., Rabinowitz, D., Rigaudier, G., Runge, K., Scalzo, R., Smadja, G., Wang, L., Weaver, B. A., & Nearby Supernova Factory. 2007, ApJ, 654, L53

Thomas, R. C., Aldering, G., Antilogus, P., Aragon, C., Bailey, S., Baltay, C., Bongard, S., Buton, C., Canto, A., Childress, M., Chotard, N., Copin, Y., Fakhouri, H. K., Gangler, E., Hsiao, E. Y., Kerschhaggl, M., Kowalski, M., Loken, S., Nugent, P., Paech, K., Pain, R., Pecontal, E., Pereira, R., Perlmutter, S., Rabinowitz, D., Rigault, M., Rubin, D., Runge, K., Scalzo, R., Smadja, G., Tao, C., Weaver, B. A., Wu, C., Brown, P. J., Milne, P. A., & Nearby Supernova Factory. 2011a, ApJ, 743, 27

Thomas, R. C., Nugent, P. E., & Meza, J. C. 2011b, PASP, 123, 237

Tonry, J. L. 1998, AJ, 115, 1

Tonry, J. L., & Kochanek, C. S. 1999, AJ, 117, 2034

—. 2000, AJ, 119, 1078

Treu, T. 2010, ARA&A, 48, 87

Treu, T., Marshall, P. J., Cyr-Racine, F.-Y., Fassnacht, C. D., Keeton, C. R., Linder, E. V., Moustakas, L. A., Bradac, M., Buckley-Geer, E., Collett, T., Courbin, F., Dobler, G., Finley, D. A., Hjorth, J., Kochanek, C. S., Komatsu, E., Koopmans, L. V. E., Meylan, G., Natarajan, P., Oguri, M., Suyu, S. H., Tewes, M., Wong, K. C., Zabludoff, A. I., Zaritsky, D., Anguita, T., Brunner, R. J., Cabanac, R., Falco, E. E., Fritz, A., Seidel, G., Howell, D. A., Giocoli, C., Jackson, N., Lopez, S., Metcalf, R. B., Motta, V., & Verdugo, T. 2013, ArXiv, 1306.1272

Turner, E. L. 1990, ApJ, 365, L43

Valenti, S., Pastorello, A., Cappellaro, E., Benetti, S., Mazzali, P. A., Manteca, J., Taubenberger, S., Elias-Rosa, N., Ferrando, R., Harutyunyan, A., Hentunen, V. P., Nissinen, M., Pian, E., Turatto, M., Zampieri, L., & Smartt, S. J. 2009, Nature, 459, 674

Valenti, S., Yuan, F., Taubenberger, S., Maguire, K., Pastorello, A., Benetti, S., Smartt, S. J., Cappellaro, E., Howell, D. A., Bildsten, L., Moore, K., Stritzinger, M., Anderson, J. P., Benitez-Herrera, S., Bufano, F., Gonzalez-Gaitan, S., McCrum, M. G., Pignata, G., Fraser, M., Gal-Yam, A., Le Guillou, L., Inserra, C., Reichart, D. E., Scalzo, R., Sullivan, M., Yaron, O., & Young, D. R. 2014, MNRAS, 437, 1519

van Dyk, S. D. 1992, AJ, 103, 1788

Vuissoz, C., Courbin, F., Sluse, D., Meylan, G., Chantry, V., Eulaers, E., Morgan, C., Eyler, M. E., Kochanek, C. S., Coles, J., Saha, P., Magain, P., & Falco, E. E. 2008, A&A, 488, 481

Waldman, R., Sauer, D., Livne, E., Perets, H., Glasner, A., Mazzali, P., Truran, J. W., & Gal-Yam, A. 2011, ApJ, 738, 21

Wambsganss, J., Bode, P., & Ostriker, J. P. 2005, ApJ, 635, L1

Wambsganss, J., Cen, R., & Ostriker, J. P. 1998, ApJ, 494, 29

Wang, X., Wang, L., Filippenko, A. V., Zhang, T., & Zhao, X. 2013, Science, 340, 170

Werner, M. C., An, J., & Evans, N. W. 2008, MNRAS, 391, 668

Wheeler, J. C., & Harkness, R. P. 1990, Reports on Progress in Physics, 53, 1467

Wiklind, T., Dickinson, M., Ferguson, H. C., Giavalisco, M., Mobasher, B., Grogin, N. A., & Panagia, N. 2008, ApJ, 676, 781

Williams, L. L. R., Foley, P., Farnsworth, D., & Belter, J. 2008, ApJ, 685, 725

Winn, J. N., Kochanek, C. S., Keeton, C. R., & Lovell, J. E. J. 2003, ApJ, 590, 26

Witt, H. J., Mao, S., & Keeton, C. R. 2000, ApJ, 544, 98

Wong, K. C., Keeton, C. R., Williams, K. A., Momcheva, I. G., & Zabludoff, A. I. 2011, ApJ, 726, 84

Wong, M. H., Pavlovsky, C., Long, K., et al. 2010, Wide Field Camera 3 Instrument Handbook, Version 2.0 (Baltimore: STScI)

Wong, O. I., Ryan-Weber, E. V., Garcia-Appadoo, D. A., Webster, R. L., Staveley-Smith, L., Zwaan, M. A., Meyer, M. J., Barnes, D. G., Kilborn, V. A., Bhathal, R., de Blok, W. J. G., Disney, M. J., Doyle, M. T., Drinkwater, M. J., Ekers, R. D., Freeman, K. C., Gibson, B. K., Gurovich, S., Harnett, J., Henning, P. A., Jerjen, H., Kesteven, M. J., Knezek, P. M., Koribalski, B. S., Mader, S., Marquarding, M., Minchin, R. F., O'Brien, J., Putman, M. E., Ryder, S. D., Sadler, E. M., Stevens, J., Stewart, I. M., Stootman, F., & Waugh, M. 2006, MNRAS, 371, 1855

Wood-Vasey, W. M., Miknaitis, G., Stubbs, C. W., Jha, S., Riess, A. G., Garnavich, P. M., Kirshner, R. P., Aguilera, C., Becker, A. C., Blackman, J. W., Blondin, S., Challis, P., Clocchiatti, A., Conley, A., Covarrubias, R., Davis, T. M., Filippenko, A. V., Foley, R. J., Garg, A., Hicken, M., Krisciunas, K., Leibundgut, B., Li, W., Matheson, T., Miceli, A., Narayan, G., Pignata, G., Prieto, J. L., Rest, A., Salvo, M. E., Schmidt, B. P., Smith, R. C., Sollerman, J., Spyromilio, J., Tonry, J. L., Suntzeff, N. B., & Zenteno, A. 2007, ApJ, 666, 694

Woosley, S. E., & Weaver, T. A. 1994, ApJ, 423, 371

Woudt, P. A., Steeghs, D., Karovska, M., Warner, B., Groot, P. J., Nelemans, G., Roelofs, G. H. A., Marsh, T. R., Nagayama, T., Smits, D. P., & O'Brien, T. 2009, ApJ, 706, 738

Yang, X., Mo, H. J., van den Bosch, F. C., Zhang, Y., & Han, J. 2012, ApJ, 752, 41

Young, P., Gunn, J. E., Oke, J. B., Westphal, J. A., & Kristian, J. 1981, ApJ, 244, 736

Zitrin, A., Meneghetti, M., Umetsu, K., Broadhurst, T., Bartelmann, M., Bouwens, R., Bradley, L., Carrasco, M., Coe, D., Ford, H., Kelson, D., Koekemoer, A. M., Medezinski, E., Moustakas, J., Moustakas, L. A., Nonino, M., Postman, M., Rosati, P., Seidel, G., Seitz, S., Sendra, I., Shu, X., Vega, J., & Zheng, W. 2013, ApJ, 762, L30